University of Mohamed Boudiaf-M’sila

FACULTY OF TECHNOLOGY

DEPARTMENT OF ELECTRONIC

Serial number:……..……..
Registration number: DE//07/15

Thesis

Presented for the graduation of

DOCTORAT OF SCIENCES

Field: Electronic
Option: Microelectronics

THEME

Contribution to the control of metal oxide thin films properties: analysis, characterization, and applications.

Presented by:
Rahal Abdelghani

Defended the: 08/11/2025

Jury members:

Mr. Mounir BOURAS	Prof. University of M’sila	Chairman
Mr. Idris BOUCHAMA	Prof. University of M’sila	Supervisor
Mr. Mohamed Amine GHEBOULI	Prof. University of M’sila	Co-supervisor
Mr. Mohamed Redha KHELLADI	Prof. University of BBA	Examiner
Mr. Djellal CHERRAD	Prof. University of Setif1	Examiner
Mr. Mounir REFFAS	M.C.A. University of Setif1	Examiner

2024/2025

Dedication

I dedicate this humble work to my entire family in general and to my dear wife in particular.

To those who did not live to see the fruit of their upbringing and toil, may it be in the balance of their good deeds.

To the spirits of my parents, May Allah have mercy on them.

Rahal Abdelghani

Acknowledgements

First and foremost, I thank and praise **Allah**, who gave me the strength and willpower to accomplish and complete this thesis.

I would like to express my sincere thanks to my thesis supervisor, Prof. **Bouchama Idris**, Professor at the Faculty of Technology, Mohamed Boudiaf University, M'sila, for the trust he placed in me by agreeing to give me the opportunity to work on this thesis subject. His scientific skills, his advice and the fact that he left the initiative to me enabled me to complete this work in excellent conditions. I was also extremely appreciative of his human qualities, his ability to listen and his understanding throughout this work.

I would like to express my deepest gratitude to my thesis co-supervisor Prof. **Ghebouli Mohamed Amine**, Professor at the Faculty of Science, Mohamed Boudiaf University, M'sila. Thank you for all the patience and availability he showed me. His advice and constructive comments enabled me to greatly improve the quality of my work and this thesis. His constant encouragement gave me the self-confidence to see this thesis through to the end.

I would like to express my heartfelt gratitude to the jury members – Prof. **Bouras Mounir**, Prof. **KHELLADI Mohamed Redha**, Prof. **CHERRAD Djellal**, and Dr. **REFFAS Mounir** – for their genuine interest in my research and their kind willingness to serve on my thesis committee.

I would like to thank everyone who helped me in finishing this thesis, especially the doctoral student **Abid Imen**, the engineers **Kanzour Abdelghani, Hamidouche Mohamed, Maayouche Rabie**, and the honorable professors **Mesalti Abdelghafour**, **Chelouche Azzeddine**, **Bahloul Ahmed**, **Messaoudi Yazid**, and **Bennouioua Tahar**, in addition I cannot fail to express my sincere gratitude to Professor **Haddadi Khelifa**, director of the Research Unit in Emerging Materials, Farhat Abbas University, Setif.

Finally, I would like to pay a special tribute to my dear wife, who has always encouraged and supported me, taught me the value of hard work and knowledge, and been patient with me all these years, for which I am very grateful.

Rahal Abdelghani

List of Figures

List of Tables

TABLE OF CONTENTS

Chapter I: Overview of Metallic Oxide Materials

Chapter II: Preparation and Characterization of ZnO Thin Films Deposited By Spray Pyrolysis

Chapter III: Elaboration and characterization of Cu_2O thin films using electrodeposition method

Chapter IV: Ab-initio Computational Study of Fundamental Properties of CuO and Cu_2O Compounds

Chapter V: Application of Metallic Oxide Thin Films in Modern Solar Cell Design

General introduction

General introduction

Energy needs have been a significant concern for human civilizations since we first became human. Historically, energy sources tended to be limited in availability and renewable, namely, wood for fire, wind for sailing ships, and water for mills. Such abundant, natural resources met the basic needs of populations to heat their homes, cook meals, and support early agricultural and handicraft work [1].

As the Industrial Revolution and society grew, it drastically increased our energy consumption. This energy usage heavily relied on fossil fuel sources, such as coal, oil, and natural gas. While these energy sources offered unprecedented progress in industrial and technological advances, they had the consequence of causing a range of irreversible environmental impacts, including environmental pollution; greenhouse gas caused global warming, and the depletion of natural resources.

Renewable energy offers a modern remedy to these challenges, which adheres to traditional systems. Renewable energy sources like water, the sun, wind, and biomass offer the promise of long-term solutions to the increasing demands of energy for human activity while lessening environmental impact. This direction of renewable energy systems also exhibits a universal commitment to finding a balance in human advancement and environmental protection by reinstating the basic principles of harmony with nature exemplified in earlier societies [2].

In this context, metal oxides have become critical materials for the development and improvement of renewable energy systems. Metal oxides are at the forefront of many sustainable energy developments attributed to their unique properties, such as conductive behavior, chemical stability, and light-interacting properties [3].

Many uses of renewable energy rely heavily on these materials. For example, as complex oxides, perovskites are paving the way toward novel, high-performance solar technologies, while zinc oxide (ZnO), titanium dioxide (TiO_2), and copper oxides (CuO and Cu_2O) are significant components of photovoltaic solar cells. In addition, metal oxides such as cobalt and ferrites are also used as catalysts in energy conversion processes; for example, during the electrolysis of water to produce hydrogen as an alternative and renewable clean energy source [4].

Metal oxide research continues to grow in importance in renewable technology, providing inventive approaches to reducing costs and improving energy efficiency. Thus, one key component in addressing the energy and environmental challenges of the 21st century is the synergy of metal oxides with renewable energy [5].

Zinc oxide (ZnO) and copper oxides (CuO) are inorganic compounds that possess unique properties, which are of interest in many scientific and technological fields. These metal oxides have great versatility and can be found in everything from electronic devices to renewable energy to antimicrobial substances to catalysis [6].

Zinc oxide (ZnO) is an n-type semiconductor with a broad bandgap and exhibits a wide range of optical, electronic, and piezoelectric properties. It has found its applications in solar cells [7, 8], light-emitting diodes (LEDs) [9-11], gas sensors [12], and photovoltaic applications. In addition, ZnO is non-toxic, has relatively high abundance, and is compatible with nanostructures, allowing for even broader applications in nanotechnology and optoelectronic devices.

On the other hand, copper(II) oxide (CuO) is a p-type semiconductor that is well-known for its remarkable catalytic properties and narrow bandgap. It is commonly used in the degradation of organic pollutants [18–21] and energy conversion mechanisms such as photocatalysis and hydrogen production [13–17]. It is especially advantageous for solar and environmental applications, chiefly because it can absorb visible light [22–24].

Copper(I) oxide (Cu_2O) is a prototypical p-type semiconductor with a deal of attention being given to it due to its defining characteristics and its ability to be employed in many technology implementations. Having a bandgap of approximately 2.1 to 2.2 eV [25–27] with a stable, crystalline, and inexpensive solid-state material is attractive, particularly considering absorption of visible light [28, 29]. The fundamental characteristics of CuO make this material a promising solution in industries such as environmental technology, optoelectronic devices, and renewable energy. Cu_2O is used in the energy sector by way of heterojunction-based solar cells, where absorption of visible light allows for better photovoltaic efficiency by optimizing the performance of the solar cell [30–32]. It is also pivotal to photocatalysis, as the material can break down organic contaminants and generate hydrogen via water splitting [33]. Furthermore, due to its chemical reactivity and electrical conductivity, it serves as a highly efficient catalyst for redox processes [34, 35]. Given its availability, low toxicity, and environmentally benign attributes, copper(I) oxide has potential as a material in some of the world's more pressing objectives in sustainable technology, energy, and environmental solutions.

While each of these oxides has unique properties, they exhibit exciting synergies in heterostructured systems and can provide new routes to energy, electronics, and environmental applications. Continued research into these materials is informing innovation in advanced materials and sustainable technology [36].

In conjunction with the experimental approach, ab initio calculations based on density functional theory (*DFT*) allow for the exploration of the electronic and structural properties of materials at the atomic scale. The CASTEP software (Cambridge Serial Total Energy Package), employed in conjunction with the Materials Studio platform, allows you to simulate crystal structures and calculate the electronic density of states (DOS), band structure, and charge density. The simulations will help to provide a better understanding of the defects, such as oxygen vacancies or doping, and their effect on the electronic properties of the material and therefore help to inform the technologist in a given situation by aiding in choosing the appropriate signal enhancement material for a specific electrochemical application [37].

SCAPS (Solar Cell Capacitance Simulator) was developed by Ghent University as modeling software specifically for the study of thin-film solar cells, primarily CdTe, $Cu(In,Ga)Se_2$ (CIGS), ZnO, Cu_2O, CuO, and many other materials. It solves the fundamental charge transport equations to model the electrical and optoelectronic behavior of multilayers. SCAPS can provide simulated outputs such as *J-V* curves, *C-V* profiles, and *QE* spectra by taking into account various physical parameters, including bandgap, doping levels, defects, recombination, and optical properties. It is very useful for evaluating alternate device designs, tuning layer properties, and simulating the impact of defects. Due to its flexibility, it is often used in research for the design, optimization, and performance prediction of solar cells [38].

In this manuscript, there are five chapters:

The **first chapter** consists of the literature review; we begin with mentioning thin-films of zinc and copper metal oxides, and their structural, electrical, electronic, optical, magnetic, and optoelectronic properties. We outline various production and characterization methods used for these thin-films, and then describe the core application areas of these metal oxides.

The **second chapter** focuses on the description of the experimental setup, substrate preparation, and deposition solution. This chapter examines the evolution of ZnO thin films on glass substrates through the pneumatic spray pyrolysis process. It also investigates the structural, morphological, electrical, electronic, and optical characteristics of ZnO layers, and this includes the effect that manganese (Mn) doping has on those characteristics. Also presented to enhance the experimental approach are calculations ab initio based on density functional theory (*DFT*).

The build-up of copper (I) oxide (Cu_2O) thin films on indium tin oxide (ITO) substrates by electrodeposition at different bath temperatures, and the electrical, optical, structural, and morphological characterization of these films, are the subject of the **third chapter**.

The **fourth chapter** investigates the structural, optical, and electrical properties of the copper oxides CuO and Cu_2O by evaluating a series of outcomes based on our simulations using the CASTEP simulator. We evaluate and compare these results in relation to the theoretical methods discussed previously.

The **last chapter** includes the thin-film solar cells based on CuO and Cu_2O absorbers simulated by SCAPS-1D, the discussion and interpretation of the data obtained from the modeling of our ZnO/CdS/CuO and ZnO/CdS/Cu_2O heterojunction solar cells. The obtained features are researched and analyzed under the effect of the adjustment of the physical and geometric parameters of the different thin layers composing our cell, such as the thickness of the absorbing layer, the density of acceptor states, and the density of defect states.

We conclude this manuscript with a general conclusion summarizing the main results of this work.

References

[1] Vaclav Smil, Energy and Civilization: A History, the MIT Press, Cambridge, USA, (2017).

[2] A. Khattabi, F. Z. Amrane, Les énergies renouvelables levier de transition entéritique et de développement territorial durable au Maroc : cas de la région de Tanger, Revue Économie & Kapital 1(2), 1–17, (2022).

[3] S. Gelin et al., PRX Energy 3, 013007, (2024).

[4] A. Singh, B. Arora, N. Verma, Journal of Energy Chemistry 59, 683–709, (2021).

[5] M. S. S. Danish et al., Metals 10(12), 1604, (2020).

[6] S. Zaman, Synthesis of ZnO, CuO and Their Composite Nanostructures for Optoelectronics, Sensing and Catalytic Applications, Phd Theses, Linkopings Universitet, Sweden, 31250061, (2012).

[7] J. A. Aranovich, D. Golmayo, A. L. Fahrenbruch, R. H. Bube, J. Appl. Phys. 51, 4260–4268, (1980).

[8] Z. C. Jin, I. Hamberg, C. G. Granqvist, B. E. Sernelius, K. F. Berggren, Thin Solid Films 164, 381–386, (1988).

[9] J. B. Webb, D. F. Williams, M. Buchanan, Appl. Phys. Lett. 39, 640–642, (1981).

[10] M. J. Brett, R. W. McMahon, J. Affinito, R. R. Parsons, J. Vac. Sci. Technol. A 1, 352–355, (1983).

[11] T. Minami, H. Nanto, S. Takata, Thin Solid Films 124(1), 43–47, (1985).

[12] S. Pizzini, N. Butta, D. Narducci, M. Palladino, J. Electrochem. Soc. 136, 1945, (1989).

[13] Z. Singh, I. Singh, Sci. Rep. 9, 1–13, (2019).

[14] M.Q. Khan, D. Kharaghani, N. Nishat, A. Shahzad, T. Hussain, Z. Khatri, C. Zhu, I. S. Kim, J. Mater. Res. Technol. 8, 1328–1334, (2019).

[15] M. P. Rao, V. K. Ponnusamy, J. J. Wu, A. M. Asiri, S. Anandan, J. Environ. Chem. Eng. 6, 6059–6068, (2018).

[16] R. Jana, A. Dey, M. Das, J. Datta, P. Das, P. P. Ray, Appl. Surf. Sci. 452, 155–164, (2018).

[17] H. C. Ananda, Murthy, T. D. Zeleke, K.B. Tan, S. Ghotekar, M. Alam, R. Balachandran, K. Y. Chan, P. F. Sanaulla, M. R. Anil Kumar, C. R. Ravikumar, Results Chem. 3, 100141, (2021).

[18] S. T. Al-Asadi, F. F. Al-Qaim, Eurasian Chem. Commun. 5, 794–811, (2023).

[19] S.S. Karbasaki, G. Bagherzade, B. Maleki, M. Ghani, J. Taiwan Inst. Chem. Eng. 118, 342–354, (2021).

[20] K. G. Chandrappa, T. V. Venkatesha, J. Exp. Nanosci. 8, 516–532, (2013).

[21] K.G. Chandrappa, T.V. Venkatesha, Mater. Corros. 64, 831–839, (2013).

[22] E. Parvizi, R. Tayebee, E. Koushki, M. F. Abdizadeh, B. Maleki, P. Audebert, L. Galmiche, RSC Adv. 9, 23818–23831, (2019).

[23] M. Alidadykhah, H. Peyman, H. Roshanfekr, Chem. Methodol. 5, 96–106, (2021).

[24] Y. K. Sadiq, Reactions 7, 112–122, (2023).

[25] L. C. Olsen, F. W. Addis, W. Miller, Sol. Cells 7(3), 247–279, (1982).

[26] W. M. Sears, E. Fortin, Sol. Energy Mater. 10(1), 93–103, (1984).

[27] B. P. Rai, Sol. Cells 25(3), 265–272, (1988).

[28] K. R. Balasubramaniam, V. M. Kao, J Ravichandran, P. B. Rossen, W. Siemons, J. W. Ager III, Thin Solid Films 520(11), 3914–3917, (2012).

[29] Y. Lin, W. J. Chen, J. Lu, et *al*. Nanoscale Res. Lett. 7, 401, (2012).

[30] N. Soundaram, R. Chandramohan, S. Valanarasu, R. Thomas, A. Kathalingam, J. Mater. Sci. Mater. Electron. 26(7), 5030–5036, (2015).

[31] R. P. Wijesundera, L. K. A. D. D. S. Gunawardhana, W. Siripala, Sol. Energy Mater. Sol. Cells 157, 881–886, (2016).

[32] D. S. C. Halin, I. A. Talib, A. R. Daud, M. A. A. Hamid, Int. J. Photoenergy 2014, 1–6, (2014).

[33] J. Dong, H. Xu, F. Zhang, Ch. Chen, L. Liu, G. T. Wu, Appl. Catal., A 470, 294–302, (2014).

[34] Q. Ma, J. P. Hofmann, A. Litke, E. J. M. Hensen, Sol. Energy Mater. Sol. Cells 141, 178–186, (2015).

[35] Z. Zhang, P. Wang, J. Mater. Chem. 22, 2456–2464, (2012).

[36] Y. Zhang, X. Wang, Y. Li, Nano Materials Science 4(1), 1–15, (2022).

[37] S. J. Clark, M. D. Segall, C. J. Pickard, P. J. Hasnip, M. I. J. Probert, K. Refson, M. C. Payne, Z. Kristallogr. 220, 567–570, (2005).

[38] M. Burgelman, P. Nollet, S. Degrave, Thin Solid Films 361–362, 527–532, (2000).

Chapter I

Overview of Metallic Oxide Materials

I.1 Introduction

Metal oxides are among the most abundant groups of compounds found on Earth, exhibiting a broad spectrum of chemical compositions, atomic structures, and crystalline forms. These materials possess unique functionalities rarely found or less effective in other solids. Notably, metal oxides form a varied and appealing class of materials that encompasses the entire range of electronic properties, from insulators and semiconductors to metallic and superconducting phases. Additionally, metal oxides display almost all known phenomena, including superconductivity, thermoelectricity, photo-electricity, luminescence, and magnetism. Consequently, metal oxides have emerged as a vital category of multifunctional materials, rich in properties and highly promising for a wide range of device application [1].

A metallic oxide is a chemical compound formed by combining metal and oxygen atoms. It is typically represented by a formula like $M_{1x}M_{2y}O_z$, where "M" stands for the metal, "O" is oxygen, and "x," "y," and "z" are natural numbers indicating the ratio of atoms. Common examples of metallic oxides include zinc oxide (ZnO), copper oxides (CuO and Cu_2O), aluminum oxide (Al_2O_3), iron oxides (Fe_2O_3 and Fe_3O_4), tin oxide (SnO_2), and barium titanate ($BaTiO_3$).

There are two main families of metallic oxides based on the nature of conduction. The first family includes p-type oxides (hole conduction) such as SnO_2, WO_3, ZnO, TiO_2, In_2O_3, and Ta_2O_5. These oxides are relatively unstable due to their tendency to exchange oxygen atoms in their structure with the air. The second family comprises n-type oxides (electron conduction) such as NiO, PdO, La_2O_3, TeO_2, Ag_2O, BaTiO, CuO, and Cu_2O. These are more stable and exhibit more favorable properties for chemisorption [2–4].

Metal oxide materials involve introducing specific atoms, known as dopants, into the crystal lattice of a semiconductor or insulator. In n-type doping, the dopant replaces a lattice atom, leaving behind an extra-unbound electron. This electron forms a donor energy level near the conduction band, making it easier for electrons to move into the conduction band and contribute to conductivity. In p-type doping, the dopant creates a shortage of electrons in the lattice, resulting in an empty acceptor energy level just above the valence band. Electrons from the valence band can fill this level, leaving behind a positive "hole," which moves through the material and facilitates electrical conduction [5].

Metallic oxides are classified into two major categories: simple metallic oxides, which consist of a single metal (e.g., SnO_2, TiO_2, SiO_2), and mixed metallic oxides, which contain two or more metals (e.g., $BaTiO_3$, $CaTiO_3$, Mg_2SiO_4, $Mg_xZn_yFe_zO$, $SnWO_4$).

Transparent conducting thin films are materials that combine high electrical conductivity with good transparency in visible light [6]. Since their invention, significant research and development have focused on turning these coatings into commercial products. Today, most commercial applications use n-doped metal oxide thin films, commonly called Transparent Conducting Oxides (TCOs).

K. Badeker [7], who applied a thin layer of cadmium via sputtering and then heated it in air, created the first TCO in 1907. This process partially oxidized the cadmium, forming a non-stoichiometric cadmium oxide with oxygen vacancies in its structure. These vacancies gave rise to pentavalent cadmium ions, which created defect energy levels that enabled electrons to move into the conduction band of the cadmium oxide. This breakthrough introduced the first n-type transparent conducting material. However, these early films had relatively high electrical resistance compared to metals and were unstable over time as further oxidation eventually degraded their properties.

Modern TCO materials include tin-doped indium oxide (ITO), fluorine-doped tin oxide (FTO), and aluminum-doped zinc oxide (AZO). Unlike earlier TCOs, which relied on natural vacancies in the metal oxide structure, these newer materials use energy levels introduced by added dopants to achieve n-type conduction.

ITO, first developed in 1954 by Rupprecht [8], was the pioneer among contemporary TCOs. However, it has notable limitations, such as the scarcity and high cost of indium and its tendency to degrade at the high temperatures needed for some manufacturing processes. To address these issues, alternatives like fluorine-doped tin oxide, antimony-doped tin oxide, and doped zinc oxide systems have been developed. Doped zinc oxide stands out as a cost-effective, durable, and high-performing option.

I.2 Zinc oxide material

I.2.1 Zinc oxide properties

Zinc oxide (ZnO) has attracted considerable interest in the scientific community as the material of the future. Since 1935 [9], the focus on ZnO has grown steadily, thanks to its exceptional emissivity in the ultraviolet and blue ranges, along with its superior chemical stability compared to GaN [10, 11], a wide bandgap of approximately 3.4 eV, and a high exciton binding energy of around 60 meV at room temperature. Additionally, ZnO can be effectively deposited on single-crystal substrates [12]. Other advantageous features include its low power threshold for optical pumping and its biocompatibility. Consequently, ZnO has gained significant attention for its versatile applications in microelectronics, spintronics, and healthcare. Numerous challenges related to ZnO fabrication, particularly in achieving p-type conductivity, have been addressed, facilitating the development of various devices [13, 14].

I.2.1.1 Structural properties

Zinc oxide is a group *II-VI* semiconductor with a hexagonal wurtzite crystal structure (Figure I.1), belonging to the space group P63mc [15]. ZnO is highly ionic, with each zinc cation (Zn) bonded to four oxygen anions (O) in a tetrahedral configuration. This tetrahedral coordination forms a sp^3-type covalent bond. The stability of the ZnO structure is influenced by the ionic radii of the anion and cation. Stability is achieved when the anions are tangent both to each other and to the central ion (cation). If the anion radius increases beyond this limit or the cation radius is very small, the anions repel each other and lose contact with the central cation, causing an increase in potential energy and rendering the system unstable.

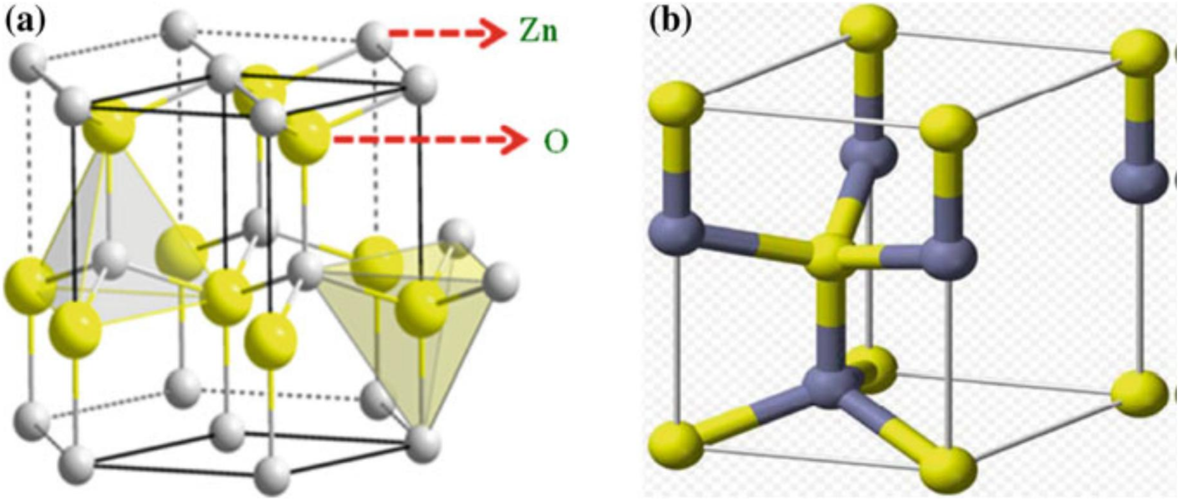

Figure I.1: (a Structure of ZnO material. (b) Unit cell of wurtzite structure.

ZnO lattice is formed by two hexagonal close-packed subplanes offset along the *c*-direction by *u.a* where *u* = 0.345 [15]. The wurtzite structure lacks a center of symmetry, resulting in a crystallographic polarity along the (001) plane parallel to the *c*-axis. The stacking of planes composed of cationic (Zn^+) and anionic (O^-) species creates a charge difference between the (001) and $(00\bar{1})$ planes. The growth rate is higher along the *c*-axis. Consequently, properties such as defect incorporation and piezoelectricity depend on the anisotropic growth of ZnO along the *c*-axis. However, ZnO can also crystallize in the ZnS blende structure when deposited on a cubic-structured substrate [16], or in the rock-salt structure under high pressure [24].

Zinc and oxygen atoms make up only 40% of the crystal's volume [17], leaving empty spaces with radii of 0.95 Å. Under certain conditions, extra zinc atoms can fill these spaces, known as interstitial positions. Each zinc atom is surrounded by four oxygen atoms, and each oxygen atom is surrounded by four zinc atoms, forming a 4:4 coordination.

The O^{2-} ions are arranged in a hexagonal close-packed lattice, while Zn^{2+} ions occupy half of the tetrahedral interstitial spaces, mirroring the arrangement of the oxygen ions (Figure I.1). The unit cell consists of 12 atoms: 2 at the vertices, 7 within the cell, 1 on the bases, and 2 along the edges.

According to Shannon et *al.* [18], the ionic radius of Zn^{2+} in a tetrahedral site is approximately 0.60 Å, and that of O^{2-} is about 1.38 Å. This ratio falls within the stability range, which accounts for the stability of the wurtzite structure of ZnO. The lattice parameters of ZnO under normal temperature and pressure conditions are a = 3.249 Å and c = 5.2042 Å [15], with a ratio that closely matches an ideal hexagonal close-packed structure (c/a = 1.633).

I.2.1.2 Electronic properties

The fundamental electronic configurations of oxygen and zinc are as follows:
O: $1s^2\ 2s^2\ 2p^4$

Zn: $1s^2\ 2s^2\ 2p^6\ 3s^2\ 3p^6\ 3d^{10}\ 4s^2$.

The band gap, located between the valence and conduction bands of ZnO, is approximately 3.37 eV at 300 K [19], making it a wide direct bandgap semiconductor (Figure I.2). This characteristic enables its use in optoelectronic applications. This bandgap width varies with temperature, and with doping and the presence of defects. ZnO naturally exhibits n-type electrical conductivity, primarily due to the presence of zinc atoms in interstitial positions [20].

Indeed, the energy gap of ZnO follows Varshni's semi-empirical relation [21], which shows the reduction of the semiconductor bandgap energy with increasing temperature. Additionally, defects and dopants can significantly alter ZnO’s properties, allowing for tailored materials suitable for specific applications by adjusting dopant characteristics (type, nature, temperature, concentration, doping technique, etc.) [7].

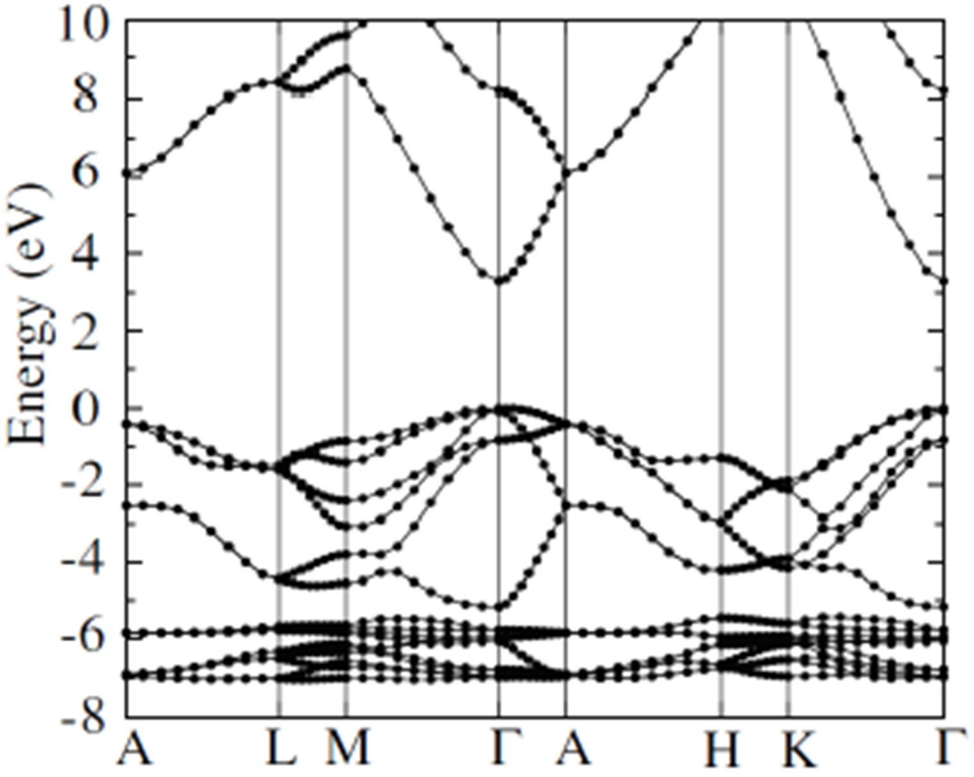

Figure I.2: The band structure of ZnO determined using the *HSE* approximation [22].

I.2.1.3 Optical properties

ZnO belongs to the family of transparent semiconducting oxides (TCOs) in the visible range, thanks to its wide band gap. In bulk form, it has a refractive index of 2 [23]. However, the absorption coefficient and refractive index depend on the fabrication conditions. Reported values for the refractive index in thin films range from 1.70 to 2.20, as noted by various authors [23, 24].

Because of its wide direct band gap, ZnO is characterized by interesting optical properties in both the near ultraviolet (UV) and visible ranges. These properties are related to the quality of crystallinity. Its light transmittance can exceed 80% in the visible range; this makes it transparent in its bulk form [25]. Temperature influences this transmittance, which can exceed 90% in the visible range for thin films deposited at high temperatures [26]. ZnO exhibits a significant absorption coefficient (~ 2.5×10^5 cm^{-1}) in the UV range (around its band gap energy), which becomes very low ($< 10^3$ cm^{-1}) in the visible range [27]. Improving the stoichiometry of ZnO results in a lower absorption coefficient and a higher band gap energy [28, 29].

Luminescence occurs in zinc oxide when it is exposed to high-energy light ($E > Eg$) or electron bombardment, causing it to emit photons. The photoluminescence of zinc oxide varies based on fabrication conditions and treatments, producing bands from near-UV (350 nm) to visible light, including green emission around 550 nm. In stoichiometric ZnO thin films, visible luminescence is linked to defects like zinc interstitials and oxygen vacancies, which are associated with deep-level emissions [30]. Fons et *al.* [31] highlighted that examining photoluminescence in the visible range can provide valuable information about the quality and purity of the material.

I.2.1.4 Electrical properties

ZnO is inherently an n-type semiconductor due to the presence of excess zinc atoms in interstitial sites or oxygen vacancies. These intrinsic defects create donor or acceptor states within the ZnO band gap, typically leading to a decrease in the material's electrical resistivity. Thus, the free electron concentration n in undoped ZnO depends on the fabrication techniques used for these layers. The concentration n reported by Murphy et *al.* [32] is 10^{16} cm^{-3} using molecular beam epitaxy (MBE). This concentration can be lower, around 10^{14} cm^{-3}, for layers with thicknesses between 0.1 and 1 mm [33, 34]. It can also be quite high, with values ranging from 10^{17} cm^{-3} to 5×10^{18} cm^{-3} [32, 35].

Depending on the crystalline quality of ZnO, Its resistivity ranges from 10^{-3} Ω·cm to 10^{12} Ω·cm [36]. Typically, thick layers exhibit high resistivity ($\rho = 10^5$ Ω·cm) [22], whereas the resistivity of thin films varies across several orders of magnitude. Depending on the fabrication technique used, thin films can be highly conductive ($\rho \sim 2–10$ Ω·cm) [37, 38] or less conductive ($\rho \sim 10^4$ Ω·cm) [39].

The electron mobility μ_e in an n-type semiconductor also depends on growth conditions and can vary between 30 and 150 cm^2/V·s [32]. The doping mechanisms are either substitutional or interstitial. The dopant type used may come from Groups *III* or *IV* of the periodic table (B, Al, Ga, In ...). Two of the outer electrons are used for ionic bonding with oxygen atoms, while the remaining electrons are donated to the conduction band. Elements from Group VII of the periodic table, such as fluorine (F), can also serve as dopants. In this case, the dopant atoms replace the oxygen atoms in the ZnO atomic lattice [40].

Potential p-type dopants for ZnO include elements from groups *I-A*, *I-B*, *V* elements and Zn vacancies (Znv) [42−48]. However, many of these dopants create deep acceptor levels, which limits their contribution to p-type conduction. Elements of group V are typically regarded as the most promising for p-type doping in ZnO, although theoretical studies indicate challenges in achieving shallow acceptor levels [45]. Numerous theoretical investigations, using first-principle calculations, have explored the microscopic mechanisms of p-type doping in ZnO [46]. Results suggest that group I elements might offer shallower acceptor levels than group V elements; however, due to their small ionic radii, group I elements typically prefer to occupy interstitial sites rather than substitutional ones [41]. K and Na doping in ZnO results in an elongation of the Zn–O bond length, leading to form compensating donor defects. P and As doped ZnO extends the bond length, causing the formation of antisites, AZn, which are known to act as donors in ZnO [46]. Nitrogen substitution at oxygen sites are considered the most effective p-type dopant for ZnO [42, 47], although some theoretical and experimental findings indicate that N can also create a deep acceptor level [45] and that N has low stability in the ZnO lattice [48].

I.2.1.5 Magnetic properties

Diluted Magnetic Semiconductors (DMS) are materials that can conduct electricity in which a portion of the host cations is substituted with magnetic ions [49]. The growing interest in DMS stems from their potential use in spintronic devices, which allow for the simultaneous control of both charge and spin [50, 51]. *II–V* and *II–VI* semiconductors can gain magnetic properties when doped with 3d transition metal ions or 4f rare-earth ions. [52]. The discovery of hole-mediated ferromagnetism in (Ga,Mn) has opened new opportunities for incorporating magnetic and spin-related phenomena into microelectronics and optoelectronics [53]. In contrast, the highest reported Curie temperature (TC) for (Ga,Mn)As grown by molecular beam epitaxy (MBE) is around 170 K [54]. For spintronic devices to be practically viable, DMS materials need to demonstrate ferromagnetism with a Curie temperature (*TC*) that exceeds room temperature.

ZnO has garnered significant interest in the quest for high Curie temperature (*TC*) ferromagnetic DMS materials, particularly following predictions by Dietl et *al.* [55]. P-type ZnO doping with Mn based DMSs have the potential to display ferromagnetism at temperatures exceeding room temperature. This potential arises from the strong p–d hybridization between the valence band p-states and the Mn 3d levels. The calculated TC values were based on an assumption of 5% Mn concentration and a hole density of 3.5×10^{20} cm^{-3}.

Expanding on the research conducted by Dietl et *al.* [55], theoretical studies by Sato et *al.* [56] have explored ferromagnetism in ZnO doped with various magnetic ions (V, Cr, Mn, Fe, Co, and Ni) using ab-initio calculations based on the local density approximation (LDA). Their results suggest that ferromagnetic ordering may also be possible in n-type TM:ZnO thin films and bulk polycrystalline powders.

I.2.2 Applications of zinc oxide material

Zinc oxide is among the oldest technological materials, dating back to the Bronze Age, when it was created as a product of copper ore smelting and used for wound healing. Historically, it was also essential in producing brass (a Cu-Zn alloy), which remained its primary application for centuries until metallic zinc became more widely used. With the onset of the industrial age in the mid-19th century, ZnO found applications in white paints (known as Chinese white), as an activator in the vulcanization of rubber, and in porcelain enamels. Below, we briefly explore several current and emerging electronic applications of ZnO. Below, we will present some applications of the ZnO materials:

I.2.2.1 Applications in photovoltaic solar cells

The photovoltaic effect is the ability of certain materials to capture photon energy to excite an electron from the valence band to the conduction band, leaving behind a vacancy called a hole. To minimize the recombination of electron-hole pair, a device made up of two semiconductors is necessary: one n-type, which is rich in electrons and the other p-type, which has an excess of positive holes.

The junction between these two p-n semiconductors creates an electric field in the depletion zone. This electric field serves to drive negative charges to one side and positive charges to the other side of the system, thereby limiting the recombination of electron-hole pairs.

Zinc oxide has been extensively studied for nanostructured solar cells (Figure I.3). Indeed, some researchers have demonstrated that using zinc oxide under certain conditions can enhance photovoltaic cell performance. Doyoung et *al.* [57] showed that light diffusion is improved with a rougher surface composed of ZnO nanowires. This increases the photon path, and also improves light absorption by reducing reflection.

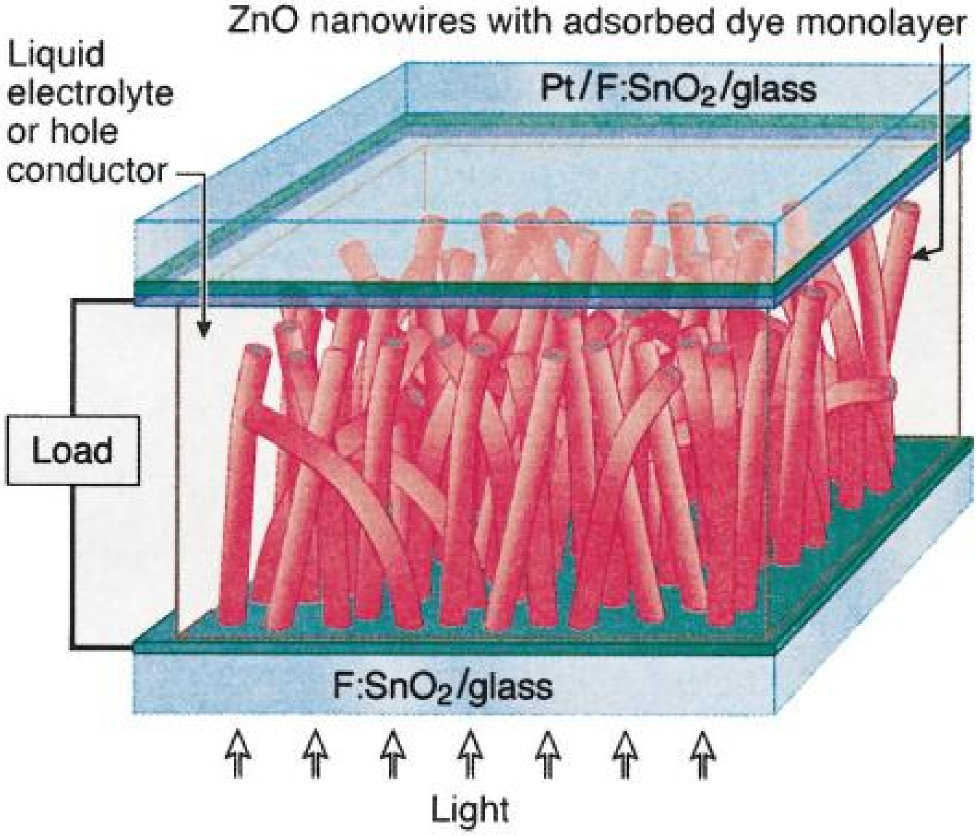

Figure I.3: Diagram of a solar cell based on ZnO nanowires [58].

The use of ZnO nanowires also facilitated the integration of dye into solar cells. Incorporating dye into solar cells leads to the broadening of the absorption spectrum of solar radiation, thereby increasing the energy efficiency of the photovoltaic cells [59].

I.2.2.2 Application in light-emitting diodes

An LED functions by converting electrical energy into light radiation (Figure I.4). The process relies on the emission of a photon produced by the recombination of an electron and a hole in a semiconductor. Zinc oxide has also been used in the fabrication of light emitting diodes owing to its large bandgap and high excitant binding energy, which enable it to exhibit light emission capability at room temperature [60]. However, achieving a p-type layer for ZnO remains challenging [61].

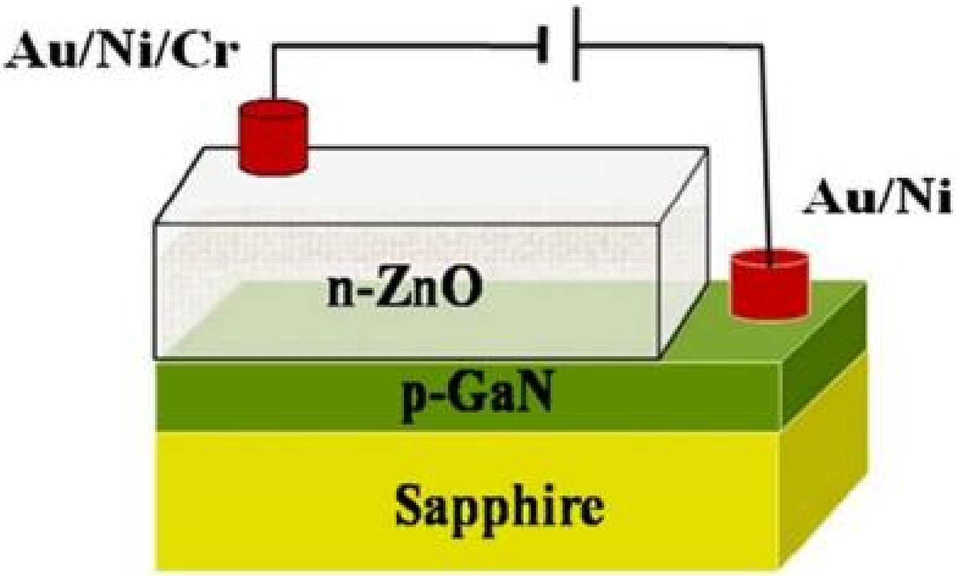

Figure I.4: Diagram of light-emitting diode cell based on a ZnO layer [61].

To address this, some researchers have developed an alternative approach to fabricate LEDs using a heterojunction of n-type ZnO with another p-type semiconductor (e.g., $CuGaS_2$ [62] or Cu_2O [63]). Given the numerous similarities between zinc oxide and gallium nitride, many researchers have attempted to create luminous diodes with an n-ZnO/p-GaN heterojunction [64, 65].

Lee et *al*. [61] also highlighted the importance of annealing on the structure, concluding that light emission cannot be observed without post-thermal treatment. Interestingly, annealing in ambient air induces yellow light emission, while annealing in a nitrogen atmosphere produces blue light emission.

I.2.2.3 Application in photocatalytic

In 1972, Fujishima [66] highlighted the photocatalytic properties of TiO_2, which has the ability to produce hydroxyl radicals under UV irradiation. These radicals serve to mineralize pollutants such as dyes, hydrocarbons, pesticides, carboxylic acids, etc., transforming them into less harmful products for the environment, such as CO_2, H_2O and N_2, among others.

As a wide bandgap semiconductor like TiO_2, ZnO has been widely used as a catalyst for water treatment [67], thanks to its strong oxidizing power. Xu et *al.* [68] compared the degradation capacity of naphthalene between ZnO nanowires and a commercial powder made of ZnO nanoparticles (size < 1 µm) under UV irradiation. Figure I.5 shows that the concentration of the residual product is significantly reduced due to the large specific surface area of ZnO nanowires.

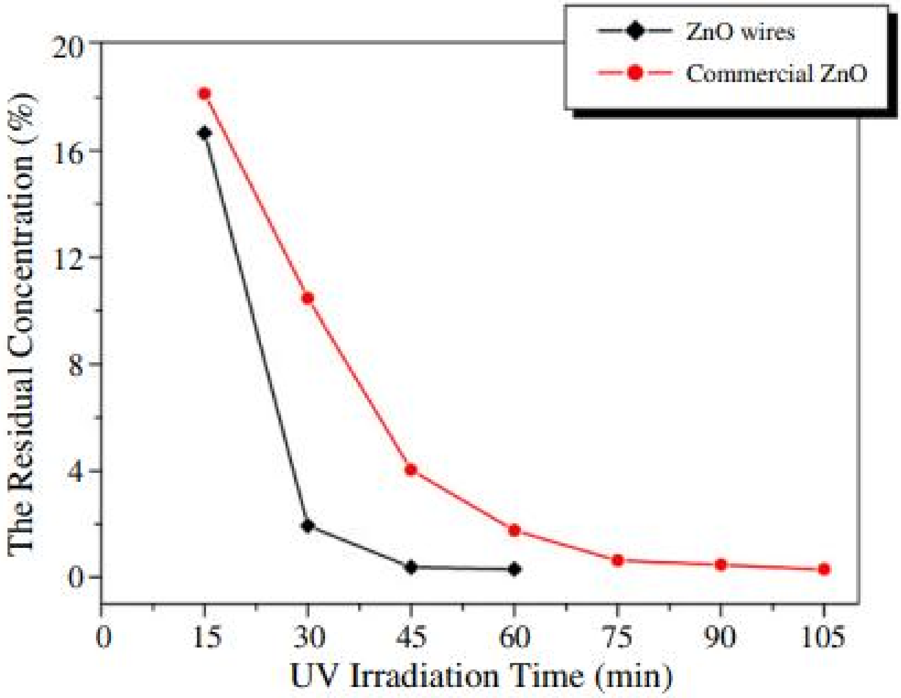

Figure I.5: Curves showing the concentration of residual naphthalene at different UV irradiation times on ZnO nanowires and commercial ZnO powders [68].

The depollution efficiency of ZnO depends not only on the specific surface area of the nanostructures but also on their structural properties, such as the degree of perfection of the crystal lattice, the concentration of vacancies, and interstitial atoms, among other factors [69].

I.2.2.4 Application in piezoelectric generators

The piezoelectric effect is characterized by the coupling between mechanical and electrical properties. This means that certain materials can electrically polarize in response to mechanical stress; conversely, they can be mechanically deformed when an electric field is applied. The Curie brothers, who discovered this phenomenon in 1880, they observed the positive and negative charges appeared on the surfaces of a quartz crystal when mechanical stress was applied [70].

Wang's research team [71] successfully converted mechanical energy at the nanoscale into electrical energy for the first time using a piezoelectric network of ZnO nanowires. These nanowires were deformed using a conductive atomic force microscopy (AFM) tip, leading to the creation of an electric field. This device achieved an efficiency of 17% to 30%.

Lin et *al*. [72] developed a transparent flexible nanogenerator using a flexible polydimethylsiloxane (PDMS) substrate on which ZnO nanowires were grown. The fully encapsulated nanogenerator exhibited good transparency, with a transmittance of 50–60% in the visible spectrum. The output voltage and current were 8 V and 0.6 mA, respectively, corresponding to a power density of 5.3 mW/cm^3. Lin et *al*. [73] also implemented a flexible ZnO nanogenerator capable of harvesting energy from human respiration. This device generated approximately 0.6 V and 0.5 µA at a low airflow rate of 2.0 m/s and about 1.3 V and 0.8 µA at an airflow rate of 5.0 m/s (Figure I.6)).

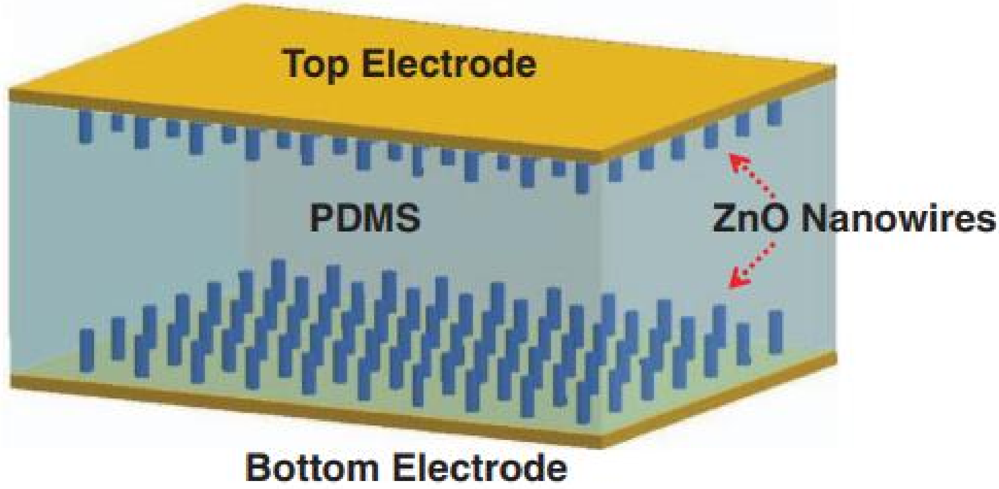

Figure I.6: Diagram of a zinc oxide-based nanogenerator [73].

I.2.2.5 Application in gas sensors

Gas detection is typically based on changes in the conductivity of zinc oxide when a polar gas species is adsorbed. Miniaturized gas sensors made from ZnO nanowires exhibit high sensitivity to a variety of gas molecules and biomolecules, such as NO_2 [74], NH_3 [75], CO [76], H_2 [77], NH_3 [78], and H_2S [79]. Oxygen vacancies in ZnO act as n-type donors on oxide surfaces and are both electrically and chemically active. When a gas encounters the sensitive layer, it either donates or accepts electrons. If it removes electrons, the electron count in the measurement circuit decreases, causing an increase in the equivalent circuit resistance; this indicates an oxidizing gas, such as NO_2 or O_3. Conversely, if the gas donates electrons, the equivalent circuit resistance decreases, indicating a reducing gas like CH_4 or C_3H_8.

Selectivity is a key challenge for these types of sensors, and doping ZnO is used to enhance this selectivity. It should also be noted that doping has a dual effect: it can increase sensitivity to a specific gas while potentially reducing sensitivity to other gases. The table below illustrates some dopants used and the target gases.

I.3 Cuprous oxide material

P-type TCOs are uncommon, and even the most effective ones perform significantly worse than n-type TCOs, especially regarding resistivity. These materials primarily include cuprous oxide (Cu_2O) and related mixed compounds, notably the delafossite phase $CuMO_2$ [80, 81] (with M representing Al, Ga, In, Y, or Sc) or mixed phases like $SrCu_2O_2$. Cu_2O, due to its simplicity, has been known for a long time. However, it was only in 1999 that it was first obtained in the form of a transparent thin layer by Chandra et *al.* [82]. While the existence and thermodynamic stability of $CuAlO_2$ were established as early as 1975, it was only much later, in 1997, that Kawazoe et al. discovered its TCO properties [83]. Finally, the existence of $SrCu_2O_2$ was discovered more recently than the other two, in 1992, thanks to the work of Jacob et *al.* [84].

I.3.1 Cuprous oxide properties

Cuprous oxide, with, Cu_2O, is a red-brown compound. While it can be synthesized, most often by oxidizing metallic copper (at least when the goal is to obtain it as a bulk material rather than in thin layers), it also occurs naturally in mineral form as cuprite. Another advantage of Cu_2O is that its components are non-toxic and very abundant on Earth. This is a definite asset, as it helps to reduce production costs. Physical properties of Cu_2O are presented in Table I.1.

Table I.1: Physical properties of Cu_2O [86-90].

Density	6.10 $g.cm^{-3}$
Molecular weight	143.092 $g.mol^{-1}$
Electron mass in the conduction band	$0.98.m_e$
Hole mass in the valence band	$0.58.m_e$
Specific heat capacity (Cp)	70 $J.K^{-1}.mol^{-1}$
Thermal conductivity (k)	4.5 $W.K^{-1}\ m^{-1}$
Thermal expansion coefficient	$2.5 \times 10^{-6}\ K^{-1}$
Thermal diffusivity (α)	0.015 $cm^2.s^{-1}$
Melting point	1508 K
Solubility	Insoluble in water and dilute acids; soluble in NH4OH and in concentrated NH_4Cl solution.

I.3.1.1 Structural properties

Cu_2O crystallizes in a Bravais cubic structure with the symmetry of space group ($Pn\bar{3}m$), illustrated in Figure I.7. Only a few other compounds share this structure, including Ag_2O, Pb_2O, $Cd(CN)_2$ and $Zn(CN)_2$ [85]. In its unit cell, copper ions form a face-centered cubic (fcc) sublattice, arranged at the vertices of a tetrahedron centered on oxygen sites, with each copper ion coordinated by two oxygen ions. In contrast, oxygen ions occupy a body-centered cubic (bcc) sublattice and are coordinated by four copper ions. Crystallographic properties of Cu_2O are summarized in Table I.2.

Table I.2: Structural properties of Cu_2O [86-90].

Formula	Cu_2O
Structure	Cubic
Space group	$Pn\bar{3}m$
Lattice parameters	a = b = c = 4.27 Å, α = β = γ = 90°
Atomic percentage (%)	Cu : 66.67 – O : 33.33
Mass percentage (%)	Cu : 88.82 – O : 11.18
Band gap width (Eg)	1.9 – 2.2 eV
Interatomic distance d-hkl	2.465 Å
Unit cell	4.27 Å
Volume of the unit cell	77.83 $Å^3$

Interatomic distances Cu-O	1.849 Å
Interatomic distances O-O	3.68 Å
Interatomic distances Cu-Cu	3.02 Å

Choosing the origin of the coordinate system at an oxygen atom, the copper ions are located at the positions (1/4, 1/4, 1/4), (1/4, 3/4, 3/4), (3/4, 1/4, 3/4), and (3/4, 3/4, 1/4), in units of the lattice parameter a (Figure I.7.a). In other words, the copper lattice is translated by a (1/4, 1/4, 1/4) relative to the body-centered cubic lattice. This structure is centro-symmetric i.e. has the inversion symmetry (Figure I.7.b). If a copper ion is selected as the origin of the unit cell, the unit cell transformed by inversion symmetry remains the same as the original. However, if an oxygen atom is chosen as the origin, the inversion must be accompanied by a translation of a (1/2, 1/2, 1/2).

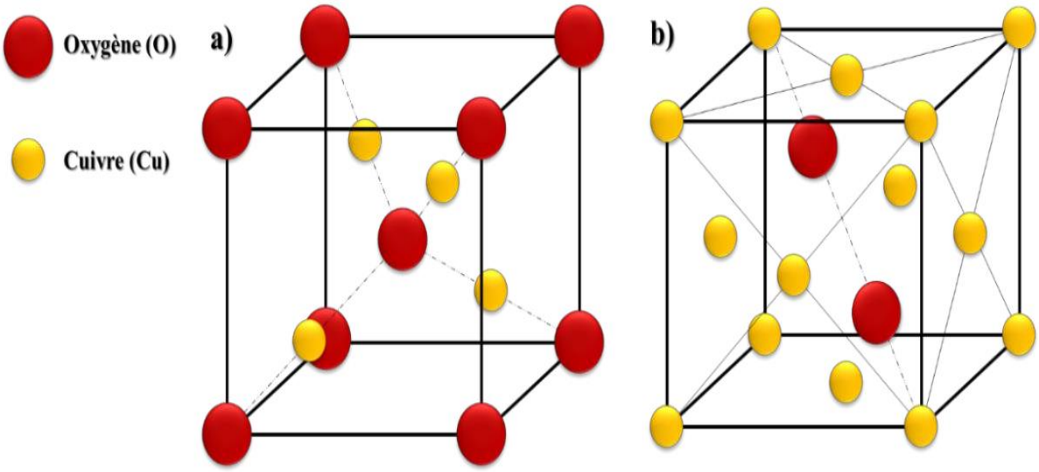

Figure I.7: Structure of Cu_2O: a) The origin of the system is an oxygen atom. b) The origin of the system is a copper atom [85].

Cu_2O undergoes a phase transition from its cuprite structure to a hexagonal form at around 10 GPa (with a = 4.18 Å at ~ 10 GPa). Between 13 and 18 GPa, it transforms into another hexagonal structure of the $CdCl_2$-type. Up to the highest applied pressure of 24 GPa, no decomposition of Cu_2O into Cu and CuO was observed. Detailed information on phase transitions, structures, lattice parameters, and volume changes can be found in [91].

It is worth noting that these values are largely temperature-independent due to Cu_2O's low expansion coefficient, as its lattice constant changes by less than 0.5% from 0 to 600 K. Interestingly, Cu_2O exhibits negative thermal expansion below 300 K [92].

I.3.1.2 Electronic properties

Oxides are naturally prone to cation deficiency, resulting in a more positive oxidation state, as represented by the general equation for most binary metal oxides (both p-type and n-type) [93]. According to this theory, the p-type conductivity in cupric oxide arises from the formation of copper vacancies in both normal and split configurations, as represented in the following equation:

$$\mathrm{Cu(I)} \rightarrow V_{\mathrm{Cu}} + V_{\mathrm{Cu,split}} + n_{\mathrm{p}} \qquad \text{(I.1)}$$

Where: V_{Cu} represents the copper vacancy and n_p is the generated holes. The split configuration indicates the copper atom's displacement halfway towards a neighboring copper vacancy site, reducing the Cu–Cu bond distance by half [94]. Figure 1.7 illustrates the normal and split configurations of a copper vacancy. This conductivity is due to excess oxygen and/or metal deficiency, which leads to a nonstoichiometric structure of the material [93]. Similarly, the formation of V_{Cu} and $V_{Cu,split}$, both with lower formation energies (yielding stable conductivity via low acceptor ionization energy), tends to produce shallow holes in the thin film [94]. This is also attributed to the anti-bonding state of Cu(I) (d^{10}) orbitals at the valence band maximum, resulting in reduced electron density between nuclei.

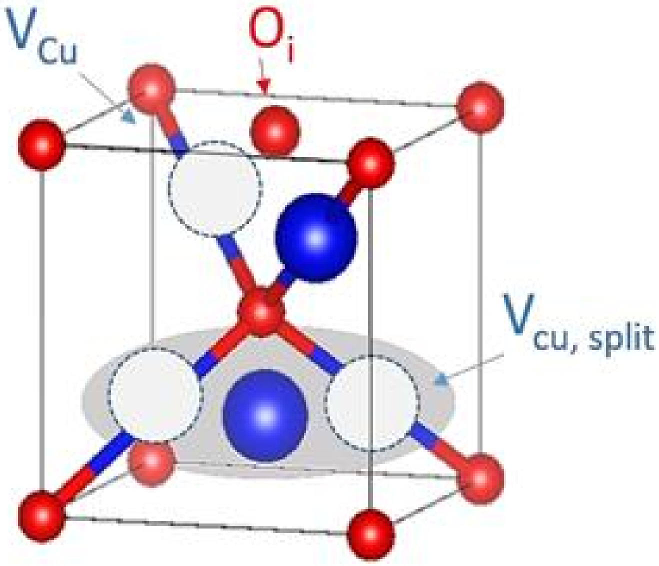

Figure 1.8: The copper formed vacancies in the normal and split configuration [93].

The optical and electronic properties of metal oxides are generally influenced by non-stoichiometric defects. In this specific oxide structure, potential intrinsic defects in the crystal lattice include Cu_O and O_{Cu} antisites, O_i and Cu_i interstitials, as well as vacancies such as V_{Cu} and V_O [95, 96]. Cu_2O can also accommodate other complex defects reported in the literature, such as Frenkel defects ($V_{Cu} – Cu_i$) and ($V_O – O_i$), and Schottky defects ($2V_{Cu}–V_O$), which are considered stoichiometric as their presence does not alter the stoichiometry [97, 98]. Additionally, the p-type conductivity in this metal oxide remains intrinsically stable due to the absence of potential hole compensators. As a result, cation vacancies lack a donor level within the bandgap (due to high formation energy relative to hole-producing defects), preventing their compensation [99].

Figure 1.9 illustrates the formation energies of defects in intrinsic cuprous oxide. The influence of polaronic behavior associated with copper vacancies (V_{Cu}) on the conductivity of Cu_2O thin films and single crystals is well established in the literature [100–103]. Both normal and split configurations of copper vacancies have been shown to function as acceptor defects, exhibiting lower formation energies compared to other defects in both oxygen-rich and oxygen-poor environments [99,100]. Moreover, their contribution is considered crucial to the conductive properties of the films [104].

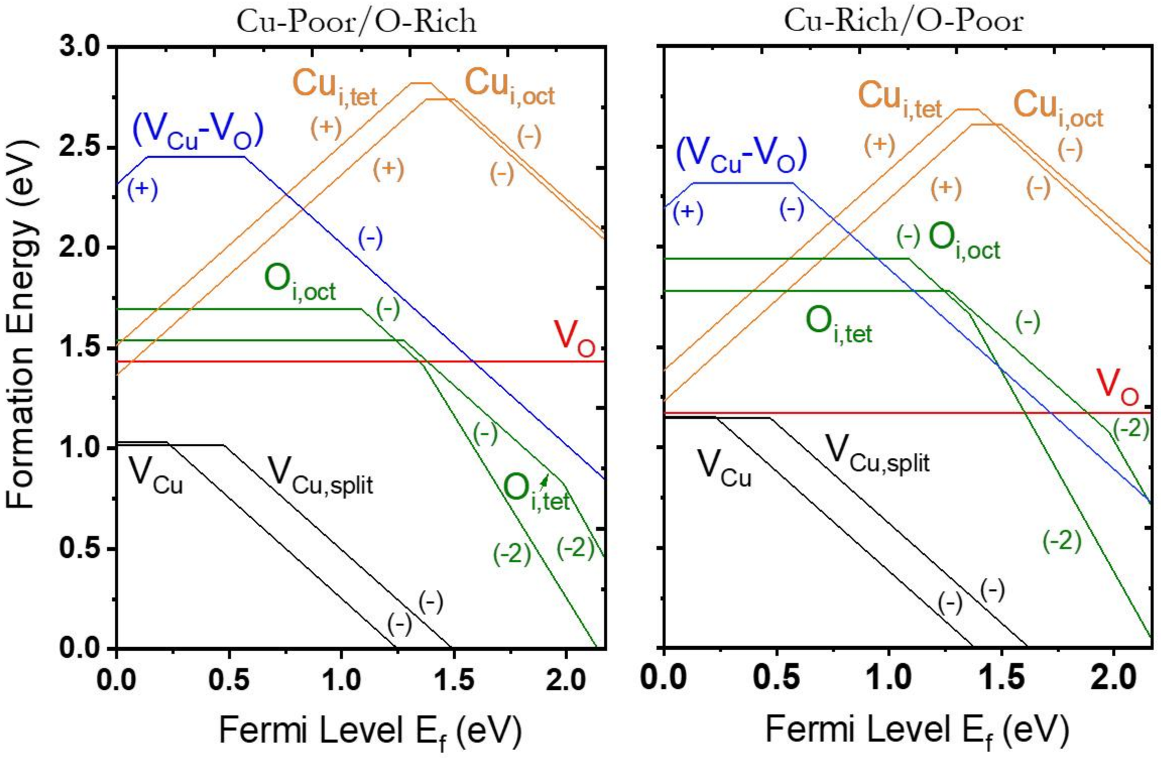

Figure 1.9: Formation energies of defects for intrinsic cuprous oxide calculated with HSE exchange correlation functional [95,100].

As a result, optimizing the transport properties presents significant challenges due to limited control over the formation of low-energy non-stoichiometric defects (V_{Cu} and $V_{Cu,\ split}$) across various deposition techniques. S. Han et *al.* investigated the conduction mechanisms and the adjustment of copper vacancy density in Cu_2O thin films, finding that the concentration of copper vacancies tends to decrease following high-temperature post-annealing in a vacuum atmosphere. This reduction restricts grain boundary conduction and primarily leads to trap-limited conduction within the film. However, this study did not evaluate the presence of the split configuration in comparison to normal vacancy sites. Additionally, multiple studies have indicated that the oxidation of Cu_2O to CuO can be readily facilitated with increasing annealing or deposition temperatures, primarily due to the oxidation mechanism of Cu^{1+} to Cu^{2+} species [105,106].

I.3.1.3 Electrical properties

The resistivity of p-type TCOs does not fall below $10^{-1} - 10^{-2}$ Ω·cm while that of n-type TCOs can drop to 10^{-4} Ω·cm, indicating a mobility issue [107]. The electrical properties of cuprous oxide films, such as mobility and carrier concentration, vary significantly with preparation methods, leading to considerable fluctuations in the resistivity of Cu_2O films [108]. The hole mobility in Cu_2O lattices was previously measured by Vogt in 1930 and by Brattain in 1953. Vogt obtained a value of 100 $cm^2/V·s$ at room temperature, while Brattain measured 120 $cm^2/V·s$ at the same temperature. Musa et *al.* [109] deposited p-type thin films of Cu_2O through thermal oxidation and found that Cu_2O layers grown in air without undergoing an annealing process exhibited resistivities ranging from 2×10^3 to 3×10^3 $Ω·cm^3$. A significant reduction in resistivity was achieved by doping the samples with chlorine during the growth and annealing stages. For eight unannealed Cu_2O samples, an average mobility of $75\ cm^2\ V^{-1}·s^{-1}$ was measured at room temperature. This average mobility increased to $130\ cm^2\ V^{-1}·s^{-1}$ after the samples were doped with chlorine and subsequently annealed. K. Han and M. Tao [110] deposited Cu_2O layers using an electrochemical method and found the following results: The resistivity of p-type Cu_2O ranged from 3.2×10^5 to 2.0×10^8 Ω·cm, while for n-type Cu_2O, it varied between 2.5×10^7 and 8.0×10^8 Ω·cm. These variations were influenced by deposition conditions, including the solution pH, deposition potential, and temperature.

I.3.1.4 Optical properties and photo-activity

Cu_2O has p-type semiconductor properties that have been known since 1917 thanks to the work of Kennard et *al.* [111]. It is the first known oxide with semiconductor properties. It found applications as early as 1926 through the work of Grondahl [112], who used it to create rectifier diodes that convert alternating current into direct current. In particular, Cu_2O was known and used as a semiconductor material before silicon, which began to be used in the late 1940s.

Its wide bandgap of 2.137 eV allows it to transmit light with wavelengths greater than 580 nm (in the yellow range) when in thin film form. However, it is important to note that in thin films, the bandgap can vary compared to this value, which pertains to the pure, bulk oxide. Furthermore, for thin films, it is often the optical gap that is considered, not the bandgap. Light with a wavelength shorter than 580 nm is partially or completely absorbed, green radiation is partially transmitted, while blue radiation is absorbed. As a result, thin Cu_2O films appear yellow and transparent to the naked eye. This partial transparency to visible light, combined with its semiconductor properties, makes cuprous oxide a promising candidate as a transparent p-type conductive oxide. As such, it is the subject of significant research activity.

Copper oxide has optical properties that depend on the light-matter interaction. A portion of the incident light with energy greater than or equal to its bandgap energy ($h\upsilon \geq E_g$) will be absorbed by the electrons (e^-) in the valence band, causing them to move to the conduction band, leaving behind holes (h^+) [113].

$$Cu_2O + \hbar\upsilon \rightarrow e^- \, (CB - Cu_2O) + h^+(VB - Cu_2O) \qquad (I.2)$$

The free electrons can be collected by an electrical system to measure the photoactivity of Cu_2O, and can be used in various applications such as solar cells. Meanwhile, light with energy lower than the bandgap energy ($h\upsilon \leq E_g$) will be partially absorbed, and this partial absorption is due to defects present in the Cu_2O crystal lattice.

Since the bandgap energy changes with fabrication conditions, the color of the copper oxide in thin films also varies from yellow to reddish-brown. The color change induces a change in the absorption coefficient and the refractive index, which are two essential parameters dependent on the semiconductor's bandgap energy [114]. Abu-Zeid et *al*. [115] showed that the refractive index ranges from 2.54 to 2.78 depending on the wavelength, while Brandt et *al.* [116] demonstrated it ranges from 2.2 to 2.71. Enhancing the stoichiometry of copper oxide reduces the absorption coefficient while increasing the bandgap energy.

I.3.2 Cuprous oxide applications

Cuprous oxide is used in a broad range of applications, such as electrochromic, solar cells, light-emitting diodes (LEDs) devices and sensors.

I.3.2.1 Application in solar cells

Cu_2O nanostructures are a promising candidate for the development of optical devices, for example heterojunction solar cells and light-emitting diodes. They have garnered attention due to their absorption coefficient and their energy conversion efficiency of 18%, which surpasses that of monocrystalline Si [117,118]. Heterojunction solar cells can be created by combining a p-type semiconductor with n-type semiconductor such as ZnO [119], CdO [120], or TiO_2 [121,122]. Among these materials, ZnO is the most stable option and has a low lattice mismatch (7.6%) between the ZnO (002) crystalline structure and Cu_2O (111) [123]. The highest efficiency reported for a ZnO-Cu_2O heterojunction, based on the work of Minami et *al*. [124], the efficiency was 3.83% (Figure I.10).

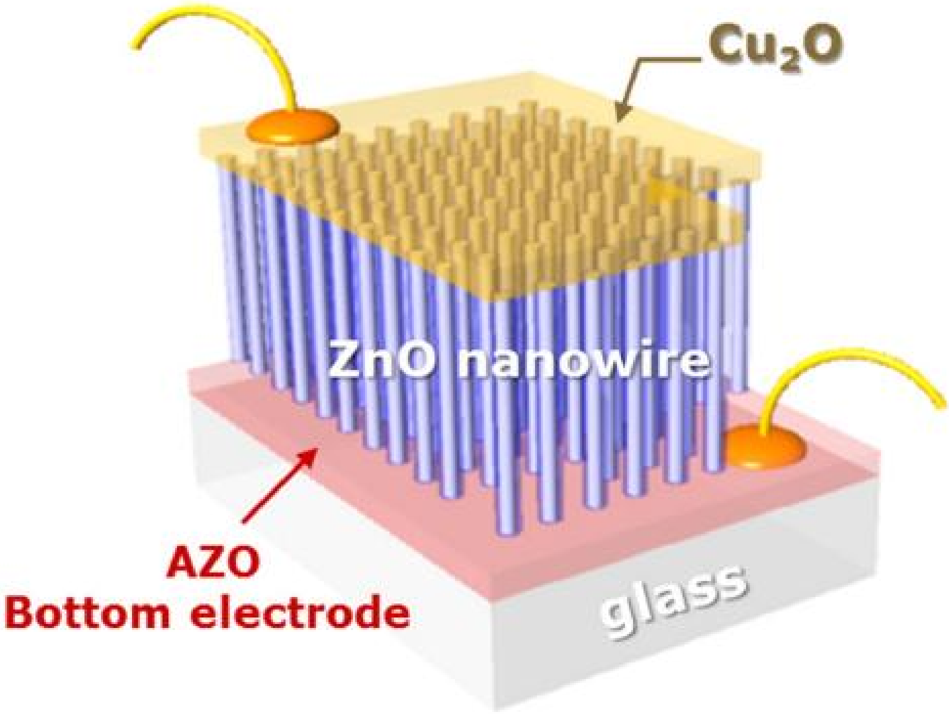

Figure I.10: Structure of a solar cell based on Cu_2O and ZnO nanowires [125].

Cu_2O has been extensively utilized in organic light-emitting diodes (OLEDs) [126,127]. Improving their efficiency requires optimizing carrier injection at the interface between the active layers and the anode. Kim et al. highlighted the advantages of employing a stoichiometric blend of CuO and Cu_2O to enhance OLED performance [126].

I.3.2.2 Application in photocatalytic

The photocatalytic activity of Cu_2O is a well-established and commonly utilized process, owing to its low bandgap energy and affordability. It is used to degrade organic contamination and for water decomposition [128–131]. A heterogeneous photocatalytic system consists of semiconductor materials (photo-catalysts) in contact with a liquid or gas. When a semiconductor is illuminated, it absorbs light with a wavelength greater than or equal to its bandgap energy. An electron (e^-) is excited from the valence band (VB) to the conduction band (CB), creating a hole (h^+) in the VB at the same time.

The photo-excited electron-hole pairs diffuse towards the surface of the photocatalytic material and chemically react with the electron-accepting (A) or electron-donating (D) molecules adsorbed or near the surface, producing highly reactive free radicals (OH^-) and (O^{2-}). These radicals are capable of mineralizing most organic molecules [128]. The simplified principle of photo-catalysis is illustrated in Figure I.11.

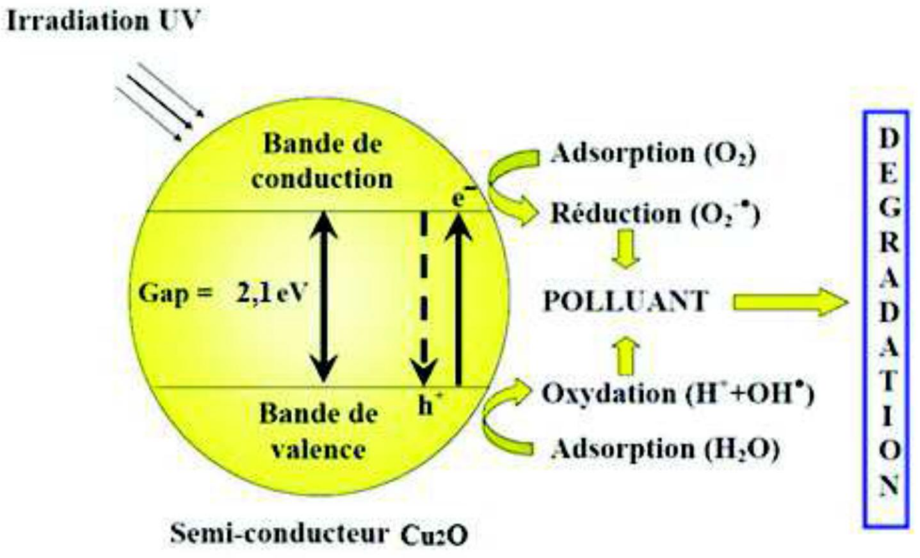

Figure I.11: Diagram illustrating the heterogeneous photocatalytic process in a Cu_2O particle under illumination.

The main factor limiting photocatalytic activity is the recombination of electron-hole pairs, which results in the loss of photoelectric energy in the form of heat (radiative recombination's) [132]. To address this issue, Cu_2O is commonly combined with other semiconductors to create heterojunctions, with TiO_2 being one of the promising candidates [133]. Barreca et *al*. highlighted the outstanding photocatalytic performance of Cu_2O in hydrogen production when methanol was present [128]. They proposed that methanol inhibits electron-hole recombination and serves as a source of hydrogen [128].

I.3.2.3 Application in electrochromic devices

These systems allow for the modulation of light transmission since electrochromic materials have the property of changing color when subjected to an electric field. Electrochromic systems based on Cu_2O nanostructures, including smart windows and optical display systems, have been researched since 1990 [134]. It has been shown that Cu_2O displays cathodic electrochromism, remaining transparent under visible light in its oxidized state and turning black in its reduced state when cations like H^+, Li^+, and Na^+ are inserted [135–137]. In general, the electrochromic process entails the transformation of Cu_2O (transparent) to CuO (black) via a reversible redox reaction [135, 137]. So far, the best coloring efficiency achieved with Cu_2O nanostructures has reached 37 $cm^2.C^{-1}$, which is about a quarter of that achieved using nanoporous WO_3 (141.5 $cm^2.C^{-1}$) [135]. Unfortunately, Cu_2O nanostructures require a high coloring voltage and exhibit low stability [136].

I.3.2.4 Application in sensors

Cu_2O also possesses other interesting properties for technological applications, such as surface absorption. The electrical conductivity of this material varies depending on the nature and amount of chemical species absorbed on its surface, making it suitable for use as a chemical, biological, and gas sensor. Additionally, it is used in photodetectors owing to its low bandgap and optoelectronic properties [138–140]. Sahoo et *al.* [139] showcased the remarkable performance of photodetectors based on Cu_2O nanotubes. They employed the metal/semiconductor/metal configuration to detect photons in both dark and illuminated environments.

The detection capabilities of Cu_2O can be optimized by reducing its size to the nanoscale and incorporating appropriate dopants. Catalytic particles such as Pd [141], Au [142], Pt [143], and Ag [143] attached to the surface of Cu_2O enhance its sensitivity due to induced effects. Thin films of Cu_2O have demonstrated high sensitivity to various gases, including C_2H_5OH [144], CO [145], NO_2 [146], and H_2S [147].

Additionally, Cu_2O has been used as electrodes in electrochemical biosensors, particularly for glucose sensors [148]. The majority of these sensors rely on the enzyme glucose oxidase.

I.4 Cupric oxide material

Copper (II) oxide, commonly referred to as cupric oxide, has been of great interest in semiconductor materials research since 1920. Its chemical formula is CuO. Copper forms two well-established stable oxides, which exist in two distinct semiconductor phases: CuO and Cu_2O [149]. These oxides exhibit distinct physical and electrical properties, as well as varying colors and structures. Cu_2O can be converted into CuO at higher temperatures, whereas CuO is more stable in air, as Cu(II) ions are much more stable in ambient air. This stability makes CuO particularly important for practical applications.

I.4.1 Cupric oxide properties

Cupric oxide have become highly advantageous in various advanced technological applications due to their remarkable properties. In its mineral form, CuO is known as tenorite. It is a byproduct of copper extraction and serves as a precursor for numerous other copper-containing products and compounds [150]. CuO is a p-type semiconductor exhibits a direct band gap energy (E_g) varying from 1.2 to 2.01 eV [151]. It is a black ionic solid with a melting point of 1326 °C and an evaporation temperature of 1100 °C. CuO is abundant in nature and non-toxic. Table I.3 provides a summary of some properties of CuO.

Table I.3: Main properties of CuO [152].

Appearance	Black
Molar mass	79.545 g/mol
Density	6.315 g/cm^3
Melting point	1326 °C
Boiling point	2000 °C
Magnetic susceptibility	$239\text{x}10^{-6}$ cm^3/mol
Refractive index	2.63

I.4.1.1 Structural properties of CuO

Copper(II) oxide can exist in various crystalline structures. Here, we focus specifically on the monoclinic structure, which is stable under normal conditions [153]. In this structure, copper atom is coordinated by four oxygen atoms in a roughly square arrangement, and it belongs to the C2/c space group (Figure I.12). Copper and oxygen atoms occupy the 4c sites (1/4, 1/4, 0) and 4e sites (0, y, 1/4) with y = 0.416 [154], respectively, with lattice parameters detailed in Table I.4.

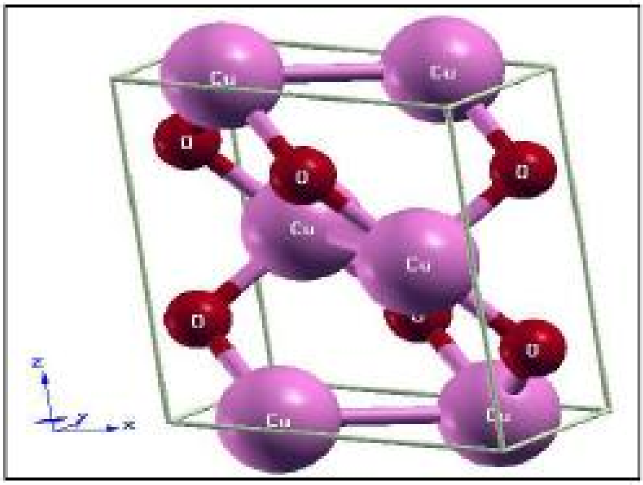

Figure I.12: Crystalline structure of copper oxide (CuO).

Table I.4: Crystallographic data for copper oxide (CuO) [155].

Formula	CuO
Structure	Monoclinic
Space group	C2/c
Lattice parameters	a = 4.6837 Å
	b = 3.4226 Å
	c = 5.1288 Å
	β = 99.54°
	α = γ = 90°
Shortest distance	
Interatomic distances Cu–O	1.95 Å
Interatomic distances O–O	2.62 Å
Interatomic distances Cu–Cu	2.90 Å
	79.57

I.4.1.2 Electrical properties of CuO

A thorough understanding of the electrical properties of copper oxide (CuO) is essential for unlocking its potential applications in electronics and optoelectronics. Copper oxide functions as a p-type semiconductor with a band gap (E_g) ranging from 1.2 to 2.01 eV [156]. The band gap corresponds to the energy needed to transfer an electron from the valence band (VB) to the conduction band (CB). In p-type semiconductors, charge carriers are primarily free holes in the valence band. The level of metal deficiency (or oxygen excess) mainly influences the concentration of these free holes in CuO in the crystal sites of the material [157]. This effect is ascribed to deviations from stoichiometry (or structural defects), which may arise due to anion vacancies, an excess of cations in interstitial positions, or adjustments in the preparation conditions of the material [158]. The precise nature of these structural defects remains uncertain in most cases.

The mobility of holes in thin CuO layers is typically in the range of 20–30 $cm^2/V \cdot s$. Since oxide crystals typically lack the capacity to accommodate large oxide ions, p-type non-stoichiometry in CuO is likely to be due to cation deficiencies. Additionally, the low impurity content in the compound and its thermal stability under low oxygen partial pressure conditions play a significant role.

The hole concentration, and thus the concentration of charge carriers and the conductivity of CuO can be regulated by modifying the oxygen partial pressure during its growth. This conductivity is highly sensitive to the presence of adsorbed molecules, making CuO highly promising for chemical and environmental sensing applications [159].

The refractive index ranges between 1.90 and 3, depending on the deposition method. This material, which has a low resistivity around 0.05 Ω.cm [160], is also an antiferromagnetic material with a local magnetic moment of 0.60 μB [161].

I.4.1.3 Optical properties of CuO

The optical properties of a material can be clearly understood by analyzing the interaction between light (an electromagnetic wave) and the material's electrons. When applying dispersion theory to a material, it is essential to distinguish between fundamental absorption and the absorption of free carriers. If only the first contribution is present, the material behaves as a dielectric. Otherwise, it behaves as a metal. For semiconductors, both contributions are significant. The first corresponds to the inter-band absorption threshold, separating the ultraviolet absorption region from the high-transparency region in the visible spectrum. The second relates to the rise in reflectivity in the infrared region, corresponding to plasma oscillations of conduction electrons. An electromagnetic wave interacting with the semiconductor will be entirely absorbed if the energy associated with the wave can transfer electrons from the valence band to the conduction band. This occurs when the energy of the wave is at least equal to the band gap width. Numerous theoretical and experimental studies have demonstrated that examining the optical properties of copper oxide in the visible region provides insights into its absorption characteristics. Figure I.13 illustrates the absorbance spectrum of copper oxide.

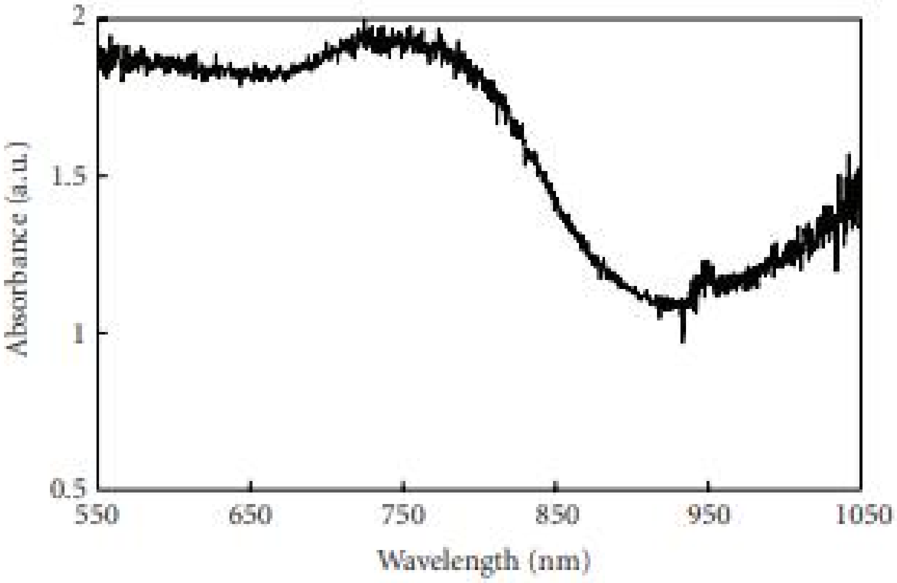

Figure I.13: UV-Visible absorption spectrum of a CuO nanowire array [162].

I.4.2 Applications of cupric oxide

The remarkable properties of copper oxide (CuO) make it suitable for a wide range of applications. It is considered one of the promising materials for various potential uses, such as electrodes in dye-sensitized solar cells [163]. It is also applied in semiconductor catalysis, gas biosensors, and field-effect transistors [164], capacitors [165], anode materials for lithium-ion batteries [166], antimicrobial agents [167], humidity sensors [168], diodes [169], and more. Due to its diverse range of applications, this section will focus on a few key uses, highlighting some of its most important properties.

I.4.2.1 Application in photovoltaic solar cells

The photovoltaic industry, crucial for future energy solutions, has advanced across various technological domains. The most developed are silicon-based technologies (amorphous, polycrystalline or monocrystalline) for conventional solar cells. To reduce the thickness of active materials, other industrial approaches have emerged at varying scales using direct band-gap materials such as $CuInSe_2$, CdTe, and GaAs. These thin-film cells offer compelling efficiency-to-cost ratios. However, issues related to toxicity, due to elements like selenium, cadmium, and arsenic, or high costs, limit their widespread use.

In recent years, a new class of thin-film solar cells made entirely of semiconductor oxides has emerged. This approach is attractive due to the intrinsic properties of oxides: chemical stability, low toxicity, and natural abundance of their constituent elements. Generally, most semiconductor oxides used in photovoltaic systems are primarily absorbing oxides, with common examples including CuO, SnO_2, and ZnO.

Copper oxide (CuO) stands out as a candidate semiconductor due to its low thermal emissivity, high optical absorption coefficient and cost-effective production. CuO, as a p-type semiconductor with a band gap near the ideal energy range for solar cells, holds significant potential for efficient solar spectral absorption. [170,171].

Photovoltaic (*PV*) technology involves converting electromagnetic energy (photons) into direct electrical current using semiconductors. The fundamental unit of a *PV* system is a solar cell (photovoltaic cell), which is the smallest component of a *PV* installation. Photons entering the cell excite electrons in the semiconductor material, generating direct current.

Sukdev and Rajkumar [172] developed a heterojunction solar cell with the structure F: SnO2/CdS/CuO/Ag deposited on glass using DC magnetron sputtering and thermal evaporation techniques (Figure I.14). These heterojunction solar cells demonstrated a high absorption coefficient (α > 105 cm^{-1}) and an efficiency varying from 2.0% to 2.1%. The cells achieved an open-circuit voltage of 0.602 V and a short-circuit current of 6.65 mA.

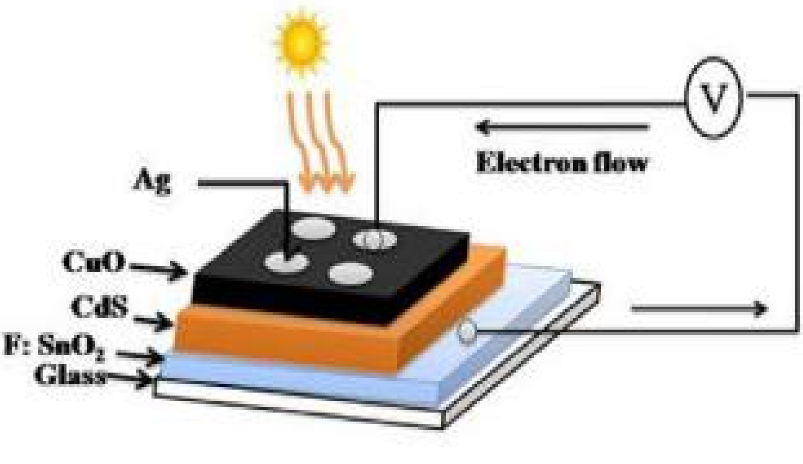

Figure I.14: Schematic of F: SnO_2/CdS/CuO/Ag solar cell structure [172].

I.4.2.2 Application in gas sensors

In recent years, the development of gas sensors has been an ever-expanding field, driven by the growing need to address pollution issues and comply with stringent safety regulations imposed by various countries in numerous industrial sectors. Gas sensors play a crucial role in gathering information, requiring sensitivity, stability, and often-high selectivity. Additionally, the widespread deployment of sensors in measurement networks and large-scale applications necessitates cost-effective manufacturing.

Among the principal types of gas sensors, those based on semiconductors offer several advantages, such as seamless integration into comprehensive detection systems, low production costs, and minimal maintenance requirements. Gas detection is achieved by the interaction between a gas and a sensitive material, which induces changes in one or more physicochemical properties (e.g., mass, electrical conductivity, optical properties). This interaction converts a chemical state into an electrical signal. The chemical state refers to attributes like concentration, partial pressure, or thermodynamic activity of a specific gas.

During operation, the target gas adsorbs onto the sensor surface and interacts with the sensor material. This interaction causes a movement of charges between the adsorbent and adsorbate, resulting in a change in the resistance of the solid material. Gas sensors operate based on variations in conductance depending on the concentration and amount of adsorbed gas, proportional to the chemical state of the monitored gas. Resistance variations also depend on temperature, deviations from the semiconductor oxide's stoichiometric ratio, and contamination or doping. Sensitivity increases as particle size approaches the nanoscale.

Given these characteristics, copper oxide (CuO) emerges as a promising candidate for gas detection applications due to its unique property of being intrinsically p-type. Its advantages include non-toxicity, efficient electron transfer capability [173], low cost and high stability. To improve sensitivity and shorten response and recovery times, maintaining an optimal operating temperature is crucial for CuO's gas detection performance.

Numerous studies have concentrated on creating innovative CuO nanostructures for the detection of various gases, including organic vapors, sulfuretted hydrogen (H_2S) [174], carbon monoxide (CO) [175], ethanol [176], ammonia (NH_3) [177], hydrogen cyanide (HCN) [178] and humidity [179].

I.4.2.3 Application in catalysis

CuO is an efficient heterogeneous catalyst for the conversion of hydrocarbons into carbon dioxide and water. It is also a good catalyst for the oxidation of aromatic aldehydes into the corresponding carboxylic acids using molecular oxygen, achieving high yields. Additionally, it is considered an excellent choice for industrial production due to its ease of collection and regeneration [180].

Vomácka et *al*. [181] showed that tin doping had a significant impact on the morphology of CuO. A progressive shrinkage of the particle morphology along the (010) lattice direction was observed as the dopant concentration increased. They obtained CuO nanoparticles in plate-like, rectangular, and rod shapes. Tin doping also affected the structural and optical properties of CuO. As the dopant amount increased, a redshift in the energy gap was observed, ranging from 1.33 eV to 1.18 eV. The excellent catalytic properties of the doped material were demonstrated by the enhanced catalytic removal of Rhodamine B in the presence of H_2O_2. Undoped CuO nanosheets only achieved 24% degradation of Rhodamine B. In contrast, the degradation of Rhodamine B reached 99% with the use of a CuO catalyst containing 4% Sn. They demonstrated a simple and scalable process for preparing Sn-doped CuO nanoparticles with highly active catalytic properties and tunable characteristics.

I.4.2.4 Application in Li-ion batteries

Modern electronic devices, such as smartphones and laptops, require miniaturized power sources. Many scientists are working in this area, aiming to improve the performance of these batteries by enhancing the base materials. Polycrystalline CuO nanowires exhibit high reversible capacity and excellent cyclic performance. The abundant crystal imperfections and grain boundaries in CuO nanowires provide additional lithium intercalation sites. The good cyclic performance is attributed to the excellent electronic conductivity of the CuO nanowires and the improved electrical contact between the nanowires. Polycrystalline CuO nanowires show strong electrochemical performance as anode materials for lithium-ion batteries [182].

Pang et *al*. [183] demonstrated that CuO nanorods on double-faced Cu superstructures have a reversible capacity of 645 mAh/g, which enhances the kinetics of the electrodes. This type of material shows promise for use in lithium-ion batteries, as the structure and electrochemical properties of the activated material are still influenced by the original structure of the prepared electrodes.

I.5 Techniques for depositing metal oxide thin films

I.5.1 Deposition by vacuum thermal evaporation technique

This technique involves initially placing grains, pellets, or small wire pieces of the material to be evaporated into a crucible made of tungsten, tantalum, molybdenum, or carbon. The crucible is then heated to a high temperature using the Joule effect. The grains melt, and the metal evaporates, depositing onto the substrate [184,185]. Figure I.15 illustrates the procedure of thermal evaporation using the Joule effect.

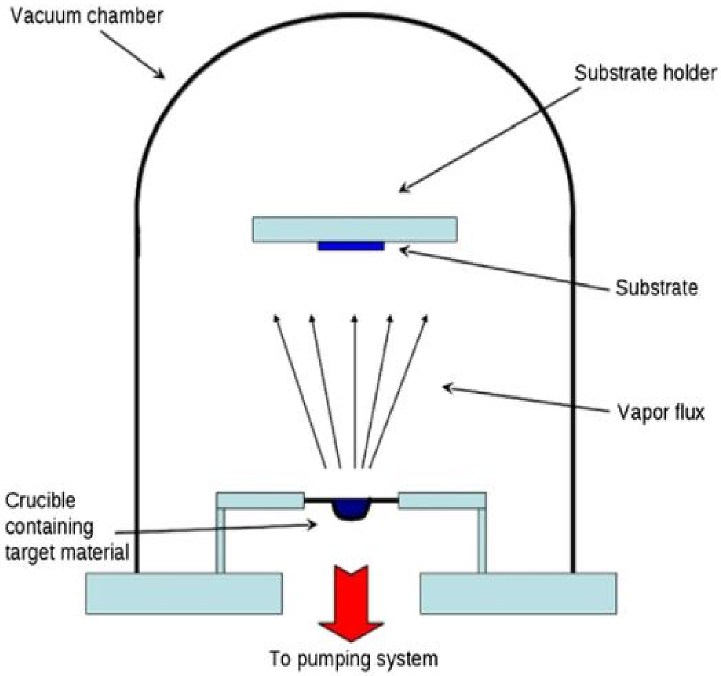

Figure I.15: Schematic of vacuum thermal evaporation system [186].

Advantages

- Simple technique.
- Suitable deposits for lift-off processes.

Disadvantages

- Potential contamination from the crucible itself.
- Inability to evaporate metals with high melting points.
- Limitation on the thickness of the deposited layer due to the small quantity of metal that can be held in the crucible.

I.5.2 Electron beam evaporation

In this method [187,193], an electron gun is used for evaporation. The process involves heating a filament to emit electrons. An electron beam is accelerated using a potential of 5–10 kV and focused on the material to be evaporated (Figure I.16). The electrons lose almost all their kinetic energy as heat. The temperature of the evaporating material increases due to electron bombardment rather than resistance heating. The melting point temperature of the target can reach up to 3000°C. At such high temperatures, extremely high evaporation rates are achieved, even for materials with the highest melting points.

It is noteworthy that electron guns come in two types, both featuring a straight-line electron beam path. Additionally, a combination of electrostatic and magnetic fields is used to focus the electron beam onto the target.

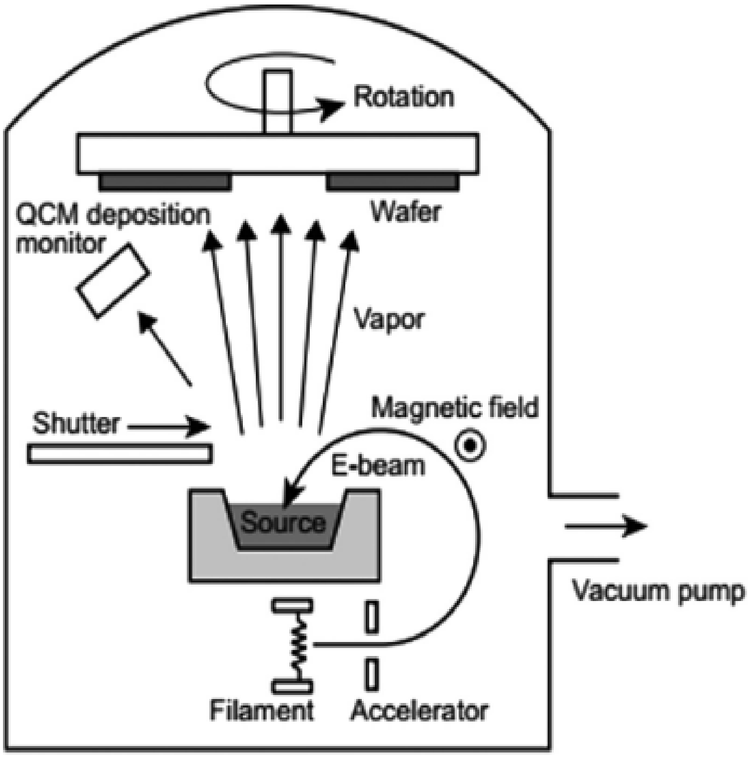

Figure I.16: Schematic of the electron beam evaporation system [194].

Advantages

- High purity of deposited layers.
- Suitable for "lift-off" deposition, requiring an incident flux close to the normal to the substrate surface.

Disadvantages

- Emission of X-rays that can damage substrate surfaces.
- Ejection of droplets from the crucible, which can deposit on substrates if excessive power is used.
- Complex evaporation of alloys, making it difficult to control the composition of the deposited layer.

I.5.3 Deposition by sputtering technique

This thin-film deposition technique enables the synthesis of various materials by applying a potential difference between the target and the reactor walls. It was initially developed for depositing metallic thin films that are challenging to evaporate. A diagram of the sputtering system is shown in Figure I.17.

Principle of sputtering deposition [195]:

- Injection of a plasma-forming gas (typically Argon) at low pressure.
- Plasma generation by applying a potential difference (DC or RF).
- Ionization of the plasma gas atoms (Ar^+).
- Acceleration of gas ions by the applied potential difference.
- Bombardment of the target atoms by the accelerated ions.
- Deposition of the ejected target atoms onto the substrate.

Operating modes of Sputtering [196,197]:

1. DC mode (suitable for conductive materials).
2. RF mode (suitable for all materials, whether simple or composite, refractory or non-refractory, conductive or dielectric).
3. DC magnetron or RF magnetron modes (addition of magnets to enhance deposition rate).

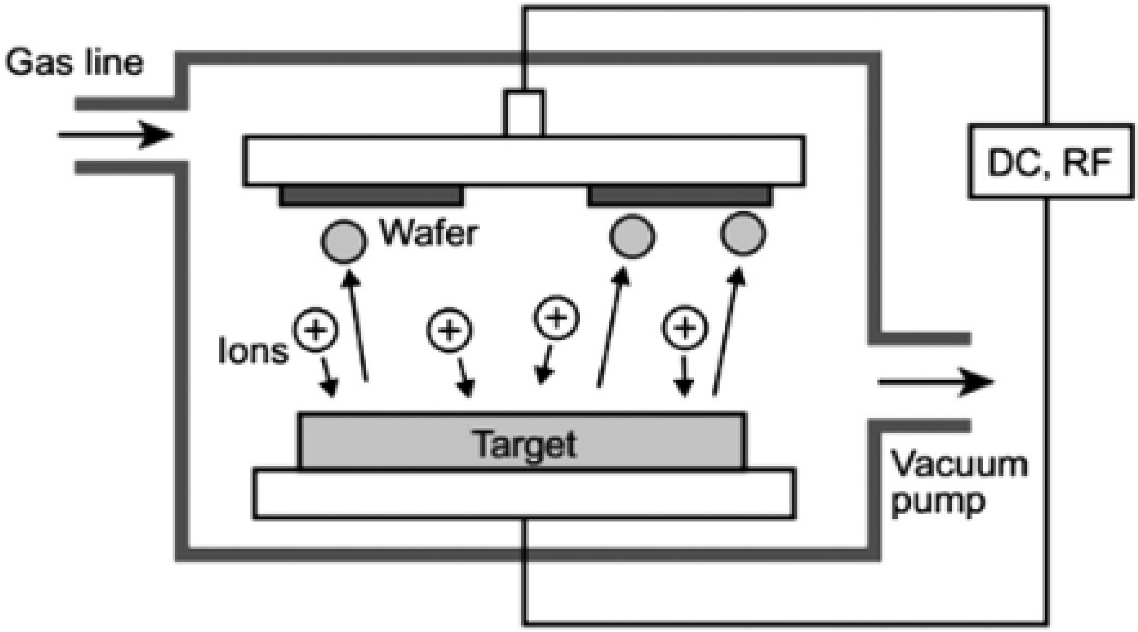

Figure I.17: Sputtering system diagram [194].

Advantages of this technique

- Low-temperature processes.
- Capability to sputter materials with very high melting points relatively easily.
- Layer composition closely matches the target material.

- Strong adhesion of deposited layers and excellent step coverage.
- Wide range of possible metallic and ceramic coatings.
- Increased density of growing layers.
- Elimination of impurities and poorly adherent species.

Disadvantages of this technique

- Difficult control of layer-by-layer growth.
- Limited growth rate.
- Potential degradation of highly sensitive substrates.

I.5.4 Chemical vapor deposition technique

The chemical vapor deposition CVD technique [198] involves depositing thin films from gas sources containing precursor elements, with a controlled thickness, onto various types of substrates. The gaseous precursors used for deposition must be condensable on the surface. This technique uses temperature to activate the reaction of the precursors during deposition.

Typically, the process is conducted in a furnace at temperatures ranging from 800 to 1000°C, where the reactive species are introduced. Inside the reactor, the gases dissociate due to the high temperature, delivering the desired material, which deposits on the substrate surface (Figure I.18).

Additionally, by adjusting the deposition pressure, the quality of the layers can be modified to achieve the desired physicochemical properties.

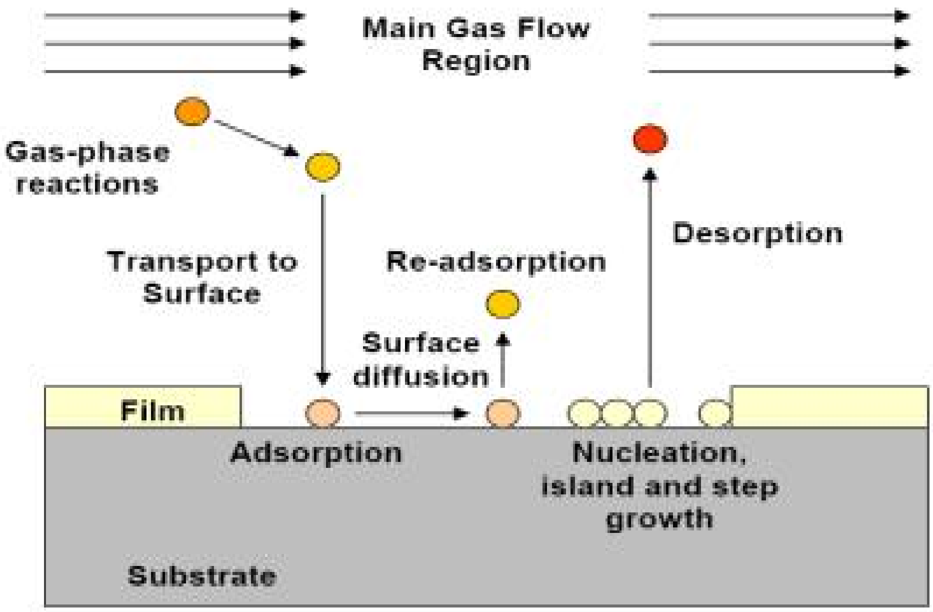

Figure I.18: Fundamental Processes of CVD [198]

I.5.5 Plasma-enhanced chemical vapor deposition technique (PECVD)

This technique [199] is based on generating species or elements for deposition at low temperatures using energy input in the form of electromagnetic waves (typically a radiofrequency source). As a result, PECVD avoids the need for high temperatures, which can, for example, cause dopant reorganization. Figure I.19 displayed the process of PECVD technique.

To improve the quality of the deposited material, the substrates are heated to a few hundred degrees. However, the thin films obtained are often contaminated by highly reactive gases produced during the chemical reaction.

Advantages

- Ease of obtaining a wide variety of elements or chemical compounds;
- High quality of the deposited layers.

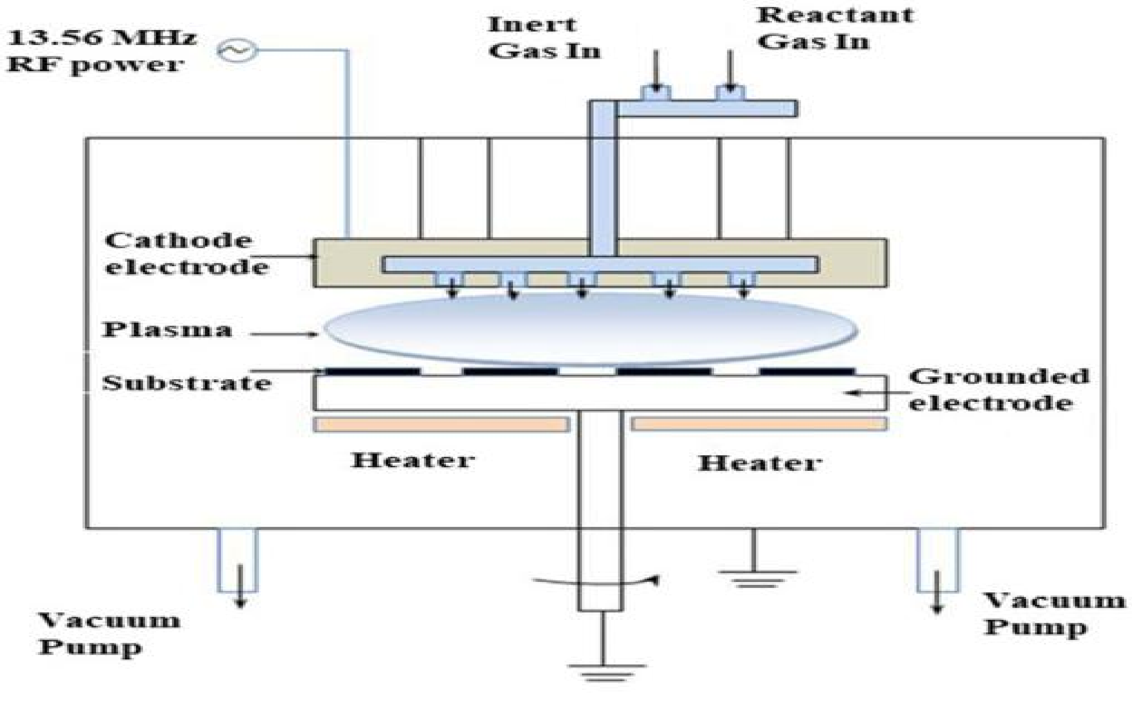

Figure I.19: Schematic of PECVD process [199].

I.5.6 Deposition by Sol-Gel technique

The sol-gel method is particularly effective for creating homogeneous materials in the form of thin films. In this process, the molecular precursors of the initial solution, known as the "sol," undergo polymerization through various mechanisms to form an oxide network, referred to as the "gel." A drying stage, followed by thermal treatments, removes organic components, resulting in the formation of an inorganic oxide [200].

Advantages

- Produces thin films with exceptional homogeneity and purity due to the molecular mixing of components in the solution.
- Allows precise control over material porosity and nanoparticle size.
- Facilitates the synthesis of materials that are challenging to obtain using other methods.
- Enables thermal treatments at lower temperatures while maintaining high optical performance [201].

Limitation

- The relatively high cost of precursors makes this technique unsuitable for large-scale industrial applications.

Thin film deposition methods in Sol-Gel

1. **Spin-Coating**
    - A fast deposition method used for flat substrates.
    - In this process, a substrate is securely held in a rotating chamber where a coating solution is applied. As the substrate spins, the solution spreads uniformly across the surface.
    - This method has been extensively studied, and key parameters affecting deposition and film thickness have been identified [202]. The spin-coating process is shown in Figure I.20.

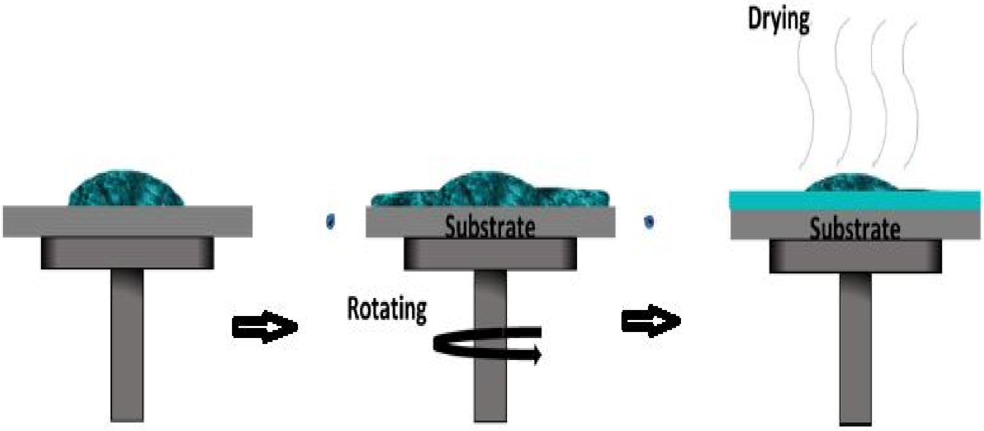

Figure I.20: Schematic of spin coating process [203].

2. **Dip-Coating**

   - A technique where a substrate is immersed in a coating solution, interacts with it, and is then withdrawn at a constant speed, leaving a wet film on the surface.
   - As excess liquid drains, the solvent evaporates, forming a thin film. This process can be repeated to achieve the desired thickness.

   - Dip-coating is effective for producing high-quality and uniform films, even on large or complex surfaces [204]. An illustration of the dip-coating process is provided in Figure I.21.

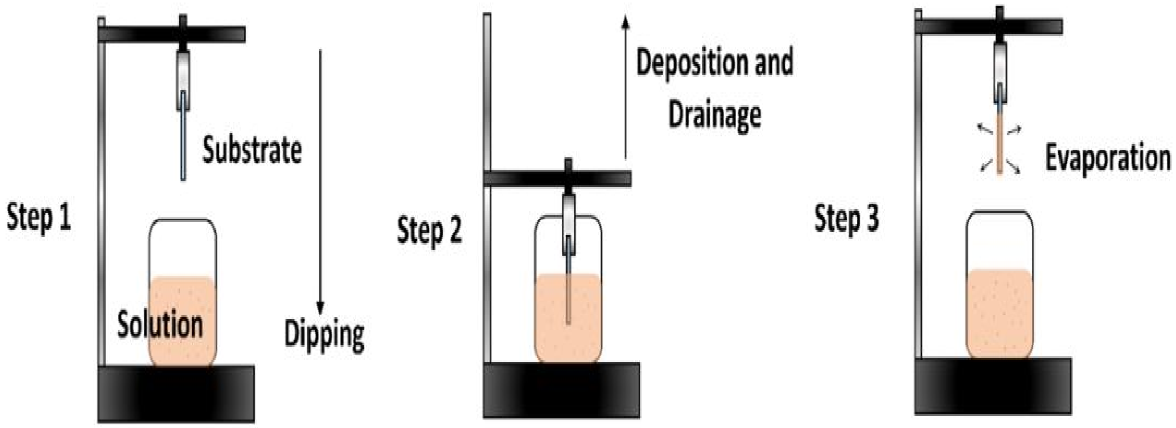

Figure I.21: Schematic of dip coating process [203].

I.5.7 Deposition by spray pyrolysis technique

A solution containing various reactive compounds is vaporized and then sprayed onto a heated substrate using an atomizer. The substrate's temperature activates the chemical reaction between the compounds [205]. This process can be conducted in air [206] or within a reaction chamber under vacuum conditions, typically around 50 Torr [207]. Figure I.22 shows a standard spray pyrolysis setup.

The formation of films via the spray pyrolysis technique can be outlined as follows:

- Formation of droplets at the nozzle's outlet.
- Decomposition of the precursor solution on the heated substrate surface through pyrolysis reaction.

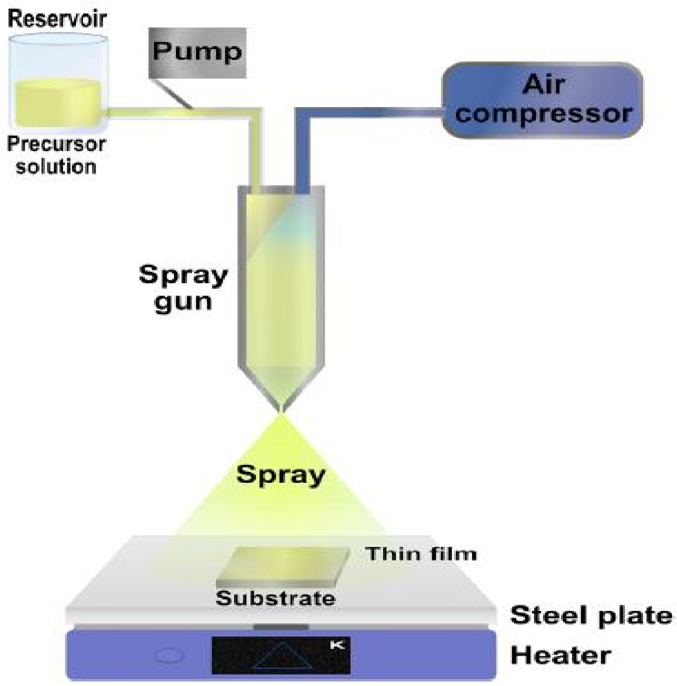

Figure I.22: Schematic of a spray pyrolysis system [208].

I.5.8 Deposition by electrodeposition method

Electrodeposition refers to an electrochemical process that allows the formation of solid deposits on the surface of conductive materials. Based on the principle of electrolysis (redox reactions), this method involves applying an electric current to transfer cations from a material through an electrolyte, thereby coating the surface of a conductive substrate with a thin layer of the desired material. Electrolytic deposits form within electrochemical cells, composed of two or three conductive or semiconductive electrodes immersed in an electrolyte. Electrodeposition can be implemented using various electrode polarization techniques: potentiostatic, galvanostatic, and both in pulsed or continuous modes. Several environments are possible (aqueous, organic, molten salts, etc.), but aqueous environments are most commonly used.

During an electrodeposition reaction in an aqueous medium, the cations present in the electrolyte are transferred to the cathode surface to form the metal deposit. It is commonly accepted that this process involves several intermediate steps, with the main ones described below [209,210]:

- Transport of the hydrated metal ion or the hydrated complex from the solution center to the cathode.
- Loss of part of the hydration of the hydrated metal ion at the cathode surface.
- Charge transfer leading to the formation of atoms (or ions) on the cathode surface.

- Nucleation formation at the cathode surface by diffusion of atoms to the electrode surface.
- Aggregation of multiple nuclei to minimize surface energy, forming stable nuclei.

The electrochemical deposition of metal oxides is typically achieved through three methods [211]:

a) **Direct oxidation of a metal electrode:** This process forms a metal oxide layer on surface of same metal (electrode), which can act as a protective coating for the metal.

b) **Anodic oxidation of dissolved metal ions:** In this method, the metal must have at least two soluble oxidation states in the solution, and the material to be deposited must be insoluble in the electrolyte [212].

c) **Cathodic electrodeposition through local pH increase:** This technique involves generating OH^- ions at the working electrode, raising the pH locally at the electrode/electrolyte interface. The OH^- ions are produced via the electrochemical reduction of a precursor. Various precursors, such as oxygen [213], nitrates [214], or hydrogen peroxide [215], are used in this method. It is commonly employed in research to deposit different oxides, such as ZnO [216].

This method is cost-effective and fast, enabling the creation of complex physical designs. The final films can cover large, intricate structures, with sizes ranging from a few nanometers to approximately ten microns, making it ideal for industrial use. The thickness of layer is committed exclusively by the current density and the duration of current flow.

I.6 Techniques for characterizing metal oxide thin films

I.6.1 X-Ray diffraction (XRD)

X-ray diffraction (XRD) is a non-destructive analysis technique used for the identification and quantitative determination of the different crystalline forms present in a solid. X-rays are electromagnetic radiation with wavelengths of the same order of magnitude as interatomic distances. When a primary X-ray beam strikes an ordered solid (i.e., the sample has a crystalline structure), it interacts with the electron cloud of its atoms via elastic scattering, causing some rays from the beam to be diffracted by the *hkl* planes that satisfy Bragg's law, given by the equation:

$$2d_{hkl}\sin\theta = n\lambda \tag{I.8}$$

Where: d_{hkl} distance between atomic planes with indices (*hkl*), θ incidence angle of the X-rays on the sample to be characterized, λ wavelength of the X-ray beam, *n*: order of diffraction.

The characterization setup consists of an automated θ - 2θ goniometer controlled by software. This technique is based on recording the intensity diffracted by the sample as it and the detector move. Both the sample and the detector rotate at uniform speeds of θ and 2θ, respectively. The spectrum recorded during the sample analysis is read by the software. Peaks appear on the spectrum, corresponding to families of planes (*hkl*). To identify each family, it is necessary to refer to ASTM files (American Society for Testing Materials).

I.6.2 Scanning electron microscopy (SEM)

Scanning electron microscopy is an analysis technique that allows the visualization of the surface morphology and thickness of thin films. The principle of the microscope is based on scanning the surface of the sample with a very fine electron beam, followed by the detection of secondary electrons emitted by the sample. This effect is transformed into an electrical signal that produces an image of the surface.

The secondary electrons result from the ionization of the target atoms (the sample). These electrons are characterized by very low energy (E < 50 KeV), and only the electrons emitted near the surface are detected. The dimensions of the area to be analyzed are of the same order as the incident beam.

The synchronization between the scanning of the surface by the incident electron beam and the detection of the secondary electrons allows for the transmission of the sample image point by point and line by line. The image is completed after a full scanning cycle.

I.6.3 Atomic force microscopy (AFM)

Atomic force microscopy (AFM) is an imaging technique that allows access to a material's structure at the nanometer scale. It is based on measuring the interaction forces between a tip of atomic dimension and the atoms on the surface of the sample. It consists of a micro-lever (cantilever) with a fine tip at its end, used to scan the surface of the samples (Figure III.19 (a)). The lever is typically made of silicon or silicon nitride, with a tip curvature radius on the order of nanometers. It is attached to a tiny piezoelectric element made from ceramic, which ensures the precise and accurate movement of the tip. This allows for an XY scan range from a few nanometers to 140 µm, with sensitivity in the Z direction down to fractions of a nanometer.

When the tip approaches the surface of the sample, the force between the tip and the sample, causes the deflection of the lever according to Hooke’s law ($F = -kx$). The forces measured in AFM include mechanical contact forces, Van der Waals forces, electrostatic forces, magnetic forces, and others. The deflection is precisely measured using a laser beam reflected off the upper surface of the lever onto a set of photodiodes. Successive deflections during a surface scan allow the reconstruction of the surface topology.

Moreover, atomic force microscopy (AFM) can operate under several modes depending on the applications. These imaging modes are divided into static modes (contact mode) and dynamic modes (non-contact and intermittent).

I.6.4 X-ray photoelectron spectroscopy (XPS)

X-ray photoelectron spectroscopy (XPS) is a surface chemical analysis technique. The depth of information ranges from 2 to 4 nanometers. The analysis is both qualitative (element identification) and quantitative (determination of concentrations). This technique also provides information about the chemical environment of the elements (nature of nearest neighbors, oxidation state, and type of bonding). The sample is placed under ultra-high vacuum (pressure around 7.5×10^{-11} Torr) and is exposed to an X-ray beam (Al $K\alpha$ line at 1486.7 eV) that ionizes the surface elements. The emitted photoelectrons are filtered by a spectrometer based on their kinetic energy and then detected. The precise measurement of this kinetic energy allows both the identification of the elements and the specification of their chemical environment.

I.6.5 UV-Vis-NIR spectrophotometry

UV-Vis-NIR spectrophotometry is an optical characterization technique (reflection, transmission, and absorption) based on the interaction of electromagnetic radiation with matter within a wavelength range from 200 to 1200 nm (from UV to near-infrared). The absorption of radiation causes an electronic transition between two energy states, meaning the transition of an electron from one electronic level to a higher energy level (excited state) due to the radiation. For semiconductor materials, this energy must be greater than or equal to the band gap (forbidden band) energy of the specific semiconductor.

I.6.6 Fourier transform infrared FTIR Spectroscopy

Fourier transform infrared (FTIR) is a method used to detect and identify molecules by analyzing the vibrations of their molecular bonds. The sample's infrared transmittance or absorbance spectrum is recorded by passing an infrared light beam through it. A Fourier transform is then applied to the signal data (interferogram) to generate a spectrum that indicates the amount of energy absorbed at each wavelength. By examining these absorption patterns, information about the molecular composition of the sample is obtained. FTIR is applicable to both crystalline and non-crystalline substances.

To obtain an accurate spectrum, a reference measurement is taken first, without the sample, followed by the measurement of the sample itself. The reference data is then subtracted, ensuring that the final spectrum represents only the sample's contributions, excluding those from the chamber atmosphere, which, despite being purged with nitrogen, typically contains trace amounts of water and carbon dioxide.

I.7 Conclusion

In this section, we first presented the various properties of metal oxides (zinc and copper oxides), such as their structural, optical, electronic, electrical and magnetic properties, and their practical applications. Secondly, we provided an overview of the different methods for fabricating metal oxide thin films (ZnO, CuO, Cu_2O), and the characterization techniques for these films. In conclusion, these oxides have very important properties that make them the focus of attention in several fields, deposition techniques and their parameters influence the various properties of metal oxides thin films.

References

[1] P. Ashrit, Elsevier, Edition: 1, 9780081018996, (2017).

[2] R. Vargas-Bernal, in Electronics Robotics and Automotive Mechanics Conference, 579–584, (2007).

[3] M. Tiemann, Chem. Eur. J. 13(30), 8376–8388, (2007).

[4] D. P. Mann, T. Paraskeva, K. F. E. Pratt, I. P. Parkin, D. E. Williams, Measurement Science and Technology 16, 1193–1200, (2005).

[5] P. Atkins, the Elements of Physical Chemistry, Oxford University Press: Oxford, 356–263, (2001).

[6] P. P. Edwards, A. Porch, M. O. Jones, D. V. Morgan, R. M. Perks, Dalton Trans. (19), 2995–3002, (2004).

[7] K. Badeker, Ann. Phys. 22, 749, (1907).

[8] G. Rupprecht, Z. Phys. 139, 504–517, (1954).

[9] C. W. Bunn, Proc. Phys. Soc. 47, 835, (1935).

[10] M. H. Huang, S. Mao, H. Feick, H. Yan, Y. Wu, H. Kind, E. Weber, R. Russo, P. Yang, Science 292(5523), 1897–1899, (2001).

[11] S. J. Pearton, D. P. Norton, K. Ip, Y. W. Heo, T. Steiner, Recent progress in processing and properties of ZnO, Superlattices and Microstructures 34, 3–32, (2003).

[12] C. Jagadish, S. J. Pearton, Zinc oxide bulk, thin films and nanostructures: processing, properties, and applications, Elsevier, (2006).

[13] A. Tsukazaki, A. Ohtomo, T. Onuma, M. Ohtani, T. Makino, M. Smiya, K. Ohtani, S. F. Chichibu, S. Fuke, Y. Segawa, H. Ohno, H. Koinuma, M. Kawasaki, Nat. Mater. 4, 42–46, (2005).

[14] J. P. Monsier, S. Chakrabarti, B. Doggett, E. McGlynn, M. O. Henry, A. Meaney, Pro. SPIE. 6474, 64740I, (2007).

[15] K. H. Hellwege, O. Madelung, Numerical data and functional relationship in science and technology, Landolt-Börnstein New Serie, Group III, 17a Springer, Berlin, (1982).

[16] L. Gerward, J. S. Olsen, Journal of Synchroton Radiation 2, 233, (1995).

[17] J. Joussot-Dubien, Nouveau Traité de Chimie Minérale, Masson and Cie, Paris 5, (1962).

[18] R. D. Shannon, C. T. Prewitt, Acta Cryst. B. 25, 925, (1969).

[19] A. Mang, K. Reimann, St. Rübenacke, Solid State Communications 94(4), 251–254, (1995).

[20] Z. Y. Xiao, Y. C. Liu, D. X. Zhao, J. Y. Zhang, Y. M. Lu, D. Z. Shen, X. W. Fan, Journal of luminescence 122–123, 822–824, (2007).

[21] K. Vanheusden, C. H. Seager, W. L. Warren, D. R. Tallant, J. A. Voigt, Appl. Phys. Lett. 68, 403–405, (1996).

[22] A. Janotti, C. G. Van de Walle, Rep. Prog. Phys. 72, 126501, (2009).

[23] R. C. Weast, Handbook of Chemistry and Physics, CRS Press, 56th Edition, 1975.

[24] E. M. Bachari, G. Baud, S. Ben Amor, M. Jacquet, Thin Solid Films 348, 165–172, (1999).

[25] T. K. Subramanyam, B. Srinivasulu Naidu, S. Uthanna, Opt. Mat. 13, 239–247, (1999).

[25] R. G. Heideman, P. V. Lambeck, J. G. E. Gardeniers, Opt. Mater. 4(6), 741–755, (1995).

[26] A. A. Othman, M. A. Osman, E. M. M. Ibrahim, Manar A. Ali, Ceram. Int. 43(1), 527–533, (2017).

[27] G. E. Jellison and L. A. Boatner, Phys. Rev. B. 58, 3586, (1998).

[28] M. Rebien, W. Henrion, M. Bär, C. H. Fischer, App. Phys. Lett. 80, 3518–3520, (2002).

[29] F. Ng-Cheng-Chin, M. Roslin, Z. H. Gu, T. Z. Fahidy, J. Phys. D: Appl. Phys. 31, L71, (1998).

[30] W. Li, D. Mao, F. Zhang, X. Wang, X. Liu, S. Zou, Q. Li, J. Xu, Nucl. Instrum. Methods. Phys. Res. B. 169, 59, (2000).

[31] P. Fons, K. Iwata, S. Niki, A. Yamada, K. Matsubara, J. Cryst. Growth. 201–202, 627–632, (1999).

[32] T. E. Murphy, D. Y. Chen, J. Phillips, J. Electron. Mater. 34(6), 699–703, (2005).

[33] D. C. Look, J. Electron. Mater. 35, 1299–1305, (2006).

[34] A. Y. Polyakov, N. B. Smirnov, A. V. Govorkov, E. A. Kozhukhova, S. J. Pearton, D. P. Norton, A. Osinsky, A. Dabiran, J. Electron. Mater. 35, 663–669, (2006).

[35] H. S. Kim, S. J. Pearton, D. P. Norton, F. Ren, Appl. Phys. A. 91(2), 255–259, (2008).

[36] F. S. Hickernell, Proceedings of the IEEE International, (2003).

[37] D. Dimova-Malinovska, Nanostructured and Advanced Materials: chapter ZnO - An Advanced Material for Solar Cell, Optoelectronic and Sensor Applications, Springer, 139–154, (2005).

[38] A. Vincze, J. Bruncko, M. Michalka, D. Figura, Central European Journal of Physics 5(3), 385–397, (2007).

[39] V. R Shinde, T. P. Gujar, C. D. Lokhande, R. S. Mane, S. H. Han, Mater. Chem. Phys. 96, 326–330, (2006).

[40] J. Hu, R. G. Gordon, Sol. Cells 30, 437–450, (1991).

[41] J. Y. Zeng, Z. Z. Ye, W. Z. Xu, D. Y. Li, J. G. Lu, L. P. Zhu, B. H. Zhao, Appl. Phys. Lett. 88, 062107, (2006).

[41] A. Tsukazaki, A. Ohtomo, T. Onuma, M. ohtani, T. Mahino, M. Sumiya, K. Ohtani, S. F. Chichibu, S. Fuke, Y. Segawa, H. Ohno, H. Koinuma, M. Kawasaki, Nat. Mater. 4, 42–46, (2005).

[43] R. J. Duclerea, M. Novotnyb, A. Meaneya, R. O. Hairea, E. McGlynna, M. O. Henrya, J. P. Mosniera, Superlattices Microstruct. 38, 397–404, (2005).

[44] H. S. Jeong, D. G. Yoo, D. Y. Kim, N. E. Lee, J. H. Boo, Thin Solid Films 516, 6598–6603, (2008).

[45] L. J. Lyons, A. Janotti, C. G. Van-de-Walle, Appl. Phys. Lett. 95, 252105, (2009).

[46] H. C. Park, S. B. Zhang, S. H. Wei, Phys. Rev. B. 66, 073202, (2002).

[47] K. Nakahara, S. Akasaka, H. Yuji, K. Tamura, T. Fujii, Y. Nishimoto, D. Takamizu, A.Sasaki, T. Tanabe, H. Takasu, H. Amaike, T. Onuma, S.F. Chichibu, A. Tsukazaki, A. Ohtomo, M. Kawasaki, Appl. Phys. Lett. 97, 013501, (2010).

[48] M. T. Barnes, K. Olson, C. A. Wolden, Appl. Phys. Lett. 86, 112112, (2005).

[49] C. Liu, F. Yun, H. Morkoc, J. Mater. Sci: Mater. Elec. 16, 555–597, (2005).

[50] H. A. M. Macdonald, P. Schiffer, N. Samarth, Nat. Mater. 4, 195–202, (2005).

[51] J. X. Wang, I. A. Buyanova, F. Zhao, D. Lagarde, A. Balocchi, X. Marie, C. W. Tu, J. C. Harmand, W. M. Chen, Nat. Mater. 8, 198–202, (2009).

[52] Z. Lu, H. S. Hsu, Y. Tzeng, J. C. A. Huang, Appl. Phys. Lett. 94, 152507, (2009).

[53] H. Ohono, Science 281(5379), 951–956, (1998).

[54] D. Chiba, K. Takamura, F. Matsukura, H. Ohno, Appl. Phys. Lett. 82, 3020, (2003).

[55] T. Dietl, H. Ohno, F. Matsukura, J. Cibert, D. Ferrand, Science 287, 1019–1022, (2000).

[56] K. Sato, H. K. Yoshida, Semicond. Sci. Technol. 17, 367, (2002).

[57] K. Doyoung, K. Hyungjun, SPIE 10, 1117–1120, (2010).

[58] J. B. Baxter, E. S. Aydil, Appl. Phys. Lett. 86, 1–3, (2005).

[59] C. Lévy-Clément, R. Tena-Zaera, M. A. Ryan, A. Katty, G. Hodes, Adv. Mater. 17, 1512–1515, (2005).

[60] L. Yang, Caractérisation de couches minces de ZnO élaborées par la pulvérisation cathodique en continu, Thèse doctorat, Université Du Littoral Coté D'opale, (2012).

[61] J. Y. Lee, J. H. Lee, H. S. Kim, C. H. Lee, H. S. Ahn, H. K. Cho, Y. Y. Kim, B. H. Kong, H. S. Lee, Thin Solid Films 517, 5157–5160, (2009).

[62] S. F. Chichibu, T. Ohmori, N. Shibata, T. Koyama, T. Onuma, Appl. Phys. Lett. 85, 4403–4405, (2004).

[63] M. Izaki, T. Shinagawa, K. T. Mizuno, Y. Ida, M. Inaba, A. Tasaka, J. Phys. D: Appl. Phys, 40, 3326–3329, (2007).

[64] K. C. Hsu, W. H. Hsiao, C. T. Lee, Y. T. Chen, D. S. Liu, Materials 8, 7745–7756, (2015).

[65] F. Schuster, B. Laumer, R. R. Zamani, C. Magén, J. R. Morante, J. Arbiol, M. Stutzmann, ACS Nano. 8, 4376–4384, (2014).

[66] A. Fujishima, K. Honda, Nature 238, 37–38, (1972).

[67] J. L. Yang, S. J. An, W. I. Park, et al., Adv. Mater. 18, 1661–1664, (2004).

[68] F. Xu, Z. Y. Yuan, G. H. Du, et al., Nanotechnology 17, 588–594, (2006).

[69] H. Kattoand, Y. Kog, Journal Electrochem. Soc. 118, 1619–1623, (1971).

[70] J. Curie, P. Curie, Comptes Rendus l'Académie des Sci. 93, 1137–1140, (1880).

[71] Z. L. Wang, J. Song, Arrays Science 312, 242–246, (2006).

[72] L. Lin, Y. Hu, C. Xu, Y. Zhang, R. Zhang, X. Wen, Z.L. Wang, Nano Energy 2, 75–81, (2013).

[73] H. I. Lin, D. S. Wuu, K. C. Shen, R. H. Horng, ECS Journal of Solid State Science and Technology 2, 400–404, (2013).

[74] P. S. Cho, K. W. Kim, J. H. Lee, J. Electroceram.17, 975–978, (2006).

[75] G. S. Devi, V. B. Subrahmanyam, S. C. Gadkari, S. K. Gupta, Anal. Chim. Acta. 568, 41–46, (2006).

[76] H. Gong, J. Q. Hu, J. H. Wang, C. H. Ong, F. R. Zhu, Sens. Actuator B. Chem. 115, 247–251, (2006).

[77] H. T. Wang, B. S. Kang, F. Ren, L. C. Tien, P. W. Sadik, D. P. Norton, S. J. Pearton, J. Lin, Appl. Phys. Lett. 86, 243503, (2005).

[78] X. Wang, J. Zhang, Z. Zhu, J. Zhu, Colloid. Surf. A. Physicochem. Eng. Asp. 276, 59–64, (2006).

[79] M. Zhao, X. Wang, L. Ning, J. Jia, X. Li, L. Cao, Sens. Actuators. B. 156, 588–592, (2011).

[80] D. Xiong, X. Zeng, W. Zhang, H. Wang, X. Zhao, W. Chen, Y.B. Cheng, Inorg. Chem. 53, 4106–4116, (2014).

[81] T. Prakash, K.P. Prasad, S. Ramasamy, B. S. Murty, Nanosci. Nanotechnol. 8(8), 4273–4278, (2008).

[82] R. Chandra, P. Taneja, P. Ayyub, Mater. 11(4), 505–512, (1999).

[83] H. Kawazoe, M. Yasukawa, H. Hyodo, M. Kurita, H. Yanagi, H. Hosono, Nature. 389, 939–942, (1997).

[84] K. Jacob, T. Mathews, J. Am. Ceram. Soc. 75(12), 3225–3232, (1992).

[85] F. Biccari, Defects and Doping in Cu_2O: General properties and applications, Doctoral Thesis, University of Rome, (2010).

[86] A. Pérez-Tomás, A. Mingorance, D. Tanenbaum, M. Lira-Cantú, in: Futur. Semicond. Oxides Next-Generation Sol. Cells. Elsevier Inc., 267–356, (2018).

[87] S. S. Sawant, A. D. Bhagwat, C. M. Mahajan, Journal of Nano- and Electronic Physics. 8(1), 01035, (2016).

[88] J. Ghijsen, L. H. Tjeng, J. van Elp, H. Eskes, J. Westerink, G. A. Sawatzky, Phys. Rev. B. 38,11322–11330, (1988).

[89] R. Restori, D. Schwarzenbach, Act. Cryst. B. 42, 201–208, (1986).

[90] K. Borgohain, N. Murase, S. Mahamuni, J. Appl. Phys. 92, 1292–1297, (2002).

[91] A. Werner, H. D. Hochheimer, Phys. Rev. B. 25, 5929, (1982).

[92] R. Mittal, S. L. Chaplot, S. K. Mishra, P. P. Bose, Phys. Rev. B. 75, 174303, (2007).

[93] P. Kofstad, Wiley. Interscience, New York, (1976).

[94] A. F. Wright, J. S. Nelson, J. Appl. Phys. 92, 5849–5851, (2002).

[95] D. Wu, Q. Zhang, M. Tao, Phys. Rev. B. Condens. Matter Mater. Phys. 73, 1–6, (2006).

[96] G. Aggarwal, S. K. Maurya, A. J. Singh, A. K. Singh, B. Kavaipatti, J. Phys. Chem. C. 123, 26057–26064, (2019).

[97] Biccari, F. Defects and Doping in Cu2O. Solid State Commun. 262, (2009).

[98] O. Porat, I. Riess, Solid State Ionics 81, 29–41, (1995).

[99] H. Raebiger, S. Lany, A. Zunger, Phys. Rev. B. Condens. Matter Mater. Phys. 76, 1–5, (2007).

[100] D. O. Scanlon, B. J. Morgan, G. W. Watson, A. Walsh, Phys. Rev. Lett. 103, 1–4, (2009).

[101] M. Nolan, S. D. Elliott, Phys. Chem. Chem. Phys. 8, 5350–5358, (2006).

[102] W. H. Brattain, Rev. Mod. Phys. 23, 203, (1951).

[103] R. J. Elliott, Phys. Rev. 124, 340–345, (1961).

[104] M. Nolan, S. D. Elliott, Thin Solid Films 516, 1468–1472, (2008).

[105] J. Resende et al, J. Phys. Chem. C. 123, 8663–8670, (2019).

[106] D. Muñoz-Rojas et al., AIP Adv. 2, 042179, (2012).

[107] G. Laia, Y. wu, L. Lin, Y. Qu, F. Lai, Applied Surface Science B. 285, 755–758, (2013).

[108] L. W. Wang, Doctoral Thesis, University of Texas at Arlington, (2006).

[109] A. O. Musa, T. Akomolafe, M. J. Carte, Solar Energy Materials and Solar Cells 51(3–4), 305–316, (1998).

[110] K. Han, M. Tao, Solar Energy Materials Solar Cells 93(1), 153–157, (2009).

[111] E. H. Kennard, E.O. Dieterich, Phys. Rev. 9, 58, (1917).

[112] L. O. Grondahl, Science 64, 306, (1926).

[113] Y. Zhang, L. Ma, Environ. Sci Technol. 41(17), 6264–6269, (2007).

[114] M. Benhaliliba, C. E. Benouis, M. S. Aida, F. Yakuphanoglu, A. S. Juarez, J. Sol-Gel Sci. Technol. 55(3), 335–342, (2010).

[115] M. E. Abu-Zeid, A. E. Rakhshani, A. A. Al-Jassar, Y. A. Youssef, Phys. Status Solidi 93(2), 613–620, (1986).

[116] I. S. Brandt, C. A. Martins, V. C. Zoldan, A. D. C. Viegas, J. H. Dias-Da-Silva, A. A. Pasa, Thin Solid Films 562, 144–151, (2014).

[117] A. S. Zoolfakar, R. A. Rani, A. J. Morfa, S. Balendhran, A. P. O'Mullane, S. Zhuiykov, K. Kalantar-zadeh, J. Mater. Chem. 22, 21767, (2012).

[118] S. M. Sze, K. K. Ng, Physics of Semiconductor Devices, Wiley, New York, USA, (2007).

[119] M. Izaki, T. Shinagawa, K. T. Mizuno, Y. Ida, M. Inaba, A. Tasaka, J. Phys. D: Appl. Phys. 40, 3326, (2007).

[120] Y. Hames, S. E. San, Sol. Energy 77, 291, (2004).

[121] D. Li, C. J. Chien, S. Deora, P. C. Chang, E. Moulin, J. G. Lu, Chem. Phys. Lett. 501, 446, (2011).

[122] M. Wang, L. Sun, Z. Lin, J. Cai, K. Xie, C. Lin, Energy Environ. Sci. 6, 1211, (2013).

[123] B. M. Fariza, J. Sasano, T. Shinagawa, S. Watase, M. Izaki, Thin Solid Films 520, 2261, (2012).

[124] T. Minami, Y. Nishi, T. Miyata, J. Nomoto, Appl. Phys. Express 4, 62301, (2011).

[125] Y.H. Ok, K.R. Lee, B.O. Jung, Y.H. Kwon, H.K. Cho, Thin Solid Films 570, 282, (2014).

[126] S. Kim, K. Hong, K. Kim, I. Lee, J. L. Lee, J. Mater. Chem. 22, 2039, (2012).

[127] G. B. Murdoch, M. Greiner, M. G. Helander, Z. B. Wang, Z. H. Lu, Appl. Phys. Lett. 93, 083309, (2008).

[128] D. Barreca, P. Fornasiero, A. Gasparotto, V. Gombac, C. Maccato, T. Montini, E. Tondello, Chem. Sus. Chem. 2, 230, (2009).

[129] Z. Zheng, B. Huang, Z. Wang, M. Guo, X. Qin, X. Zhang, P. Wang, Y. Dai, J. Phys. Chem. C 113, 14448, (2009).

[130] S. P. Meshram, P.V. Adhyapak, U. P. Mulik, D. P. Amalnerkar, Chem. Eng. J. 204–206, 158–168, (2012).

[131] P. E. de Jongh, D. Vanmaekelbergh, J. J. Kelly, Chem. Commun. 103, 1069, (1999).

[132] G. K. Mor, O. K. Varghese, R. H. T. Wilke, S. Sharma, K. Shankar, T. J. Latempa, K. S. Choi, C. A. Grimes, Nano Lett. 8, 1906, (2008).

[133] W. Siripala, A. Ivanovskaya, T. F. Jaramillo, S. H. Baeck, E. W. McFarland, Sol. Energy Mater. Sol. Cells 77, 229, (2003).

[134] N. Özer, F. Tepehan, Sol. Energy Mater. Sol. Cells 30, 13, (1993).

[135] R. Neskovska, M. Ristova, J. Velevska, M. Ristov, Thin Solid Films 515, 4717, (2007).

[136] M. Ristova, R. Neskovska, V. Mirˇceski, Sol. Energy Mater. Sol. Cells 91, 1361, (2007).

[137] O. Akhavan, H. Tohidi, A. Z. Moshfegh, Thin Solid Films 517, 6700, (2009).

[138] S. B. Wang, C. H. Hsiao, S. J. Chang, K. T. Lam, K. H. Wen, S. C. Hung, S. J. Young, B. R. Huang, Sens. Actuators A 171, 207, (2011).

[139] S. Sahoo, S. Husale, B. Colwill, T. M. Lu, S. Nayak, P. M. Ajayan, ACS Nano. 3, 3935, (2009).

[140] S. Manna, K. Das, S. K. De, ACS Appl. Mater. Interfaces 2, 1536, (2010).

[141] H. Kim, C. Jin, S. Park, S. Kim, C. Lee, Sens. Actuators B. 161, 594, (2012).

[142] X. Gou, G. Wang, J. Yang, J. Park, D. Wexler, J. Mater. Chem. 18, 965, (2008).

[143] G. X. Zhu, H. Xu, Y. Y. Xiao, Y. J. Liu, A. H. Yuan, X. P. Shen, ACS Appl. Mater. Interfaces 4, 744, (2012).

[144] D. Barreca, E. Comini, A. Gasparotto, C. Maccato, C. Sada, G. Sberveglieri, E. Tondello, Sens. Actuators B 141, 270, (2009).

[145] Y. S. Kim, I. S. Hwang, S. J. Kim, C. Y. Lee, J. H. Lee, Sens. Actuators B 135, 298, (2008).

[146] D. D. Li, J. Hu, R. Q. Wu, J. G. Lu, Nanotechnology 21, 485502, (2010).

[147] F. Zhang, A. W. Zhu, Y. P. Luo, Y. Tian, J. H. Yang, Y. Qin, J. Phys. Chem. C. 114, 19214, (2010).

[148] S. Park, H. Boo, T. D. Chung, Anal. Chim. Acta 556, 46, (2006).

[149] V. Patil, D. Jundale, S. Pawar, M. Chougule, P. Godse, S. Patil, B. Raut, S. Sen, Journal of Sensor Technology 1(2), 36–46, (2011).

[150] H. W. Richardson, Ullmann's Encyclopedia of Industrial Chemistry, Wiley-VCH, (2002).

[151] O. Madelung, Semiconductors data handbook Berlin, New York, Springer, (2004).

[152] https://enwikipediaorg/wiki/Copper(II)_oxide.

[153] K. L. Liu, S. L. Yuan, H. N. Duan, X. F. Zheng, S. Y. Yin, Z. M. Tian, C. H. Wang, S. X. Huo, J. Appl. Phys. 107, 023911, (2010).

[154] J. B. Forsyth, S. Hull, J. Phys. Condens. Matter. 3, 5257–5261, (1991).

[155] S. Rehman, A. Mumtaz, S. K. Hasanain, J. Nano. Part. Res. 13, 2497–507, (2010).

[156] A. Rahnama, M. Gharagozlou, Optical and Quantum Electronics 44, 313–322, (2012).

[157] A. H. Jayatissa, K. Guo, A. C. Jayasuriya, Appl. Surf. Sci. 255(23), 9474–9479, (2009).

[158] N. Banerjeea, S. Kundoo, K. K. Chattopadhyay, Thin Solid Films 440, 5–10, (2003).

[159] B. J. Hansen, N. Kouklin, G. Lu, I. K. Lin, J. Chen, X. Zhang, J. Phys. Chem. C 114(6), 2440–2447, (2010).

[160] D. Gopalakrishna, K. Vijayalakshmin, C. Ravidhas, Ceramics International 39(7), 7685–7691, (2013).

[161] D. X. Wu, Q. M. Zhang, M. Tao, Phys. Rev. B 73, 235206, (2006).

[162] B. J. Hansen, G. Lu, J. Chen, Journal of Nanomaterials 7, 830474, (2008).

[163] S. Sumikaru, S. Mori, S. Shimizu, H. Usami, E. Suzuki, Journal of Photochemistry and Photobiology A: Chemistry 194(2–3), 143–147, (2008).

[164] J. Chen, S. Z. Deng, N. S. Xu, J. Appl. Phys. Lett. 83, 746, (2003).

[165] H. Zhang, M. Zhang, Mater. Chem. Phys. 108,184, (2008).

[166] J. C. Park, J. Kim, H. Kwan, H. Song, Adv. Mater. 21, 803, (2009).

[167] G. Ren, D. Hu, E. W. Cheng, M. A. Vargas-Reus, P. Reip, R. P. Allaker, International Journal of Antimicrobial Agents 33(6), 587–590, (2009).

[168] J. Xu, K. Yu, J. Wu, D. Shang, L. Li, Y. Xu, Z. Zhu, J. Phys. D : Appl. Phys. 42, 075417, (2009).

[169] I. Y. Erdogan, O. Gullu, J. Alloy. Compd. 492, 378, (2010).

[170] L. C. Olsen, R. C. Bohara, M. W. Urie, App. Phys. Lett. 34, 47–50, (1979).

[171] J. Herion, E. A. Niekisch, G. Schari, Sol. Energy Mater. Sol. cells 4, 101–112, (1980).

[172] S. Dolai, R. Dey, S. Hussain, R. Bhar, A. K. Pal, Materials Research Bulletin 109, 1–9, (2018).

[173] O. Akhavan, E. Ghaderi, J. Mater. Chem. 21, 12935, (2011).

[174] B. Urasinska-Wojcik, J. W. Gardner, IEEE Sensors Journal 18, 3502–3508, (2018).

[175] A. Aslani, V. Oroojpour, Physica B: Condensed Matter 406(2), 144–149, (2011).

[176] K. M. Kim, H. M. Jeong, H. R. Kim, K. I. Choi, H. J. Kim, J. H. Lee, Sensors 12(6), 8013–2805, (2012).

[177] M. Mashock, K. Yu, S. Cui, S. Mao, G. Lu, J. Chen, ACS Appl. Mater. Interfaces 4(8), 4192–4199, (2012).

[178] S. Jana, S. Das, N. S. Das, K. K. Chattopadhyay, Mater. Res. Bull. 45, 693–698, (2010).

[179] H. T. Hsueh, T. J. Hsueh, S. J. Chang, F. Y. Hung, T. Y. Tsai, W. Y. Weng, C. L. Hsu, B. T. Dai, Sensor Actuat. B: Chem. 156, 906–11, (2011).

[180] Q. Tian, D. Shi, Y. Sha, Molecules 13(4), 948–957, (2008).

[181] P. Vomácka, V. Štengl, J. Henych, M. Kormunda, Journal of Colloid and Interface Science 481, 28–38, (2016).

[182] L. B. Chen, N. Lu, C. M. Xu, H. C. Yu, T. H. Wang, Electrochimica Acta 54(17), 4198–4201, (2009).

[183] H. Pang, J. Deng, B. Yan, Y. Ma, G. Li, Y. Ai, J. Chen, J. Zhang, H. Zheng, J. Du, Int. J. Electrochem. Sci. 7, 10735–10747, (2012).

[184] S. A. Campbell, The Science and Engineering of Microelectronic Fabrication, Oxford University Press, (2001).

[185] A. G. Khairnar, Deposition and Characterization of High-k Dielectric Thin Films for MOS Capacitors, Department of Electronics, North Maharashtra University, Jalgaon, India, (2014).

[186] R. J. Martin-Palma, A. Lakhtakia, in: Engineered Biomimicry, Elsevier Inc., 383–398, (2013).

[187] J. L. Vossen, W. Kern, W. Kern, Thin Film Processes II, vol. 2, Gulf Professional Publishing, (1991).

[188] A. C. Lokhande, R. B. V. Chalapathy, M. He, E. Jo, M. Gang, S. A. Pawar, C. D. Lokhande, J. H. Kim, Sol. Ener. Mater. Sol. Cells 153, 84–107, (2016).

[189] A. Barranco, A. Borras, A. R. G. Elipe, A. Palmero, Progress Mater. Sci. 76, 59–153, (2016).

[190] J. J. Merkel, T. Sontheimer, B. Rech, C. Becker, J. Cryst. Growth 367, 126–130, (2013).

[191] S. Mukherjee, D. Gall, Thin Solid Films 527, 158–163, (2013).

[192] U. Schulz, S. G. Terry, C. G. Levi, Mater. Sci. Eng. A. 360(1–2), 319–329, (2003).

[193] B. Yang, H. Duan, C. Zhou, Y. Gao, J. Yang, Appl. Surf. Sci. 286, 104–108, (2013).

[194] J. X. J. Zhang, K. Hoshino, in: Molecular Sensors and Nanodevices, 43–111, (2019).

[195] H. Angusmacleod, In: Piegari A, Flory F, editors. Optical Thin Films and Coatings from Materials to Applications. Oxford: Woodhead Publishing Series, 3–25, (2013).

[196] C. Morosanu, V. Dumitru, E. Cimpoiasu, C. Nenu, In: M. A. Prelas, A. Benedictus, L. T. S. Lin, G. Popovici, P. Gielisse, editors, Diamond Based Composites and Related Materials, 1st ed, Petersburg, Russia: Springer Science+Business Media Dardrecht, 127–132, (1997).

[197] V. Dumitru, C. Morosanu, V. Sandu, A. Stoica, Thin Solid Films 359, 17–20, (2000).

[198] Z. Chen et al., IEEE Long Island Systems, Applications and Technology Conference, New York, (2010).

[199] N. K. Jain, M. S. Sawant, S. H. Nikam, S. Jhavar, L. Shohet, Encyclopedia Plasma Technol., 722–740, (2016).

[200] C. Mastail, Modélisation et simulation du dépôt des oxydes à forte permittivité par la technique du Monte-Carlo cinétique, Thèse doctorat, Université Toulouse III - Paul Sabatier, 33-36, (2010).

[201] J. Livage, M. Henry, C. Sanchez, Progress in Solid State Chemistry 18(4), 259–341, (1988).

[202] A. Jilani, M. S. Abdel-Wahab, A. H. Hammad, Mod. Technol. Creat. Thin. Film. Syst. Coat. 2, 137–149, (2017).

[203] Y. Yunus, N. A. Mahadzir, M. N. Mohamed-Ansari, T. H. T. Abd-Aziz, A. M. Afdzaluddin, H. Anwar, M. Wang, A. G. Ismail, Polymers 14, 1112, (2022).

[204] J. E. Elshof, Epitaxial Growth of Complex Metal Oxides, 69–93, (2015).

[205] M. S. Aida, Cours post graduation, (2005).

[206] S. Zerkout, Thèse de doctorat, Université de Constantine.

[207] G. K. Wehner, Phys. Rev, 690, (1971).

[208] D. B. A. Dubach, A. R. S. L. J. Gauckler, J. Electroceram. 16, 221–228, (2006).

[209] J. Amblard, Electrocristallisation –Aspects fondamentaux, Techniques de l'Ingénieur D906, (1976).

[210] N. Kanani, Electroplating – Basic Principles, Processes and Practrice, Elsevier, 353, (2004).

[211] T. Brouri, Élaboration et étude des propriétés électriques des couches minces et des nanofils de ZnO, Thèse de Doctorat, Université Paris-Est, France, (2011).

[212] J. Lee, H. Varela, S. Uhm, Y. Tak, Electrochem. Commu. 2(9), 646–652, (2000).

[213] T. Pauporté, D. Lincot, Electrochim. Acta 45(20), 3345–3353, (2000).

[214] J. S. Wellings, N. B. Chaure, S. N. Heavens, I. M. Dharmadasa, Thin Solid Films 516(12), 3893–3898, (2008).

[215] T. Pauporté, D. Lincot, J. Electroanal. Chem. 517, 54–62, (2001).

[216] O. Baka, A. Azizi, S. Velumani, G. Schmerber, A. Dinia, J. Mater. Sci: Mater. Electron. 25, 1761–1769, (2014).

Chapter II

Preparation and characterization of Mn doped ZnO thin films

II.1 Introduction

Zinc oxide (ZnO) is a wide bandgap semiconductor with a bandgap of 3.37 eV and an exciton binding energy of 60 meV [1], which is 2.4 times the effective thermal energy at room temperature. ZnO can be produced in a variety of nanostructures including nanowires, nanoribbons, nanobelts nano-combs, nanoparticles, nanofibers, and nanowires. The best advantage provided by ZnO is that its components are plenty on earth and non-toxic. This is an undeniable asset as it allows a reduction in production costs. It has certain physical and optical properties that both fascinate and interest multiple application groups: light-emitting diodes [2], field-effect transistors [3], sensors [4–6], solar cells [7–9], lasers [10, 11], photocatalytic systems [12–14] and ultra-violet (UV) photodetectors [15–21]. This oxide can be synthesized in various ways: chemical vapor deposition (CVD) [22, 23], thermal evaporation [24], pulsed laser deposition (PLD) [25], aqueous chemical growth [5, 11], sol-gel procedures [6, 26], hydrothermal procedures [27, 28], electrochemical techniques [29–34], spray pyrolysis technique SPT [35].

In this work, we chose spray pyrolysis, which is a simple and cost-effective method. Moreover, one of the advantages of its mild chemical route is the ability to easily modify and control various parameters, such as the solution concentration, deposition time, the distance between the nozzle and the substrate, and the types of precursors. The most important variables that control the material's conductivity are doping and substrate temperature [36–40]. This process allows for the production of well-adhered, transparent deposits with good crystalline quality. In this process, the jet droplets strike the hot substrate directly where the pyrolytic reaction occurs, leading to the formation of a thin film.

Mn doping introduced magnetic properties into ZnO, thus, it has been proposed as a spintronic material and is of interest as a magnetic sensor. Moreover, Mn lowered the recombination rate of charge carriers enabling much better performance of ZnO in these applications of photocatalytic degradation and energy conversion. ZnO is a TCO (transparent conductive oxide) with a level of both electrical conductivity and optical transparency of ca. 85% in visible light, an optical band gap of 3 eV or greater and it can be semi-conductive or highly conductive.

From research on 3d transition metals (like Co, Ni, Mn, and Cu) in ZnO, it has been demonstrated that ZnO turns into a dilute magnetic semiconductor (DMS), a recent and emerging material for spintronic applications [47]. Single-crystalline architectures and most likely functional properties can be expected for Co-doped ZnO films grown by MBE, according to findings from Lu et *al.* [48]. Co-doped ZnO films synthesized by using the PST method were deposited onto glass substrates heated to 450 °C. By using PLD, the magnetic properties of Co-doped ZnO thin films were shown by Tietze et al. [49]. Hexagonally matched micro-rods of Co-doped ZnO films with different dissolution percentages (0, 1, 3 and 5%) prepared using PST will fabricate Bacaksiz et *al.* [50]. Various Mn concentrations (x = 0, 4, 6, 8, and 10%) were screened using Mn-doped ZnO thin films by means of PST to illustrate the impact of doping on material properties of ZnO. R. Grothe et *al.* [51] produced ZnO films on ZnMgAl substrates using the spray coating process, where a concentrated solution of zinc acetate dihydrate (250 g/l) in ultra-pure water (0.055 µS/cm) was used to improve deposition efficiency. Likewise, the spray pyrolysis technique has shown to be an efficient method for quickly depositing thin oxide films onto metal substrates. Doped ZnO films (Ag and Au) were successfully sprayed on glass substrates that were ultrasonically cleaned, which led to improved electrical and optical properties [52-54]. Carbon-doped ZnO nanoparticles were synthesized by thermal decomposition of zinc citrate precursors, forming 2D-ZnO nanoparticles with an optical bandgap of 2.9 eV [55]. Al-doped ZnO films were deposited on glass substrates using sol-gel methods, where all samples crystallized in a polycrystalline structure without any impurity phases [56]. Recent studies demonstrate more possibilities of ZnO in different applications. For example, Al Abdulaal et *al.* [57] revealed that visible light illumination considerably enhances the photocatalytic performance of ZnO doped with Y_2O_3 for electronic and environmental applications. Higher figure of merit (688×10^{-6} m^3) was seen for silver nanowire doped ZnO (ZnO:Ag NWs), whereas aluminum-doped ZnO (ZnO:Al) did demonstrate promising performance (295.4×10^{-6} m^3), thereby qualifying the materials for applications in high-efficiency photovoltaic devices [58]. Ayana A et *al.* [59] reported the important role that deposition temperature plays in determining the microstructure and piezoelectric characteristics of ZnO films spray pyrolyzed on p-type silicon substrates. The morphology, structure, optical properties and performance with respect to the sensing of NO_2 gas have been assessed for ZnO nanoparticles synthesized through annealing four precursors-a zinc carbonate hydroxide-at four different annealing temperatures (200, 400, 600, and 800 °C)-and incorporated into gas sensors to improve their enhanced response and selectivity towards NO_2 [60,61]. Li et *al.* [62] have also demonstrated potential applications of ZnO as an electrode of lithium-ion batteries, where its high surface area and conductivity have proved to enhance improvements in charge/discharge cycles. Moreover, ZnO as semiconductor boasts a rather wide band gap, excellent chemical stability, and cost efficiency [63]. Nanostructured ZnO thin films deposited using a simple spray pyrolysis technique (SPT) on glass/FTO substrates at 450 °C demonstrated a crystalline nature with nanovial-like morphology [64]. The synthesis, by microwave-assisted method, formed microflowers of ZnO with an average size of 5 µm and a bandgap of 3.19 eV due to the hexagonal structure of ZnO [65]. The undoped and cadmium-doped ZnO (Cd-ZnO) thin films are obtained by a low-cost spray pyrolysis technique carried out on glass substrates, where all films exhibit a preferred orientation along the (002) plane and decreasing bandgap with an increase in Cd content [66]. Likewise, spray pyrolysis was used for layer deposition of these quaternary materials by varying substrate temperatures from 250 to 450 °C [67].

II.2 ZnO thin films deposition

II.2.1 Substrates preparation

The thin films were deposited in air onto soda-lime glass substrates (optical glass slides). The choice of glass as the deposition substrate was made due to its amorphous nature, which provides good thermal expansion compatibility with ZnO to minimize stress at the substrate-film interface [68,69], for economic reasons, and for its transparency, which is well-suited for the optical characterization of the films in the visible range. The dimensions of the substrate are fixed at 2 × 2 cm^2.

The substrates need to be carefully prepared to ensure they can support the deposition. Cleaning is a crucial step that must be taken in a clean environment, as it affects the adhesion and uniformity of the deposited layers. The substrates must be free from grease, scratches, dust, and any flatness issues. The cleaning process involves using an ultrasonic bath at room temperature, and it follows these steps:

- Washing with acetone for 5 minutes.
- Washing with ethanol for 5 minutes.
- Washing with distilled water for 5 minutes.
- Drying in an oven at 100 °C.

We used organic solvents, such as acetone and ethanol, to remove organic impurities, while HCl and distilled water were used to eliminate inorganic impurities. To prevent contamination, we made sure not to touch the substrate surface with our hands.

II.2.2 Solutions preparation

Many precursors can be used for zinc oxide (ZnO) deposits; ZnO thin films can be prepared from zinc nitrate ($Zn(NO_3)_2$) powders [41], or zinc chloride ($ZnCl_2$) [42], or zinc acetylacetonate ($Zn(C_5H_{10}O_2)_2$) [43], or zinc acetate ($Zn(CH_3COO)_2$) [44], dissolved in a volatile solvent such as methanol or ethanol [45]. Furthermore, ZnO films obtained by spray pyrolysis can be easily doped with a wide variety of elements by adding an additional precursor during deposition. Typical dopants used to enhance the physical properties of ZnO films belong to Group *III* elements (B, Al, In, Ga) of the periodic table. To achieve p-type doping of ZnO, which is a significant challenge and one of the keys to the development of ZnO-based components, elements from Group I or V can be used. It appears that the nitrogen approach is the most promising as demonstrated by S. Golshahi et *al*. [46].

Since the properties of ZnO depend heavily on the sample preparation methods, the choice of products to be used is crucial. Zinc acetate dehydrate ($Zn(CH_3COO)_2$, $2H_2O$) has proven to be a preferable organometallic compound for the growth of zinc oxide thin films by the spray pyrolysis process. Manganese acetate tetrahydrate ($Mn(CH_3COO)_2$, $4H_2O$) is used as the dopant source at various doping percentages (0, 2, 4, 6, 8, and 10%) and the deposited films are denoted by ZnO, $Mn_{0.02}Zn_{0.98}O$, $Mn_{0.04}Zn_{0.96}O$, $Mn_{0.06}Zn_{0.94}O$, $Mn_{0.08}Zn_{0.92}O$, and $Mn_{0.1}Zn_{0.9}O$, respectively. The solvent used is a mixture of isopropyl alcohol ($CH_3CH(OH)CH_3$) and distilled water (H_2O), and monoethanolamide [$NH_2CH_2CH_2OH$] was added to the solution as a stabilizer. Table II.1 presents the quantities of powders and volumes of solvents used.

Tableau II.1: The quantities of powders and the volumes of solvents used.

Molarity (*M*)	**Zinc acetate mass (*g*)**	**Manganese acetate mass (*g*)**	**Isopropanol volume (*ml*)**	**Distilled water volume (*ml*)**
0.2	18.437	0.000	50	20
0.2	18.068	0.048	50	20
0.2	17.700	0.097	50	20
0.2	17.331	0.151	50	20
0.2	16.962	0.206	50	20
0.2	16.593	0.263	50	20

II.2.3 Experimental conditions

The experimental conditions for the deposition process are as follows:

- Liquid flow rate: 1 ml/min.
- Static air pressure: in air.
- Deposition duration: 10 min.
- Deposition temperature: 350 °C.

The deposition process begins right after preparing the substrates and solutions, and it involves several steps. First, the substrate holder is placed above a heating element connected to a temperature controller. To prevent thermal shock, the holder is gradually heated from room temperature up to the desired deposition temperature (350 °C). Once the heating is complete, the solution flow rate is adjusted, and very fine droplets are sprayed onto the heated substrate. This triggers a chemical reaction through pyrolysis, causing the solvent to evaporate as the two compounds react endothermically to form the thin film. After the deposition is finished, the heating is turned off, and the substrates are allowed to cool on the holder until they reach room temperature to avoid any thermal shock that could break the glass. Finally, the samples are collected.

II.3 Characterization of deposited ZnO thin films

This dissertation aims to explore how manganese (Mn) doping affects the structural, optical, and electrical characteristics of ZnO thin films, particularly in the context of their potential use in advanced technologies such as optoelectronics, spintronics, and magnetic sensors. The research focuses on how varying Mn concentrations influence the crystal structure, light transmission, and electrical behavior of the films, helping to shed light on the underlying mechanisms that govern their performance. The findings from this study could contribute to the design of optimized ZnO-based materials for applications in photovoltaics, catalysis, and energy storage.

These films are characterized using various techniques for X-ray diffraction spectra used Philips Pananalytical X'Pert PRO MPD powder X-ray diffractometer coupled to an X'Celerator detector, operating at voltage of 45 kV and current of 35 mA on the Bragg-Brentano geometry. The radiation used was Cu-$K\alpha$ line of wavelength λ = 1.54059 Å and the symmetrical sweep began from 2θ = 20° to 2θ = 80°. The data was processed utilizing X'Pert HighScore software. Optical transmission was measured for the films with a UV-Vis-Near spectrophotometer covering wavelengths between 800 nm and 200 nm. FTIR spectra were recorded on a Shimadzu FTIR spectrophotometer within the range of 4000 cm^{-1} to 400 cm^{-1}.

II.3.1 Morphological characterization

II.3.1.1 Characterization by scanning electron microscopy SEM

Energy-dispersive X-ray (EDX) analysis was carried out to examine Mn-doped ZnO samples, confirming that the films are nearly stoichiometric in composition. Figure II.1 presents representative EDX spectra for $Mn_{0.02}Zn_{0.98}O$ thin films deposited using the PST method at 350 °C in air. The analysis shows the presence of oxygen, manganese, and zinc, indicating that Mn ions substitute Zn ions within the ZnO lattice. This substitution plays a key role in altering the films' optical and electrical properties.

With increasing Mn content, slight variations in elemental ratios were observed—particularly a modest decrease in zinc levels—while oxygen content remained relatively stable across all samples. This consistency in oxygen levels suggests that Mn incorporation does not significantly disturb the ZnO crystal lattice, where oxygen forms a crucial structural component. The enhanced interaction between Mn and the ZnO matrix appears to improve the sample's chemical behavior and catalytic efficiency.

Furthermore, electrical conductivity was found to increase with higher Mn concentrations, pointing to improved charge transport properties. Spin-orbit coupling effects are also evident in the EDX spectra, where the Zn 2p peak splits into Zn: $2p_{3/2}$ and Zn: $2p_{1/2}$ components. For Mn, the Mn: 3d peaks associated with spin-orbit coupling (J = 5/2 and 3/2) appear at 5.8 keV and 6.5 keV, respectively, showing a characteristic energy separation of 700 eV.

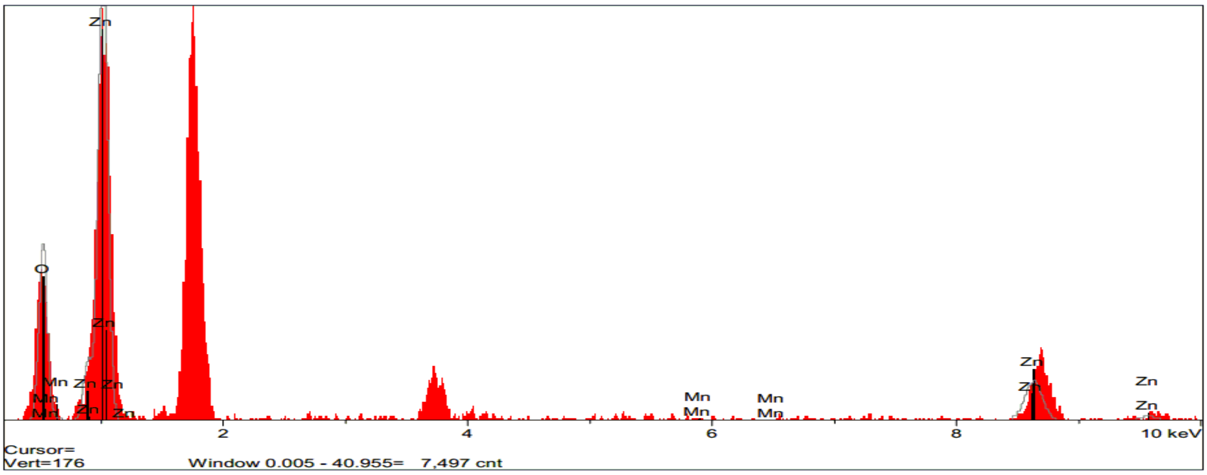

Figure II.1: EDX spectra of $Mn_{0.02}Zn_{0.98}O$ thin films deposited by PST at 350 °C in air.

Figure II.2 shows SEM images of undoped, and manganese (Mn) doped zinc oxide thin films.

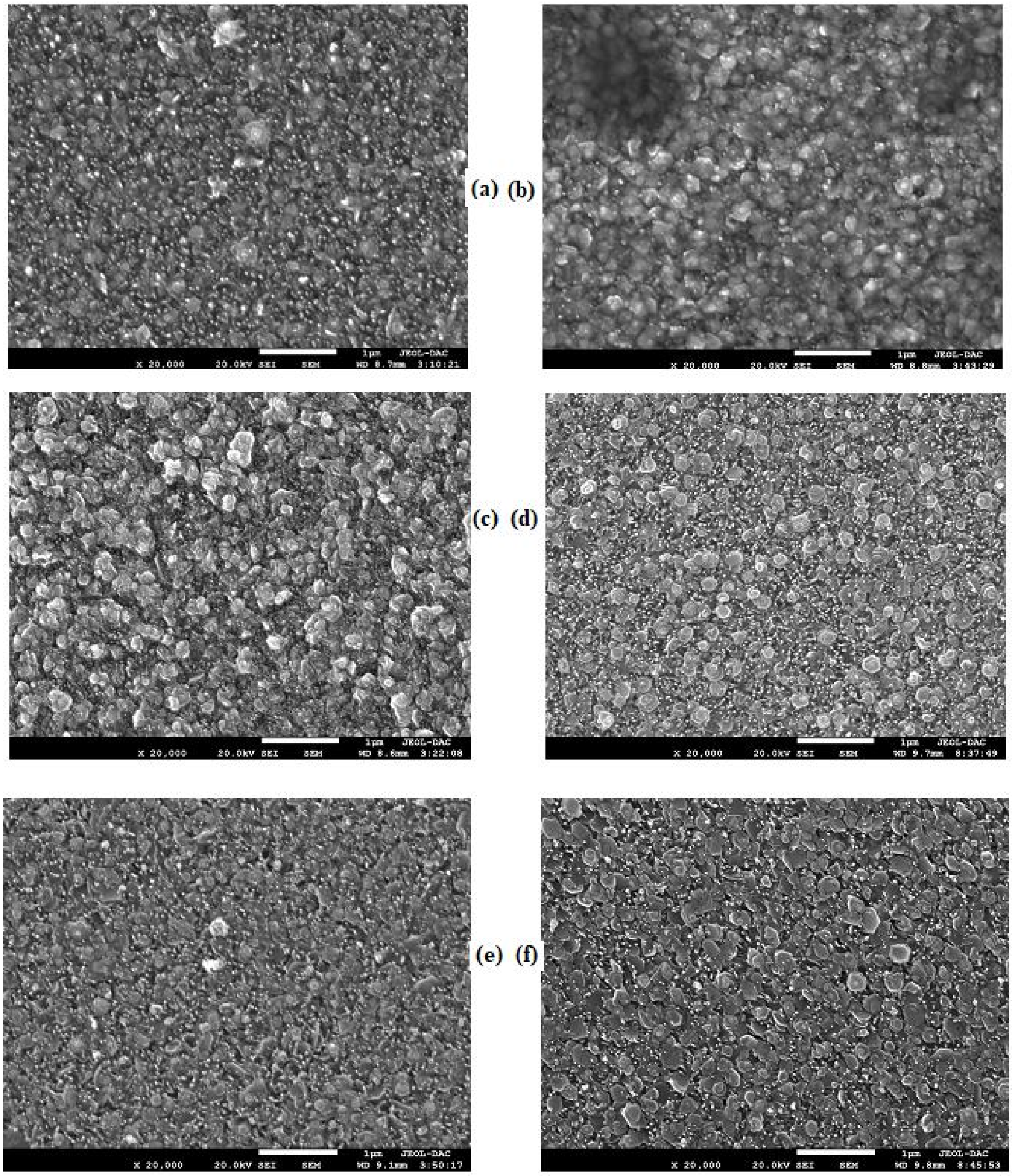

Figure II.2: SEM images of thin films of $Zn_{1-x}Mn_xO$ for: (a) x = 0, (b) x = 0.02, (c) x = 0.04, (d) x = 0.06, (e) x = 0.08, (f) x = 0.1.

The morphology of Mn- doped ZnO was likely to low agglomeration, better distribution and spherical nanocrystallites characteristics. The nanomaterials of Mn-doped ZnO were synthesized using a hexagonal wurtzite crystal structure. Meanwhile, the EDX analysis pertains to nanoparticles which is evidence with the synthesis of Mn doped ZnO. This study focused on the evolution of surface microtopography with varying ratios of Mn/Zn (0, 2, 4, 6, 8, and 10 %). This can be visualized in cleared micrographs of different atomic rearrangements that are surrounded with manganese nanoparticles. These results confirmed the formation of Mn-ZnO nanocomposited by means of EDX. It was observed that the agglomerated grains located on the surface of ZnO thin film are rather homogeneously distributed where average sizes are of order 15 nm. Furthermore, it was noted that every agglomeration was made up of tiny spherical grains of about 15 nm. It has been reported on the increase of the concentration of Mn doping that the crystallite size of ZnO as well as Mn-doped nanoparticles that are prepared via sol-gel auto combustion processes decreased from 38.42 to 27.54 nm [70].

II.3.1.2 Characterization by atomic force microscopy AFM

An image obtained by AFM is a type of image that depicts the topography of a sample surface and will give rise to a topographic map of the surface features. AFM images of ZnO, $Mn_{0.02}Zn_{0.98}O$, $Mn_{0.04}Zn_{0.96}O$, $Mn_{0.06}Zn_{0.94}O$, $Mn_{0.08}Zn_{0.92}O$, and $Mn_{0.1}Zn_{0.9}O$ are shown in Figure II.3. The samples show non-uniform extended lines with heights ranging from 3 nm to 40 nm and widths ranging from 5 nm to 60 nm, as well as spherical grains, where the size decreases with increasing manganese content.

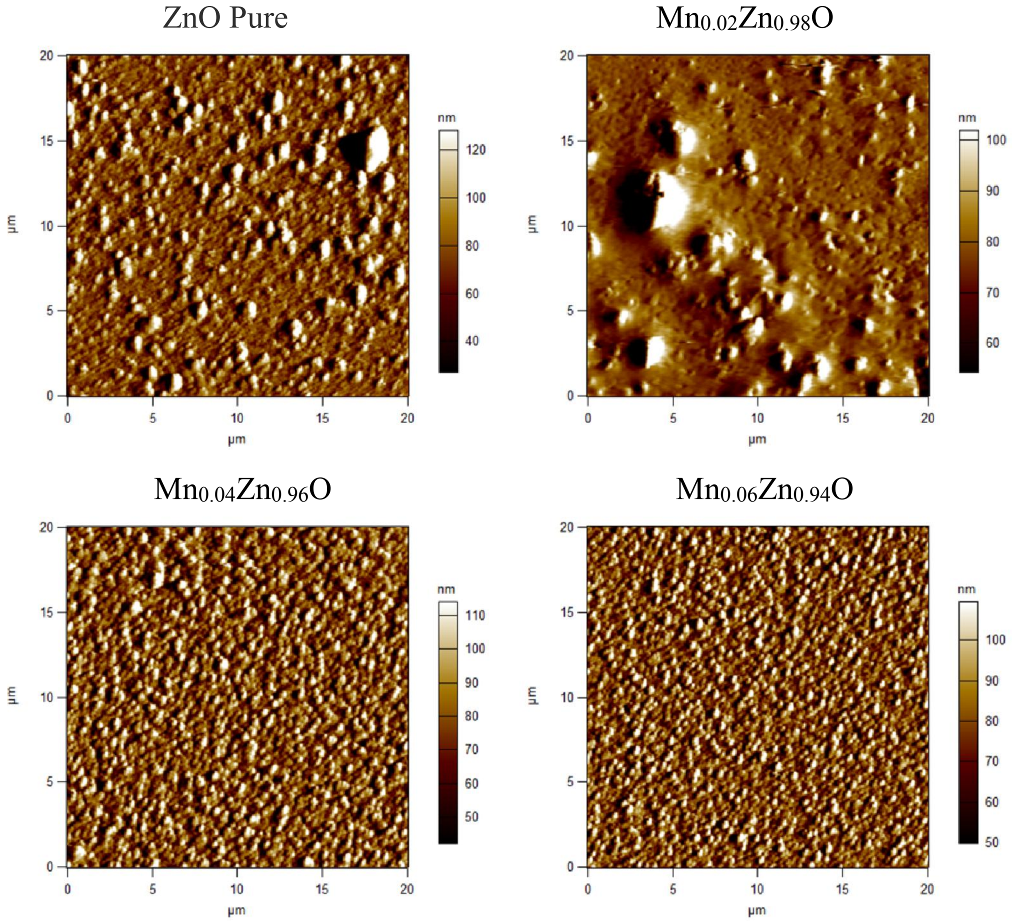

ZnO Pure

$Mn_{0.02}Zn_{0.98}O$

$Mn_{0.04}Zn_{0.96}O$

$Mn_{0.06}Zn_{0.94}O$

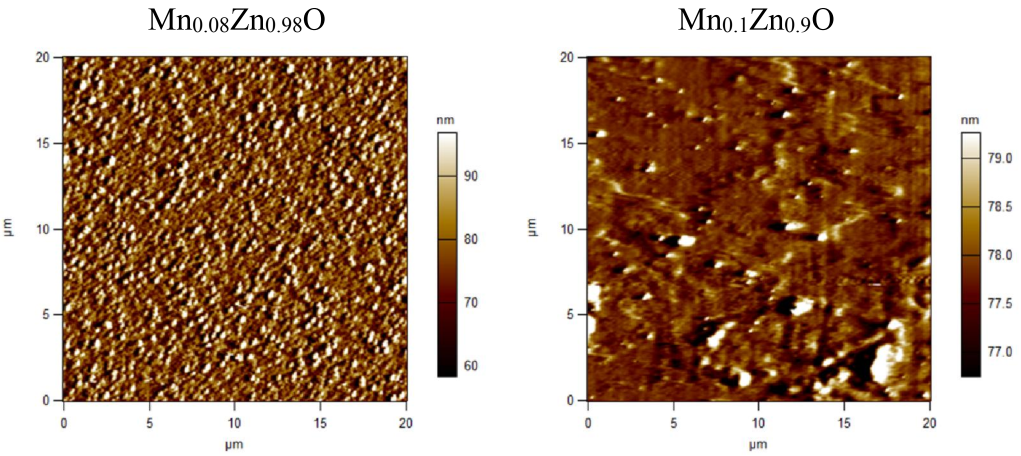
$Mn_{0.08}Zn_{0.98}O$ $Mn_{0.1}Zn_{0.9}O$

Figure II.3: AFM images of ZnO, $Mn_{0.02}Zn_{0.98}O$, $Mn_{0.04}Zn_{0.96}O$, $Mn_{0.06}Zn_{0.94}O$, $Mn_{0.08}Zn_{0.92}O$ and $Mn_{0.1}Zn_{0.9}O$.

II.3.2 Structural characterization

ZnO has been developed from a pure material, but growth has been achieved in several orientations with preferential orientation along (002). Measurements were made using X-Ray powder diffraction (XRD) with Cu-$K\alpha$ (λ = 0.154059 nm): According to Bragg's law, this relates the parallel of the atomic distance within a crystal to the angle in which waves sent to the crystal are diffracted:

$$2 d_{hkl} \sin \theta = n \lambda \tag{II.1}$$

n, θ and λ are the diffraction order, the diffraction angle and the wavelength.

The lattice parameters are calculated according to the direction [hkl] by the relation [71]:

$$d_{hkl} = \frac{a}{\sqrt{\frac{4}{3}\left(h^2 + k^2 + hk\right) + l^2 \frac{a^2}{c^2}}} \tag{II.2}$$

The investigation with XRD reveals the structural variations of thin films ZnO, $Mn_{0.02}Zn_{0.98}O$, $Mn_{0.04}Zn_{0.96}O$, $Mn_{0.06}Zn_{0.94}O$, $Mn_{0.08}Zn_{0.92}O$, and $Mn_{0.1}Zn_{0.9}O$. The synthesized samples exhibited polycrystalline nature with a hexagonal crystal structure, as shown in figure II.4. The XRD spectral pattern of the films exhibits peaks corresponding to the (100), (002), (101), (102), (103), (112), and (004) planes in the hexagonal ZnO structure. The more significant factor here would be that the (002) peak position of ZnO doped with Mn concentration approaching ≥ 1 % is closer to 34.426° [72] than that of ZnO powder, and this value is in good agreement with our value 34.672 °. When this Mn doping increases to 6%, the intensity of this (002) peak decreases while its width increases. These findings suggest that the crystallinity of the ZnO thin films is progressively compromised due to lattice strain arising from the ionic radius mismatch between Mn^{2+} and Zn^{2+} ions. Detailed X-ray diffraction (XRD) analysis reveals subtle modifications in the lattice parameters of Mn-doped ZnO films, as evidenced by a shift of the diffraction peaks toward higher 2θ values. Despite these shifts, all observed peaks correspond to the characteristic hexagonal wurtzite structure, indicating that the fundamental crystal structure of ZnO remains intact across all doping levels. The initial diffraction peaks of the doped samples show a slight deviation from those of undoped ZnO, confirming the successful incorporation of Mn into the ZnO lattice. The absence of any secondary phases or additional peaks in the diffraction patterns further supports the conclusion that Mn doping does not introduce structural impurities or alter the crystal phase. Moreover, the uniform distribution of Mn throughout the film suggests a homogeneous doping process without significant phase segregation. However, the intensity of the diffraction peaks does not exhibit a straightforward correlation with increasing Mn concentration. This non-linear trend may be attributed to phenomena such as dopant saturation—typically observed at higher concentrations (e.g., 8–10%)—where Mn atoms may no longer occupy regular lattice sites. The increasing lattice distortion caused by the ionic radius disparity between Zn^{2+} and Mn^{2+} introduces internal strain, which in turn influences the peak intensity and overall crystallographic quality of the films.

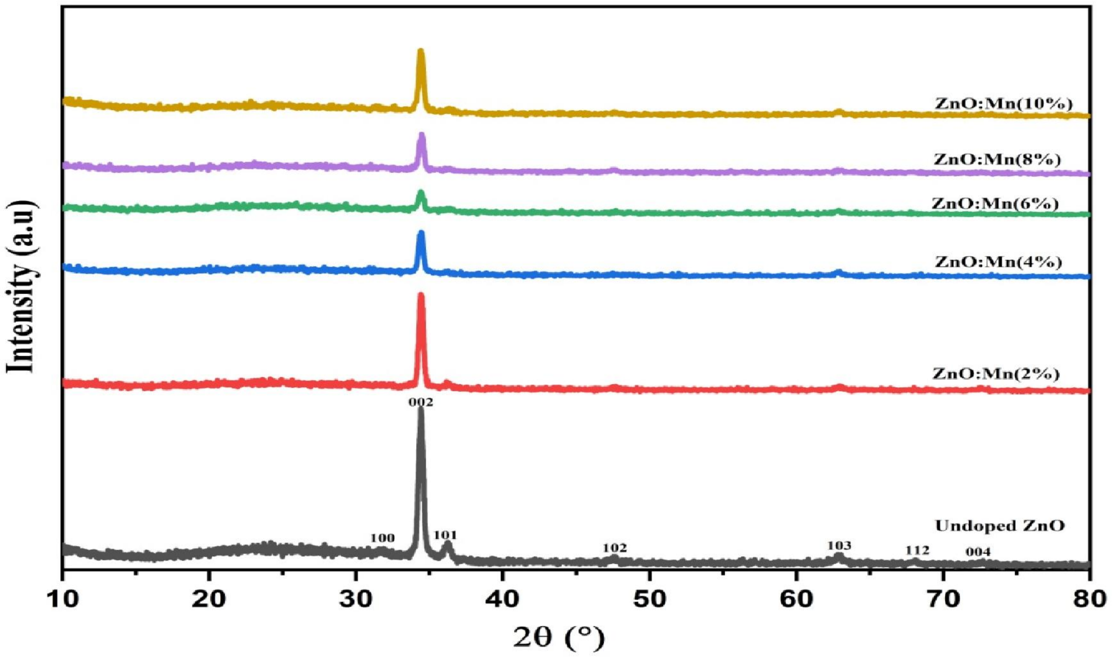

Figure II.4: Diffraction spectra of ZnO (a), $Mn_{0.02}Zn_{0.98}O$ (b), $Mn_{0.04}Zn_{0.96}O$ (c), $Mn_{0.06}Zn_{0.94}O$ (d), $Mn_{0.08}Zn_{0.92}O$ (e), and $Mn_{0.1}Zn_{0.9}O$ (f).

The effect of Mn doping on the lattice parameters of ZnO was also investigated theoretically, as illustrated in Figure II.5. Our results indicate a linear increase in both lattice parameters *a,* and *c* with increasing Mn concentration. The experimentally determined values for undoped ZnO — a = 3.1453 Å, and c = 5.1353 Å— are in good agreement with those obtained from theoretical calculations. Consistent with previous reports [73], X-ray diffraction analysis confirmed that both lattice constants increased as the Mn content rose, suggesting successful substitutional doping of Mn into the ZnO lattice.

Transmission electron microscopy (TEM) images further revealed that the Mn-doped ZnO nanoparticles exhibit a size distribution ranging from 20 to 80 nm [74]. Additionally, XRD patterns showed only peaks corresponding to the hexagonal wurtzite phase of ZnO, with no evidence of secondary phases, confirming the structural integrity of the crystal upon Mn incorporation [75].

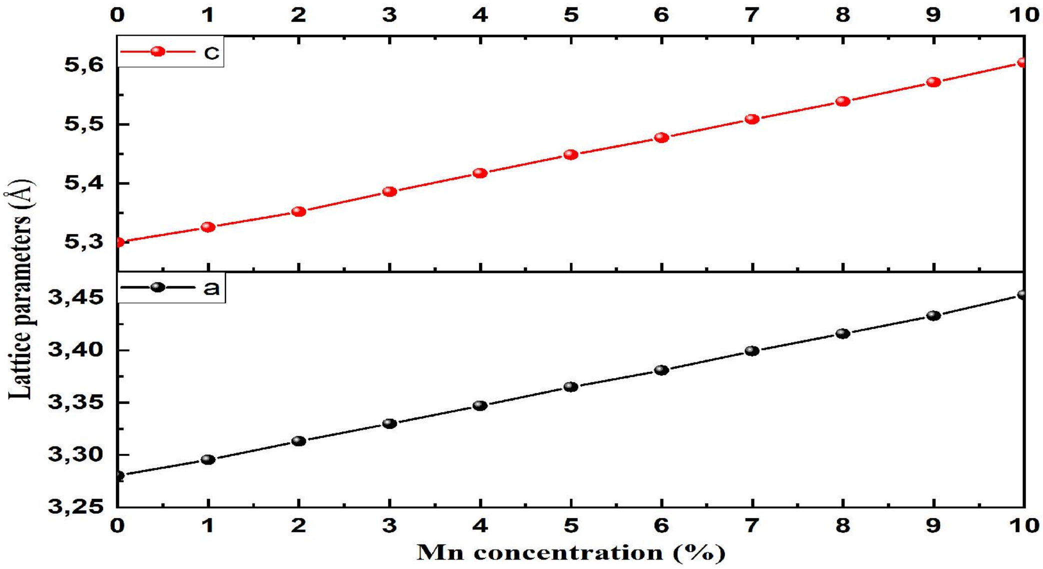

Figure II.5: Lattice parameters of ZnO_xMn_{1-x} as a function of Mn doping.

II.3.3 Electronic properties

The electronic band structure plays a critical role in determining a material's suitability as an absorber in photovoltaic applications, primarily due to its direct relationship with the band gap. Accurate estimation of the band gap is essential; therefore, the GGA-mBJ exchange–correlation potential was employed, as it provides values that closely align with experimental results [76, 77]. Figure II.6 presents the calculated band structures for pure ZnO, $ZnO_{0.99}Mn_{0.01}$, and $ZnO_{0.90}Mn_{0.10}$ at their respective equilibrium lattice constants. For both undoped ZnO and lightly doped $ZnO_{0.99}Mn_{0.01}$, the absence of electronic states near the Fermi level in the first conduction band confirms that these materials retain a direct Γ–Γ band gap, characteristic of semiconductors. In contrast, $ZnO_{0.90}Mn_{0.10}$ exhibits a metallic character, as evidenced by the presence of states near the Fermi level.

As shown in Figure II.5, the lattice parameters *a* and *c* increase with higher Mn content, while Figure II.6 illustrates a corresponding decrease in the band gap. This observation highlights an inverse relationship between the band gap energy and the lattice dimensions, suggesting that Mn incorporation induces lattice expansion while simultaneously narrowing the band gap.

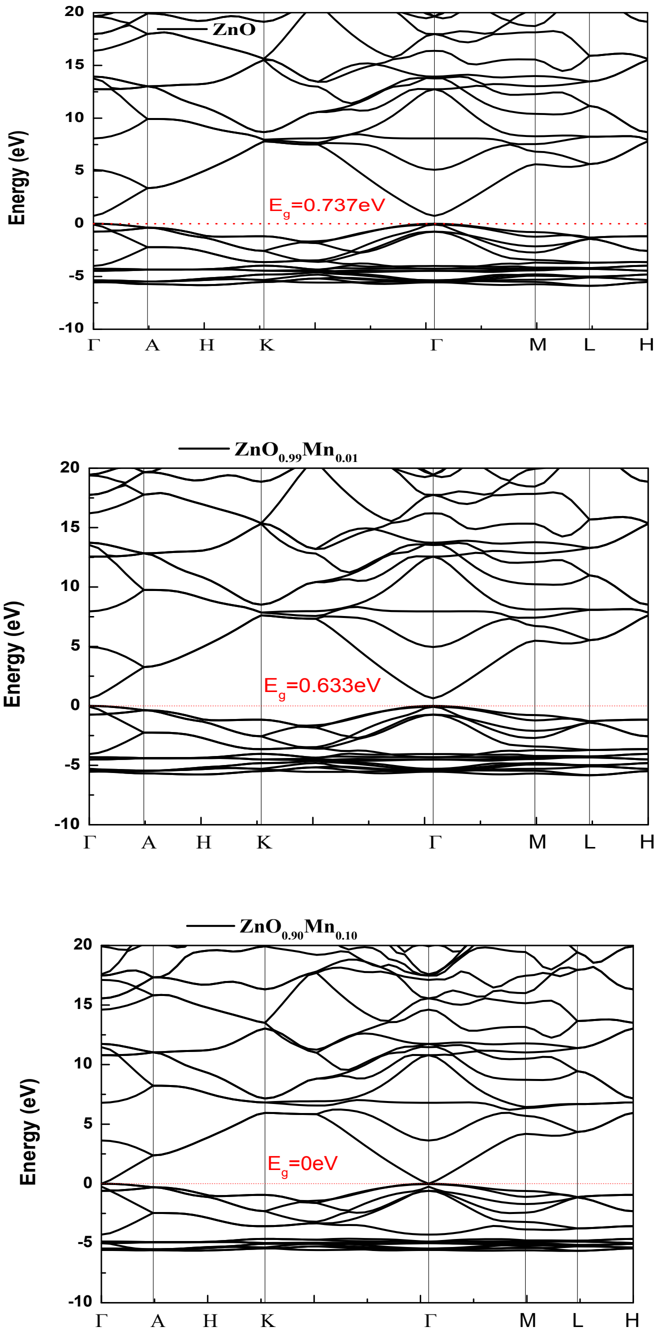

Figure II.6: Electronic band structure of ZnO, $ZnO_{0.99}Mn_{0.01}$and $ZnO_{0.90}Mn_{0.10}$.

Figure II.7 visualizes the influence of manganese incorporation on the band gap. An almost linear decrease in the band gap against doping is seen as 8 %, after which it becomes metallic.

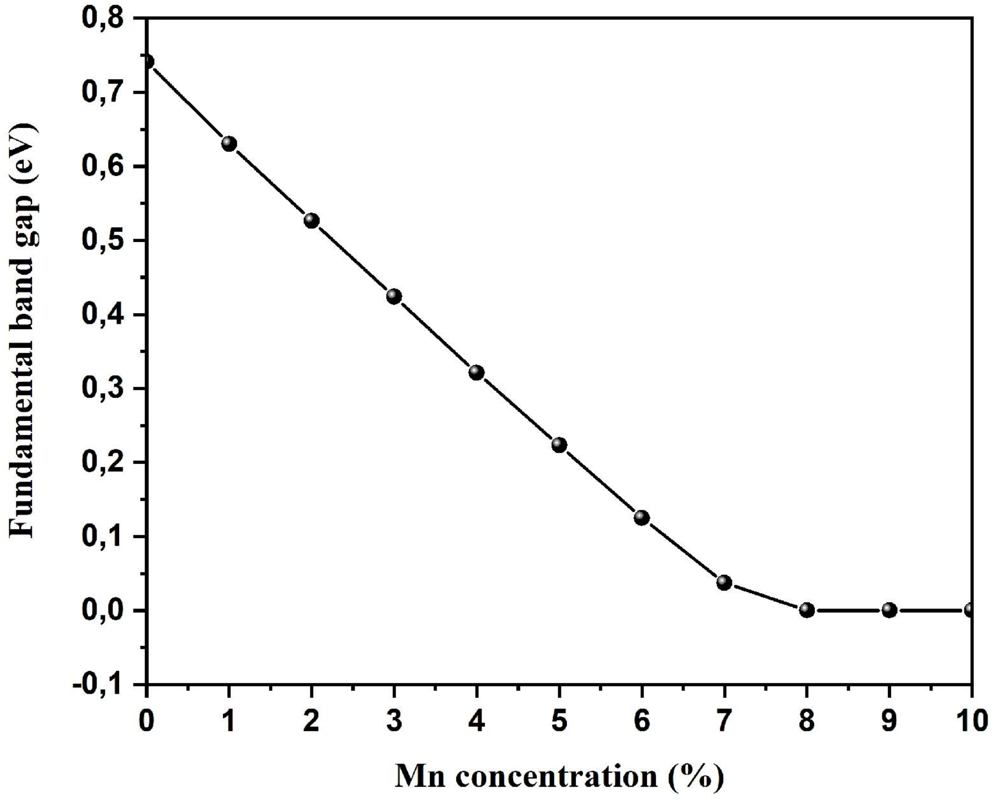

Figure II.7: Modification of electronic band structure through Mn doping.

The influence of manganese doping on the band gap is clearly observed, with the most significant changes occurring at doping levels between 0% and 4%, particularly at the Γ point. In the intermediate range of 5% to 10% Mn concentration, the band gap exhibits reduced sensitivity, maintaining a relatively stable direct nature. However, as the Mn content approaches 8% and beyond, a further decrease in the band gap is observed, eventually leading to a transition toward metallic behavior.

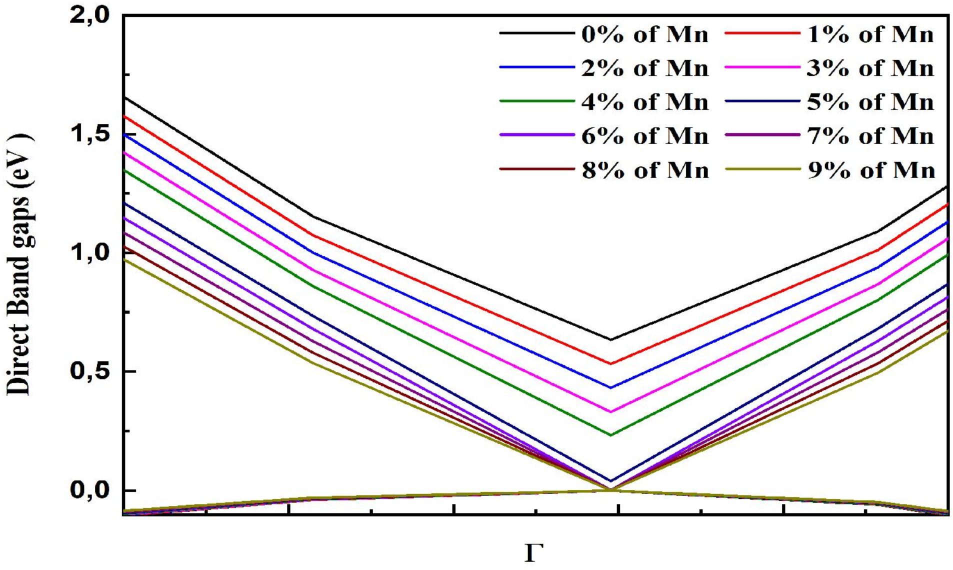

Figure II.8: Variation of the band gap in the Brillouin zone induced by Mn doping.

To better understand the electronic band structure depicted in Figure II.9, the total and partial densities of states (DOS) were calculated as a function of energy for undoped ZnO. The upper valence band is primarily composed of contributions from Zn 3d and O 2p orbitals. The semiconducting nature of ZnO is confirmed by the absence of states at the Fermi level, as indicated by a zero total density of states (TDOS) at that energy. As shown in Figure II.10, the incorporation of Mn modifies the electronic structure, with the Mn 3d electrons playing a significant role in shaping both the nature of the material and its band gap.

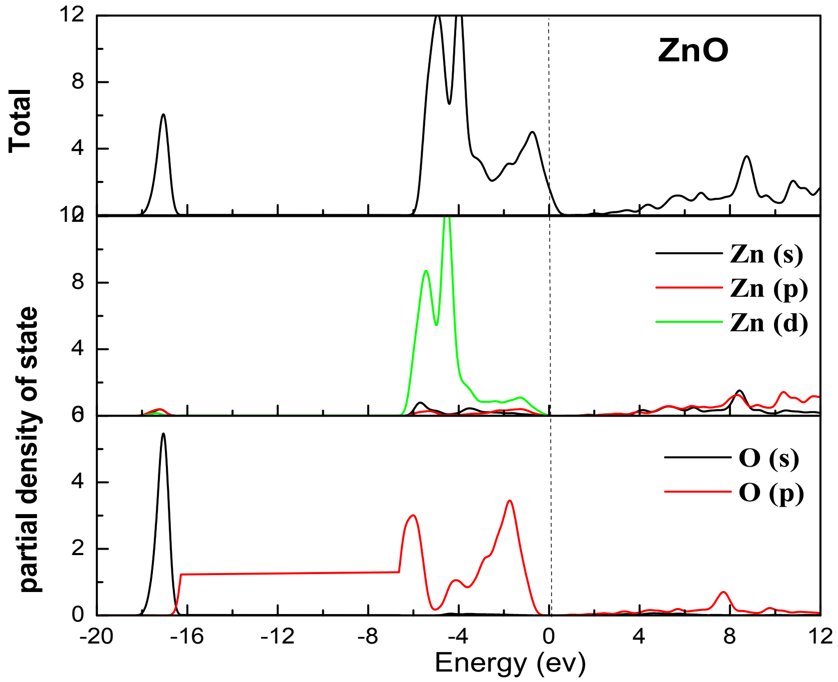

Figure II.9: Total and partial electronic states distribution in ZnO.

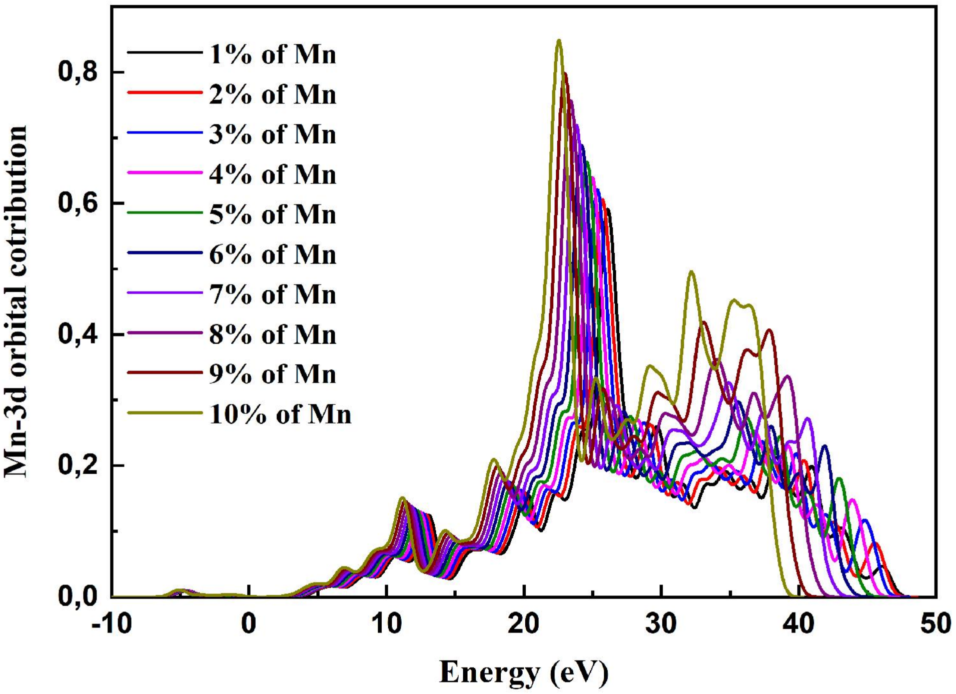

Figure II.10: Impact of Mn 3d orbitals on band gap characteristics at different energies.

It appears that the concentration of Mn has no influence on the intensity of the peaks and their corresponding energies below the Fermi level and the first conduction band extending to 2.5 eV. The peaks of the Mn:d orbitals and other energy positions have some bearing on the conduction bands located beyond 5 eV. The amount of Mn dopant affects the intensity of the peaks that shift to lower energies, thus a corresponding decrease in the band gap.

II.3.4 Optical characterization

II.3.4.1 Characterization by UV-Visible Spectroscopy

Transmission measurements on thin films are significant for electronics research. A schematic of optical transmission versus wavelength is shown in Figure II.11 for varying Mn content. Transmission measures how much light passes a material. Due to the high absorption of a material, light scatters and is attenuated. The optical transmission shows a resonance peak, which shifts towards lower wavelength when the percentage of Mn doping is increased. Clearly it is stated that the resonance peak has a redshift since the wavelength of the photons increases with the percentage of Mn doping. The resonance peak and optical performances are due to the absorption of multiphonons at higher wavelengths. Photons with sufficient energy are absorbed by excited electrons across the band gap. ZnO films doped Mn are highly transparent in the visible range with an average transmittance value located between 84% to 95%.

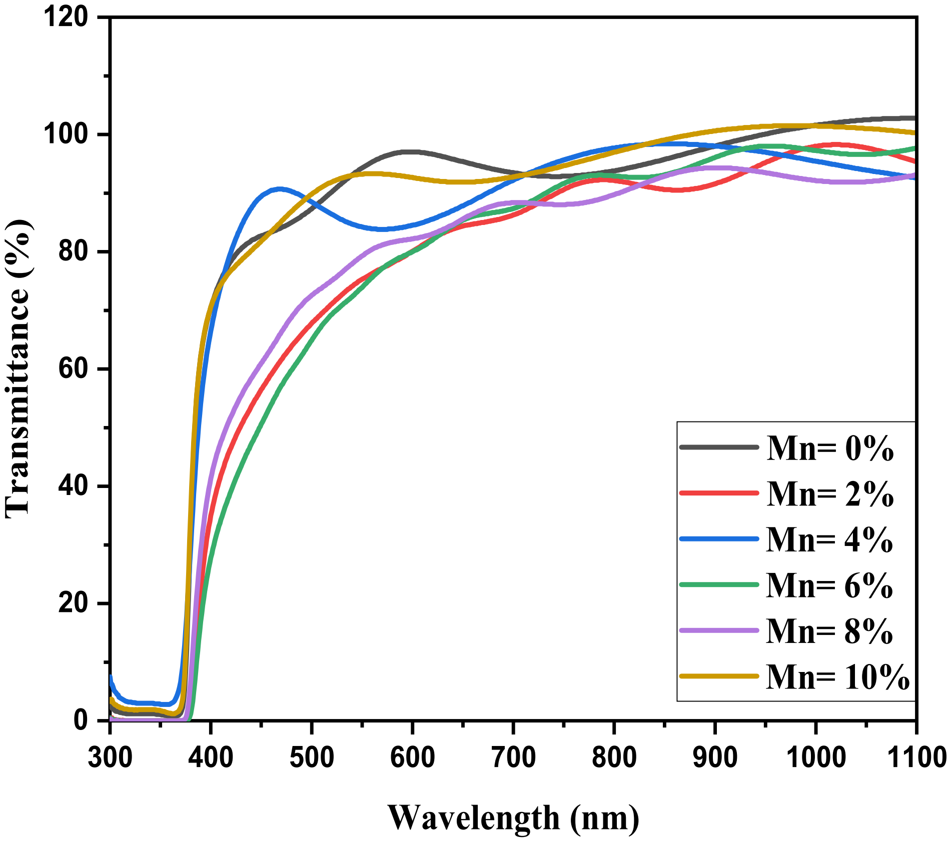

Figure II.11: Transmittance spectra of ZnO thin films for different Mn doping values.

The absorption coefficient of Mn-doped ZnO films was determined using the following equation, which relates transmittance (T) and film thickness [78]:

$$\alpha = \frac{1}{d} \ln\left(\frac{1}{T}\right) \tag{II.3}$$

And $$(\alpha h \nu)^2 = A(h\nu - E_g) \tag{II.4}$$

Where: E_g is the band gap energy, $h\nu$ is the incidence photon energy, and A is a constant [79].

A plot of $(\alpha h\nu)^2$ against $h\nu$ is made to determine E_g using the linear fit. The detailed fitting process is shown in Figure II.12, for various Mn content. It is reported that $(\alpha h\nu)^2$ increases with the increase in $h\nu$ and this increase is not very sensitive for lower values of $h\nu$. The effect of Mn doping on $(\alpha h\nu)^2$ is not uniform. The optical band gap (E_g) is estimated by taking the origin of the extrapolation at zero absorption with the photon energy axis, that is to say $(\alpha h\nu)^2 = 0$.

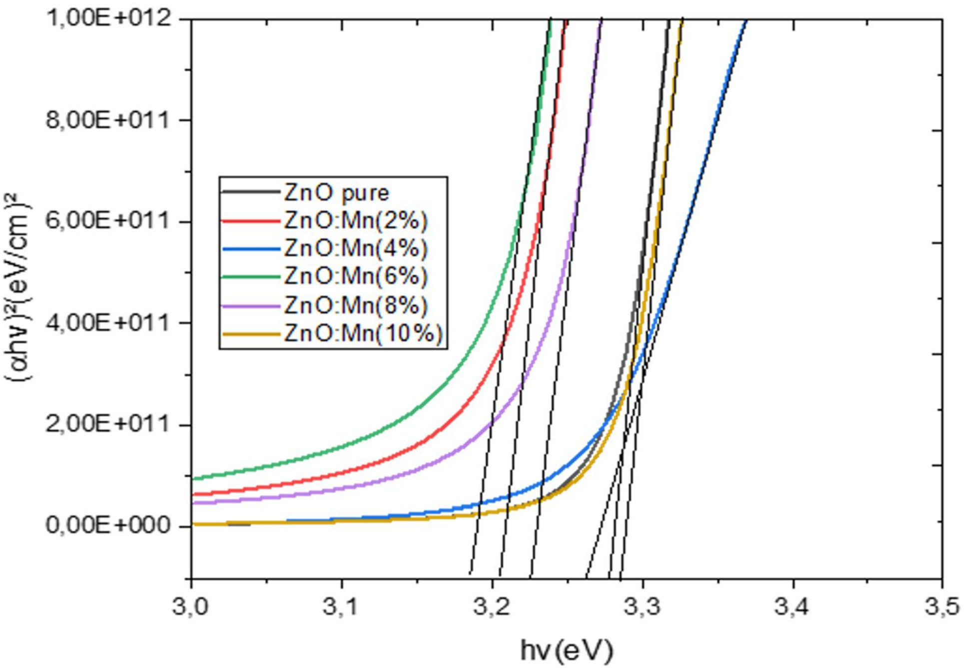

Figure II.12: Plot of $(\alpha h\nu)^2$ as a function of photon energy for ZnO doped with different Mn values.

As shown in the absorbance spectra (Figure II.13), with increasing Mn-doped ZnO nanoparticles, the excitonic absorption peak shifts to lower wavelength. The PL spectra of undoped ZnO exhibits wide visible emission at 560 nm and UV emission at 388 nm with different intensity peaks.

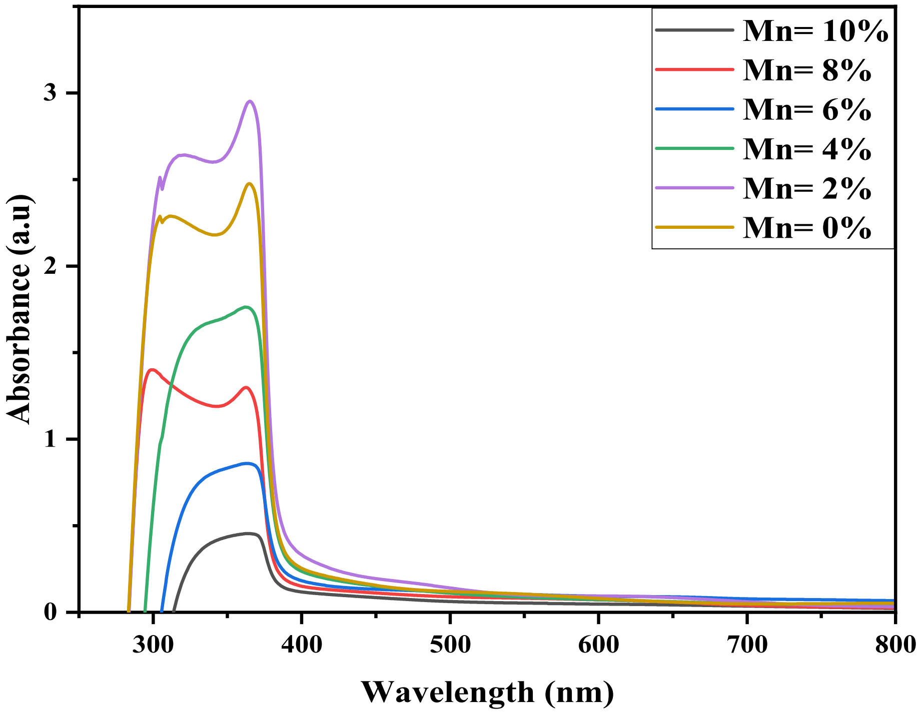

Figure II.13: Absorbance spectra for different Mn doping values.

The effect of percentage Mn doping on the optical band gap E_g is depicted in Figure II.14. The estimated band gap of ZnO of 3.271 eV is consistent with other reports of the band gap of 3.3 eV reported by Srikant et *al.* [80] at room temperature.

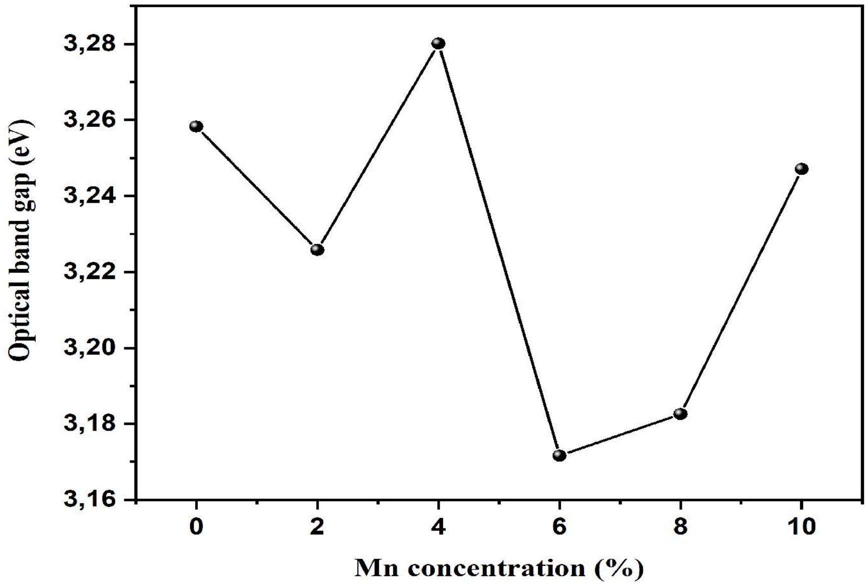

Figure II.14: Optical band gap as function of Mn doping percentages.

The incorporation of manganese into ZnO films enhances their crystallinity. This improvement is accompanied by a decrease in the optical band gap from 3.22 eV to 3.15 eV, correlating with a reduction in average grain size from (76 ± 1) nm to (25 ± 0.5) nm [81]. Analysis of the absorption edge indicates an optical band gap ranging from 3.20 to 3.21 eV, consistent with a direct electronic transition [82]. The band gap (E_g) values were determined from linear fits to plots of $(\alpha h\nu)^2$ versus photon energy ($h\nu$), as illustrated in Figure II.12. E_g is obtained by extrapolating the linear portion to intersect the photon energy axis. Calculated band gap values for the doped samples fall between 3.18 and 3.25 eV, slightly lower than the commonly reported ZnO band gap of 3.4 eV [83]. Mn doping introduces donor states by substituting Zn sites in the native n-type ZnO semiconductor, where excess electrons ionized by these impurities populate the conduction band minimum.

II.3.4.2 Characterization by Fourier Transform Infrared Spectroscopy

Fourier Transform Infrared (FTIR) spectroscopy provides information about the molecular interactions and structural changes induced by the incorporation of Mn into the ZnO matrix. In Figure II.15, the normalized absorbance is plotted against wave number for different concentrations of Mn doping, wherein various prominent peaks appear characteristically towards specific vibrational modes within the ZnO matrix and at the sites where Mn atoms are substituted. The basic peaks are observed at low frequencies (500–600 cm^{-1}) and represent the fundamental stretching and bending vibrations of Zn-O bond. In the presence of Mn within the ZnO matrix, subtle changes in the position and intensity of the peaks are observed, implying a change in the local bonding environment of Zn-O. The peaks show a shift toward lower wave numbers with increasing Mn concentrations, a phenomenon that indicates weakening of the Zn–O bond or a modification of the bond length due to the Mn ingress. This behavior symbolizes the structural distortions and interactions caused by the dopants. Bending vibrations of the O–Zn–O linkages indicate a 600 to 1300 cm^{-1} wavenumber range; these vibrations are very informative unto the symmetry of the ZnO crystal structure. The broadening of the peaks suggests that these Mn atoms introduce some local structural change that then can alter their lattice dynamics and the vibrational behavior of the O–Zn–O bonds.

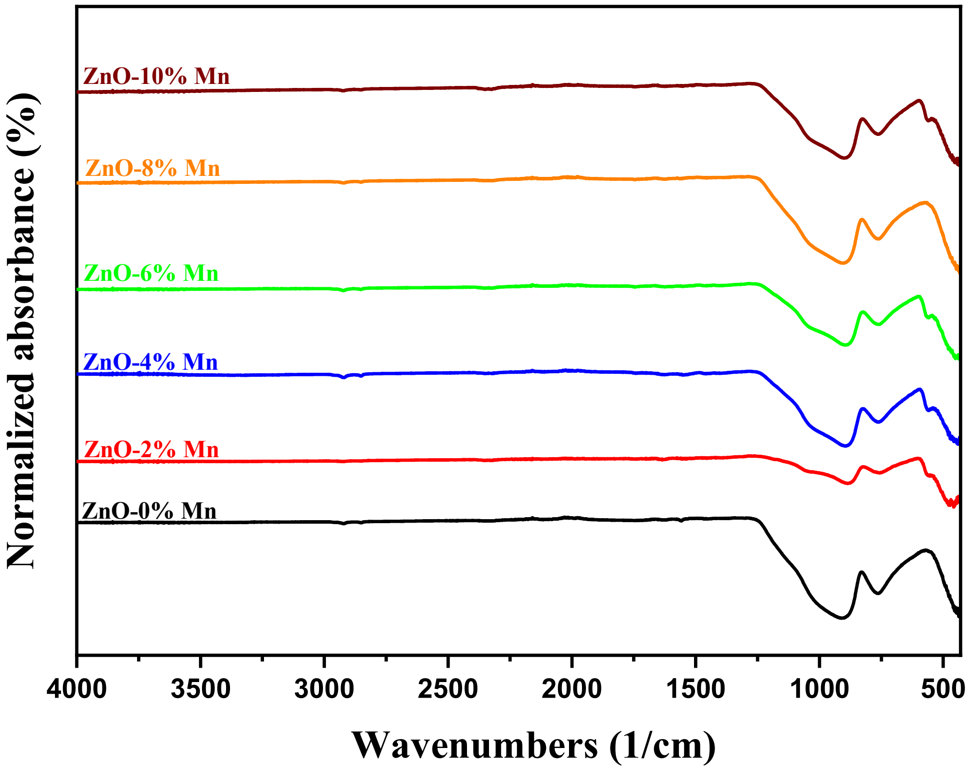

Figure II.15: FTIR spectra for different Mn doping values.

II.4 Conclusion

Mn-doped ZnO thin films were synthesized on glass substrates using the pneumatic spray method, with varying concentrations of manganese. Energy-dispersive X-ray (EDX) analysis confirmed the successful incorporation of Mn into the ZnO lattice, indicating substitution of Zn ions by Mn ions. X-ray photoelectron spectroscopy (XPS) revealed characteristic spin-orbit splitting of Zn 2p and Mn 3d states, reflecting strong interaction between Mn and the ZnO lattice. Morphological studies showed that the films consist of non-uniform elongated structures and spherical grains, with grain size decreasing as Mn concentration increases. X-ray diffraction (XRD) analysis verified the hexagonal wurtzite structure of the films, predominantly polycrystalline, with lattice parameters experimentally determined as a = 3.1453 Å and c = 5.1353 Å, consistent with theoretical values obtained from CASTEP calculations.

Optical characterization indicated approximately 80% absorption in the visible range, with absorption increasing from blue to red wavelengths as Mn content rose, suggesting effective band gap modulation. The lattice parameters exhibited an approximately linear increase with Mn doping concentration. Correspondingly, the band gap progressively decreased with increasing Mn content, transitioning to metallic behavior at around 80% doping. Both pure ZnO and ZnO with 1% Mn doping exhibit a direct Γ–Γ band gap, whereas ZnO doped with 10% Mn displays metallic characteristics. The impact of Mn concentration on the band gap is most pronounced between 0 and 4%, particularly at the Γ point, while changes between 5% and 10% are more subtle. This band gap reduction is primarily attributed to interactions involving Mn d-orbital electrons, with Mn doping showing negligible effect on the upper valence band below the Fermi level.

Furthermore, Mn-doped ZnO films demonstrate high optical transparency, though excessive Mn incorporation reduces photoluminescence intensity. These findings highlight Mn-doped ZnO thin films as promising materials for tunable optoelectronic applications**.**

References

[1] J. F. Wager, Transparent Electronics, Science 300, 1245, (2003).

[2] O. Lupan, T. Pauporte, T. Le Bahers, I. Ciofini, B. Viana, J. Phys. Chem. C 115, 14548, (2011).

[3] H. W. Kang, J. Yeo, J. O. Hwang, S. Hong, P. Lee, S. Y. Han, J. H. Lee,Y. S. Rho, S. O. Kim, S. H. Ko, H. J. Sung, J. Phys. Chem. C 115, 11435, (2011).

[4] Y. K. Park, H. S. Choi, J. H. Kim, J. H. Kim, Y. B. Hahn, Nanotechnology 22, 185310, (2011).

[5] C. M. Chang, M. H. Hon, I. C. Leu, J. Sol-Gel Sci.Technol. 68, 1, (2013).

[6] M. Kashif, M. E. Ali, S. M. U. Ali, U. Hashim, Ceram. Int. 39, 6461, (2013).

[7] S. H. Ko, D. Lee, H. W. Kang, K. H. Nam, J. Y. Yeo, S. J. Hong, C. P. Grigoropoulos, H. J. Sung, Nano Lett. 11, 666, (2011).

[8] S. Sarkar, A. Makhal, T. Bora, K. Lakhsman, A. Singha, J. Dutta, S. K. Pal, ACS Appl. Mater. Interfaces 4, 7027, (2012).

[9] J. H. Lee, J. Shin, J. Y. Song, W. Wang, R. Schlaf, K. J. Kim, Y. Yi, J. Phys. Chem. C 116, 26342, (2012).

[10] P. Yang, H. Yan, S. Mao, R. Russo, J. Johnson, R. Saykally, N. Morris, J. Pham, R. He, H. J. Choi, Adv. Funct. Mater. 12, 323, (2002).

[11] K. Govender, D. S. Boyle, P. O'Brien, D. Brinks, D. West, D. Coleman, Adv. Mater. 14, 1221, (2002).

[12] X. Li, J. Wang, J. Yang, J. Lang, J. Cao, F. Liu, Y. Jiang, Mater. Chem. Phys. 141, 929, (2013).

[13] O. Yayapao, T. Thongtem, A. Phuruangrat, S. Thongtem, J. Alloys Compd. 576, 72, (2013).

[14] N. L. Tarwal, A. V. Rajgure, A. I. Inamdar, R. S. Devan, I. Y. Kim, S. S. Suryavanshi, Y. R. Ma, J. H. Kim, P. S. Patil, Sens. Actuators A: Phys. 199, 67, (2013).

[15] H. Chen, H. Liu, Z. Zhang, K. Hu, X. Fang, Adv. Mater. 28, 403, (2016).

[16] D. Jiang, R. Liu, Q. Zhang, R. Li, Q. Duan, J. Qin, X. Shen, J. Hou, J. Zhao, Q. Liang, S. Gao, J. Phys. D: Appl. Phys. 48, 275104, (2015).

[17] B. Zhao, F. Wang, H. Chen, Y. Wang, M. Jiang, X. Fang, D. Zhao, Nano Lett. 15, 3988, (2015).

[18] N. Nasiri, R. Bo, F. Wang, L. Fu, A. Tricoli, Adv. Mater. 27, 4336, (2015).

[19] L. Peng, L. Hu, X. Fang, Adv. Mater. 25, 5321, (2013).

[20] J. Yu, C. X. Shan, X. M. Huang, X. W. Zhang, S. P. Wang, D. Z. Shen, J. Phys. D: Appl. Phys. 46, 305105, (2013).

[21] H. Chen, K. Liu, L. Hu, A. A. Al-Ghamdi, X. Fang, Mater. Today 18, 493–502, (2015).

[22] D. N. Montenegro, A. Souissi, C. Martínez-Tomás, V. Muñoz-Sanjosé, V. Sallet, J. Cryst. Growth 359, 122, (2012).

[23] B. Xiang, P. W. Wang, X. Z. Zhang, S. A. Dayeh, D. P. R. Aplin, C. Soci, D. P. Yu, D. Wang L, Nano Lett. 7 323, (2007).

[24] C. H. Ahn, W. S. Han, B. H. Kong, H. K. Cho, Nanotechnology 20, 15601, (2009).

[25] T. Premkumar, Y. S. Zhou, Y. F. Lu and K. Baskar, ACS Appl. Mater. Interfaces 2, 2863, (2010).

[26] V. Kumar, N. Singh, R. M. Mehra, A. Kapoor, L. P. Purohit and H. C. Swart, Thin Solid Films 539, 161, (2013).

[27] A. Rivera, J. Zeller, A. Sood, M. Anwar, Proc. SPIE 8626, Oxide-Based Materials and Devices IV, 86260B, (2013).

[28] S. N. Sarangi, S. Nozaki, S. N. Sahu, J. Biomed. Nanotechnol. 11, 988, (2015).

[29] L. F. Xu, Q. W. Chen, D. S. Xu, J. Phys. Chem. C 111, 11560, (2007).

[30] T. Pauporté, D. Lincot, B. Viana, F. Pellé, App. Phys. Lett. 89, 23311, (2006).

[31] O. Lupana, V. M. Guerin, I. M. Tiginyanu, V. V. Ursaki, L. Chow, H. Heinrich, T. Pauporte, J. Photochem. Photobiol. A 211, 65, (2010).

[32] O. Lupan, T. Pauporté, L. Chow, B. Viana, F. Pellé, L. K. Ono, B. Roldan-Cuenya, H. Heinrich, Appl. Surf. Sci. 256, 1895, (2010).

[33] C. H. Yi, I. Yasui, Y. Shigesato, Japan. J. Appl. Phys. 34, 1639, (1995).

[34] T. Shinagawa, M. Izaki, RSC Adv. 4, 30999, (2014).

[35] O. Milošević,V. Gagić, J. Vodnik, A. Mitrovič, L. karanovič, B. Stojanovič, L. Živkovič, Thin Solid Films 296, 44–48, (1997).

[36] P. Nunes, E. Fortunato, R. Martins, Thin Solid Films 383, 280, (2001).

[37] K. L. Chopra, S. Major, D. K. Panday, Thin Solid Films, 102–105, (1983).

[38] N. Attaf, Etude énergétique d'une décharge luminescente utilisée dans le dépôt de couches minces de a-Si : H, thèse de doctorat, Université Mohamed Khider, Biskra, (2003).

[39] M. Maache, Dépôt et Caractérisation de Couches Minces de ZnO par Spray Pyrolyse, thèse de doctorat, Université Mohamed Khider, Biskra, (2005).

[40] Géraldine Huertas, Etude de nouveaux matériaux d'électrode positive et d'électrolyte solide vitreux sous forme de couches minces pou des couches minces microbatteries au Lithium, thèse de doctorat, Bordeaux, France, (2006).

[41] S. A. Studenikin, N. Golego, M. Cocivera, Journal of Applied Physics 83(4), 2104–2111, (1998).

[42] C. Messaoudi, D. Sayah, M. Abd-Lefdil, Physica Status Solidi (A) Applied Research 151(1), 93–97, (1995).

[43] A. Maldonado, M. de la Luz-Olvera, S. Tirado-Guerra, R. Asomoza, Solar Energy Materials & Solar Cells 82, 75– 84, (2004).

[44] M. Krunks, E. Mellikov, Thin Solid Films 270(1–2), 33–36, (1995).

[45] R. Romero, D. Leinen, E. A. Dalchiele, J. R. Ramos-Barrado, F. Martin, Thin Solid Films 515(4), 1942–1949, (2006).

[46] S. Golshahi, S. M. Rozati, R. Martins, E. Fortunato, Thin Solid Films 518(4), 1149–1152, (2009).

[47] Z. L. Lu, H. S. Hsu, Y. H. Tzeng, F. M. Zhang, Y. W. Du, J. C. A. Huang, Appl. Phys. Lett. 95, 102501, (2009).

[48] N. L. Tarwal, K. V. Gurav, T. Prem Kumar, Y. K. Jeong, H. S. Shim, I. Y. Kim, J. H. Kim, J. H. Jang, P. S. Patil, J. Anal Appl Pyrol. 106, 26–32, (2014).

[49] T. Tietze, M. Gacic, G. Schütz, G. Jakob, S. Brück, E. Goering, New J. Phys. 10, 055009, (2008).

[50] E. Bacaksiz, S. Aksu, B.M. Basol, M. Altunbas, M. Parlak, E. Yanmaz, Thin Solid Films 516, 7899, (2008).

[51] R. Grothe, S. Knust, D. Meinderink, M. Voigt, A. G. Orive, G. Grundmeier, Surf. & Coat. Technol. 394, 125869, (2020).

[52] N. L. Tarwal, V. L. Patil, J. R. Rani, K. V. Gurav, J. S. Shaikh, M. S. Khandekar, N. S. Harale, P. S. Patil, J. H. Jang, Chin. J. of Phys. 73, 581–588, (2021).

[53] Y. Bouznit, A. Henni, Materials Science in Semiconductor Processing 118, 105208, (2020).

[54] T. C. Bharat, Shubham, S. Mondal, H. S. Gupta, P. K. Singh, A. K. Das, Mater. Today: Proc. 11, 767–775, (2019).

[55] N. M. Hosni, I. Gomaa, M. G Elmahgary, M. A. Ibrahim, Scientific Reports 13, 14173, (2023).

[56] H. Munawaroh, S. Wahyuningsih, A. H. Ramelan, IOP Conf. Ser.: Mater. Sci. Eng. 176, 012049, (2017).

[57] T. H. AlAbdulaal, M. AlShadidi, M. S. A. Hussien, A. Bouzidi, I. S. Yahia, Opt. Mater. 139, 113751, (2023).

[58] D. Kumar, V. Stoichkov, E. Brousseau, G. C. Smith, J. Kettle, Nanoscale 11(12), 5771, (2019).

[59] A. Ayana, H. Fei, S. Jan, B.V. Rajendra, S. Pankaj, Mater. Sci. Semicond. Process. 146, 106680, (2022).

[60] F. Fan, Y. Feng, S. Bai, J. Feng, A. Chen, D. Li, Sens. Actuator B-Chem. 185, 377–382, (2013).

[61] D. Kumar, M. Singh, M. Kushwaha, G. Makarana, M. R. Yadav, Indian J. Agron. 66(4), 466–473, (2021).

[62] H. Li, Y. Huo, X. He, L. Yao, H. Zhang, Y. Cui, H. Xiao, W. Xie, D. Zhang, Y. Wang, S. Zhang, H. Tu, Y. Cheng, Y. Guo, X. Cao, Y. Zhu, T. Jiang, X. Guo, Y. Qin, J. Sha, Nature 612, 725–731, (2022).

[63] T. Wei, N. Zhang, Y. Ji, J. Zhang, Y. Zhu, T. Yi, Chin. Chem. Lett. 33 (2), 714–729, (2022).

[64] N. L. Tarwl, D. P. Mali, K. V. Patil, S. L. Patil, V. L. Patil, V. B. Patil, C. C. Revadekar, T. D. Dongale, P. S. Patil, P. M. Shirage, J. H. Jang, Appl. Phys. A 129, 7, (2023).

[65] S. S. Pawar, R. S. Redekar, N. L. Tarwal, Inorg. Chem. Commun. 162, 112106, (2024).

[66] N. L. Tarwal, A. R. Patil, N. S. Haral, A.V. Rajgure, S. S. Suryavanshi, W. R. Bae, P. S. Patil, J. H. Kim, J. H. Jang, J. Alloys Compd. 598, 282–288, (2014).

[67] K. V. Patil, R. S. Redekar, A. A. Bhoite, V. L. Patil, P. S. Patil, J. H. Jang, N. L. Tarwal, Mater. Lett. 357, 135689, (2024).

[68] B. L. Zhu, X. H. Sun, X. Z. Zhao, F. H. Su, G. H. Li; X. G. Wu, J. Wu, R. Wu, J. Liu, Vacuum 82, 495–500, (2008).

[69] A. Debelle, Contraintes microstructure et sollicitation sous irradiation aux ions de films minces élaborés par pulvérisation ionique : modélisation et application à l'étude des effets interfaciaux dans des multicouches métalliques, Thèse doctorat, Université de Poitiers, 14–24, (2005).

[70] S. Kanwal, M. T. Khan, V. Tirth, A. Algahtani, T. Al-Mughanam, A. Zaman, ACS Omega 8(31), 28749, (2023).

[71] Y. Epelboin, André Authier, Acta Cryst. A 79(4), 385– 386, (2023).

[72] S. A. Ahmed, Results in Physics 7, 604–610, (2017).

[73] A. Zahid, Z. Mukhtar, M. A. Qamar, S. Shahid, S. K. Ali, M. Shariq, H. J. Alathlawi, M. Abul Hasan, M. S. Khan, S. Islam, B. R. Patil, M. S. Al Ansari, Z. Nawaz, M. Sher, Catalysts 13 (1), 105, (2023).

[74] M. Otadi, Z. P. Shayegh, M. Monajjemi, Biointerface Research in Applied Chemistry 5(11), 12471–12482, (2021).

[75] T. Guomei, L. Hua, Z. Wei, Advances in Materials Science and Engineering 2013 (1), 4, (2013).

[76] G. Vijayaprasath, R. Murugan, S. Palanisamy, N. M. Prabhu, T. Mahalingam, Y. Hayakawa, G. Ravi, Mater. Res. Bull. 76, 48–61, (2016).

[77] O. A. Yassin, Optik 127, 1817–1821, (2016).

[78] J. I. Pancove, Optical Processes in Semiconductors, Dover Publication, Inc., New Work, (1975). (Unabridged republication of the work originally published by Prentice-Hall, Inc., 1971).

[79] J. Tauc, R. Grigorvici, A. Vancu, Physica Status Solidi (b) 15, 627–637, (1966).

[80] V. Srikant, D. R. Clarke, J. Appl. Phys. 83, 5447–5451, (1998).

[81] S. Dutta, S. Chattopadhyay, M. Sutradhar, A. Sarkar, M. Chakrabarti, D. Sanyal, D. Jana, J. Condens. Matter Phys. 19(23), 236218, (2007).

[82] Y. Natsume, H. Sakata, Thin Solid Films 372, 30–36, (2000).

[83] D. C. Look, Mat. Sci. and Eng. B 80, 383–387, (2001).

Chapter III

Elaboration and characterization of Cu_2O thin films using electrodeposition method

III.1 Introduction

Copper(I) oxide (Cu_2O) is a p-type semiconductor in the metal oxide family and is characterized by a wide direct band gap (~ 2.1 eV) [1]. It typically exists as a reddish-brown solid and displays many intriguing physicochemical properties, such as excellent chemical stability, adjustable electrical conductivity, and photo-catalytic activities under visible light.

Due to the optoelectronic properties of Cu_2O, it has a wide range of applications, including photovoltaic cells [2], gas sensors [3], photo-catalysis in the degradation of organic pollutants [4, 5], and energy storage devices [6−10], Cu_2O can also be an interesting option for more expensive or not as common materials, especially in the pursuit of sustainable energy options.

Various methods of depositing Cu_2O thin films have been used, including sputtering [11], chemical vapor deposition (CVD) [12], spray pyrolysis [13], sol-gel techniques [14], thermal evaporation [15], and electrodeposition [16]. The choice of deposition method is influenced by the required conditions of the film in the application, particularly regarding crystallinity, adhesion, thickness, and purity.

In recent years, electrodeposition has become one of the most attractive methods for synthesizing semiconductor oxide thin films. Its main advantages are low temperature deposition, low cost and more homogeneous layers.

This chapter focuses on the characterization of Cu_2O nanostructures electrodeposited on an ITO substrate. In this section, we will explore the effect of the bath temperature on:

- ✓ Topography and surface morphology of the deposits, through a quantitative study quantitative examination of atomic force microscopy (AFM) images.
- ✓ Structure, average crystallite size, and stress using X-ray diffraction (XRD.
- ✓ Fundamental optical properties employing UV-visible, photoluminescence (PL) spectroscopy, and FTIR spectrophotometry.

III.2 Key parameters affecting the electrodeposition of Cu_2O nanostructures

An intensive literature search was done to determine ideal circumstances leading to high transparency and conductivity in Cu_2O thin films of pure phase and improved characteristics. We considered how several electrodeposition parameters—deposition potential, electrolyte pH, bath temperature, and substrate type—affect the morphology and structural features of Cu_2O thin films.

III.2.1 Substrate influence

The parameters of the surface of a substrate introduce a considerable effect on some important aspects of thin films, e.g., their average crystallite size, roughness, and shape. The substrate choice is particularly essential in determining the growth characteristics of Cu_2O.

Cu_2O thin films were produced in the laboratory by Liu et *al.* [17] using an alkaline bath containing copper sulfate, lactic acid, and NaOH. Various materials were employed as working electrodes, such as indium tin oxide (ITO), silicon (Si), and a gold (Au) wire. The scanning electron microscopy (SEM) measurements showed that the films deposited on the ITO featured pyramidal grains of around 2 µm size, which grew preferentially along the (111) crystallographic orientation. Likewise, the films placed on silicon substrate showed the formation of four-faceted pyramidal forms, similarly oriented along the (111) direction. The size of grains fell dramatically to roughly 100 nm on the Si substrate as compared to the bigger granules on ITO. Films formed on the gold substrate, however, have a (100) orientation with great crystallinity. Such discrepancies are often connected to the lattice mismatch between the substrate and the deposited Cu_2O layer (i.e., lattice parameter mismatch). The n-type Si substrate has a (100) orientation, and its lattice parameter is a = 5.43 Å. The lattice misfit for the Cu_2O/Si system is estimated to be almost 21.4%. This huge mismatch makes it quite difficult for Cu_2O to develop on the same preferred orientation as it has been found on the ITO substrate.

El-Mezayyen et *al.* [18] have investigated the influence of substrate conductivity on the morphology of Cu_2O nanostructures. The authors proceeded to electrochemically synthesize Cu_2O nanostructures on three substrates: ITO, FTO, and ITO/PET, having significantly distinct resistivities, and observed drastically different morphologies, namely fern-like structures on ITO substrates, dendritic formations on FTO, and compact dense films on ITO/PET substrates. Moreover, Mott-Schottky measurements confirmed the p-type semiconductor behavior of all deposited films, with density carrier values ranging between 1.4×10^{18} and 1.2×10^{19} cm^{-3}.

The fabrication of Cu_2O/ZnO heterojunctions included applying a potentiostatic electrodeposition approach, which was undertaken by Sakellis et *al.* [19]. For this reason, ZnO nanorods served as the substrate onto which Cu_2O layers were produced. Two different crystal morphologies of Cu_2O were obtained: cubic and truncated cubic ones that have diameters between 500 nm and 6 µm. Indeed, it was obvious that morphology was linked with tip morphology of the ZnO nanorods. Jeong et *al.* [20] also reported a similar result and so validated the hypothesis that the type and structure of the substrate greatly affect the resulting Cu_2O nanostructures.

III.2.2 Electrolyte pH influence

The crystallinities of Cu_2O thin films are relevant to their functional qualities. Consequently, altering deposition parameters has demonstrated that the electrolyte pH could be the most essential component in contributing to crystallite size. Assessment of this association has been undertaken in many studies. Golden et *al.* [21] started the research of pH on the structural parameters of p-type Cu_2O films deposited by electro-reduction of copper(II) lactate in alkaline solutions of 0.4 M copper sulfate and 3 M lactic acid. The results reveal that the surface roughness of Cu_2O films is highly impacted by the pH of the deposition bath. At a pH of 9, the films displayed a (100) preferable orientation, but at a higher pH of 12, a (111) texture was favored.

Other researchers have found similar findings: The Cu_2O films at pH 9 show largely (100) crystallographic orientation, while the (111) is more favored at pH 11 [22−24]. Wang et *al*. [25] also discovered a third orientation (110) that prevailed in a restricted pH range of 9.4 – 9.9.

When the pH of the electrolyte is less than 8, the predominant phase of the deposited films is Cu_2O, while metallic copper emerges as a secondary phase. At pH values below 5, structural characterization evidence that the coatings transition into a pure metallic copper phase [26].

Zhou et *al.* [27] also showed that bigger Cu_2O grains could be created by altering the pH of the electrolyte between 8 and 12. The improvement in growth was linked to a shift in the deposition rate with varied pH levels. Other than particle size, considerable variations from one approved film shape to another could also be observed: four-faced pyramidal structures at pH 9, truncated pyramids at pH 10, and three-faced pyramids at pH 12. The authors found that this crystallographic orientation may be controlled successfully by merely adjusting the pH of the deposition solution.

Understanding Wang et *al.* [28], the electrical conductivity type (either n-type or p-type) of electrochemically deposited Cu_2O was shown to be dependent on the pH of the electrolyte solution. The article of theirs showed that Cu_2O films formed at a pH < 7.5 are n-type semiconductors because of the existence of oxygen vacancies or interstitial copper atoms. Films created above pH 9 have p-type conductivity and were recognized as largely connected to copper vacancies.

These findings provide information concerning pH values in electrolyte solutions altering amounts of oxygen integrated into the Cu_2O lattice during deposition. The pH reduces oxygen incorporation levels and in turn alters copper and oxygen vacancy concentrations, thereby moving from p-type to n-type conductivity. Photocurrent measurements were in keeping with this discovery in that samples deposited at $pH < 7.5$ displayed anodic photocurrents, which were linked with n-type conductivity, while those acquired at $pH > 9$ provided cathodic photocurrents supporting p-type behavior.

The same investigation was undertaken by Wang et *al.* [29], which indicated similar results. Furthermore, a Mott-Schottky study conducted by Jiang et *al.* [30] demonstrated a steady increase in acceptor carrier density (N_a) in Cu_2O films with increasing pH: from 6.67×10^{15} cm^{-3} at pH 9 to 8.61×10^{16} cm^{-3} at pH 10, reaching values as high as 3.01×10^{17} cm^{-3} at pH 11. All these values fit within the range of what is normally expected for charge carrier concentrations typical for Cu_2O, commonly in the literature ranging between 10^{15} and 10^{18} cm^{-3} [31, 32].

III.2.3 Electrolyte bath temperature influence

The temperature of the electrolyte bath remains another key parameter for optimizing the electrodeposition conditions of Cu_2O thin films. Natter et al. [33] give the rationale that with increasing electrolyte temperature, the deposition rate becomes faster and is attributed to the enhanced lateral mobility of metal atoms in the growing film so that these atoms would, with greater ease, reach the active nucleation sites on the substrate surface where they would, in turn, promote finer grain formation.

Shahrestani [34] evaluated the effect of the deposition temperature varying from 25 °C to 80 °C. The research indicated that raising the temperature opens the electrochemical deposition window toward more cathodic potentials and an associated rise in current density. The recommended temperature range for Cu_2O electrodeposition is between 60 and 70 °C. In addition, films deposited at 60 °C were more crystalline than films deposited at room temperature (25 °C), exhibiting fewer cracks and structural flaws, again supporting the beneficial effects of higher temperature on film quality and structural integrity.

Tang et *al.* [35] examined the fluctuation in configuration and microstructural features of Cu_2O thin film formed on TiO_2 substrate under the increased electrolyte bath temperature, which ranged from 0 °C to roughly 60 °C. Their findings demonstrated that a rise in temperature raised the film thickness; consequently, the process was linked to the higher Cu_2O deposition rate at such high temperatures. The deposition rates at 30, 45, and 60 °C additionally recorded 3.5, 3.6, and 8.3 nm/min, respectively.

Significant morphological changes are again detected with increasing deposition temperature, as revealed in scanning electron microscopy photos. In the lower temperature range (0–30 °C), the films develop a granular form and hence yield particles that have sizes of about 40–50 nm. However, at 45 °C, these changes into dendritic structures, while grain sizes rise dramatically, spanning between 200 and 400 nm. The microstructure evolves once more at 60°C into a more pronounced ring-like morphology, which highlights better the way temperature drastically affects the development behavior and surface characteristics of Cu_2O films.

Y. Tang et *al.* [35] underwent air annealing treatment at 200, 300, and 400 °C for 30 minutes following deposition of Cu_2O films for the enhancement of electrical characteristics. The scientists additionally reported that annealing altered the electrical resistivity of the films greatly. Specifically, resistivity dropped from 6 × 105 Ω.cm (as deposited) to 2×10^5 Ω.cm and again to 1×10^4 Ω.cm when conducted at 300 °C and 400 °C.

Such a drop in resistivity could be due to a rise in the concentration of holes, which contributes effectively to the high charge carrier density of the Cu_2O matrix. Thus, these results can be suggestive of the crucial role performed by thermal treatment in optimizing the conductivity conditions of Cu_2O in thin films, which are otherwise valuable in future applications in electrical and optoelectronic devices.

II.2.4 Deposition potential influence

Zhou et *al.* [27] underlined that applied deposition potential was a significant parameter for the electrodeposition of Cu_2O thin films. They reported that appropriate film development occurs when the voltage is in the range of – 0.2 to – 0.6 V with respect to the reference electrode. Beyond greater cathodic potentials, considerable co-deposition of metallic copper with Cu_2O can take place, compromising phase purity.

They also found that smaller grain structures emerge toward larger negative deposition potentials (– 0.35 to – 0.90 V). This behavior has been ascribed to an increase in current density, which, with increased cathodic potentials, enhances the deposition rate and decreases grain size.

Such evidence has always been substantiated by literature [36, 37] and combines well the detector-applied potential, deposition kinetics, and resultant films' microstructural features.

The exploratory investigation performed by Jiang et *al.* [38] evaluated the influence of applied deposition potential on the creation of Cu_2O thin films by a method of electrodeposition on titanium foils, utilizing acetate-based aqueous solutions. Films were developed at various potentials (– 0.1, – 0.3, – 0.5, – 0.7, and – 0.9 V vs. a reference electrode). X-ray diffraction (XRD) investigation verified the presence of cubic-phase Cu_2O for all samples but demonstrated that metallic copper (Cu^0) was created at potentials equal to or more negative than – 0.5 V.

The SEM photographs revealed that applied potential plays a major role in altering surface morphology, whereas octahedral and cubic Cu_2O were also found, combined with Cu/ Cu_2O agglomeration at higher cathodic potentials. This morphological modification directly links with deposition dynamics, affected by increasing current density at higher over potentials. In addition, the optical bandgap of electrodeposited films was observed to fluctuate from 1.83 eV to 2.03 eV with the deposition potential, an indication of the influence of applied potential on the electronic structure of the produced Cu_2O films.

Similarly, Jiang et al. [39] conducted the same electrochemical study as previously detailed by using an FTO-type substrate. They obtained Cu_2O thin films with Cu:O stoichiometric ratios ranging from 2.5:1 to 20.9:1 as the applied potential became more negative. The optical band gap values for these films decreased from 2.35 eV to 1.63 eV as the applied potential varied from – 0.1 V to – 0.8 V. The decrease was attributed to the co-deposition of metallic copper, along with Cu_2O.

Additional research has been done on the effect of deposition potential on the characteristics of Cu_2O thin films [40]. For the results, both grain size and optical bandgap showed variations when the applied potential was moved from – 0.35 V to – 0.65 V. Within this potential window, all electrodeposited Cu_2O films demonstrated a preferential crystallographic orientation along the (111) plane. It also confirmed the p-type semiconductor behavior using photocurrent measurements with the films.

Meanwhile, Han et *al.* [41] created p-type Cu_2O thin films employing electrodeposition onto copper substrates through their sulfate-based electrolyte. From electric characterizations on the material, resistivity was observed to decline dramatically from 2×10^8 Ω·cm to 3.2×10^5 Ω·cm depending on deposition parameters such as solution pH, applied voltage, and temperature. The large discrepancy in resistivity was attributable to grain size refinement resulting from varied experimental conditions of deposition rates.

To ameliorate Cu_2O thin films from poor electrical resistivity, Mahalingam et *al.* [42] created p-type Cu_2O thin films on copper and SnO_2 foils or substrates. The electrodeposition occurred in an aqueous electrolyte of 0.45 M copper sulfate and 3.25 M lactic acid with 2.4 g NaOH added. Post-deposition samples were annealed at a temperature between 70 and 350 °C for 30 min. The study discovered that there is a decline of resistivity in a film from 50 to 30 $\Omega\cdot cm$ with a corresponding optical bandgap of 1.99 eV. This decrease in resistivity was mostly related to increased hole concentration, which ultimately enhanced the overall charge carrier density.

In a different study, Mizuno et *al.* [43] analyzed the synergism of deposition potential and electrolyte pH in influencing the electrical performance of Cu_2O films. Corresponding with their conclusions, when the applied potential increases, so does the solution's pH, and these improve the electrical characteristics. All the copper oxide samples indicated positive current flow, with resistivity lying between 10^4 and 10^6 $\Omega\cdot cm$, carrier density between 10^{12} and 10^{14} cm^{-3}, and mobility from 0.4 to 1.8 $cm^2\cdot V^{-1}\cdot s^{-1}$. They found through testing that there is a strong link between the number of charge carriers in the films and the ratio of copper to oxygen in the films, while they related mobility to the size of the Cu_2O grains.

III.2.5 Deposition time influence

Zhai et al. [44] produced Cu_2O thin films with high crystallinity and dimensionally different morphologies, namely, cubes, tetrahedra, truncated cubes, and truncated octahedra, using an electrochemical technique in a sulfate-based electrolyte containing citric acid. The changes in morphologies were attributed to varying the electrodeposition time between 1 and 4 hours. Optical studies show that the bandgap energy of the films changed from 2.21 eV to 2.43 eV with deposition time, which is related to quantum confinement phenomena. All results show a very essential impact of deposition time on both the shape and the optoelectronic properties of the final Cu_2O films.

III.3 Experimental setup

III.3.1 Electrochemical equipment

This experimental setup (Figure III.1) consists of a three-electrode electrochemical cell having the capacity of 150 ml and it has been made of PYREX glass. An electrolyte solution will then be filled into the electrochemical cell. The electrodes will undergo control via a CORRTEST CS310M EIS Potentiostat/Galvanostat (CORRTEST Instruments, China) linked to computer-operated CS Studio 6 software. Finally, the entire device has been integrated into a thermostatic bath to maintain and regulate the temperature during the electrochemical cell deposition processes.

Figure III.1: Experimental setup used.

The following are the components of the three-electrode electrochemical cell used in this study:

- Working Electrode (Cathode): The deposition will be performed on the substrate. The working electrode's characteristics are important; it is chosen based on stability, polarization range, lattice constants, and any specific studies, which are designed for subsequent characterization of the deposited material. In our case, the working electrode is a glass substrate coated with a conductive layer of indium tin oxide (ITO), which acts as the working electrode. It has an active surface area of the ITO film measuring 1 × 2.5 cm^2, and it has a sheet resistivity of 20 $\Omega\cdot cm^{-2}$.
- Counter Electrode (Auxiliary Electrode): A platinum (Pt) plate was used to make the counter electrode for having the necessary passage of current within the electrochemical system.
- Reference Electrode: The reference electrode is a non-polarizable electrode that allows serves to authorize and monitor the applied voltage at the working electrode, thus giving a stable reference potential. Standard hydrogen electrode (SHE) is the standard

reference in electrochemistry, whose potential is defined as the origin of thermodynamic potentials, to all temperatures. This type of reference electrode is not convenient for routine work and is conventionally a secondary reference electrodes such as the saturated calomel electrode (SCE, + 0.244 V *vs*. SHE), the mercury/mercurous sulfate electrode (MSE, + 0.651 V *vs*. SHE), or the silver/silver chloride electrode (Ag/AgCl, + 0.221 V *vs*. SHE). All these electrodes use a fiber type junction contact to the solution and the electrode is through a very fine capillary. The saturated calomel electrode (SCE; $Hg/Hg_2Cl_2/KCl$) is used as a reference electrode with a standard potential of + 0.244 V against normal hydrogen electrode (NHE) at 25 °C.

III.3.2 Substrate preparation

Before the Cu_2O electrodeposition, the ITO glass substrates had to be cleaned thoroughly to remove surface contaminants, such as dust, oils, and other residues. This cleaning was vital for the better nucleation of Cu_2O and the uniform and adherent growth of films on the substrate [44]. The cleaning process is accomplished with an ultrasonic bath at a temperature of 50 °C and includes the following:

- Cleaning in acetone (CH_3COCH_3) for 10 minutes.
- Cleaning in ethanol (CH_5OH) for 10 minutes.
- Cleaning in distilled water for 10 minutes.

After cleaning, the cleaned substrates were dried in air prior to deposition.

III.3.3 Electrodeposition Bath

The electrodeposition solutions were comprised of:

- Copper source: copper(II) sulfate pentahydrate ($CuSO_4 \cdot 5H_2O$, Sigma Aldrich 98.5% of purity, USA): strong copper(II) ion source at 0.05 M.
- Complexing agent: 1 M citric acid ($C_6H_8O_7$, Labo Chimie PVT-LTD, 99.5% of purity, India) to inhibit copper hydroxide ($Cu(OH)_2$) solid formation and maintain conductivity of the electrolyte throughout the electrodeposition procedure [45]. This compound can increase hardness and resistivity, decrease roughness, and modify the deposit structure and morphology. In fact, citric acid causes a shift of the copper cathodic peak potential toward more negative values [46].
- Adjusting the pH: Sodium hydroxide (NaOH, SPECILAB, Algeria) was slowly added to the solution for pH adjustment.

- The solvent was distilled water (H_2O) to a fixed volume of 100 ml. Stirring of the solution was maintained while adding NaOH until pH 11 was reached.

Experimental conditions for the electrodeposition procedure:

- Deposition time: 15 minutes.
- Applied potential: – 0.5 V *vs*. SCE (Saturated Calomel Electrode).
- pH of the solution: 11.
- Temperature of the bath is fixed at 40, 60, and 80 °C.
- Working electrode: ITO-coated glass substrate.

III.4 Electrochemical study

III.4.1 Cyclic voltammetry study

Cyclic voltammetry helps us understand the electrochemical reactions related to the creation and reduction of different copper types on the working electrode surface, enabling us to improve the conditions for depositing Cu_2O. The overall shape of the voltammogram shows hysteresis, which is expected for these poorly reversible, solid-phase deposits. The difference between those oxidation and reduction curves indicates that there are irreversible growth processes taking place that can lead to the continuous nucleation followed by the growth of Cu_2O crystals. The peak heights will depend on the concentration of the Cu^{2+} ions, pH, temperature of the electrolyte, and the real surface area in contact with the working electrode. Reproducible peaks with a well-defined maximum indicate stable electrochemical behavior, which allows for controlled electrochemical deposition for thin films.

Figure III.2 shows the voltammogram of the substrate immersed in an electrolyte containing 1 M $C_3H_6O_3$, and 0.05 M $CuSO_4.5H_2O$ at pH = 11 and a temperature of 40 °C, the potential was varying between + 0.5 and – 0.5 V *vs*. SCE, with a scan speed of 20 mV/s.

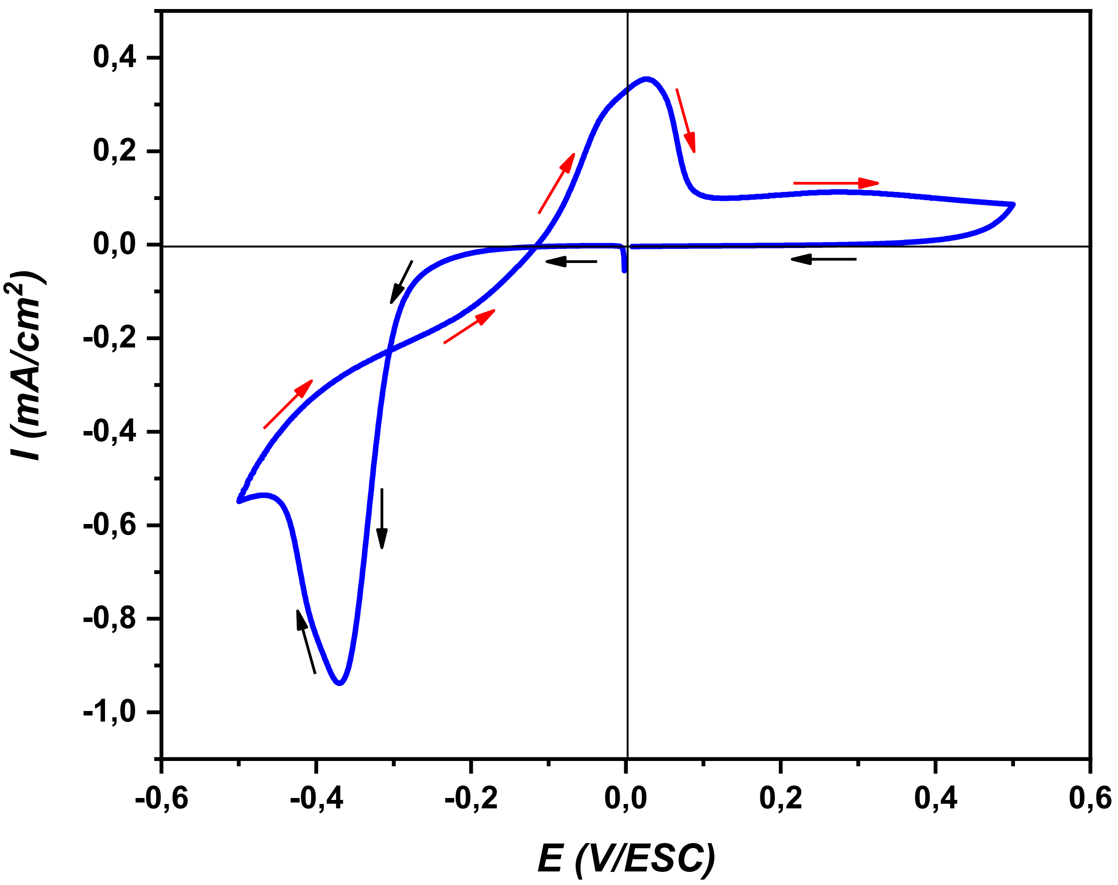

Figure III.2: Cyclic voltammogram of the ITO glass substrate immersed in 1 M $C_3H_3O_3$ + 0.05 M $CuSO_4{\cdot}5H_2O$ electrolyte (pH 11, 40 °C).

During cathodic scanning (towards negative potentials):

- A reduction peak is observed around – 0.2 V *vs*. SCE, indicating the reduction of Cu^{2+} ions to Cu according to the following reaction:

$$2Cu^{2+} + 2e^{-} \rightarrow Cu. \qquad \text{(III.1)}$$

The pH of the electrolyte is basic (pH=11) due to the presence of hydroxide ions (OH^-) generated by the addition of NaOH. Cu^+ ions will therefore combine with (OH^-) to form copper hydroxide as follows:

$$Cu^{+} + 2OH^{-} \rightarrow Cu(OH)_2. \qquad \text{(III.2)}$$

The temperature of the electrolyte is a parameter in this type of deposition, providing the energy needed to activate the chemical reactions, i.e., the dehydration of this hydroxide to form Cu_2O (reaction III.7).

$$2CuOH \rightarrow Cu_2O + H_2O. \tag{III.3}$$

Tang et *al*. [35] have shown that, kinetically, this dehydration is very slow at room temperature (around 30 °C). Nevertheless, even if, from a thermodynamic point of view, oxides are more stable than hydroxides whatever the temperature, it is necessary to work at sufficiently high temperatures to have a fast, quantitative dehydration and give an oxide possessing few defects [47].

- If the potential reaches more negative values (– 0.37 V), it is possible to observe the reduction of Cu^+ to Cu (reaction III.4), which can lead to the formation of metallic copper instead of Cu_2O. This is accompanied by a decrease in current due to the hydrogen evolution reaction.

$$Cu^+ + 2e^- \rightarrow Cu. \tag{III.4}$$

$$2H^+ + 2e^- \longrightarrow H_2. \tag{III.5}$$

The above results indicate that metallic copper and copper oxide can be co-deposited, which is in line with the results published by Hu et *al*. [48].

During the anodic scanning (towards positive potentials):

An oxidation peak appears at 0.03 V *vs*. SCE, corresponding to the oxidation of Cu^+ to Cu^{2+}, or even the oxidation of metallic Cu in solution if this was formed during cathodic scanning, this may also reflect partial dissolution of the deposited Cu_2O according to the following reactions [49]:

For Cu_2O:

$$Cu_2O + 2H^+ \rightarrow 2Cu^{2+} + H_2O + 2e^-. \tag{III.6}$$

For Cu:

$$Cu \rightarrow Cu^+ + e^-. \tag{III.7}$$

A crossover between the anodic and cathodic branches appears in the curve when the potential shifts to the positive direction (at $E = – 0.30$ V), which is characteristic of a nucleation process and growth of a new phase on the substrate surface [50].

The potential sweep between –0.5 V and +0 .5 V *vs*. SCE delineates the ideal electrochemical window for the formation of Cu_2O thin films without the appearance of undesirable phases. Cyclic voltammetry analysis is therefore essential for optimizing deposition parameters and guaranteeing the quality of the resulting film.

III.4.2 Chronoamperometry study

The technique consists of applying a fixed potential for a time interval t and recording the current as a function of time. It is important for processes that involve the formation of a new phase during deposition because it allows a straightforward separation of nucleation and crystalline growth processes. Figure III.3 depicts the chronoamperograms of Cu_2O thin films elaborated by electrodeposition at different temperatures of the electrolytic bath 40, 60, and 80 °C.

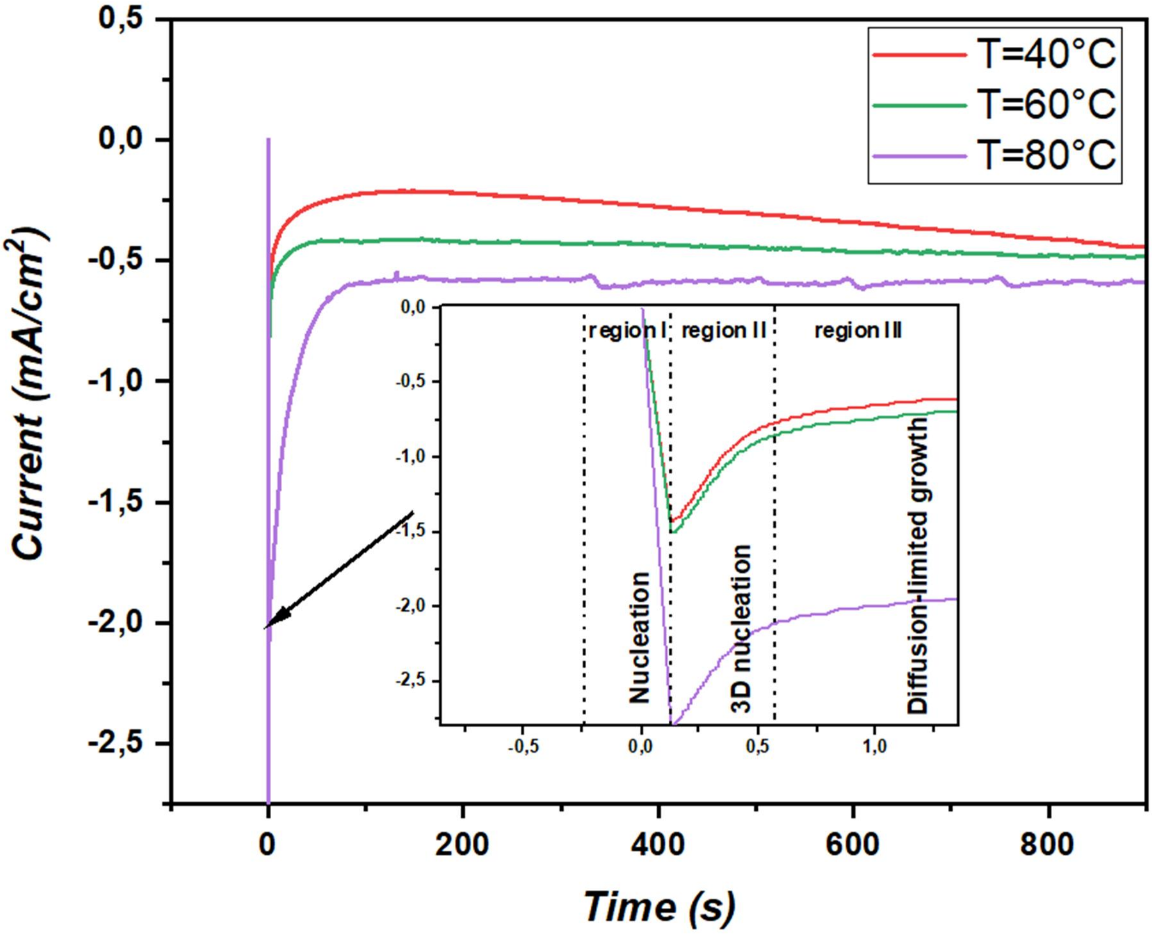

Figure III.3: Chronoamperometric curves obtained during Cu_2O thin films electrodeposition at different bath temperatures 40, 60, and 80 °C.

The chronoamperometric curves for Cu_2O thin films electrodeposited at different bath temperatures (40, 60, and 80 °C) exhibit three distinct regions (Figure III.3). Initially, the current rises sharply to a peak value (i_{max}) at a characteristic time (t_{max}), then decreases, before stabilizing over longer durations (up to 900 seconds). In the first region (0 – 1.25 s), the current rapidly drops to − 1.48 mA at 40 °C, − 1.50 mA at 60 °C, and − 2.75 mA at 80 °C. This initial decline reflects double-layer charging and the onset of nucleation. The higher the bath temperature, the faster the charge transfer, due to increased ion mobility and enhanced reduction kinetics. During the second phase (around 0.6 s), the current reaches a maximum ($i_{max} \approx -1.15$ mA for 40 °C and 60 °C), indicative of progressive three-dimensional nucleation and growth. At 80 °C, the peak current is marginally higher, but occurs at a similar time, suggesting a quicker transition to diffusion-limited growth. In the final region, the current levels off at − 0.45 mA (40 °C), − 0.50 mA (60 °C), and − 0.57 mA (80 °C), marking a diffusion-controlled growth regime once surface coverage is achieved. The sustained higher current at elevated temperatures is attributed to enhanced mass transport and thermal activation.

Overall, these findings indicate that higher temperatures (80 °C) promote faster deposition but may compromise film uniformity, while moderate temperatures (40 – 60 °C) offer more controlled growth conditions, consistent with a mechanism involving instantaneous nucleation followed by diffusion-limited growth [36, 51].

The overall shape of the current transients aligns well with the theoretical profile of a three-dimensional nucleation and growth process under diffusion control [51, 52]. Additionally, the progressive increase in current density with rising bath temperature confirms the enhanced deposition rate of Cu_2O under these conditions.

III.5 Characterization of Cu_2O thin films

III.5.1 Structural characterization by X-ray diffraction

We began our characterization with X-ray diffraction (XRD), a highly efficient and essential method for determining crystal structure. First, it confirms the formation of the desired layers and their purity. For all our samples, we used a Rigaku SmartLab diffractometer equipped with a copper anticathode $K\alpha$ = 1.54148 Å in a 2θ angle range between 10° and 80°. Thickness measurements are done using a KLA Tencor D500 profilometer.

Figure III.4 illustrates the diffraction spectra of Cu_2O thin films grown by electrochemical method for different values of bath temperature with an electrolyte containing 1 M $C_3H_6O_3$, and 0.005 M $CuSO_4.5H_2O$ at pH = 11, a deposition potential fixed in – 0.5 V *vs*. SCE, and for 15 min deposition time.

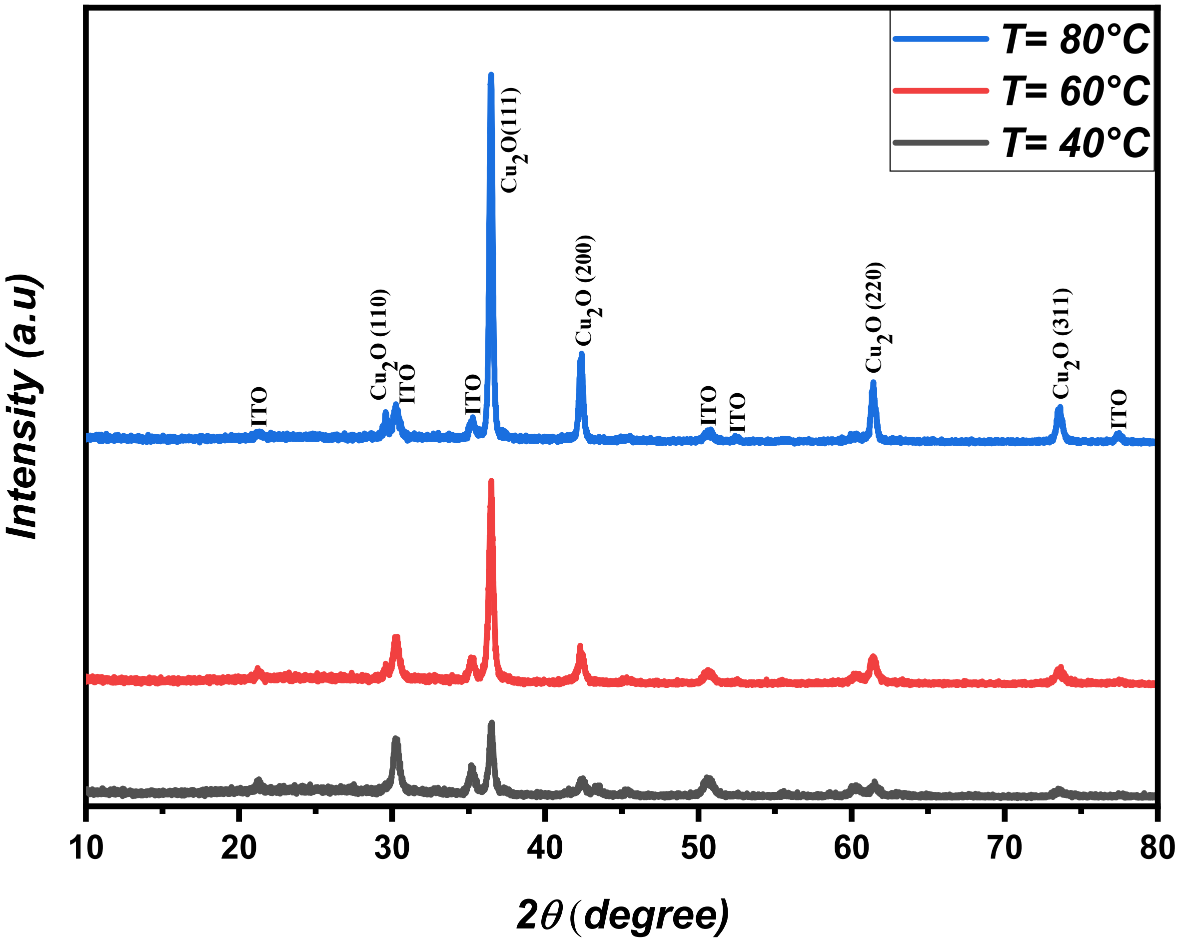

Figure III.4: Diffraction spectra of Cu_2O thin fimls at different bath temperatures.

Analysis of the spectra revealed the presence of 5 characteristic structural lines at diffraction angles in *2θ*: 29.50°, 36.47°, 42.38°, 61.42°, and 73.63°. With a very good resolution that we find in almost all publications relating to Cu_2O thin films. Comparison of the diffraction spectra with JCPDS (Joint Committee on Powder Diffraction Standards) file **No. 00-001-1142** (Figure III.5.a) enabled us to identify the cubic phase (Figure III.5.b) of the *Pn-3m* space group of copper oxide and the various diffraction planes (110), (111), (200), (220), and (311) corresponding respectively to the 5 previous diffraction lines.

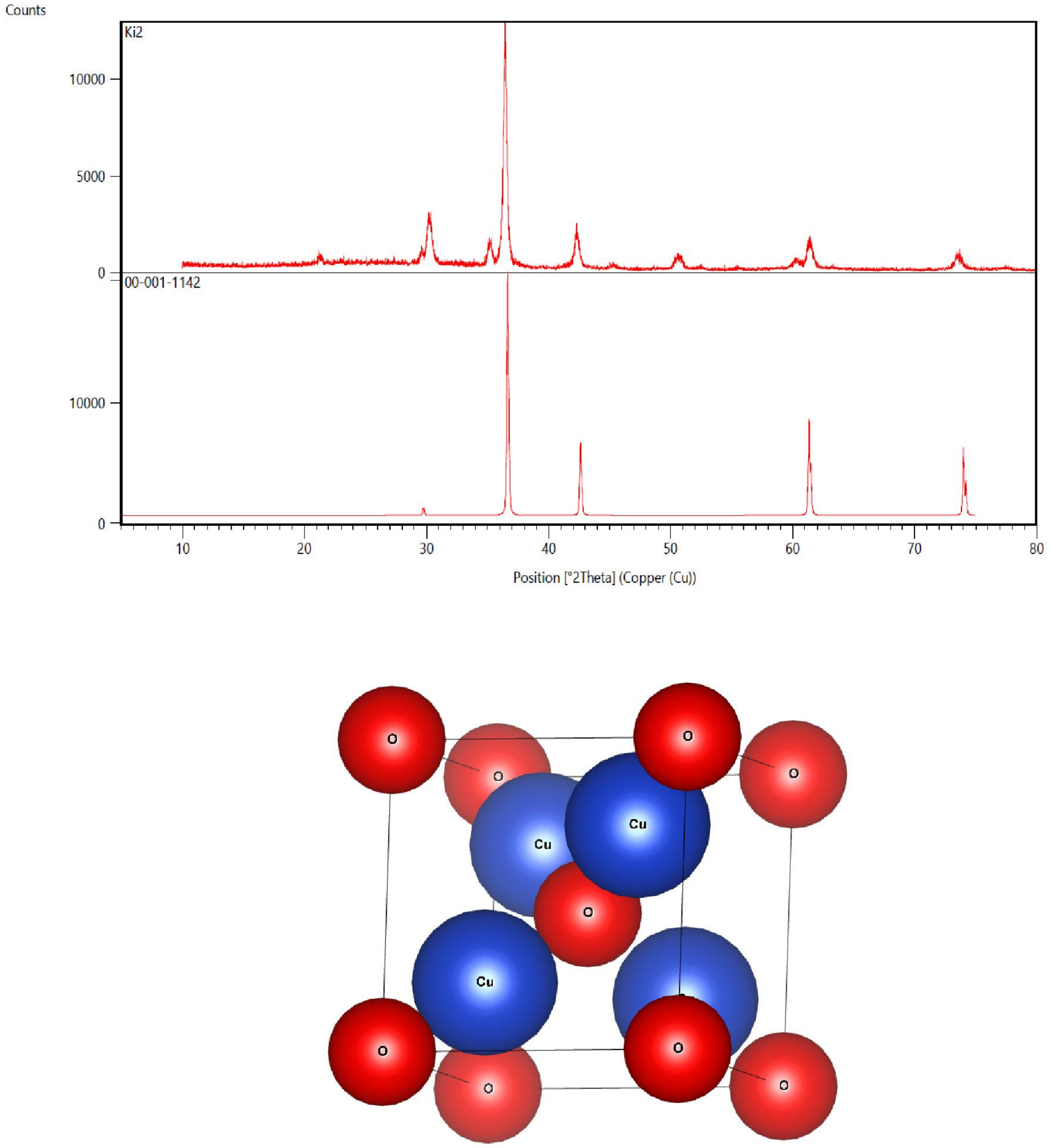

Figure III.5: a) - Comparison of XRD spectra with simulated spectra from file JCPDS file N°. **00-001-1142**. b) - Cubic structure of Cu_2O drawn by *Vesta.*

Figure III.4 shows that the crystalline quality of the samples increases with increasing bath temperature. The samples show better crystalline qualities, with well-defined peaks of remarkable intensity and no noise or traces of amorphous material. The intensity of the peaks increases with increasing bath temperature, which translates into improved crystalline quality: the higher the temperature, the better the layer in terms of crystallinity. There are no additional peaks in the diffraction spectra, except for substrate (ITO), which proves the purity of the layers and the absence of secondary phases.

The interreticular distance d is calculated from Bragg's law [53]:

$$2d\sin\theta = n\lambda \tag{III.8}$$

Where *d*: interreticular distance, i.e. distance between two crystallographic planes; *θ*: Bragg angle or the value of the diffraction angle in radian = half angle of deflection, *n*: diffraction order; λ: X-ray wavelength used (λ = 1.5406 Å).

The lattice parameter *a* was calculated using the formula [54]:

$$\frac{1}{d^2} = \frac{h^2}{a^2} + \frac{k^2}{b^2} + \frac{l^2}{c^2} \tag{III.9}$$

When all calculations are based on the most intense peak (111), and the structure of Cu_2O thin films is a cubic structure where $a = b = c$; the formula (III.9) becomes:

$$\frac{1}{d^2} = \frac{3}{a^2} \rightarrow a = \sqrt{3}.d \tag{III.10}$$

The crystallite size of thin films was calculated from Scherrer's formula [53]:

$$D = \frac{0.9\lambda}{\beta\cos\theta} \tag{III.11}$$

Where *D* is the average particle size, λ is the X-ray wavelength (λ = 1.5406 Å), β is the full width at half-maximum (*FWHM*) of the diffraction peak and θ is the diffraction angle value.

The values of the lattice parameter, the inter-reticular distance, and the crystallite sizes have been calculated and are listed in Table III.1.

Table III.1: Diffraction angle, full width at half-maximum, interreticular distance, lattice parameter, crystallite size, and the thickness of Cu_2O thin films at different bath temperature.

T (°C)	***2θ* (°)**	***β* (°)**	***dhkl* (nm)**	***D* (nm)**	***a* (Å)**	***Thickness (*nm*)***
80	36,4560	0,32492	2,4626	26,8858	4,2654	453
60	36,4603	0,40698	2,46236	21,4650	4,26484	252
40	36,4779	0,41900	2,4612	20,8503	4,26284	178

Lattice parameters and inter-reticular distance of Cu_2O thin films prepared by electrodeposition do not change with increasing electrolyte bath temperature, while crystallite sizes increase from 20.8503 nm to 26.8858 nm with increasing of bath temperature from 40 °C to 80 °C, It may be linked to the increase in nucleation sites, which causes stronger cohesion of deposited particles and hence leads to better crystallinity.

According to Table III.1, the thickness of Cu_2O thin films varies proportionally with bath temperature. As bath temperature increases from 40 °C to 80 °C, the thickness of the thin films obtained increases from 178 nm to 453 nm. At higher temperatures, the extra heat helps Cu^{2+} ions move more easily in the solution, speeds up the chemical reactions at the electrode (ITO)/electrolyte surface, and increases both the growth of the material and the rate it is deposited, which results in a thicker layer being formed in the same amount of time.

III.5.2 Characterization by FTIR spectroscopy

FTIR spectra are obtained with a SHIMADZU IRSprit-T spectrophotometer, with wavelengths ranging from 400 to 4000 cm^{-1}.

The FTIR spectra of Cu_2O thin films fabricated by electrodeposition at different bath temperatures are illustrated in the figure III.6 are virtually identical under all conditions, the Cu_2O phase being the only one to be detected, with some trace of organic bonding that we will discuss**:**

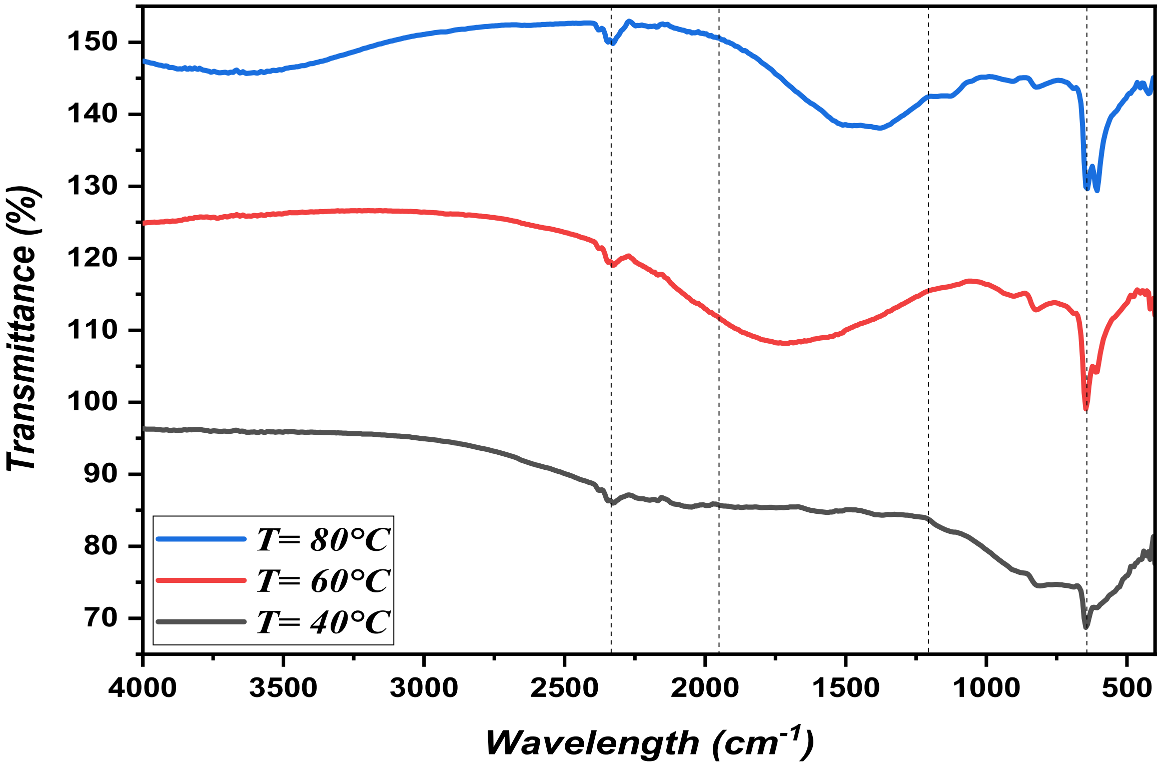

Figure III.6: FTIR spectra of Cu_2O thin films at different bath temperatures.

Comparing the FTIR spectra of Cu_2O, we note that the spectra of the three different Cu_2O samples show the following characteristic bands:

1- A trace around 2333 cm^{-1} attributed to the O-H stretching mode (probably due to the use of citric acid in the synthesis).
2- A very broad, low-intensity band between 1900 cm^{-1} and 1100 cm^{-1}, which includes several maxima that can be divided as follows: A band at 1660 cm^{-1} showing bonding vibrations due to the H_2O molecule. Vibrational bands in the 1500 –1300 cm^{-1} region attributed to bending and deformation of C-H [54]; and a band at 1150 cm^{-1} is linked to vibrations of the C-O bond (probably due to adsorption to the surface during deposition).
3- A band at 610 cm^{-1} is linked to the Cu-O bond in all three samples [55].

Despite the bands we found between 2333 and 1100 cm^{-1}, these results show that this organic part is only products used in the synthesis or atoms adsorbed on the surface, which confirms the results of the X-ray diffraction. Our procedure gives pure layers with total consumption of starting materials such as copper sulfate. However, the two very intense bands at 610 cm^{-1} correspond to the Cu_2O bond. We note that they increase with increasing bath temperature or are distinctive at 80 °C.

III.5.3 Morphological characterization with AFM spectroscopy

AFM images of Cu_2O thin films grown by electrodeposition are achieved using an Asylum Rechearch MFP-3D Origin AFM in contact mode.

Figure III.7 displays 2D and 3D AFM images of the different Cu_2O thin films obtained at different bath temperatures electrodeposited on ITO at $E = -0.5$ *vs*. SCE and for 15 min of deposition.

Increasing the temperature of the electrolytic bath considerably affects the morphology of Cu_2O deposits. At higher temperatures, ion mobility is greater and the reactions taking place at the electrode surface are voided. This generally results in a faster rate of crystal growth, leading to grain coalescence, hence a smoother surface, larger grain size, less intergranular void, and makes the deposit density more uniform. However, morphology can become irregular beyond a critical temperature, depending on whether this is due to disordered growth or the formation of by-products, and this fact can compel the calculation of an optimization temperature interval. Thus, temperature is one of the keys to modulating the surface texture and/or morphology of Cu_2O, according to application needs.

The morphological differences previously observed were used to quantify the roughness distributions of the motive obtained by AFM image processing and the following RMS roughness measurements: 14.624 nm, 13.915 nm, and 5.473 nm for bath temperatures of 80°C, 60°C, and 40°C, respectively.

Measurements of the roughness of the samples have shown that this increases considerably as the bath temperature rises. It is well known that the roughness of a layer increases with its thickness [56].

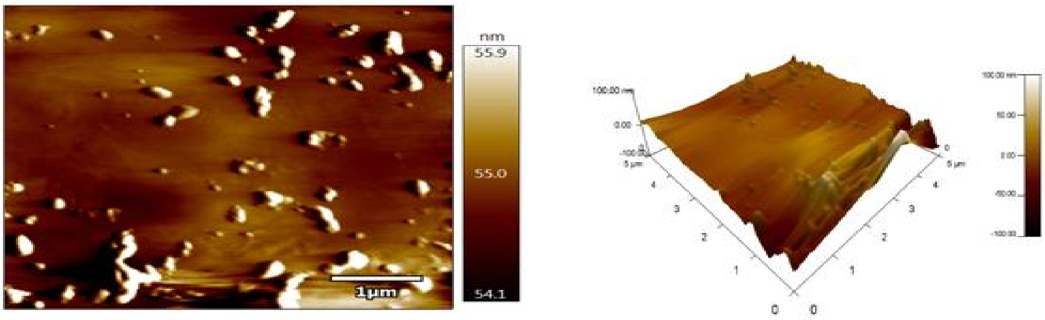

(a) T=40°C

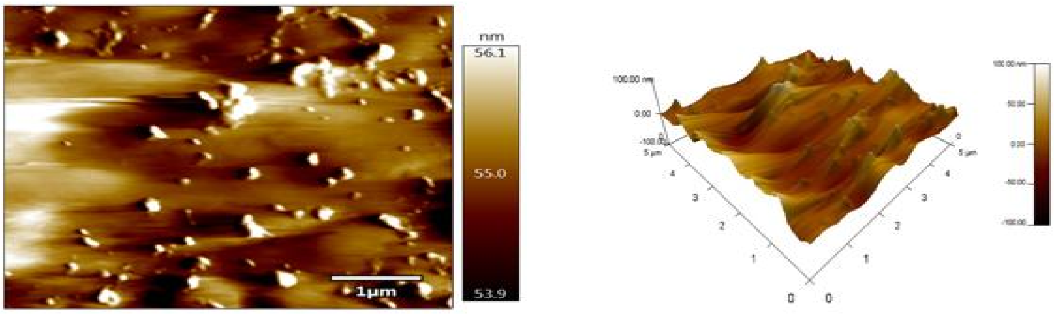

(b)T=60°C

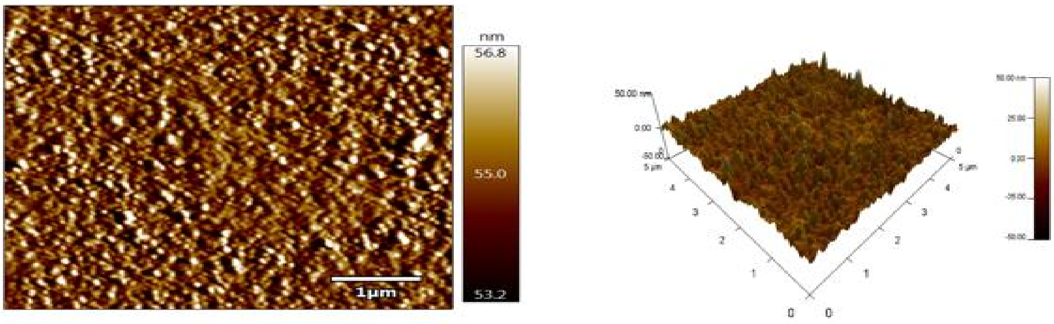

(b) T=80°C

Figure III.7: 2D and 3D AFM images of Cu_2O thin films obtained by electrodeposition for different bath temperature values.

III.5.4 Optical characterization

III.5.4.1 UV-visible spectroscopy

UV-visible transmittance and absorbance spectra were obtained using a SHIMADZU UV-1900i spectrophotometer with wavelengths varying from 300 nm to 900 nm at room temperature.

a) Optical transmittance

Figure III.8 shows the variation in transmittance of Cu_2O thin films at different bath temperatures.

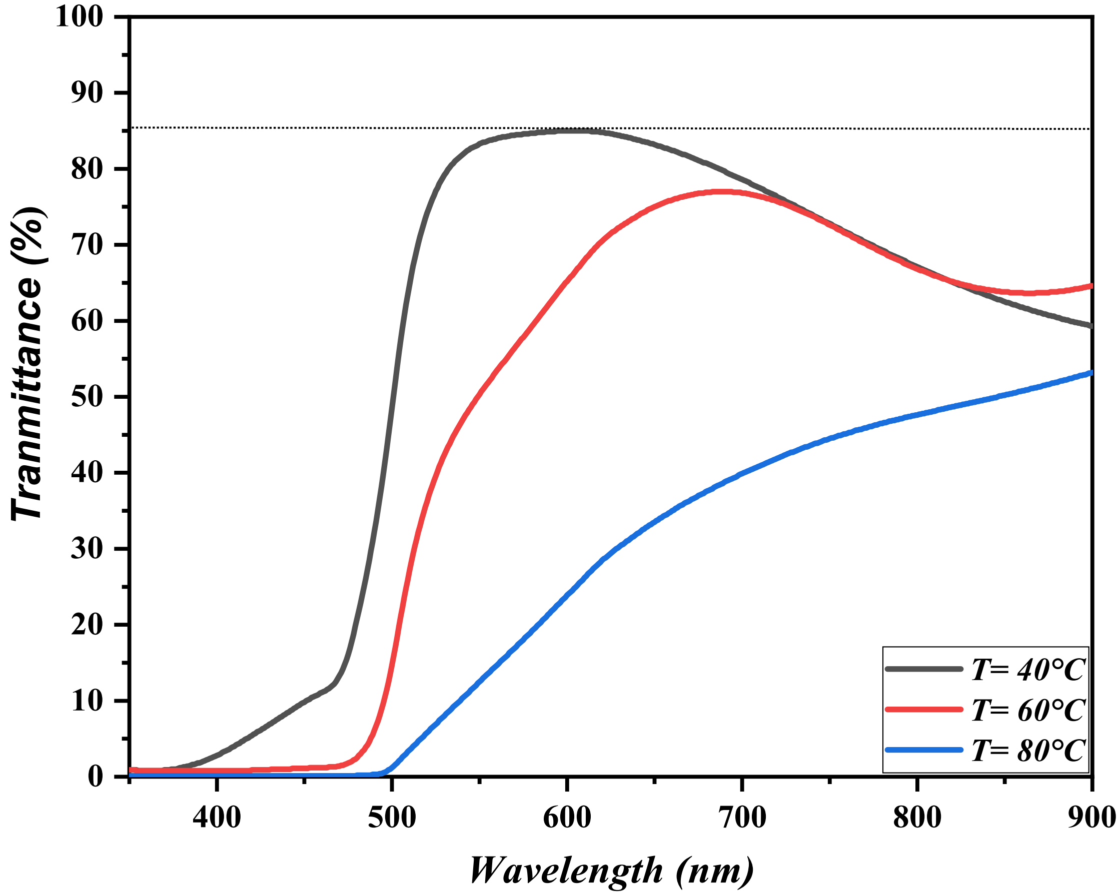

Figure III.8: Transmittance spectra of Cu_2O thin layers at different values of bath temperature.

The transmittance of copper oxide Cu_2O thin films produced by electrochemical deposition varies significantly with the temperature of the electrolytic bath, which in this case was set successively at 40 °C, 60 °C, and 80 °C.

At 40°C, the transmittance is significantly elevated (85%) due to the thinner, less thick, or poorly crystalline layers facilitating greater light passage. An elevation in temperature to 60°C often reduces transmittance. This situation exhibits enhanced crystallinity and increased layer thickness, which likely significantly improved light absorption, resulting in reduced transmitted light. At 80°C, the transmittance persists in declining, maybe linked to enhanced absorption due to increased layer thickness [20].

The transmittance of Cu_2O thin films is declining with increasing electrolyte bath temperature because the optical absorption is increasing due to the growth and densifying of the film, and this relationship can become more complicated at higher bath temperatures.

From the general appearance of these spectra, we may discern two transmittance areas depending on wavelength:

- A region of high transmittance located between 500 and 900 nm (visible range). The transmittance value climbs dramatically by 30 to 85%, depending on the potential applied. Several writers [20, 44] have reported these values. This remarkable transparency is one of the qualities that explains the interest in Cu_2O nanostructures.

- A region characterized by strong absorption and poor transmission of radiation, which corresponds to the fundamental absorption of $\lambda < 500$ nm. It is manifested by the rapid reduction in the transmittance spectrum. This absorption is due to the interband electrical transition between the valence band and the conduction band. The transmittance fluctuation in this region is exploited to calculate the optical gap of films.

We note the absence of so-called Fabry-Perot interference bangs in the long-wavelength region. These are owing to the numerous reflections of light created between the film/air surface and the layer/substrate contact [57]. It should be emphasized that these interference bangs only arise when the film/air interface is entirely smooth; in the presence of surface roughness, the light will be dispersed rather than reflected.

b) Optical absorbance

Figure III.9 shows the absorbance spectra of Cu_2O thin films at different bath temperatures, prepared by electrochemical deposition, then the electrolyte containing 1 M of $C_3H_6O_3$ and 0.05 M of $CuSO_4.5H_2O$ at pH = 11, a potential of deposition was fixed at – 0.5 V, and 15 min time of deposition.

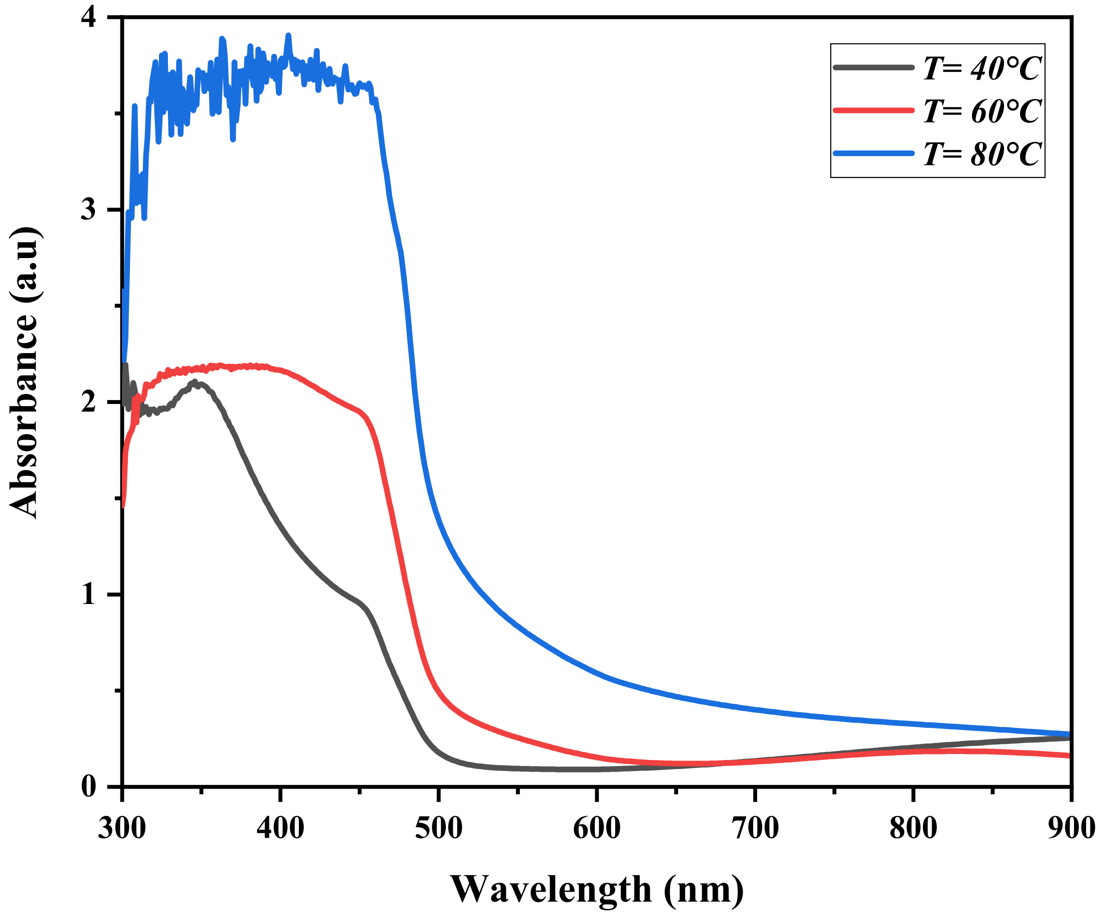

Figure III.9: Absorbance spectra of Cu_2O thin films at different bath temperatures.

The absorbance of Cu_2O thin films formed by electrodeposition is substantially influenced by the temperature of the electrolytic bath. In general, when the bath temperature increases, the absorbance of the layers tends to increase.

Strong absorbance can be observed for Cu_2O deposits in the range where $\lambda < 500$ nm due to excitation and migration of electrons from the valence band to the conduction band. There is also a considerable drop in absorbance in the visible area (between 500 nm and 900 nm) that approaches zero.

This evolution can be explored using numerous aspects that relate to temperature:

1. Better crystal formation: at moderate temperatures, the thermal energy used supports a more rapid velocity of Cu^+ ions in solution, providing better orderly crystal growth for Cu_2O crystals in terms of denser, more homogeneous layers that absorbed more light.

2. More manufactured thickness: by the nature of a physical vapor deposition application, the deposit rate can also rise with rising temperature, which would ultimately yield a thicker film, which is beneficial for absorbance.

3. High-quality deterioration: at and above a temperature, a degradation in film quality is noticed, giving flaws, subsequent CuO oxidation, or a dissolution of the substrate causing a drop of absorbance.

Determination of the optical gap is based on the model proposed by Tauc, where E_g is related to the absorption coefficient α by the following relationship [38, 40]:

$$(\alpha h\nu)^2 = A(h\nu - E_g) \tag{III.12}$$

Where $h\nu$ is the photon energy, E_g is the optical bandgap of the material, and A is a parameter that depends on the transition probability.

On the Tauc curve (the plot of $(\alpha h\nu)^2$ versus energy $(h\nu)$), plot the linear portion of the graph, extrapolating this portion until it intersects the x-axis (the $h\nu$ axis); the intersection gives the gap energy E_g of Cu_2O thin films in eV as demonstrated in Figure III.10.

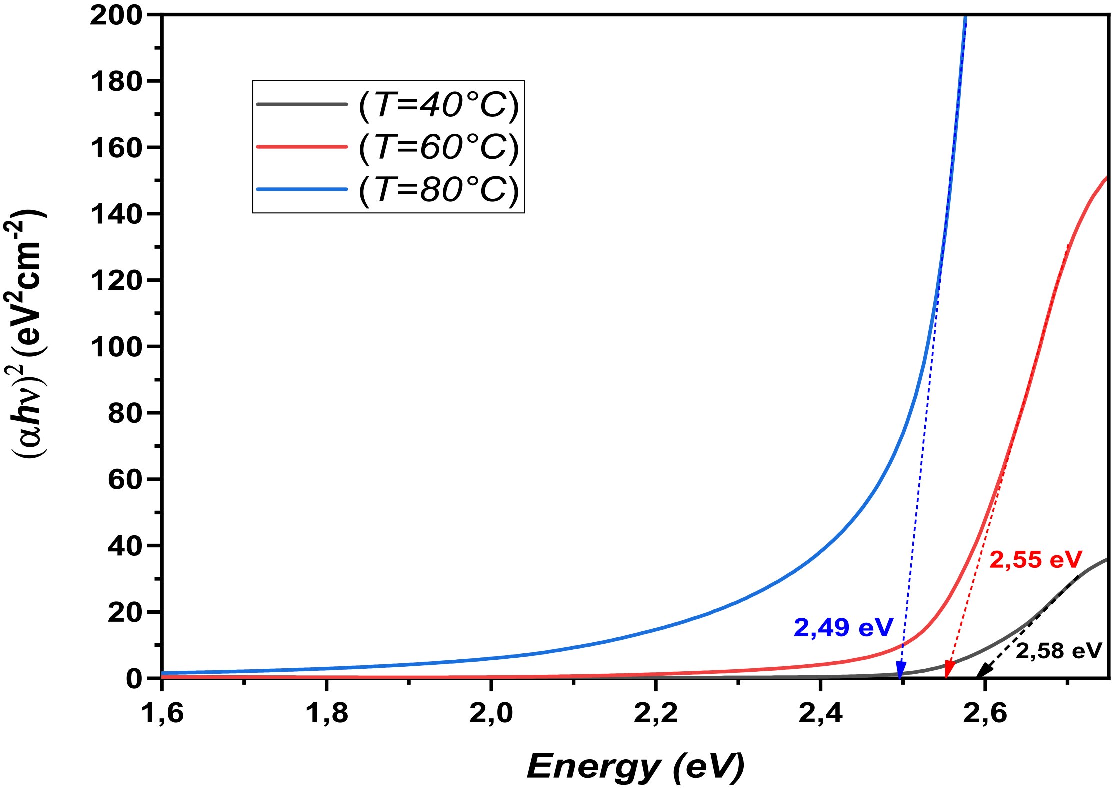

Figure III.10: Tauc pattern of Cu_2O thin films at different bath temperatures.

Figure III.11 shows the variation in optical gap energy of Cu_2O thin films elaborated by the electrodeposition method as a function of bath temperature.

For all our structures, the optical gap energy of Cu_2O thin films generally decreases with increasing electrolytic bath temperature due to improved crystallinity and reduced quantum confinement. At moderate temperatures, the ion mobility is increased, which permits more merging of ions and subsequently forms larger, better-quality crystals. Better crystallinity means fewer defects in the material's structure, which in turn reduces the localized states in the bandgap (in contrast to the free states, which can slightly narrow the optical gap with sub-gap transitions). Temperature can decrease such internal stress and increase long-range ordering of ions, which can stabilize the cubic structure of Cu_2O, leading to a gap energy that is more representative of the intrinsic value (~ 2.0 eV). In cases where the layers are small, the effect of lower temperatures will be to create smaller grains, and this will induce a quantum confinement effect, which will artificially increase the gap energy. Raising the temperature leads to larger, more nucleated grains, which reduces this apparent gap due to reduced quantum confinement.

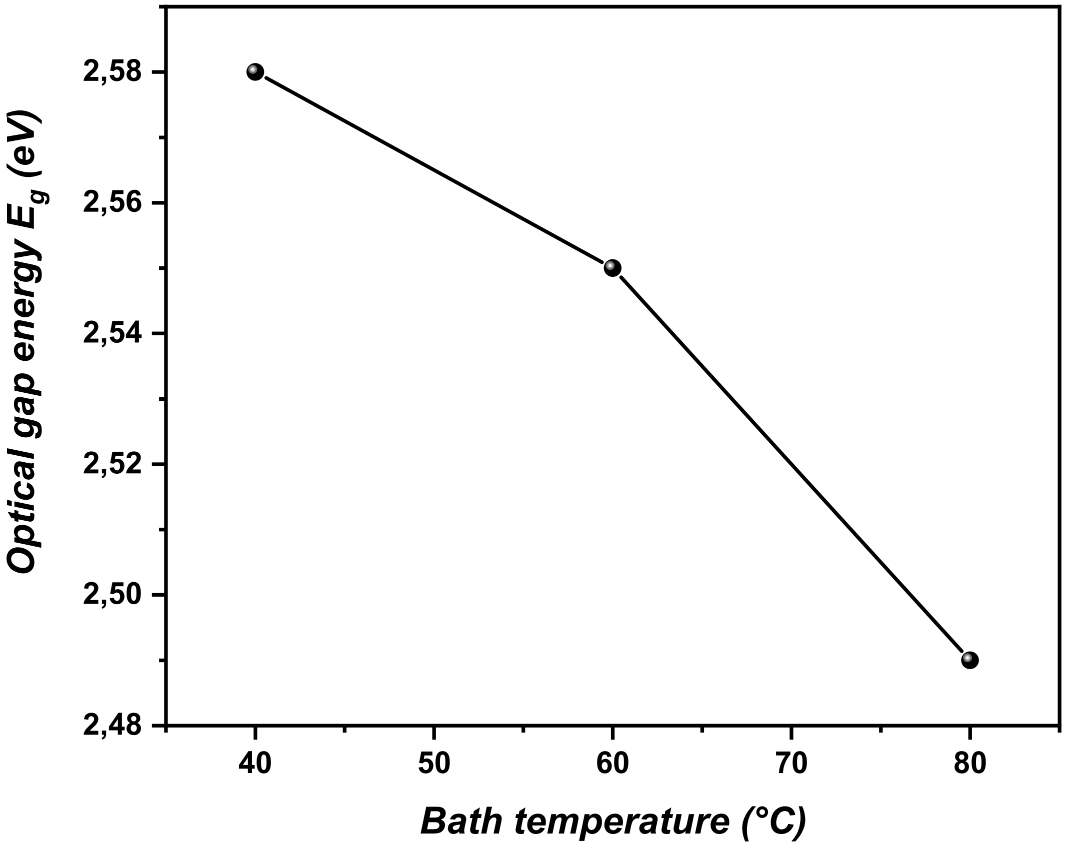

Figure III.11: Variation of optical gap energy of Cu_2O thin films as a function of bath temperature.

III.5.4.2 Photoluminescence spectroscopy

The photoluminescence spectra (PL) for Cu_2O thin films prepared by electrodeposition technic are taken using the Edinburgh FLS1000 Spectrometer.

Photoluminescence is a characterization for exploring the optical properties of materials. More precisely, it can be used to study intrinsic properties and structural defects. PL spectra of Cu_2O thin films electrodeposited on ITO were carried out at room temperature in a wavelength range from 600 to 850 nm, with an Nd-YAG (Neodymium-doped Yttrium Aluminium Garnet) laser emitting at a wavelength of 325 nm (3.8 eV) used to excite our samples. The photoluminescence spectra of Cu_2O thin films formed by electrodeposition are depicted in figure III.12.

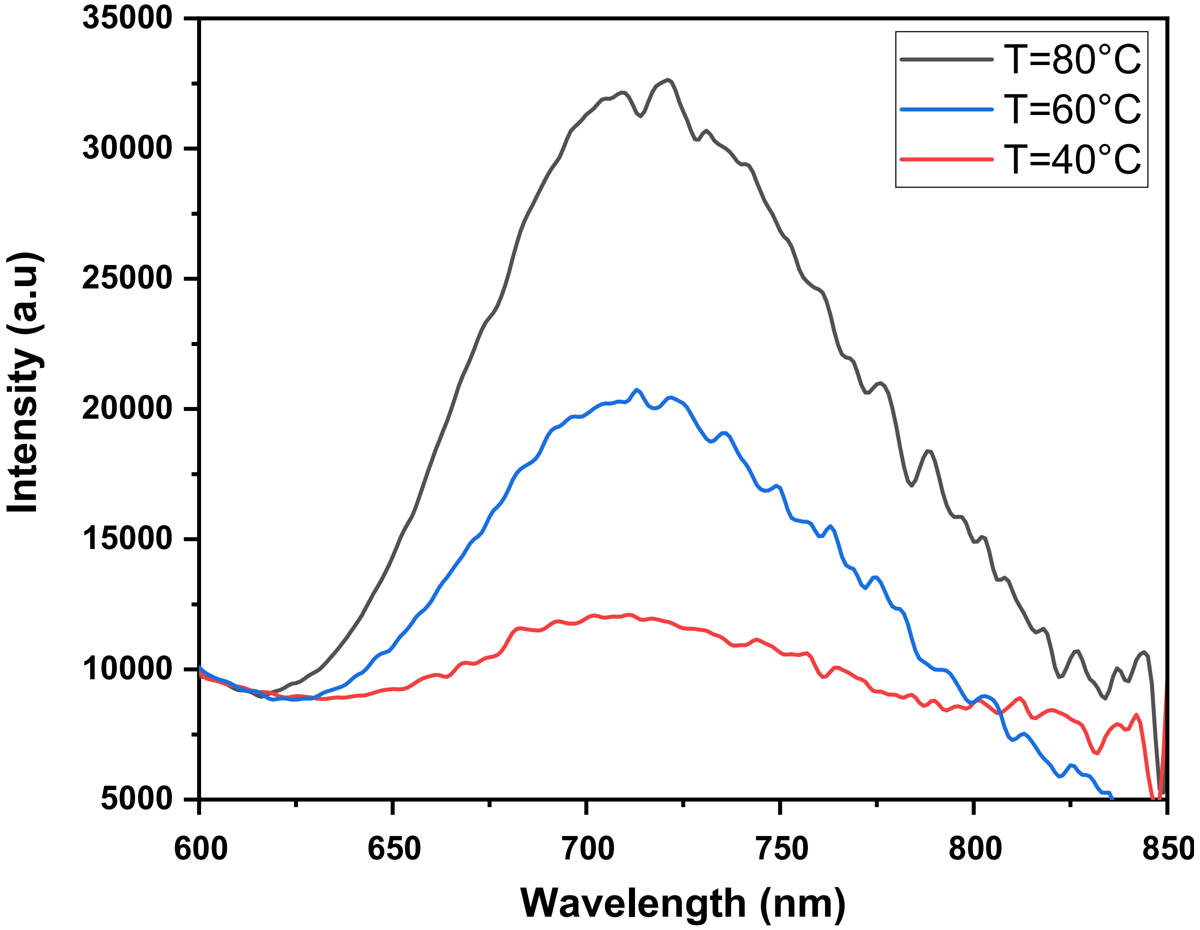

Figure III.12: Photoluminescence emission spectra of Cu_2O thin films at different bath temperatures with an excitation length of λ = 325 nm.

From Figure III.12, we note the presence of a broad asymmetric band centered around 715 nm extending from 625 to 825 nm, which is associated with the recombination of excitons bound to oxygen and copper vacancies [58, 59]. Its origin may be related to the recombination of excitons that are bound to doubly charged oxygen vacancies in Cu_2O thin films. In addition, the rise in photoluminescence (PL) intensity with increasing bath temperature is likely to be related to enhanced crystallinity, as seen in X-ray diffraction (XRD) tests, as well as the presence of copper vacancies, and the PL spectra obtained corroborate the p character of Cu_2O films, in agreement with the observations of Wang et *al*. [60] and Toboonsung et *al*. [61].

III.6 Conclusion

Cu_2O thin films were electrodeposited on ITO from a bath of copper sulfate pentahydrate (0.05 M) and citric acid as complexing agent (1 M), with pH adjusted to 11, at a deposition potential of – 0.5 V and a deposition time of 15 minutes. We analyzed the impact of bath temperature on the various properties of these thin films. We first examined the mechanisms of Cu_2O electrodeposition using cyclic voltammetry and chronoamperometry. Morphological analyses by AFM reveal a significant transformation of Cu_2O grain morphology as a function of bath temperature. In addition, the surface of the deposits becomes less rough as bath temperature increases. X-ray diffraction analysis revealed that all samples have a cubic structure with a preferential orientation in the (111) direction. In addition, the average crystallite size increased with increasing bath temperature. Analysis by UV-Vis spectroscopy and photoluminescence enabled us to determine the optical properties of Cu_2O thin films, such as absorption, transmission, gap energy and emission domains. The transmission of our samples is high, reaching around 85% in the visible range, while the optical gap varies between 2.49 and 2.58 eV, often correlated with crystalline quality. Hall Effect results indicate that Cu_2O nanostructures electrodeposited at different bath temperatures exhibit p-type conductivity. Consequently, tight temperature control optimizes the performance of Cu_2O layers for applications in photovoltaic devices, sensors, and photocatalysts.

The temperature of the electrolytic bath is crucial for regulating the structural, morphological, and optical properties of Cu_2O thin films obtained by electrodeposition.

References

[1] M. A. M. Patwary et al., RSC Adv. 12, 32853, (2022).

[2] T. Minami, Y. Nishi, T. Miyata, J. Appl. Phys. Express 9, 052301, (2016).

[3] M. Hadiyan, A. Salehi, H. Mirzanejad, J. Korean Ceram. Soc. 58, 94–105, (2021).

[4] M. Hara, T. Kondo, M. Komoda, S. Ikeda, K. Shinohara, A. Tanaka, J. N. Kondo, K. Domen, Chem. Commun., 357–358, (1998).

[5] I. Ali, New generation adsorbents for water treatment, Chem. Rev. 112, 5073–5091, (2012).

[6] S. S. Jeong, A. Mittiga, E. Salza, A. Masci, S. Passerini, Electrochem. Acta 53, 2226–2231, (2008).

[7] M. K Song, S. Park, F. M. Alamgir, J. Cho, M. Liu, Mater. Sci. Eng. R 72, 203–252, (2011).

[8] C. Rossi, K. Zhang, D. Esteve, P. Alphonse, P. Tailhades, C. Vahlas, J. Microelectromech. Syst.16, 919–931, (2007).

[9] P. S. Selvamani, J. J. Vijaya, L. J. Kennedy, B. Saravanakumar, M. Bououdina, J. Mater. Lett. 275, 128095, (2020).

[10] S. Satheeskumar, S. Vadivel, K. Dhanabalan, A. Vasuhi, A. T. Ravichandran, K. Ravichandran, J. Mater. Sci.: Mater. Electron. 29, 9354–9360, (2018).

[11] A. Lakshmanan, Z. C. Alex, S. R. Meher, J. Materials Science in Semiconductor Processing 148, 106818, (2022).

[12] V. Singh et al., J. Mater. Chem. C 11, 7356–7366, (2023).

[13] M. Ugalde-Reygadas et al., J. Materials Today Communications 32, 103999, (2022).

[14] Y. F. Lim et al., J. Phys. Chem. Chem. Phys.16, 25928–25934, (2014).

[15] S. Choudhary, J. V. N. Sarma, S. Gangopadhyay, J. AIP Conf. Proc. 1724, 020116, (2016).

[16] Y. Hu, P. S. Chen, Y. -C. Ko, C. H. Tsai, International Journal of Electrochemical Science 19 (8), 100688, (2024).

[17] Y. L. Liu, Y. C. Liu, R. Mu, H. Yang, C. L. Shao, J. Y. Zhang, Y. M. Lu, D. Z. Shen, X. W. Fan, Semicond. Sci. Technol. 20, 44, (2005).

[18] A. S. El-mezayyen, S. Guan, F. M. Reicha, I. M. El-Sherbiny, J. Zheng, C. Xu, J. Phys. D: Appl. Phys. 48, 175502, (2015).

[19] I. Sakellis, S. Giamini, I. Moschos, C. Chandrinou, A. Travlos, C. Y. Kim, J. H. Lee, J. G. Kim, N. Boukos, Energy Procedia 60, 37, (2014).

[20] Y. S. Jeong, H. Kim, H. S. Lee, J. Alloys Compd. 573, 163, (2013).

[21] T. D. Golden, Chemistry of Materials 8, 2499, (1996).

[22] V. Avrutin, N. Izyumskaya, H. Morkoç, Superlattices Microstruct. 49, 337, (2011).

[23] L. C. Olsen, F. W. Addis, W. Miller, Solar Cells 7, 247, (1982).

[24] A. E. Rakhshani, A. A. Al-Jassar, J. Varghese, Thin Solid Films 148, 191, (1987).

[25] L. C. Wang, N. R. de Tacconi, C. R. Chenthamarakshan, K. Rajeshwar, M. Tao, Thin Solid Films 515, 3090, (2007).

[26] T. Mahalingam, J. S. P. Chitra, S. Rajendran, M. Jayachandran, M. J. Chockalingam, J. Cryst. Growth 216, 304, (2000).

[27] Y. Zhou, Y. A Switzer, Scripta Mater. 38, 1731, (1998).

[28] L. Wang, M. Tao, Electrochem. Solid-State Lett. 10, H248, (2007).

[29] W. Wang, D. Wu, Q. Zhang, L. Wang, M. Tao, J. appl. Phys. 107, 123717, (2010).

[30] T. Jiang, T. Xie, L. Chen, Z. Fu, D. Wang, Nanoscale, R. Soc. Chem. 5, 2938, (2013).

[31] F. Caballero-Briones, J. M. Artes, I. Diez-Perez, P. Gorostiza, F. Sanz, J. Phys. Chem. C 113, 1028, (2009).

[32] N. Tabuchi, H. Matsumura, Jpn. J. Appl. Phys. 41, 5060, (2002).

[33] H. Natter, R. Hempelmann, Electrochim. Acta 49, 51, (2003).

[34] S. M. Shahrestani, Thèse de Doctorat, Université de Montréal Québec, Canada, (2013).

[35] Y. Tang, Z. Chen, Z. Jia, L. Zhang, J. Li, Mater. Lett. 59, 434, (2005).

[36] S. Bijani, L. Martinez, M. Gabas, E. A. Dalchiele, J. R. Ramos-Barrado, J. Phys. Chem. C 113, 19482, (2009).

[37] Y. Matsomoto, J. Hombo, C. Qiong, J. Electroanal. Chem. 279, 331, (1990).

[38] X. Jiang, M. Zhang, S. Shi, G. He, X. Song, Z. Sun, Nanoscale. Res. Lett. 9, 219, (2014).

[39] X. Jiang, M. Zhang, S. Shi, G. He, X. Song, Z. Sun, J. Electrochem. Soc. 161, D640, (2014).

[40] A. El-Shaer, A. R. Abdelwahed, A. Tawfik, M. Mossad, D. Hemada, Int. J. Emerging Technol. Adv. 4(12), 595, (2014).

[41] K. Han, M. Tao, Sol. Energy Mater. Sol. Cells 93, 153, (2009).

[42] T. Mahalingam, J. S. P. Chitra, S. Rajendran, M. Jayachandran, M. J. Chockalingam, J. Cryst. Growth 216, 304, (2000).

[43] K. Mizuno, M. Izaki, K.Murase, T. Shinagawa, M. Chigane, M. Inaba, A. Tasaka, Y. Awakura, J. Electrochem. Soc. 152, C179, (2005).

[44] Y. Zhai, H. Fan, Q. Li, W. Yan, Appl. Surf. Sci. 258 (7), 3232–3236, (2012).

[45] Z. G. Chen, Y. W. Tang, Z. J. Jia, L. S. Zhang, J. L. Li, Y. Yu, J. Inorg. Mater. 20, 367, (2005).

[46] L. Mentar, Orient. J. Chem. 27(2), 477– 483, (2011).

[47] T. Pauporté, E. Jouanno, F. Pellé, B. Viana, P. Aschehoug, J. Phys. Chem. C. 113, 10422, (2009).

[48] F. Hu, K. C, Chan, T. M. Yue, Thin Solid Films 518 (1), 120–125, (2009).

[49] S. Laidoudi, A. Y. Bioud, A. Azizi, G. Schmerber, J. Bartringer, S. Barre, A. Dinia, Semicond. Sci. Technol. 28, 115005, (2013).

[50] J. T. Matsushima, L. C. D. Santos, A. B. Couto, M. R. Baldan, N. G. Ferreira, J. Electrochem. Soc. 159, D246, (2012).

[51] A. L. Daltin, F. Bohr, J. P. Chopart, Electrochim. Acta 54, 5813, (2009).

[52] S. Bijani, R. Schrebler, E. A. Dalchiele, M. Gabás, L. Martínez, J. R. Ramos-Barrado, J. Phys. Chem. C. 115, 21373, (2011).

[53] S. Singh, N. Kumar, M. Kumar, A. Agarwal, B. Mizaikoff, Chem. Eng. J. 313, 283–292, (2017).

[54] R. Kizil, J. Irudayaraj, K. Seetharaman, J. Agric. Food Chem. 50, 3912–3918, (2002).

[55] S. Kumar, A. K. Ojha, D. Bhorolua, J. Das, A. Kumar, Phys. B 558, 74–81, (2019).

[56] D. W. Nam, I. T. Cho, J. H. Lee, J. Vac. Sci. Technol. B 30, 060605, (2012).

[57] W. Septina, S. Ikedaa, M. A. Khana, T. Hirai, T. Harada, M. Matsumura, L. M. Peter, Electrochim. Acta 56, 4882, (2011).

[58] T. Ito, T. Masumi, J. Phys. Soc. Jpn. 66, 2185–2193, (1997).

[59] W. L. Yu, Y. Z. Lin, X. W. Zhu, Z. G. Hu, M. J. Han, S. S. Cai, L. L. Chen, H. H. Shao, J. Appl. Phys. 117, 045701, (2015).

[60] T. Wang, X. L. Wang, Y. Lu, Q. Xiong, X. Zhao, J. Cai, S. Huang, C. Gu, J. Tu, RSC Adv. 4, 322–330, (2014).

[61] B. Toboonsung, P. Singjai, J. Alloys Compd. 509(10), 4132–4137, (2011).

Chapter IV

Ab initio computational study of fundamental properties of CuO and Cu_2O compounds

IV.1 Introduction

In this chapter, we have investigated some physical properties such as structural, electronic, and optical properties of CuO and Cu_2O compounds using the fist principal calculation based on the density fonctionnelle theory within pseudopotential and plane wave method as implemented in the package CASTEP code "Cambridge Serial Total Energy Package" [1]. Our study continents two principal's parts. The first one concerns the structural, electronic, and optical properties of CuO compound and the second part is about the structural, electronic, and optical properties of Cu_2O material.

Using the state-of-the-art pseudo-potential plane wave method (PP-PW), in the formalism of the density functional theory (DFT), to describe the electronic structure of materials. To fully and take advantage of these properties for eventual technological applications, this allows researchers to investigate a wide range of properties, including but not limited to crystal structures, electronic densities, band structures energies and optical parameters [2].

Our studied compounds CuO and Cu_2O have attracted significant interest in various fields due to their specifics properties such as electrical conductivity, catalytic activity and optical properties. Researchers study these materials for applications in microelectronics, solar cells and catalysis. By means a computational method like first principles calculation based on the density functional theory (DFT) to investigate their structural, electronic, and optical properties for eventual technological and potential applications [3].

IV.2 Overview of the CASTEP program

CASTEP (Cambridge Serial Total Energy Package) is an ab-initio software package that utilizes density functional theory (DFT) [4–9], allowing the composition of materials involving their electronic, structure, and vibrational properties straight from first principles with no empirical parameters. With CASTEP, the electronic Schrödinger equation [10–19] is solved in the Kohn-Sham approximation of DFT [20, 21]. It has several functional types for the electron-exchange correlation energy: Local Density Approximation (LDA) [22, 23] and the Generalized Gradient Approximation (GGA) [24–26] allowing a trade-off between accuracy and computational efficiency. CASTEP employs a plane-wave basis set to represent the electronic wavefunctions, which are ideal for computing periodic systems. Pseudopotentials are adopted to treat the electron-ion interactions, meaning that the calculations do not involve explicitly dealing with the core electrons [27–33].

With this combination of methods, CASTEP has grown into one of the most widely employed software packages that accurately predict fundamental material properties in disciplines such as physics, chemistry, and materials science.

IV.2.1 Main CASTEP features

Electronic structure

- Electronic band calculation.
- Density of states (DOS).
- Band diagrams and orbital analysis.

Optical and dielectric properties

- Absorption spectra and reflectivity.
- Dielectric function and refractive index.
- Non-linear optical response.

Vibrational and thermodynamic properties

- Phonon calculations (Raman spectrum, IR).
- Phonon dispersion and dynamic stability.
- Calculation of Gibbs free energy.

Molecular dynamics and structure optimization

- Atomic relaxation and structure optimization.
- Temperature-controlled simulation (ab initio molecular dynamics).
- Phase transition studies.

Surface and adsorption studies

- Surface and interface energy.
- Adsorption of molecules on surfaces.
- Catalysis and corrosion studies.

IV.2.2 Advantages and disadvantages of CASTEP

Advantages

- Precise approach with plane waves and pseudopotentials.
- Compatible with Materials Studio (intuitive graphical interface).
- Wide range of calculations available.

Disadvantages

- Very demanding in terms of computing resources.
- Less efficient for disordered systems (isolated molecules, complex defects).

IV.2.3 CASTEP applications

- Semiconductors and electronic materials (Si, GaN, TiO_2, Cu_2O...).
- Photocatalysis and solar energy (conversion of light energy).
- Surface chemistry and catalysis.
- Nanomaterials and biosensors.

The previously mentioned studies that applied LDA or GGA in the calculations for Cu_2O underestimated the bandgap by around 0.5 eV– 0.7 eV [34]. This is largely due to the inherent autocorrelation of these functionals as well as the poorly defined Cu d-states. Hybrid functionals, such as HSE06, can then be used in place of the former, which provided a much better prediction in the gap at 2.0 eV [35]. Tajudeen et *al.* [36] applied CASTEP using GGA-PBE to find the electronic and optical properties of Cu_2O. They found that it was a 0.6 eV bandgap, promising as an optical material since they obtained good optical in the visible, which they thought could lead to solar cell applications. Ishaq et *al.* [37] had extensive study (structure, band, density of states, optical absorption) with CASTEP. They indicated that Cu d-states are highly localized, this is why they approached the problem with DFT+U, and hence the bandgap prediction was poor. Zhao et *al.* [38] showed that if you can tune the U in DFT+U and use CASTEP, the electronic structure of Cu_2O could be approximated to experimental band gaps.

Ibrahim et *al.* [39] consider CuO using CASTEP, both with and without GGA and DFT+U. They reported that with U = 8 eV, the gap is 1.4 eV, consistent with experimental measurements. Jeyalakshmi et *al.* [40] investigated the electronic structure, mechanical, and optical properties of CuO, again with CASTEP. They reported a gap of 1.3 eV using GGA+U and interesting semiconducting properties for sensors. Musa et *al.* [41] used CASTEP to study the properties of CuO with added dopants (Zn, Ni) and without dopants. They noted that the density of states and absorption changes in the UV-visible regions with doping; demonstrating the utility of the CASTEP study for modelling modified materials.

IV.3 Computational details

About the structural properties of both considered CuO and Cu_2O phases, we employed the CASTEP software, which is based on density functional theory. This software enabled us to analyze the arrangement of atoms within their cubic crystal lattices (where all edges are of equal length and 90° angles). This is reflected by the $Pn\bar{3}m$ space group, which defines the atomic positions.

To calculate the electronic structures within the CASTEP code, we employ a (8 × 8 × 8) k-point sampling scheme with a 750 eV plane-wave cut-off energy, balancing accuracy and computational efficiency for both compounds. Then, we use the well-established Perdew-Burke-Ernzerhof (PBE) functional for the Generalized Gradient Approximation (GGA) as exchange and correlation terms. This consistent selection of space group, k-point sampling, plane-wave cut-off energy and the approximation (PBE-GGA) establishes a robust CASTEP framework for analyzing the structural properties of both CuO and Cu_2O materials, confirming reliable and comparable results for these closely related materials.

IV.4 Structural, electronic and optical properties of CuO material

IV.4.1 Structural properties

Geometric optimization in CASTEP simulations is a method that enables researchers to identify stable and energetically favorable atomic configurations of materials. To attain the optimal convergence for both computed structures and energies necessitate the calculation of total energy as a function of K-points and cut-off energy.

IV.4.1.1 Total energy as a function of k-points and cut-off Energy

In the field of materials science and computational physics, "k-points" refer to the points in reciprocal space that are sampled during calculations using periodic boundary conditions. These "k-points" are a key aspect of the Brillouin zone sampling technique, which is used to describe the electronic structure of materials.

In geometry optimization with BFGS algorithm, the term "cut-off" signifies the maximum distance beyond which interactions between atoms are supposed to be negligible and are excluded from the calculation. This parameter serves to regulate the computational cost associated with the optimization process by confining the scope of interactions that necessitate consideration during the calculation process.

Both compounds exhibited Pn̄3m space groups. Figure IV.1 depicts the total energy with different values of k-points mesh and with a cut-off energy about 750 eV. Following the computations, we determined that employing a (8 × 8 × 8) Brillouin zone k-point is suitable for our calculation.

Figure IV.2 displays the total energy with different values of cut-off energies for CuO compounded, which is stable and suitability for our analysis.

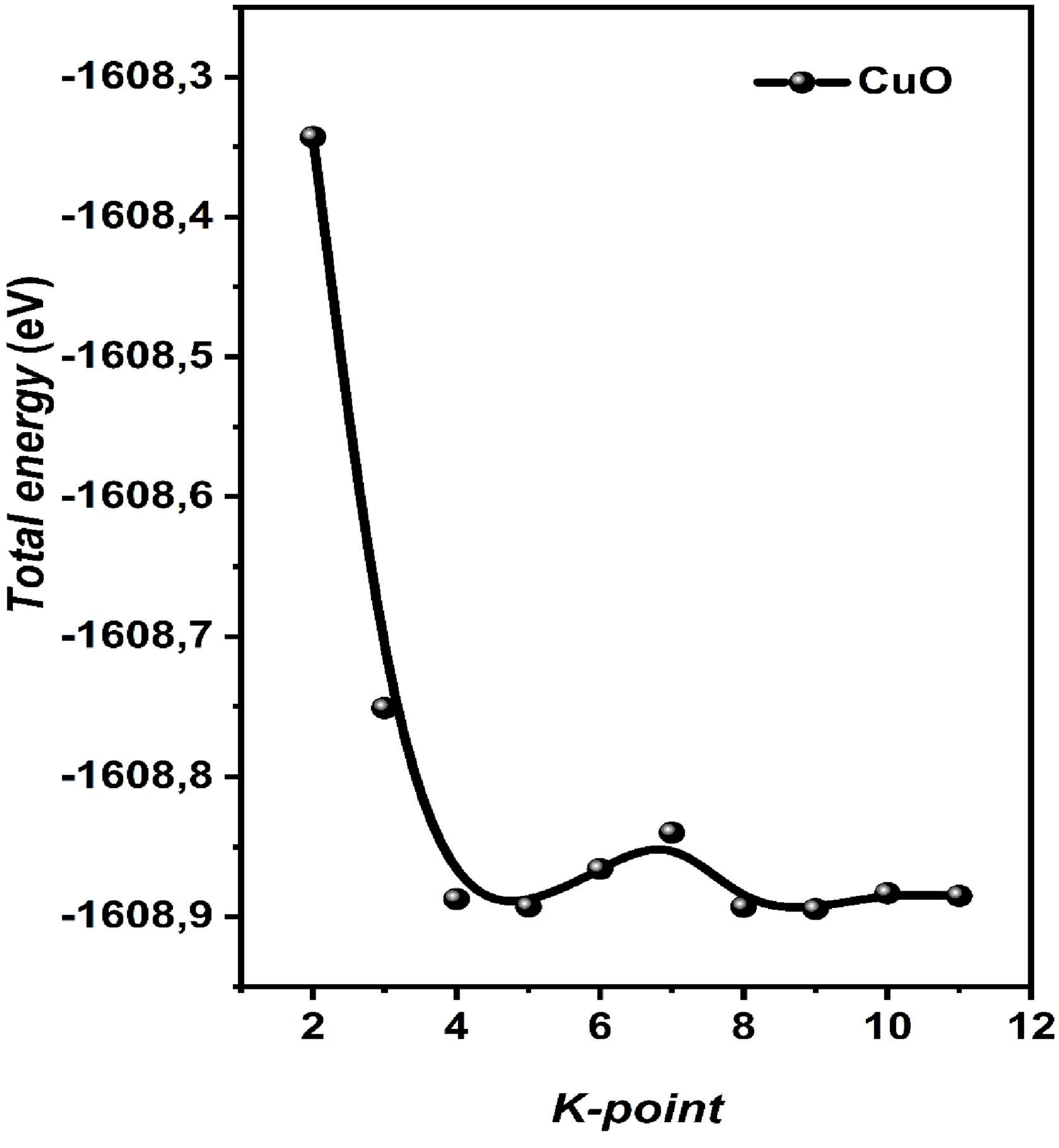

Figure IV.1: Total energy versus K-points for CuO material.

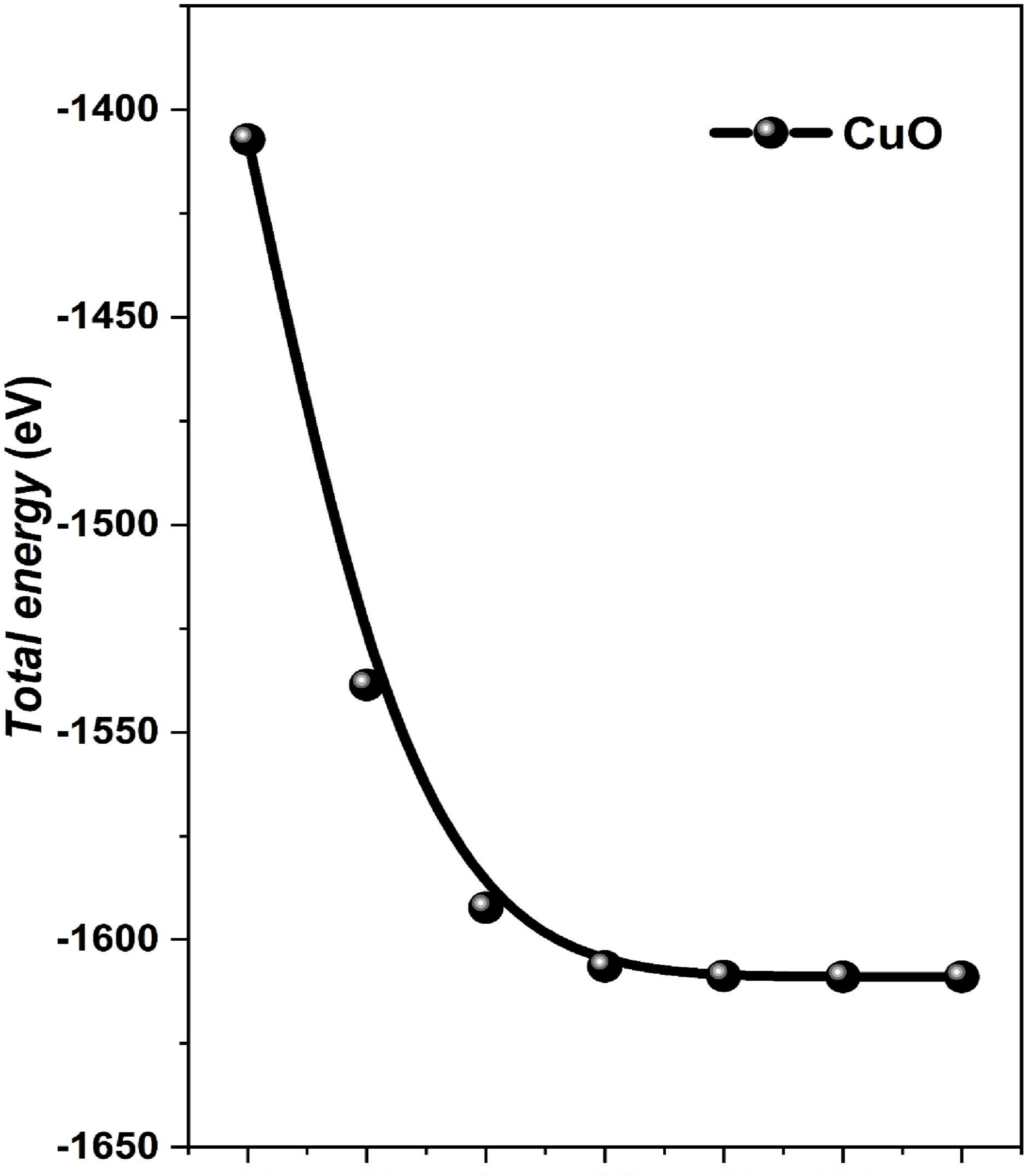

Figure IV.2: Total energy versus cut-off energy for CuO material.

IV.4.1.2 Total energy as a function of volume

Figure VI.3 displays the total energy versus volume of the unit cell that is an important tool for understanding the structural and energetic properties of materials.

In our case, we have obtained the total energy versus volume curve by changing the volume of the CuO unit cell and calculating the total energy for each volume. The energy versus volume curve typically exhibits a distinct peak representing the optimal unit cell volume for the system, where the total energy is at its minimum level.

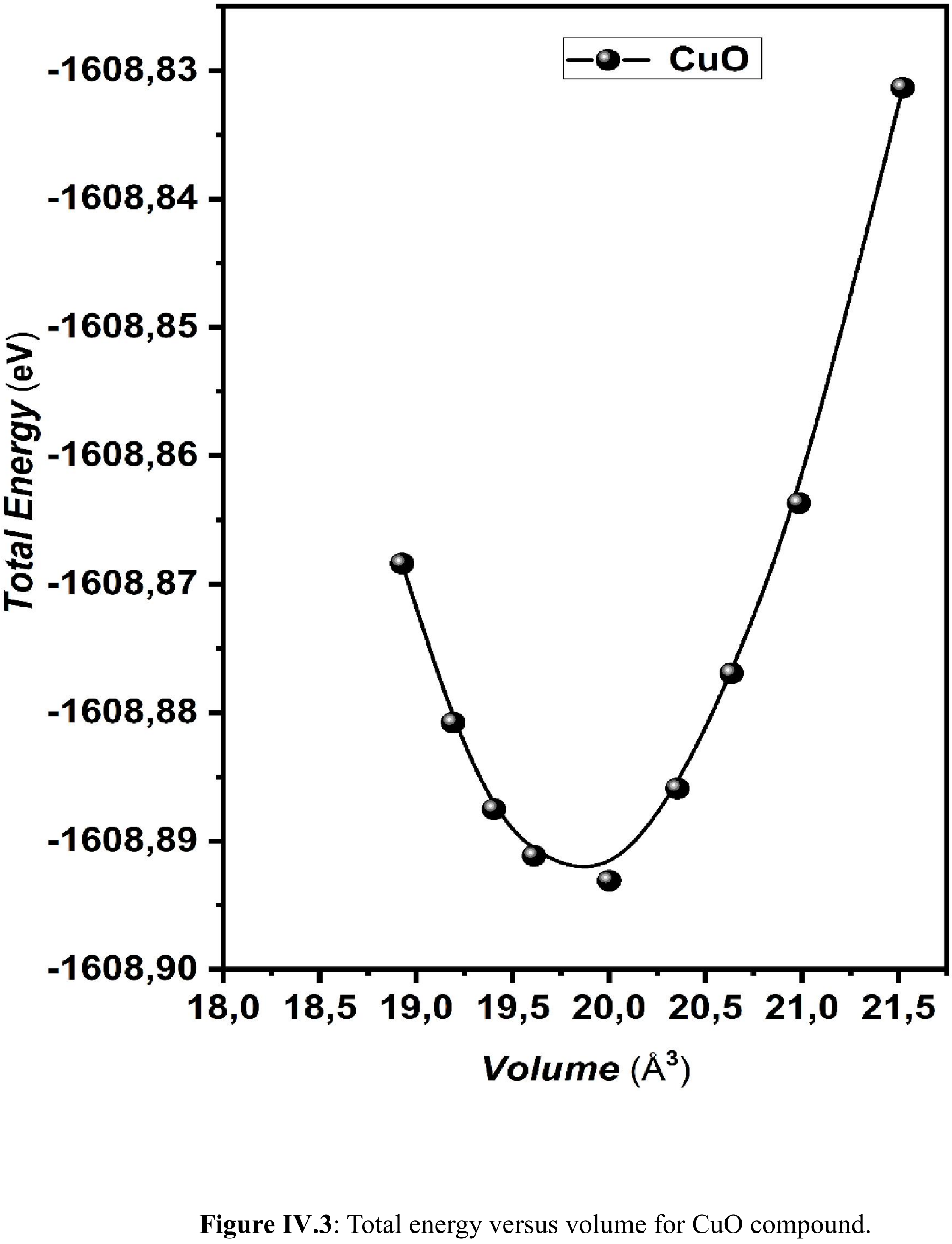

Figure IV.3: Total energy versus volume for CuO compound.

IV.4.1.3 Lattice parameters calculation of CuO material using CASTEP

Using the Local Density Approximation (LDA) method for the exchange and correlation term within the Perdew-Burke-Ernzerhof (PBE) approach. We have employed the cubic crystal structure, and the primitive lattice one representation is a face-centered cubic (FCC) and the arrangement of atoms in CuO compounds are shown in Figure IV.4. The lattice constant, the volume and the bulk modulus calculated value are mentioned in Table IV.1.

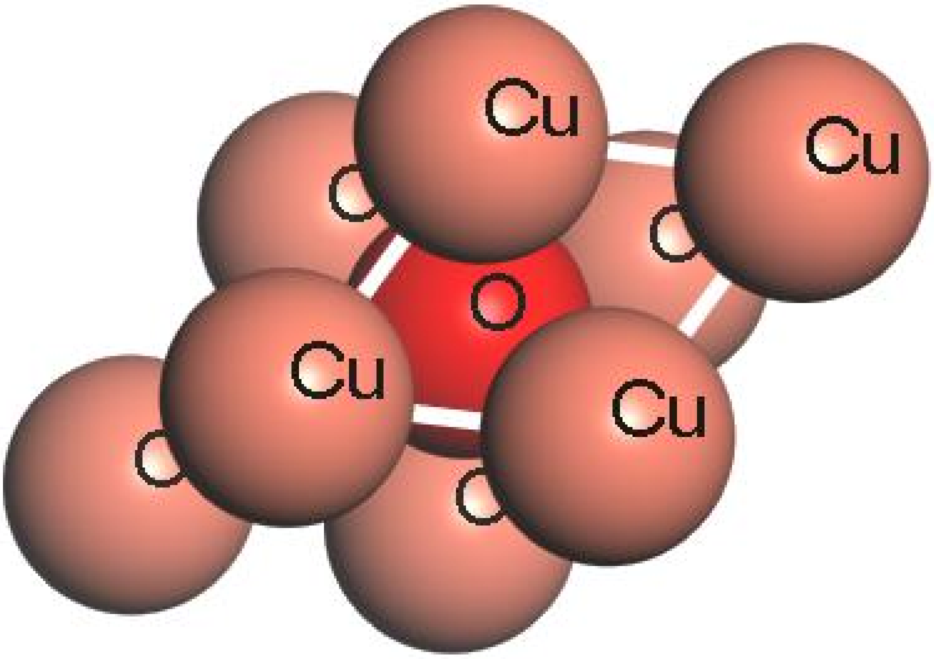

Figure IV.4: Arrangement of atoms in CuO compound: crystal structure.

Table IV.1: Lattice constant, volume, bulk modulus calculated of CuO compound.

Compound	***a = b = c (Å)***	***α = β = γ (°)***	**Volume (Å3)**	**Bulk Modulus (GPA)**
CuO	3.04712	90.0000	20.0057	158.214

IV.4.2 Electronic properties

IV.4.2.1 Band gap energy

Electronic properties, especially the energy gap that plays an essential role for the comprehension of bonding character, electronic conductivity, optical responses and the compound's character, will be conductor, semiconductor or insulator. Notably, the energy gap's influence extends to optical attributes governing the material's photovoltaic behaviors.

As shown in Figure IV.5, the CuO compound has conductor behaviors. At ambient temperature of 300K, the available experimental results confirmed that there is an indirect band gap of up to 1.5 eV, but these results occurred due to temperature changes and improvements to the calculations. We stress that the LDA approximation underestimates the band gap energy value.

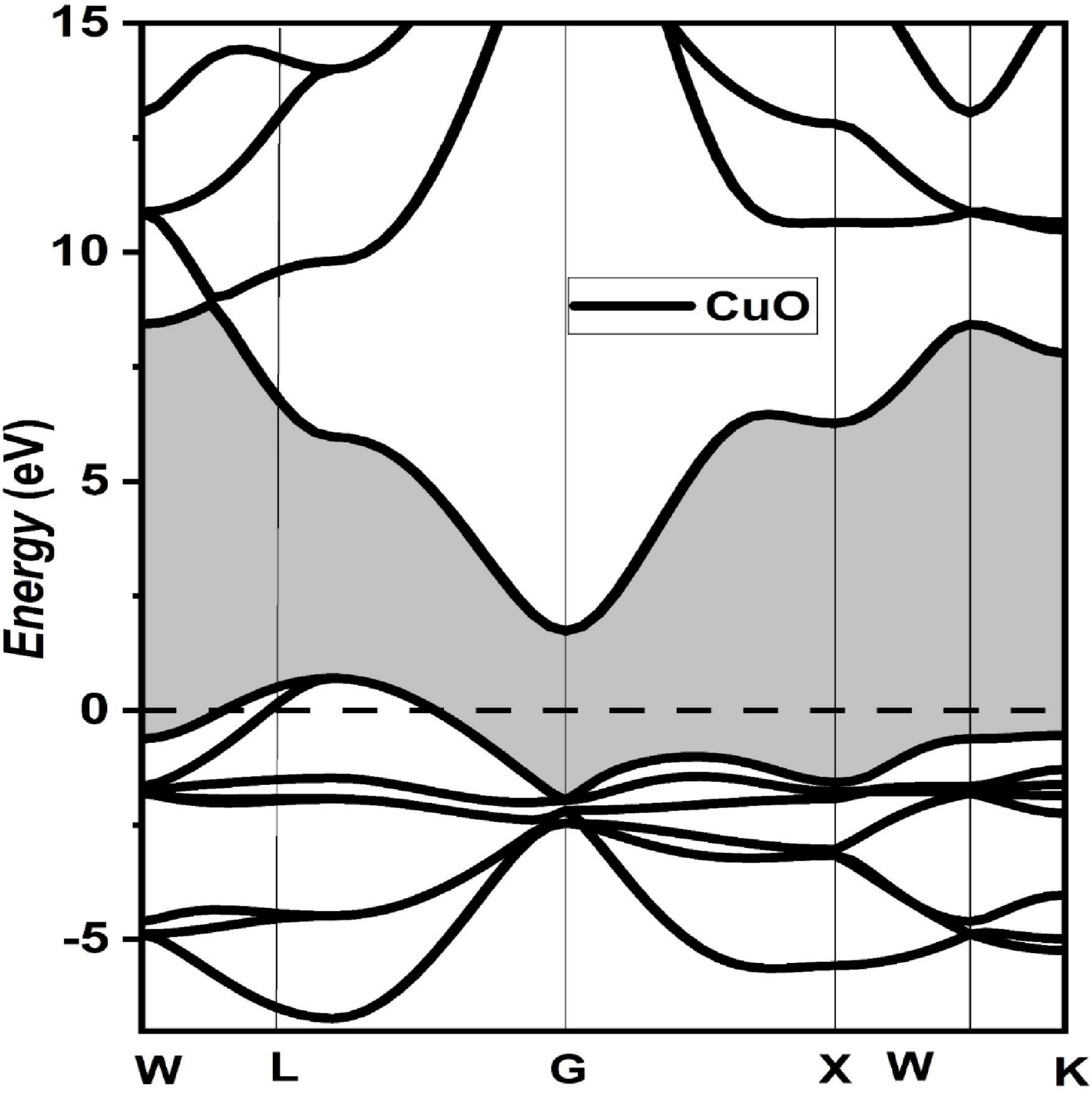

Figure IV.5: Calculated band structure for CuO compound.

IV.4.2.2 Total and partial densities of states (TDOS and PDOS)

The density of states (DOS) represents the electronic states distribution of in a material with respect to their energy levels. It provides information about the electronic structure of the material, including the number of available electronic states at different energy levels. In addition, TDOS represents also the total number of electronic states available at different energy levels in a material. It provides an overall picture of the electronic structure of the material, showing the distribution of electronic states across the entire energy spectrum. Figure IV.6 displays the Total Density of States (TDOS) for CuO compound. On the other hand, the partial density of state PDOS breaks down the total density of states into contributions from individual atoms or atomic orbitals in the material. It provides information about the electronic states associated with specific atomic species or orbital types, allowing for a more detailed analysis of the material's electronic structure. Figure IV.7 displays the partial density of states (PDOS) spectra of our studied compound CuO.

From Figure IV.6, The TDOS results showed that there was a BV region that exceeded the Fermi level. In Figure IV.7, the BV regions are dominated by *Cu*-d and *O*-p states. The second region BC originates from the *O*-d states. Therefore, there is a strong hybridization between *O*-p state and *Cu*-d sate formed the responsible energycal band on the conduction phenomenon in the studied compounded CuO.

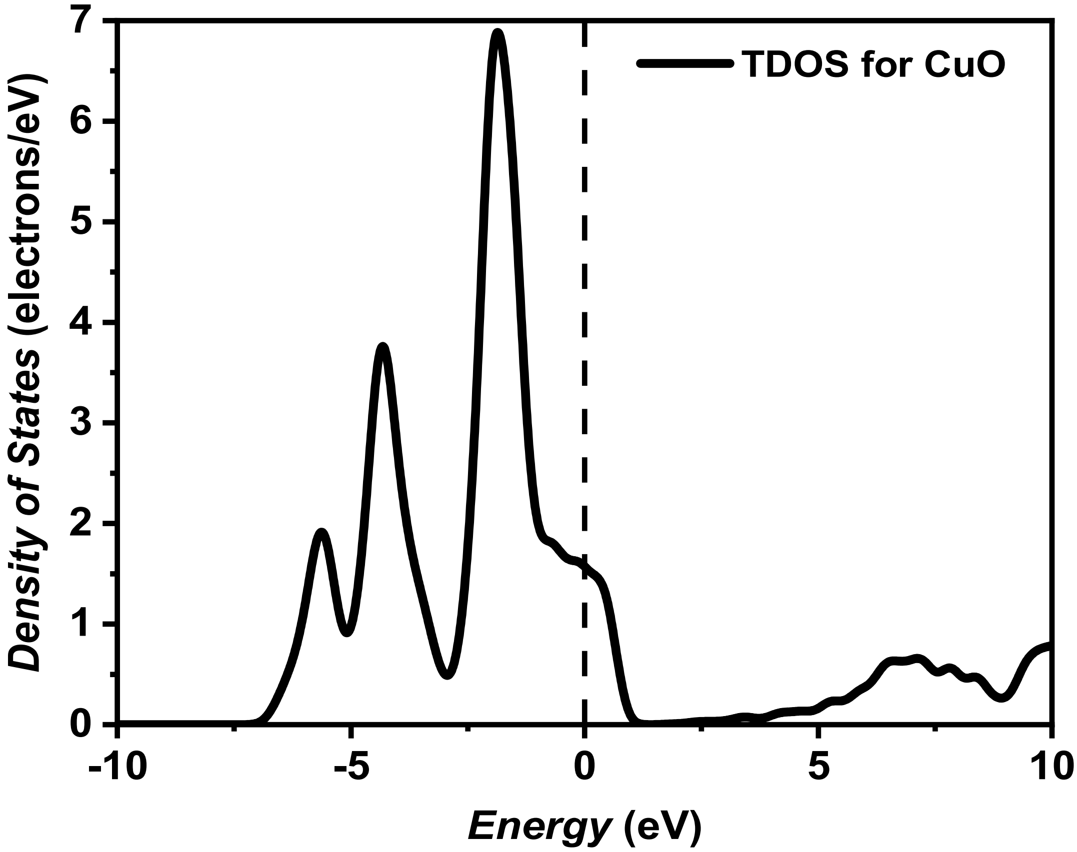

Figure. IV.6: Total Density of States for CuO compound.

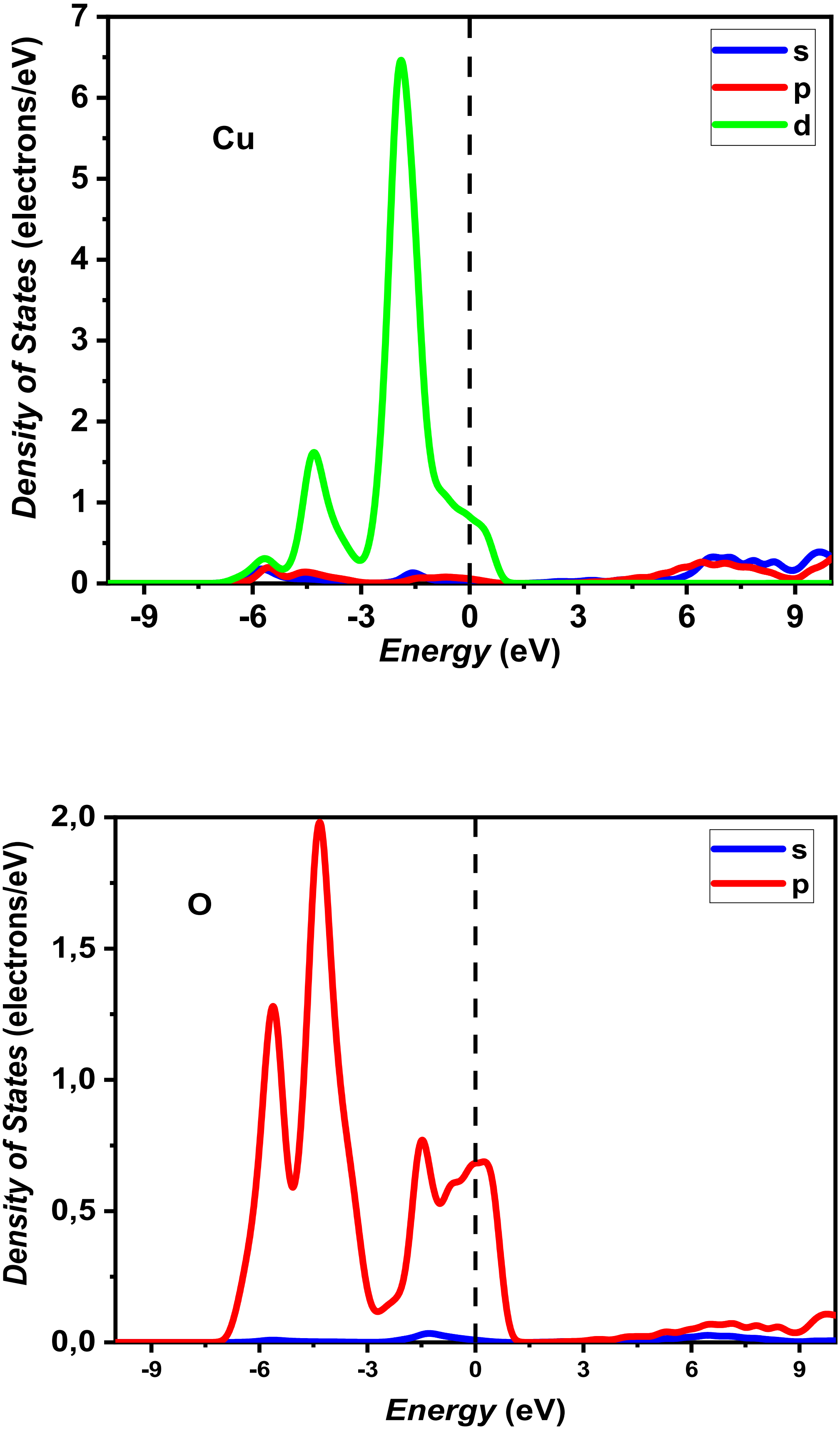

Figure IV.7: PDOS spectra calculated for CuO compound.

IV.4.3 Optical properties

The optical properties of CuO parameters such as the optical absorption, the refractive index, and the reflectivity spectrum are important for understanding how the material interacts with light. Here is a brief overview of each:

IV.4.3.1 Absorption spectrum

The absorption spectrum of CuO material describes how the material absorbs light at different wavelengths. It provides information about the energy levels of electrons in the material and their electronic transitions. By measuring the absorption spectrum, one can identify the energy of electronic transitions and determine factors such as band gaps and excitant energies. Figure IV.8 displays the absorption spectra calculated for CuO material in the range of wavelengths 0 to 1000 nm.

In our calculated spectrum, the CuO compound has been found to exhibit a high absorption in the ultraviolet regions, with values reaching up to 350000 × 10^4 cm^{-1} (Figure IV.8). As results, the absorption properties of CuO compounds researchers can design materials with specific absorption properties for eventual optoelectronic applications.

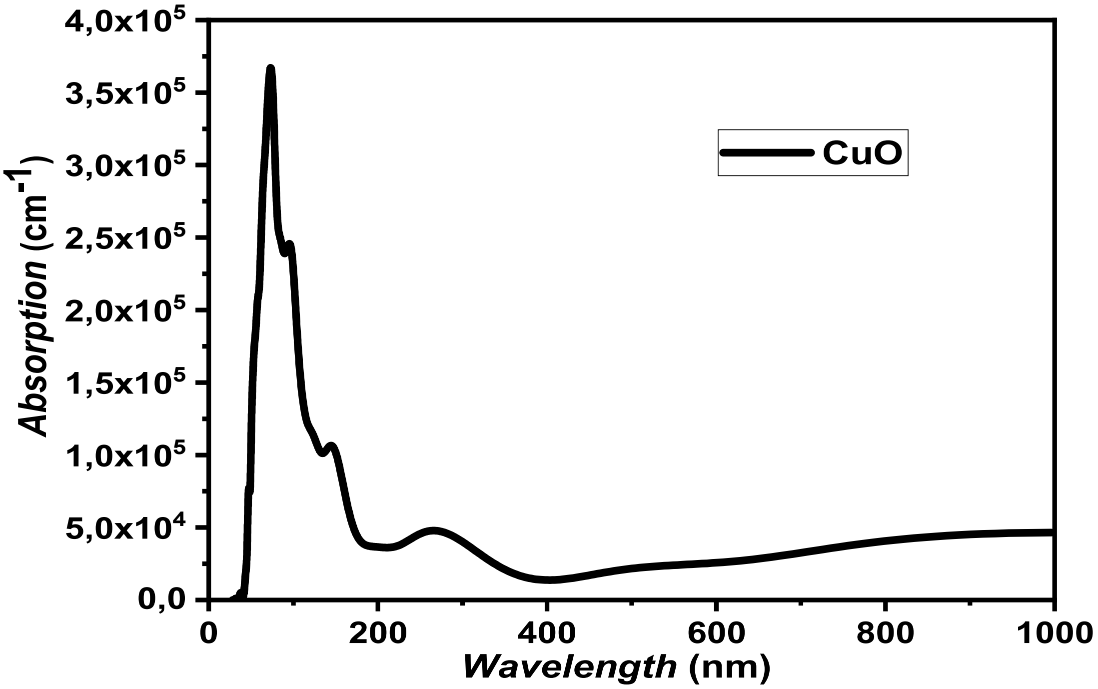

Figure IV.8: Absorption spectra calculated for CuO compound.

VI.4.3.2 Refractive Index

The refractive index of CuO compound indicates how much light is refracted, as it passes through a material. It is determined as the ratio of the speed of light in a vacuum to the speed of light in a material. The refractive index is related to the material's electronic and structural properties and affects phenomena such as reflection and transmission of light at interfaces. Figure IV.9 illustrates the calculated refractive index n and K for CuO compound.

From Figure VI.9, CuO material has high refractive indices in the ultraviolet regions, respectively, with values reaching up to 5 at high wavelength.

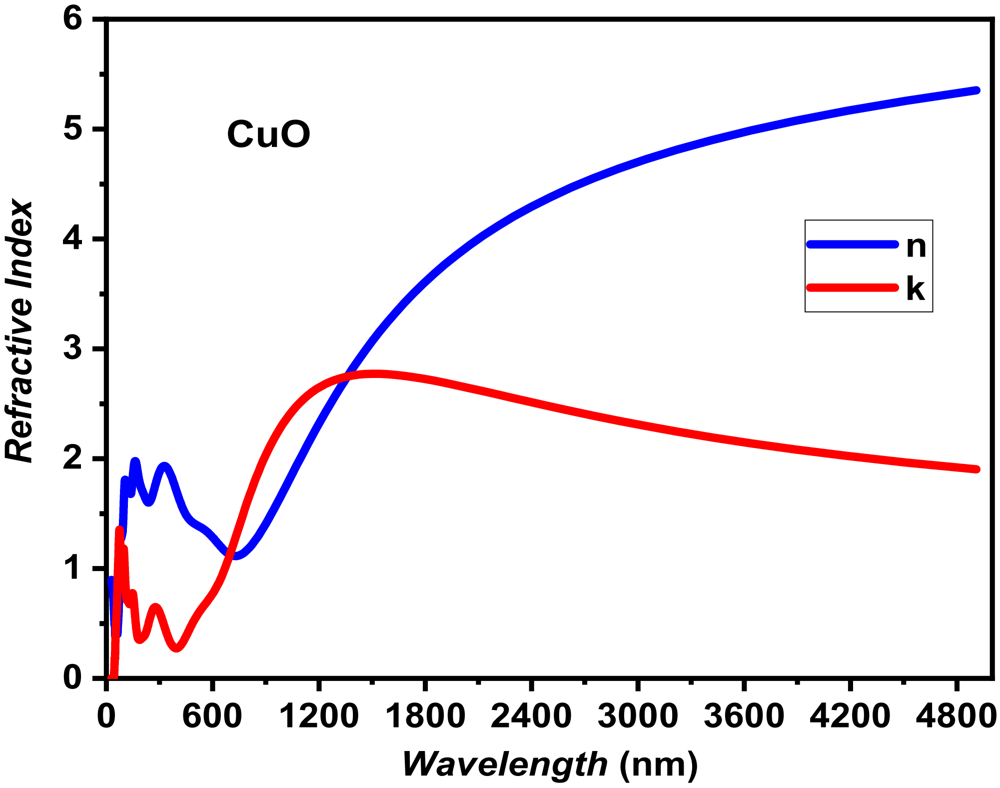

Figure IV.9: Refractive index n and K calculated for CuO compound.

IV.4.3.3 Optical reflectivity

Reflectivity is an optical parameter, which describes how much light is reflected from the surface of a material at different wavelengths. This parameter is influenced by many factors such as the material's composition, surface roughness and the angle of incidence of light. The optical reflectivity spectrum can provide visions into the optical properties of CuO material and its eventual applications in areas such as photovoltaic, optical coatings and sensors. Figure IV.10 presents the reflectivity (R) spectra calculated for CuO material.

Copper oxide CuO compound reveals a strong reflective nature, particularly in the ultraviolet range of the light spectrum. In fact, its reflectivity can reach up to 40%. This knowledge of CuO reflective properties permits researchers to develop materials with tailored optical characteristics, this makes them in very important place for an eventual technological application in optoelectronics (Figure IV.10).

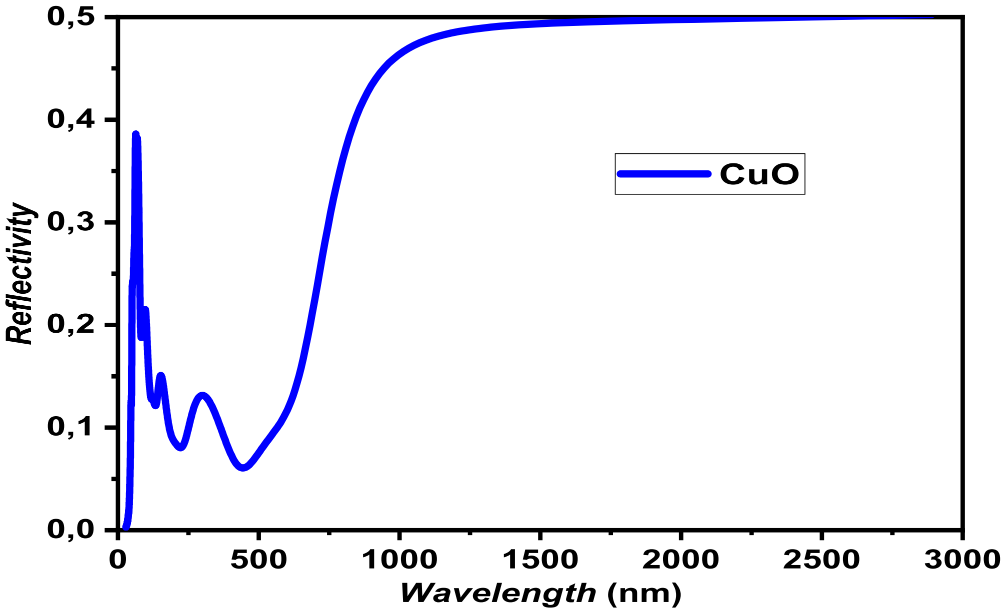

Figure IV.10: calculated reflectivity (R) spectrum for CuO material.

IV.5 Structural, electronic and optical properties of Cu_2O material

IV.5.1 Structural properties

Cu_2O material, well known as cuprous oxide, is a compound that contains a copper (Cu) and an oxygen (O). Then it has a simple crystalline structure (P), with each copper atom surrounded by four oxygen atoms formed a tetrahedral configuration.

IV.5.1.1 Total energy as a function of k-points and cut-off Energy

The studied Cu_2O presented a cubic structure with a $Pn\bar{3}m1$ space groups. Subsequent the computations, we have chosen employing with an (8 × 8 × 8) Brillouin zone k-point. Figure IV.11 shows the total energy with different values of k-points mesh and fixed the cut-off energy about 800 eV.

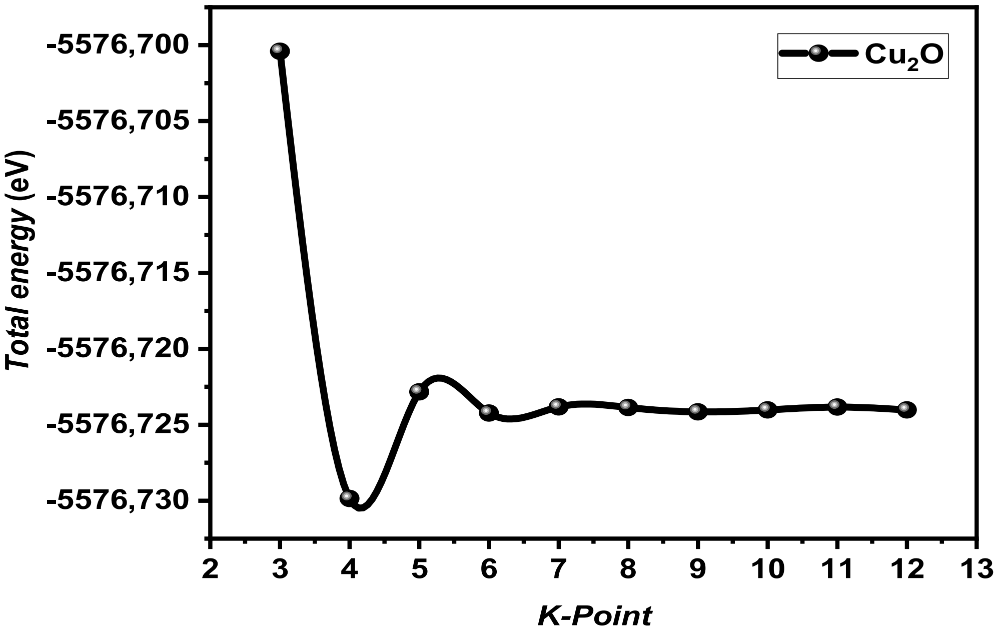

Figure IV.11: Total energy versus K-points for Cu_2O material.

Figure IV.12 displays the total energy versus different values of cut-off energies for Cu_2O, which resulted in stability and suitability for our computation processing.

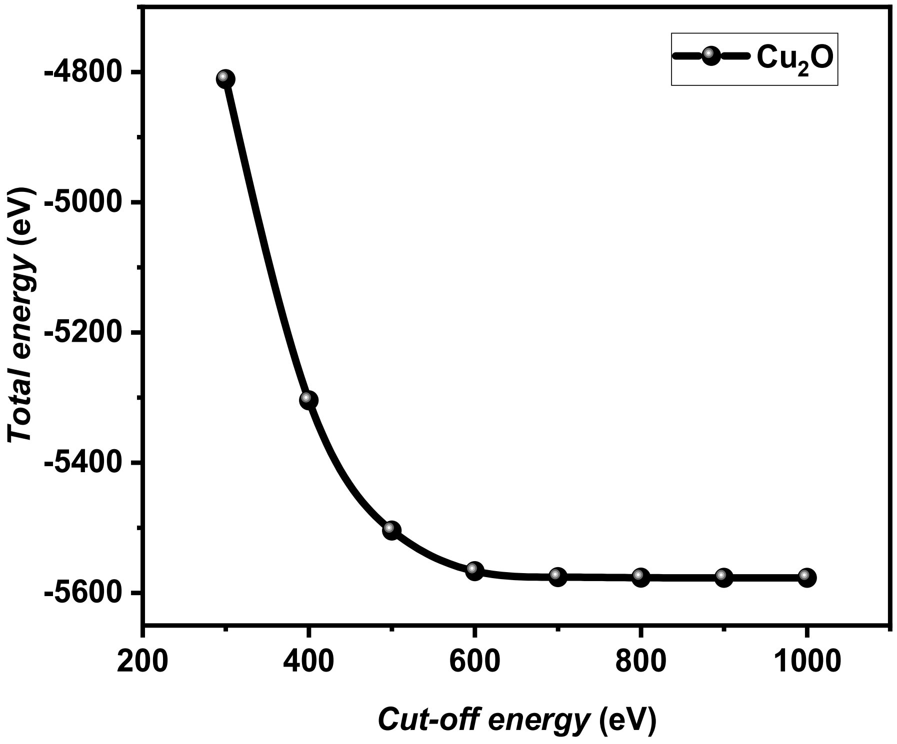

Figure IV.12: Total energy versus cut-off energy for Cu_2O material.

IV.5.1.2 Total energy versus volume

Figure IV.13 displays the total energy of Cu_2O material as a function of its volume. The curve has a minimum point, which is the equilibrium volume V_0 of this material. That represents which the substance is most stable. At the equilibrium volume, the forces that are acting on the substance are balanced.

If the volume of the substance is less than V_0, the substance dilates because the forces that are pushing the atoms apart are stronger than the powers that are pulling them together.

If the volume of the substance is greater than the equilibrium volume, the substance will contract. This is because the forces that are pulling the atoms together are stronger than the forces that are pushing them apart.

Energy versus volume permits us to predict the bulk modulus of a material, which is a measure of how much the volume of the material changes in the range of applied pressure.

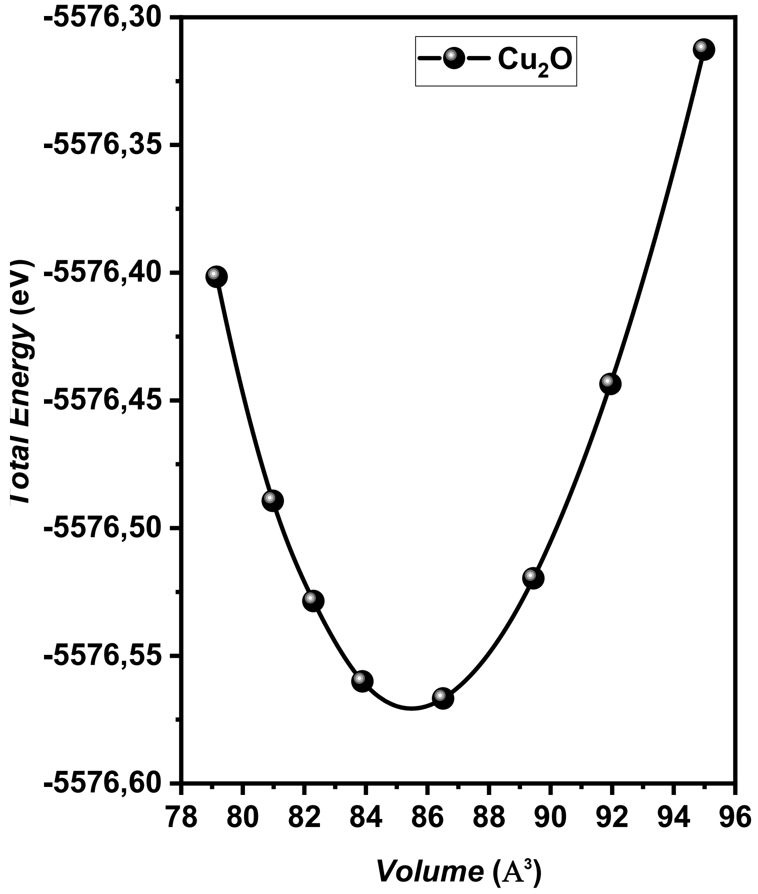

Figure IV.13: Total energy versus volume of Cu_2O compound.

IV.5.1.3 Lattice parameters calculation of Cu_2O using CASTEP

In Figure IV.14, we have represented the crystal structure of Cu_2O compound. The lattice parameter refers to the length of the edges of the cubic unit cell. Table IV.2 illustrates the lattice parameter, volume and bulk modulus calculated of Cu_2O compound E (V) curve using the *EOS* function (equation of state).

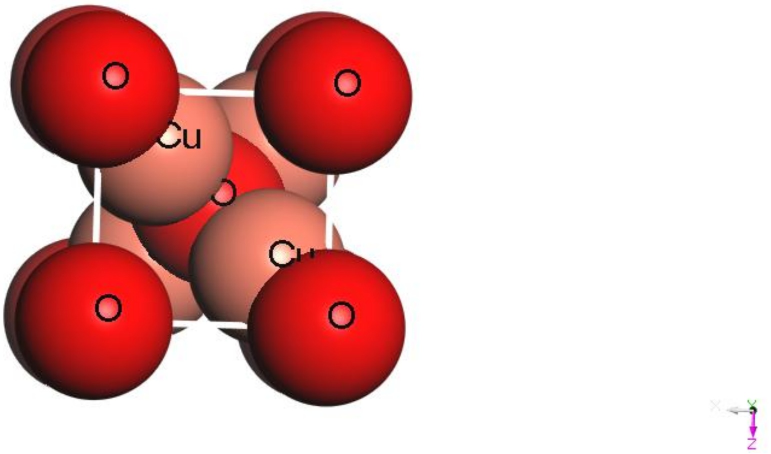

Figure IV.14: crystal structure of Cu_2O compound.

Table IV.2: Lattice constant, volume, bulk modulus calculated of Cu_2O compound.

Compound	$a = b = c$ (Å)	$\alpha = \beta = \gamma$ (°)	**Volume (Å^3)**	**Bulk Modulus (GPa)**
Cu_2O	4.4227	90.0000	86.5107	899.109

IV.5.2 Electronic properties

IV.5.2.1 Band gap energy

Figure IV.15 shows that the Cu_2O material is a semiconductor behavior with a narrow band gap of about 0.212 eV. This means that it takes very little energy to excite an electron from the valence band to the conduction band. As a result, Cu_2O has several interesting properties and potential applications such as follows.

- **High electrical conductivity**: With more free electrons to move in the conduction band, Cu_2O has more electronic conductivity than a semiconductor with a wide band gap.
- **Light absorption:** The small band gap allows Cu_2O to absorb infrared light. This makes it useful in infrared detectors and sensors technology.

- **Direct Band Gap:** Cu_2O is a direct band gap material, making it potential for high efficient solar cells application.

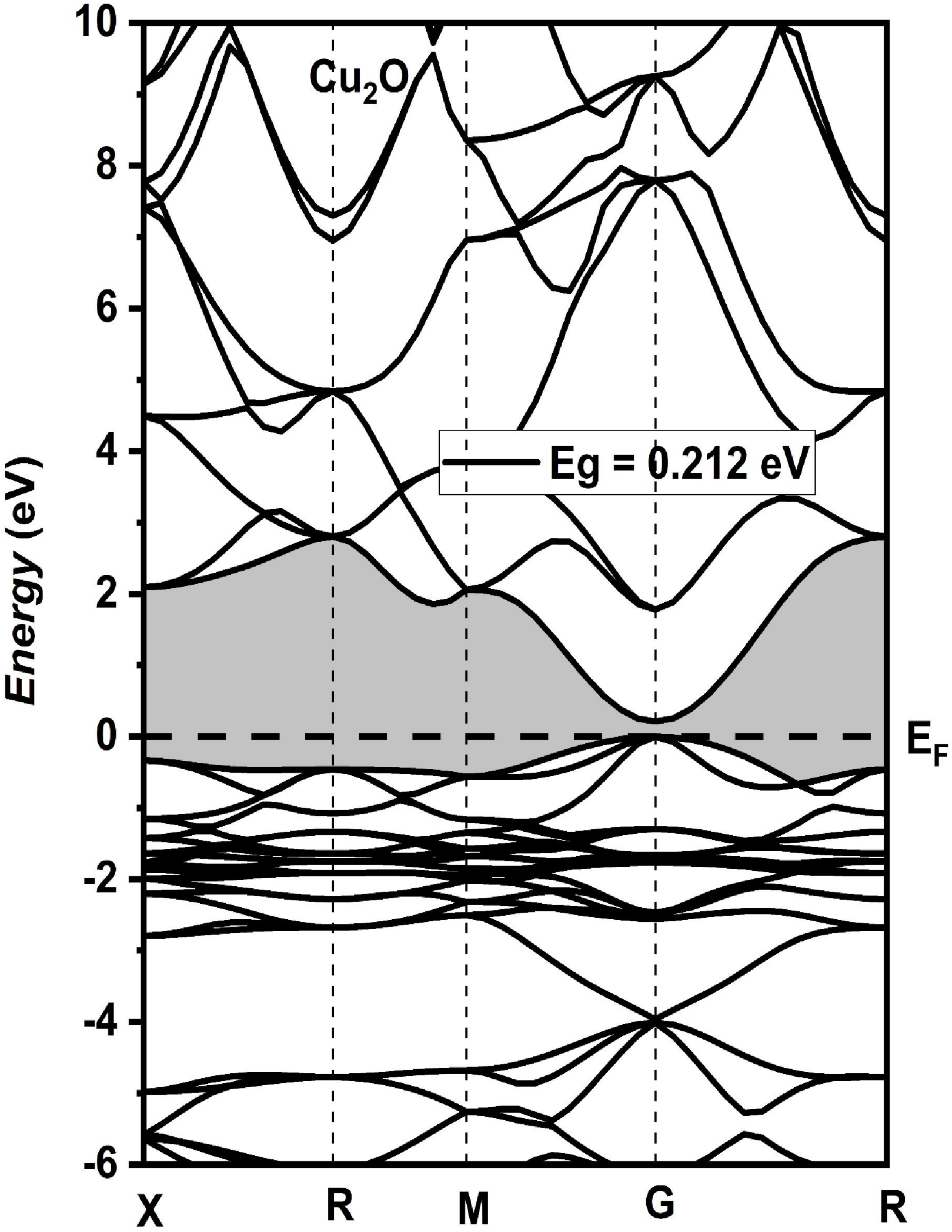

Figure IV.15: Calculated band structure of Cu_2O.

IV.5.2.2 Total and partial densities of states

In Figure IV.16, we have represented the TDOS that provides an overall picture of Cu_2O's electronic structure by showcasing the distribution of electronic states across the entire energy spectrum.

Contrasting the TDOS, the partial density of states (PDOS) breaks down the total number of states into contributions from individual atoms or atomic orbitals within Cu_2O. Figure IV.17 shows cases a more detailed analysis of Cu_2O's electronic structure using PDOS.

As shown in Figure IV.16, the DOS results indicate the presence of a valence band (BV) region do not exceeding the Fermi level. By analyzing Figure IV.17, we can further understand that Cu-d state and O-p state dominate in the formation of the BV region in Cu_2O.

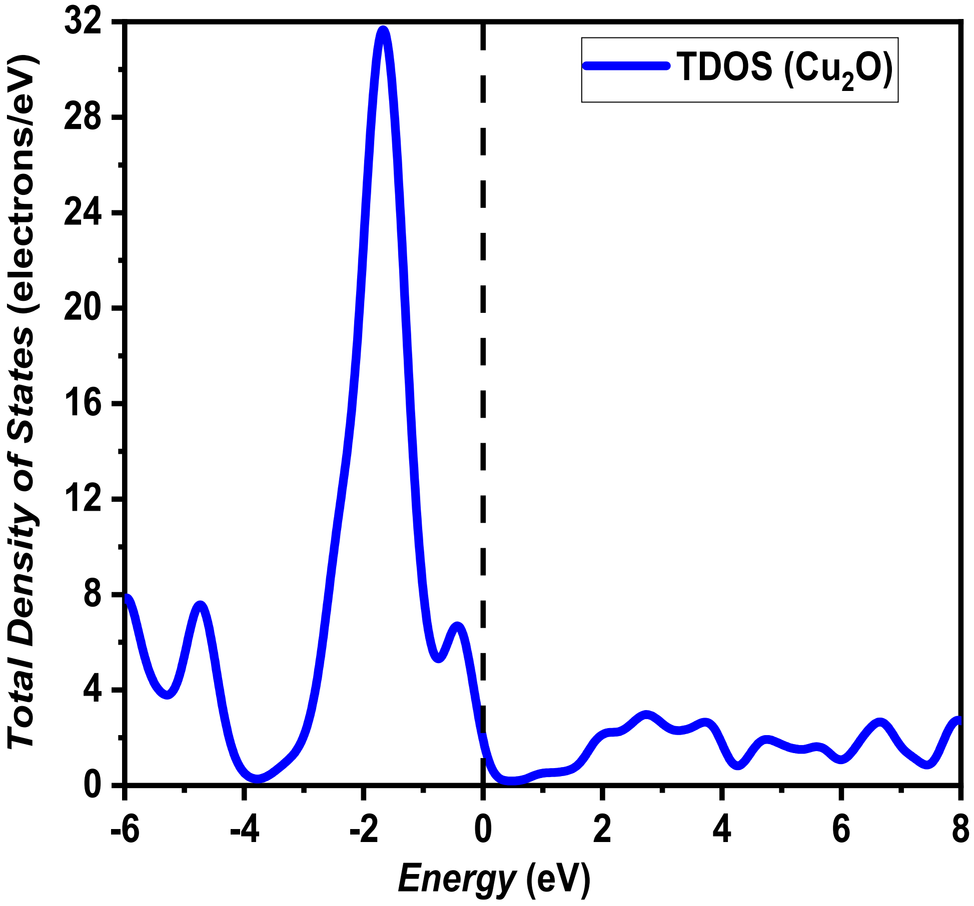

Figure IV.16: Total density of states for Cu_2O compound.

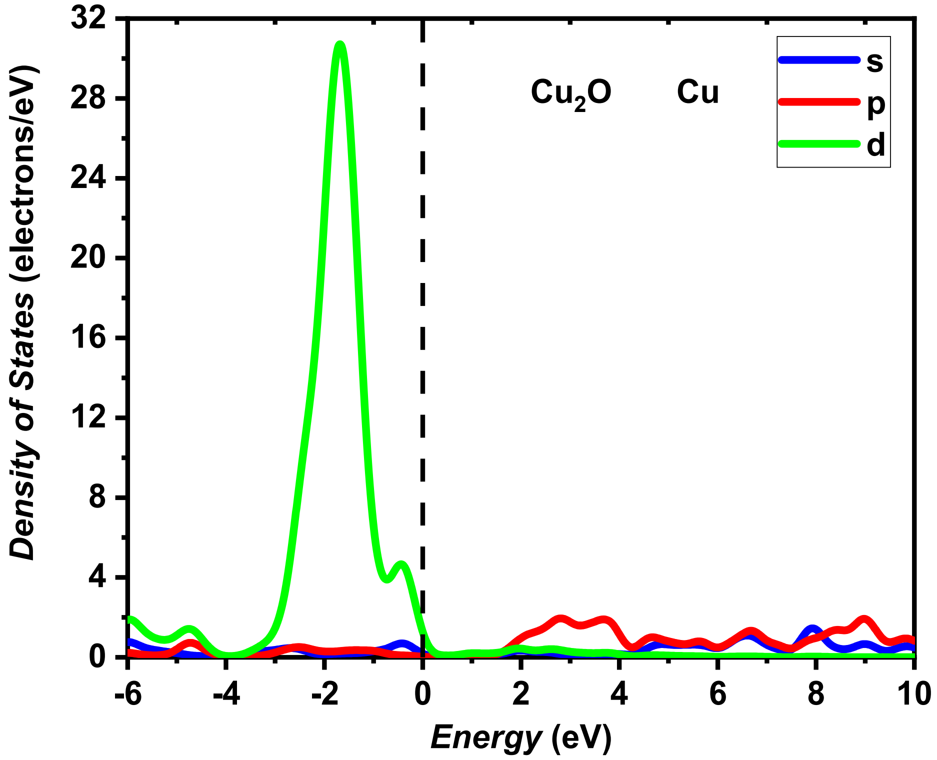

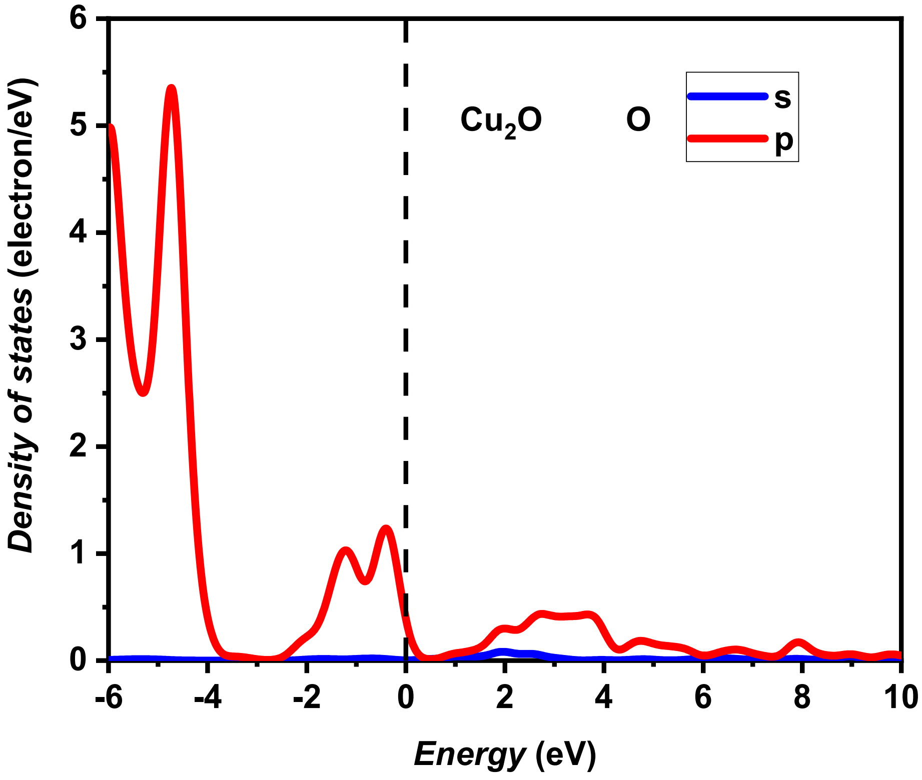

Figure IV.17: PDOS spectra calculated for Cu_2O compound.

IV.5.3 Optical properties

IV.5.3.1 Absorption spectrum

Figure IV.18 shows the absorption spectrum of Cu_2O as function as the wavelengths in the range from 0 to 1500 nm. The absorption coefficient indicates how strongly the material at a specific wavelength absorbs light, so a higher value indicates a stronger absorption.

The absorption coefficient of Cu_2O material is relatively low throughout most of the wavelength range. There seems to be a sharp increase in absorption coefficient around 200 nm. This indicates that Cu_2O material strongly absorbs light at wavelengths around 200 nm, this suggests it might be useful in ultraviolet (UV) filtering applications.

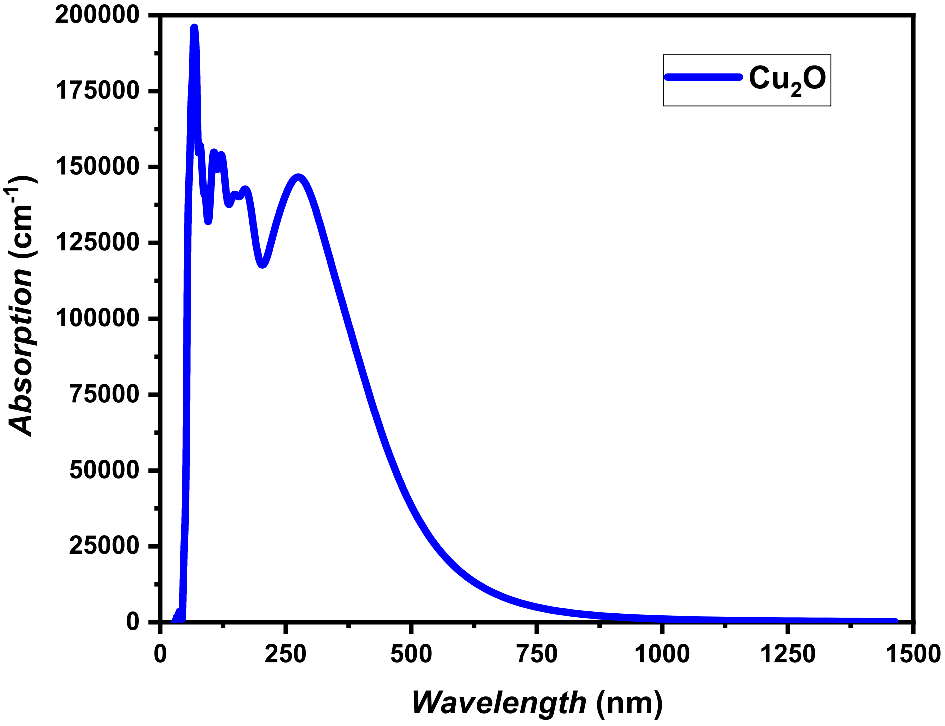

Figure IV.18: Calculated absorption spectrum for Cu_2O.

IV.5.3.2 Refractive Index

The refractive index *n* and extinction coefficient *k* spectra of Cu_2O are depicted in Figure IV.19. The blue curve represents the refractive index *n* of Cu_2O; it shows that the refractive index of Cu_2O decreases with increasing wavelength. This means that light bends less as the wavelength of light increases. The red curve represents the extinction coefficient *k* of Cu_2O; it shows that the extinction coefficient of Cu_2O increases with decreasing wavelength. This means that Cu_2O absorbs more light at shorter wavelengths. The refractive index of Cu_2O material is relatively high in the visible range of light from 400 to 700 nm; accordingly, the Cu_2O is a good reflector of visible light. The extinction coefficient of Cu_2O material is relatively low in the visible range of light, as a result, the Cu_2O is relatively transparent to visible light. The extinction coefficient of Cu_2O material increases abruptly in the ultraviolet (UV) range of light, below 400 nm, so the Cu_2O material is a good absorber in the UV light.

The optical properties of Cu_2O material make it a promising material for a variety of applications, including:

- **UV filters:** Cu_2O material can be used to block harmful UV radiation from reaching the skin.
- **Solar cells:** Cu_2O material can be used to absorb sunlight and convert it into electricity.
- **Sensors:** Cu_2O material can be used to detect changes in the environment, such as the presence of gases or chemicals.

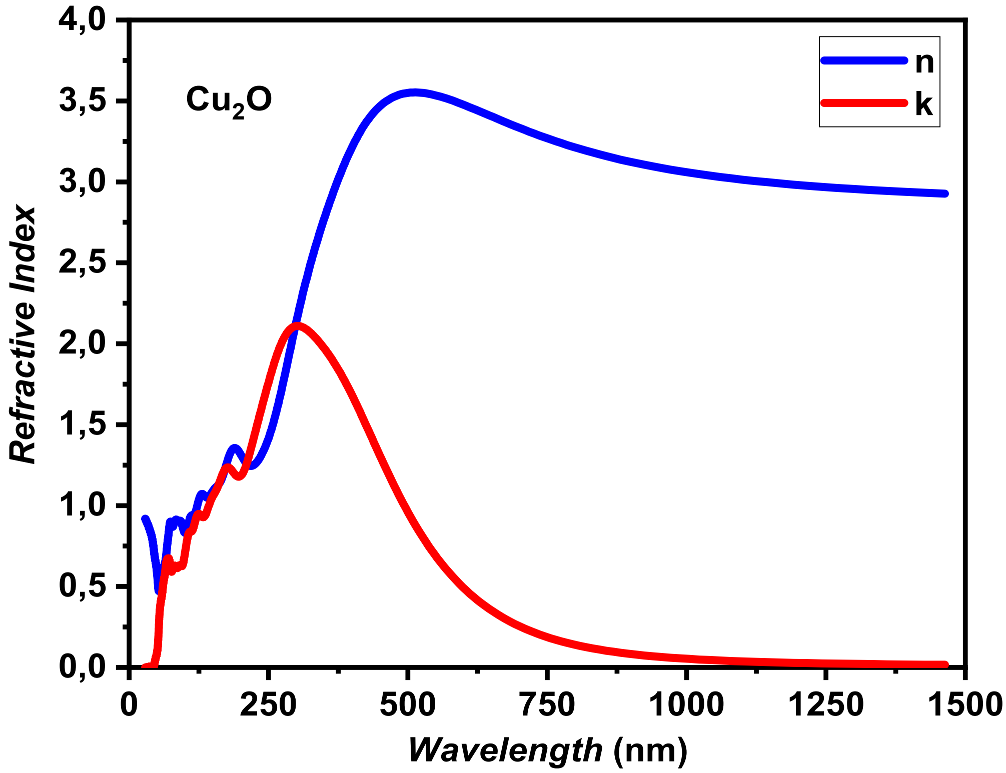

Figure IV.19: Refractive index *n* and *K* calculated for Cu_2O.

IV.5.3.3 Reflectivity spectrum

Figure IV.20 represents the reflectivity of the light for Cu_2O as function the wavelength. This optical parameter indicates how much of the incident light is reflected back by the material at a specific wavelength.

The reflectivity of the material is particularly high in the ultraviolet (UV) range of light, below 400 nm. This means that the material reflects a large amount of UV light. The reflectivity of the Cu_2O is relatively low in the visible range of light from 400 to 700 nm. This means that the Cu_2O reflects a relatively small amount of visible light. The reflectivity of the Cu_2O decreases again in the infrared range of light, above 700 nm. This means that the Cu_2O reflects a moderate amount of IR light.

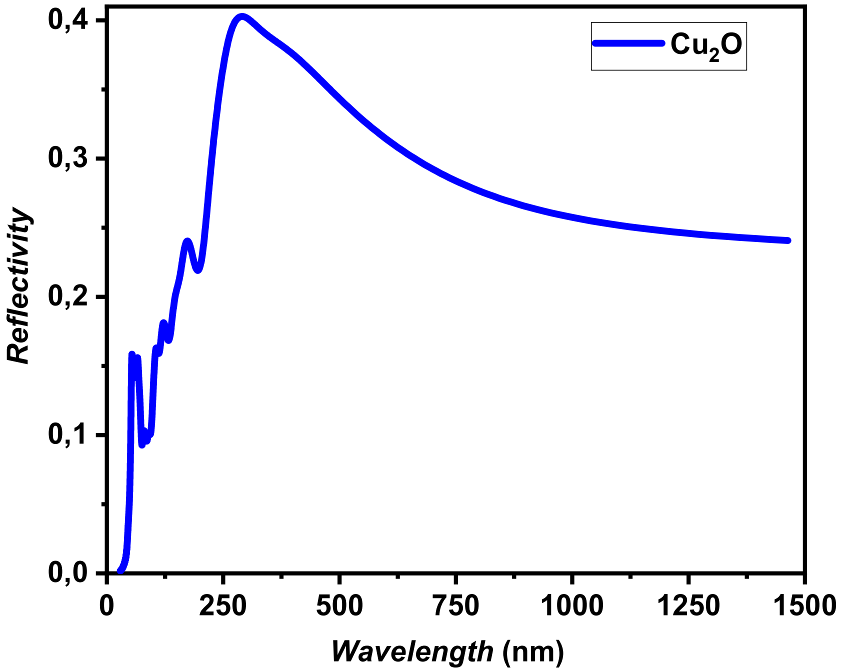

Figure IV.20: The calculated reflectivity *R* spectra for Cu_2O.

IV.6 Comparison between CuO and Cu_2O materials and potential applications

This study aims to provide a comprehensive understanding of the structural, electronic, and optical properties of CuO and Cu_2O materials using the CASTEP computational software. The results obtained were compared with theoretical and experimental data, and the potential applications of these compounds were discussed.

Copper(I) oxide (CuO) and copper (II) oxide (Cu_2O) materials are both compounds that can exhibit cubic crystal structures. However, they differ significantly in their physical and electronic properties.

a) Structural Properties

CuO:

- Lattice Parameters: $a = b = c = 3.04712$ Å
- Angles: $\alpha = \beta = \gamma = 90^\circ$
- Volume: 20.0057 $Å^3$
- Bulk Modulus: 158.21355 GPa

Cu_2O:

- Lattice Parameters: $a = b = c = 4.42273$ Å
- Angles: $\alpha = \beta = \gamma = 90°$
- Volume: 86.510711 $Å^3$
- Bulk Modulus: 899.10913 GPa

b) Electronic Properties

CuO:

- Bandgap: 0 eV
  - This indicates that CuO behaves as a metallic conductor in this context, allowing free movement of electrons between energy bands.

Cu_2O:

- Bandgap: Typically, around 0.212 eV
  - Cu_2O typically acts as a semiconductor, with a significant bandgap that restricts electron flow between the valence and conduction bands unless sufficient energy is provided.

c) Comparison of Physical Properties

- Lattice Parameters:
  - Cu_2O has significantly larger lattice parameters (4.42273 Å) compared to CuO (3.04712 Å), indicating a more extended crystal structure.
- Unit Cell Volume:
  - Volume of Cu_2O (86.510711 $Å^3$) is much larger than that of CuO (20.0057 $Å^3$).

- Bulk Modulus:
  - The bulk modulus of Cu_2O (899.10913 GPa) is substantially higher than that of CuO (158.21355 GPa), indicating that Cu_2O is much more resistant to compression.

IV.7 Conclusion

In summary, from this study of some physical properties of CuO and Cu_2O materials exhibit significant differences in their crystal structures, resistance to pressure, and electronic behavior.

Cubic CuO material, with an indirect bandgap of about 0 eV, behaves as a metallic conductor, making it suitable for applications requiring high electrical conductivity. In contrast, cubic Cu_2O material, with a typical direct semiconductor bandgap, is useful in electronic applications such as sensors or photovoltaic devices that rely on its semiconducting properties.

References

[1] M. D. Segall, P. J. D. Lindan, M. J. Probert, C. J. Pickard, P. J. Hasnip, S. J. Clark, M. C. Payne, J. Phys.: Condens. Matter 14, 2717, (2002).

[2] S. J. Clark, et al., J. Zeitschrift für kristallographie-crystalline materials 220(5–6), 567–570, (2005).

[3] M. Rahaman, D. Pradhan, D. Ghosh, S. Ghosh, Cupric oxide (CuO) nanoparticles as catalysts: A review. Nano-Structures & Nano-Objects 8, 111–123, (2016).

[4] R. G. Parr, Density functional theory, Annual Review of Physical Chemistry, 631–656, (1983).

[5] P. Giannozzi et al., Journal of physics: Condensed matter 21(39), 395502, (2009).

[6] X. Gonze et al., Computer Physics Communications 180(12), 2582–2615, (2009).

[7] G. Kresse, J. Furthmüller, Computational materials science 6(1), 15–50, (1996).

[8] P. Edwards, V. Kuznetsov, D. Slocombe, R. Vijayaraghavan, The electronic structure and properties of solids, J. Reedikj, K. Poeppelmeier, eds, Comprehensive Inorganic Chemistry II, Elsevier, (2013).

[9] M. B. Bever, Encyclopedia of materials science and engineering, Pergamon Press., Elmsford, NY (USA), (1985).

[10] E. Schrödinger, Quantisierung als eigenwertproblem, Annalen der physik, 385(13), 437–490, (1926).

[11] D. F. Schroeter, Introduction to quantum mechanics, Cambridge university press, England, (2016).

[12] D. A. McQuarrie, Quantum chemistry. University Science Books, California, USA, (2008).

[13] T. D. Rasmussen, P. Ren, J. W. Ponder, F. Jensen, International Journal of Quantum Chemistry 107(6), 1390–1395, (2007).

[14] C. J. Taylor et al., Chemical Reviews 123(6), 3089–3126, (2023).

[15] J. C. Poggendorff, E. Wiedemann, G. H. Wiedemann, Annalen der Physik. JA Barth, (1889).

[16] I. N. Levine, D. H. Busch, H. Shull, Quantum chemistry, Pearson Prentice Hall Upper Saddle River, NJ, (2009).

[17] D. J. Griffiths, D. F. Schroeter, Introduction to quantum mechanics, Cambridge University press, (2018).

[18] N. Zettili, Quantum mechanics: concepts and applications, Second edition, John Wiley & Sons Ltd, United Kingdom, (2009).

[19] P. A. M. Dirac, Proceedings of the Royal Society A 123(792), 714–733, (1929).

[20] P. Hohenberg, W. Kohn, Physical review 136, B864, (1964).

[21] W. Kohn, L. J. Sham, Physical review 140, A1133, (1965).

[22] J. P. Perdew, A. Zunger, Physical Review B 23(10), 5048, (1981).

[23] J. P. Perdew et al., Physical review letters 100(13), 136406, (2008).

[24] J. P. Perdew, K. Burke, M. Ernzerhof, Physical review letters 77(18), 3865, (1996).

[25] B. Hammer, L. B. Hansen, J. K. Nørskov, Physical review B 59(11), 7413, (1999).

[26] J. A. Steckel, D. Sholl, Density Functional Theory, John Wiley & Sons Ltd, Hoboken, (2009).

[27] F. Bloch, Zeitschrift für physic 52(7–8), 555–600, (1929).

[28] F. Bloch, Z. Phys 52, 555–600, (1928).

[29] H. J. Monkhorst, J. D. Pack, Physical review B 13(12), 5188, (1976).

[30] M. Methfessel, A. Paxton, Physical Review B 40(6), 3616, (1989).

[31] G. Kresse, J. Furthmüller, Physical review B 54(16), 11169, (1996).

[32] S. Baroni, S. De Gironcoli, A. Dal Corso, P. Giannozzi, Reviews of modern Physics 73 (2), 515, (2001).

[33] D. Vanderbilt, Physical review B 41(11), 7892, (1990).

[34] A. Soon et al., Phys. Rev. B 73, 165424, (2006).

[35] J. Paier et al., J. Chem. Phys. 124, 154709, (2006).

[36] A. M Tajudeen et al., J. Mater. Sci. Chem. Eng. 4, 34–42, (2016).

[37] A. Ishaq et al., Materials Today: Proceedings 33, 1523–1529, (2020).

[38] Z. Zhao et al., Physica B: Condensed Matter 508, 60–65, (2017).

[39] M. Ibrahim et al., Journal of Theoretical and Applied Physics 7, 15, (2013).

[40] R. Jeyalakshmi et al., Materials Research Express 5, 045901, (2018).

[41] H. A. Musa et al., Applied Physics A 127, 535, (2021).

Chapter V

Application of metallic oxide thin films in modern solar cell design

V.1 Introduction

Significant efforts have been made to design efficient optoelectronic devices. ZnO/Cu_2O and/or ZnO/CuO junctions have been considered very promising candidates in this regard. These junctions exhibit an atomic arrangement and conduction band alignment at the p-n interface, creating a favorable structure for the transport of electric charges [1]. The current efficiency of ZnO/Cu_2O heterojunction solar cells is 8.1% [2], and about 4.1% [3] has already been achieved for a solar cell based on a ZnO/CuO heterojunction, which is significantly lower than the theoretical conversion efficiency limit (20%). The performance of these heterojunctions has been improved through internal work. Involves achieving controlled doping of the n and p layers to adjust the band gaps, thereby minimizing misalignments in the structure, while inserting a limited-thickness buffer layer between the n and p layers. To this end, researchers have found that doping ZnO with Al or Mg increased the band gap and improved the performance of Cu_2O/ZnO-based solar cells [4]. The choice of these elements, Mg and Al, also results from their abundance and low cost, which is preferable for the solar cell industry. Other research has also shown that the insertion of buffer layers prepared by physical methods, such as CdS and ZnS, has increased the efficiency of the cells [5].

Over the past few years, optoelectronic devices have attracted significant interest, as they are essential components of electronic and optical systems, notably in photovoltaics. Due to the intricate physical mechanisms in these devices, numerical simulation plays a crucial role in analyzing performance and optimizing design [6]. Numerical simulation involves running a computer program to model real and complex physical phenomena. In scientific research, these simulations are based on theoretical models. They are thus an adaptation of mathematical modeling to digital means; they help analyze how a modeled system works, explore its properties, and predict how it will evolve.

Optimization is a theory of methods that allow improving the performance, efficiency, or response of a system by maximizing or minimizing associated functions [7]. It is therefore an essential tool for modeling. No matter the structure of a solar cell, optimizing its parameters is essential for achieving high efficiency. Solar cell optimization typically involves adjusting factors like doping profiles, thickness and levels, optical confinement mechanisms, and contact design. The values of the optimal parameters, of course, depend on the solar cell structure, the quality of the material (lifetime, mobility), the quality of the ohmic contacts, the surface recombination velocity (front and rear surfaces), etc… The optimal parameter values depend on the material quality (such as lifetime and mobility), solar cell structure, surface recombination velocity at the front and rear surfaces, and the effectiveness of ohmic contacts.

Simulation-based optimization is the process of identifying the best-input variable values from all possible options. The aim of simulation-based optimization is to use minimal resources while maximizing or minimizing the output variables in a simulation experiment. When optimization through simulation is performed using a mathematical model of a system, this model is called a simulation model [8]. Optimization through simulation eliminates the need to create multiple prototypes with varying parameters. It is independent of the technology used, enabling a broad range of parameter adjustments, and allows for isolating the impact of different cell regions, even when parameters like mobility, diffusion length, and lifetime are interdependent.

Several software programs have been developed with the specific goal of modeling solar cells. While they vary in capabilities and limitations, they are all based on the same fundamental principles. Use any numerical software that can solve fundamental semiconductor equations to, in theory, model thin-layer solar cells. Many of these simulation tools were developed by universities or research institutes and are usually available free, though they often come without support. All of these are one-dimensional and can be used to assess solar cell performance, either directly or indirectly. This category of software includes SimWindows, TCAD-SILVACO, PC-1D, ADEPT-F, ASPIN, SCAPS-1D, ASA, AMPS-1D, and AFORS-HET [9]. We use SCAPS-1D software for our research work due to its robust capabilities and the abundance of literature available for photovoltaic device modeling and performance analysis.

V.2 Presentation of SCAPS-1D simulation software

SCAPS (Solar Cell Capacitance Simulator one Dimension) is a numerical simulation software for thin-film heterojunction solar cells. It was developed by Marc Burgelman et *al.* [10], at Ghent University in Belgium using LabWindows/CVI from National Instruments. It was made available to the research community in photovoltaics after the second World Conference on Photovoltaic Energy Conversion (PV), held in Vienna in 1998.

Initially, SCAPS was developed to model photovoltaic systems comprising $CuInSe_2$ and CdTe semiconductors. Subsequently, this program was expanded to include other types of cells, such as crystalline cells (Si and GaAs) and amorphous cells (a-Si and micro-morph Si).

Since version 2.8, SCAPS has also been adapted for graded solar cells [11]. It allows the simulation of solar cells consisting of up to seven layers, each having different properties such as doping profile, thickness, energy distribution of donor or acceptor levels, optical absorption, etc. Parameters such as the bandgap and mobility are independent of temperature. Each layer can have up to three deep levels, with three interface states positioned between layers. These deep levels can be distributed energetically within the bandgap in various ways, including single-level, uniform, Gaussian, or exponential tail distributions. Deep bulk levels can also change spatially within a layer, following uniform, stepwise, linear, or exponential distributions. However, all other properties remain uniform within each layer. As a result, creating graded junctions in the device requires using multiple layers.

The front and back contacts can be defined, and tunneling can also be enabled. For illumination, a variety of standard and other spectra are included, such as AM0, AM1.5D, AM1.5G, AM1.5 Gedition2, monochromatic, white, etc. The lighting can be applied from the P-side or N-side.

In SCAPS-1D, the calculation capabilities are largely extended to various parameters such as voltage, frequency, and temperature, as well as energy bands, concentrations, and currents. Numerical simulation allows the illustration of *J-V* characteristics, alternative characteristics (C and G as functions of V / f), and spectral response (also with light or bias voltage).

The program is organized into several modules and menus, where the user can define parameters or view the results. A scripting language, including a custom user function, provides a very intuitive user interface. A scripting language feature is added to run SCAPS-1D from a "script file," and all internal variables can be accessed and plotted through the script. SCAPS-1D has a built-in curve-fitting function and a field for interpreting admittance measurements.

The main theory of SCAPS-1D consists of solving the Poisson equations and the continuity equations. Each calculation starts from an initial assumption, represented by quasi-Fermi levels, to determine the equilibrium state, where no light or voltage is applied. If the operating point is set in the dark, the equilibrium condition is used to compute the solution. Under illumination, the short-circuit condition is first calculated, and this result serves as the starting point for the next step [12].

SCAPS-1D uses a Gummel-type iteration scheme for convergence, along with the Newton-Raphson algorithm for numerical calculations. Once a calculation point is set, SCAPS-1D uses the Newton-Raphson algorithm to iteratively compute the solution until the optimal value is reached.

V.3 Physical parameters of CuO and Cu_2O thin film solar cells

V.3.1 CuO and Cu_2O solar cell strucuters

The structure of both CuO and Cu_2O solar cells is illustrated in Figure V.1. It includes a glass substrate, a molybdenum back contact layer, a p-type CuO or Cu_2O absorber layer, an n-type CdS buffer layer, and an n-type transparent conducting oxide (TCO) ZnO window layer. This design is aimed at optimizing light absorption, charge transport, and charge collection within the CuO and Cu_2O absorber layers.

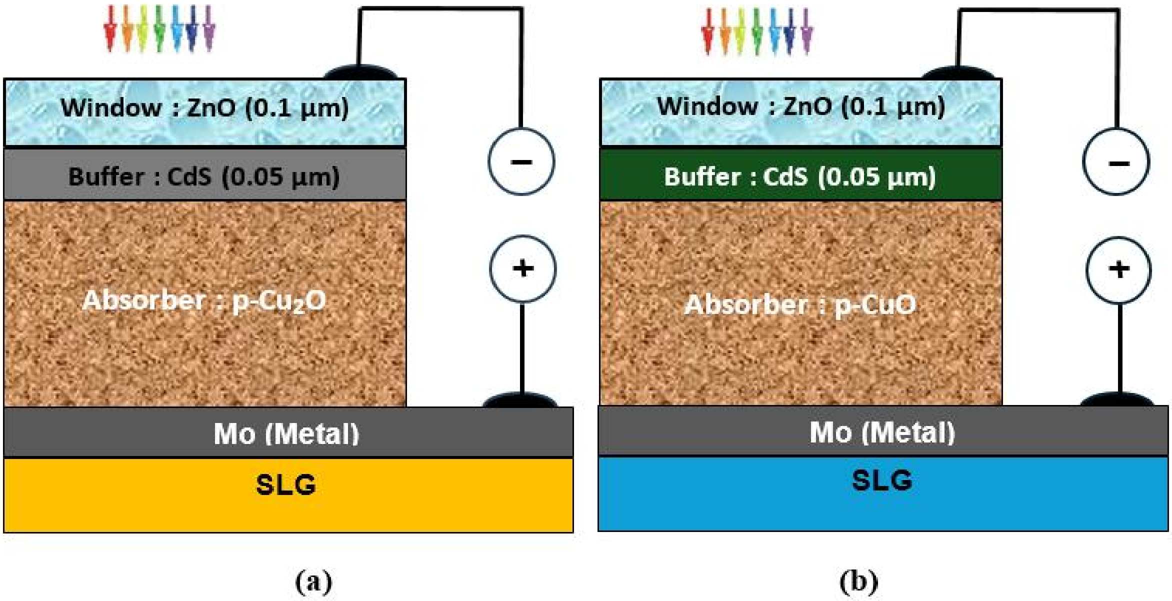

Figure V.1: Block diagram of a) Cu_2O/CdS/ZnO and b) CuO/CdS/ZnO solar cell structures.

V.3.2 Input parameters

Table V.1 presents the essential physical input parameters required for modeling CuO/CdS/ZnO and Cu_2O/CdS/ZnO solar cells in the SCAPS-1D simulation environment. These parameters include thickness, permittivity, bandgap energy, electron affinity, electron and hole mobilities, effective density of states in the conduction and valence bands, and donor/acceptor concentrations.

Due to the polycrystalline nature of all the layers, they inherently contain various defects. [13]. For the CuO and Cu_2O materials, we employed two Gaussian distributions for deep donor defects, while for the ZnO and CdS layers, two Gaussian distributions for deep acceptor defects were used. The surface recombination velocities for holes and electrons (S_n/S_p) at the front and back contacts were set to 1×10^7 cm s^{-1} [14]. Electron and hole thermal velocity in all layers is taken as a value of 1×10^7 cm s^{-1} [15, 16].

The reflection on the front face was assumed to be negligible to account for parasitic absorptions, meaning that most of the incident photons are absorbed within the bulk of the materials. However, it is necessary to consider the rear reflection when the thickness is significantly reduced, as some photons may reach the rear contact without being absorbed.

In this numerical analysis, the AM1.5G spectrum is used as the incident illumination to calculate the current-voltage characteristics under illumination and the solar cells quantum efficiency. This spectrum indicates that the path of light through the atmosphere is 1.5 times longer than the shortest path from the sun, that is, when it is at the Zenith, and the average solar energy falling on the surface of the Earth for this spectrum is approximately equal to 1000 W/m².

Table V.1: Physical parameters used in the simulation [13–25].

Material properties	**CuO**	**Cu_2O**	**CdS**	**ZnO**
Thickness [um]	*Varied*	*Varied*	0.1	0.08
Band gap [eV]	1.51	2.17	2.4	3.3
Electron affinity [eV]	4.07	3.20	4.2	4.6
Dielectric permittivity (relative)	18.10	7.11	10	9
CB (conduction band) effective density of states [cm^{-3}]	2.2×10^{19}	2×10^{17}	2×10^{18}	2.2×10^{18}
VB (valence band) effective density of states [$1/cm^3$]	5.5×10^{20}	1.1×10^{19}	1.5×10^{19}	1.8×0^{19}
Electron mobility μ_n[$cm^2/V.s$]	100	200	100	100
Hole mobility μ_p [$cm^2/V.s$]	0.1	80	25	25
Shallow uniform donor density N_D [$1/cm^3$]	0	0	1×10^{17}	1×10^{19}
Shallow uniform acceptor density NA [$1/cm^3$]	1×10^{16}	1×10^{18}	0	0

V.3.3 Optical parameters of CuO and Cu_2O thin films

The absorber layer's absorption coefficients play a key role in the simulation process. In SCAPS-1D, the optical absorption coefficient can be configured either by using a file, typically obtained from literature and formatted as a two-column ASCII input file, or by defining it through a model. The absorption coefficient model $\alpha(\lambda)$ [26] for both Cu_2O and CuO absorber films is given by SCAPS as presented in Figure V.2.

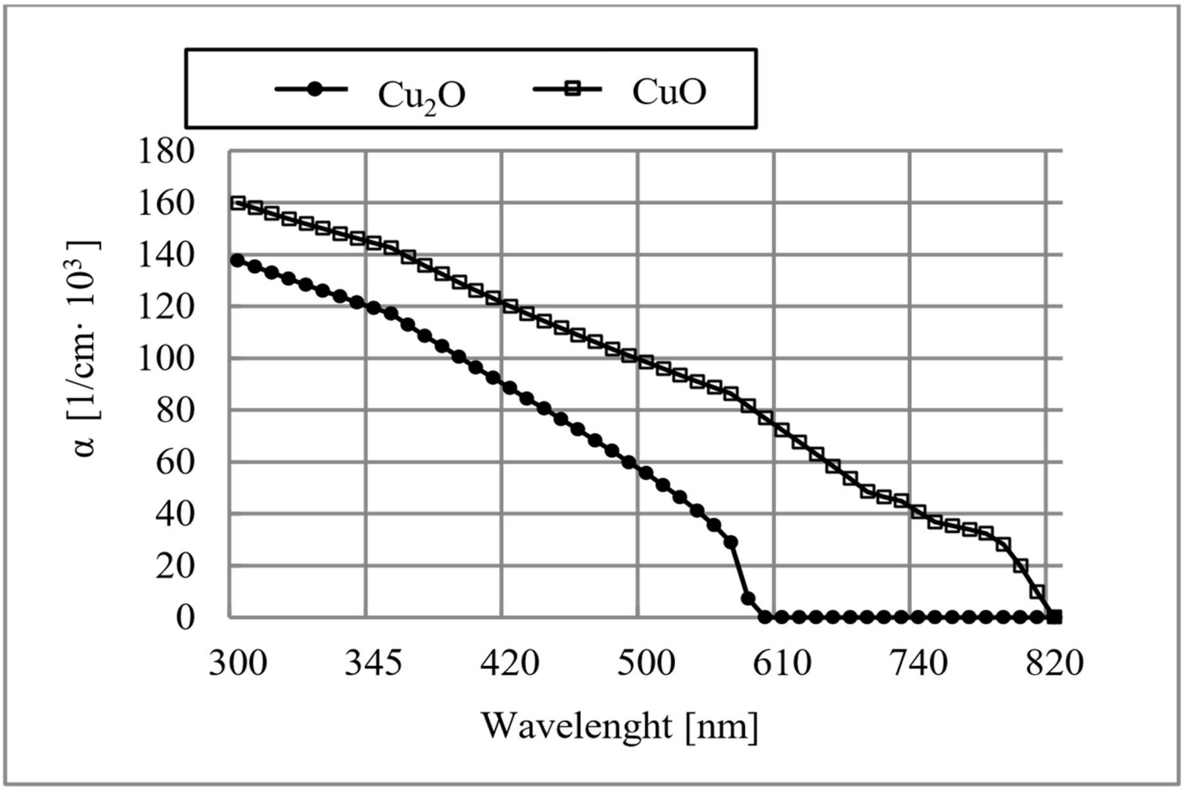

Figure V.2: Absorption coefficient curves of CuO and Cu_2O absorbers used in the simulation.

V.4 Results and discussion

V.4.1 Band diagram

The energy band diagrams of the simulated CuO/CdS/ZnO and Cu_2O/CdS/ZnO solar cells are shown in Figure V.3 under AM1.5G illumination. These diagrams were obtained for analysis from SCAPS output. It provides insights into the properties of the photovoltaic cells, clearly showing that CuO has a band gap of about 1.51 eV (Figure V.3.a) and Cu_2O has a band gap of about 2.17 eV (Figure V.3.b). For optimal light absorption and efficient energy conversion, the energy of the incident light photons should be equal to or exceed the maximum value of 1.51 eV for CuO and 2.17 eV for Cu_2O eV.

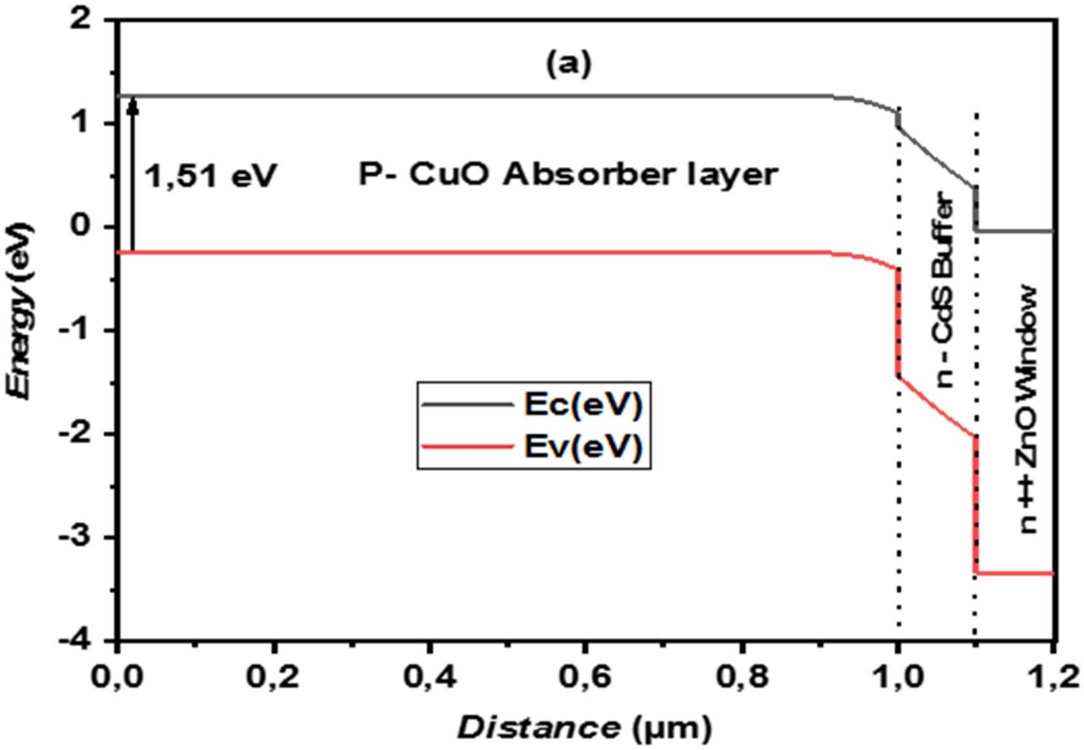

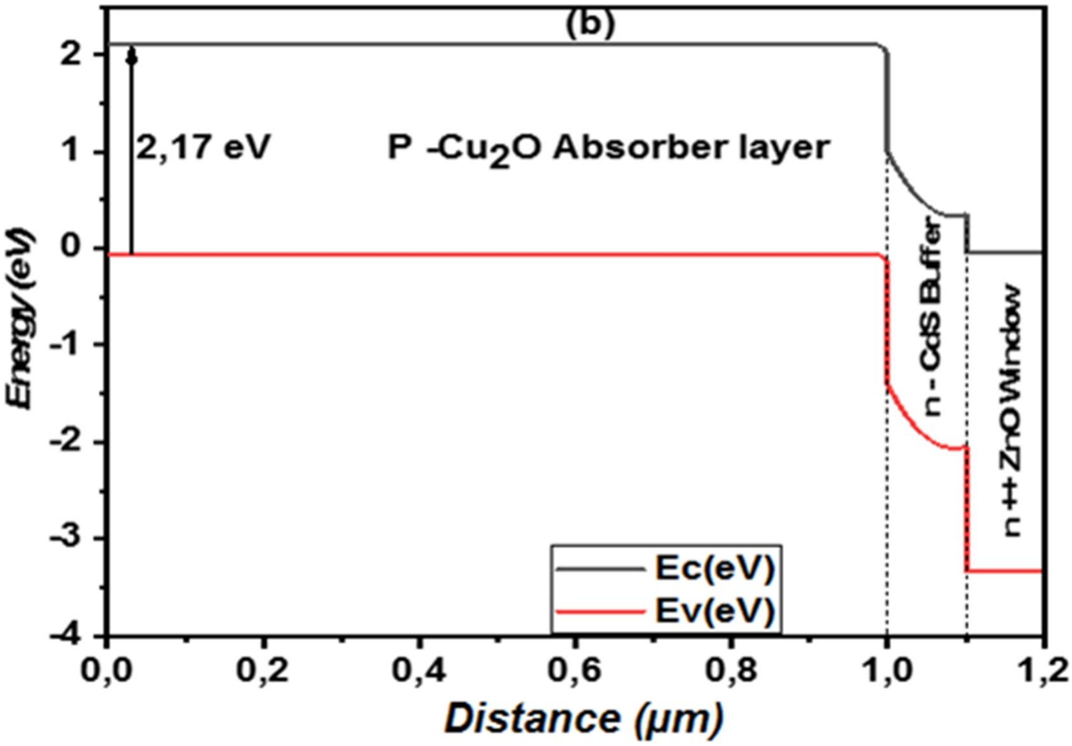

Figure V.3: Band diagram for (a) CuO and (b) Cu_2O solar cells structures.

V.4.2 Effect of absorber layer thickness on solar cell performance

In this section, the influence of the variation in the thickness of the p-CuO and p-Cu_2O absorber layers has been examined to gain qualitative insights into the device's performance. The thickness of the p-CuO and p-Cu_2O absorber layers was adjusted between 1 and 10 µm. Additionally, the bandgap energy values of the CuO and Cu_2O absorbers were kept constant at 1.51 eV and 2.17 eV, respectively, as shown in Table V.1. The results indicate that the absorber layer material is crucial in a solar cell, as it plays the key role of absorbing incident photons and generating additional charge carriers. Figure V.4 displays the effects of the variation in thickness of the p-CuO layer on the device performance parameters.

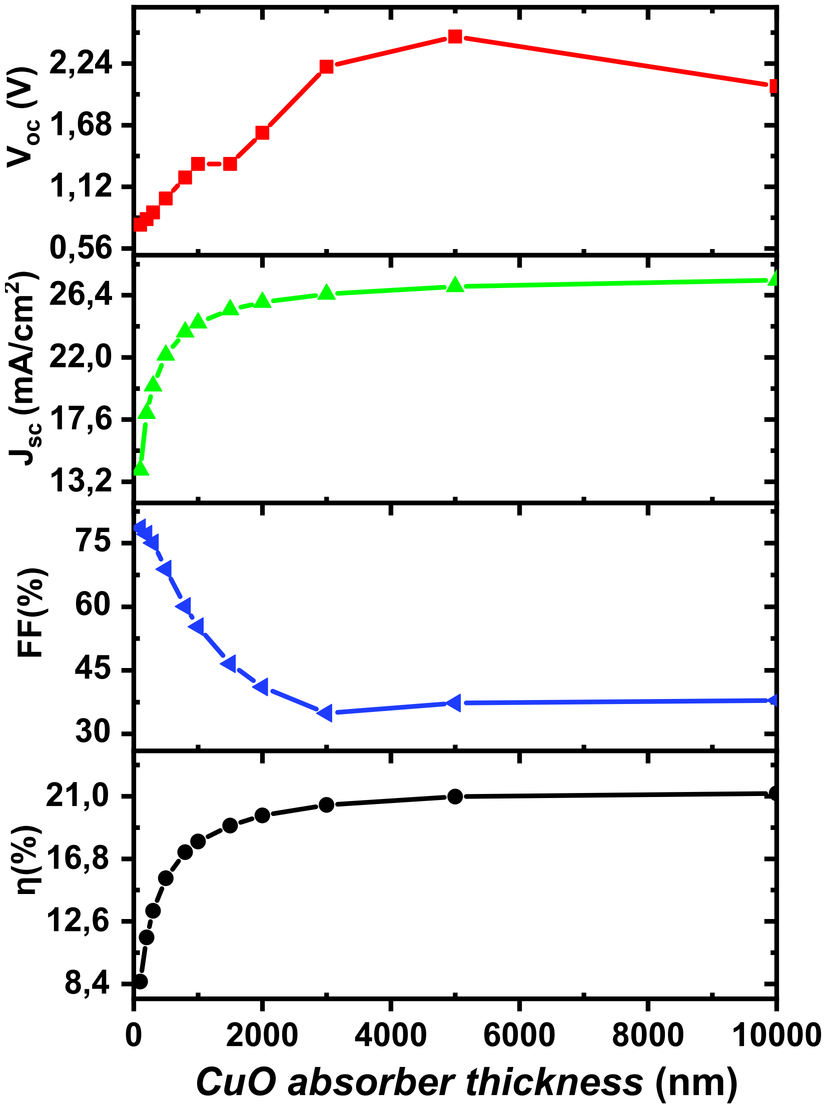

Figure V.4: Cell performance parameters as a function of CuO absorber layer thickness.

As the thickness of the CuO absorber layer increases from 0.1 to 10 µm, J_{sc} nearly doubles, rising from 13.8 mA/cm^2 to around 26.4 mA/cm^2, while efficiency experiences a rapid increase from 8.4% to about 21%. V_{oc} reaches 2.24 V, and *FF* is recorded at 37%.

The effects of the variation in the thickness of the p-Cu_2O layer on the device performance parameters are presented in Figure V.5. As a result, when the thickness of the Cu_2O is adjusted between 0.1 and 10 µm, J_{sc} rises from 6.8 mA/cm² to around 13.8 mA/cm^2, with η increasing from 3% to roughly 9%. V_{oc} reaches 1.3 V, and *FF* reaches 50.7%.

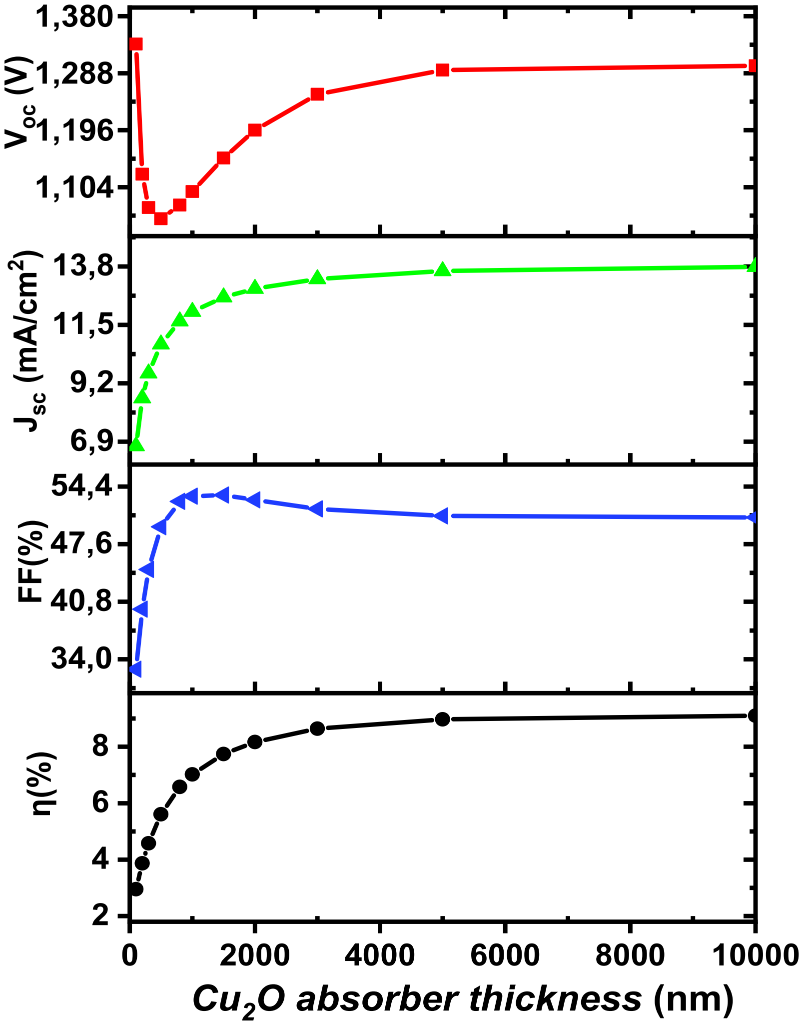

Figure V.5: Cell performance parameters as a function of Cu_2O absorber layer thickness.

When the absorber layer is thicker, more photons are captured, generating a greater number of electron-hole pairs, which leads to an increase in the photo-generated current [26]. It is evident that a thicker absorber layer enhances the performance of the solar cell. Consequently, a thickness of 3 µm is selected as the optimal thickness for the CuO and Cu_2O

absorber layers in the efficient ZnO/CdS/CuO and ZnO/CdS/Cu_2O solar cells [27]. Reducing the absorber layer thickness brings the back contact closer to the depletion region [28].

The quantum efficiency (*QE*) was computed for absorber layer thicknesses between 0.1 and 3 µm. Below 400 nm and above 650 nm, all structures exhibit nearly identical behavior. However, in the range between 430 nm and 850 nm, a noticeable loss is observed. As the thickness increases from 0.1 µm to 3 µm, the maximum quantum efficiency also rises, peaking at the thickness of 3 µm. Figure V.6 shows the quantum efficiency (*QE*) for CuO and Cu_2O layers.

(a)

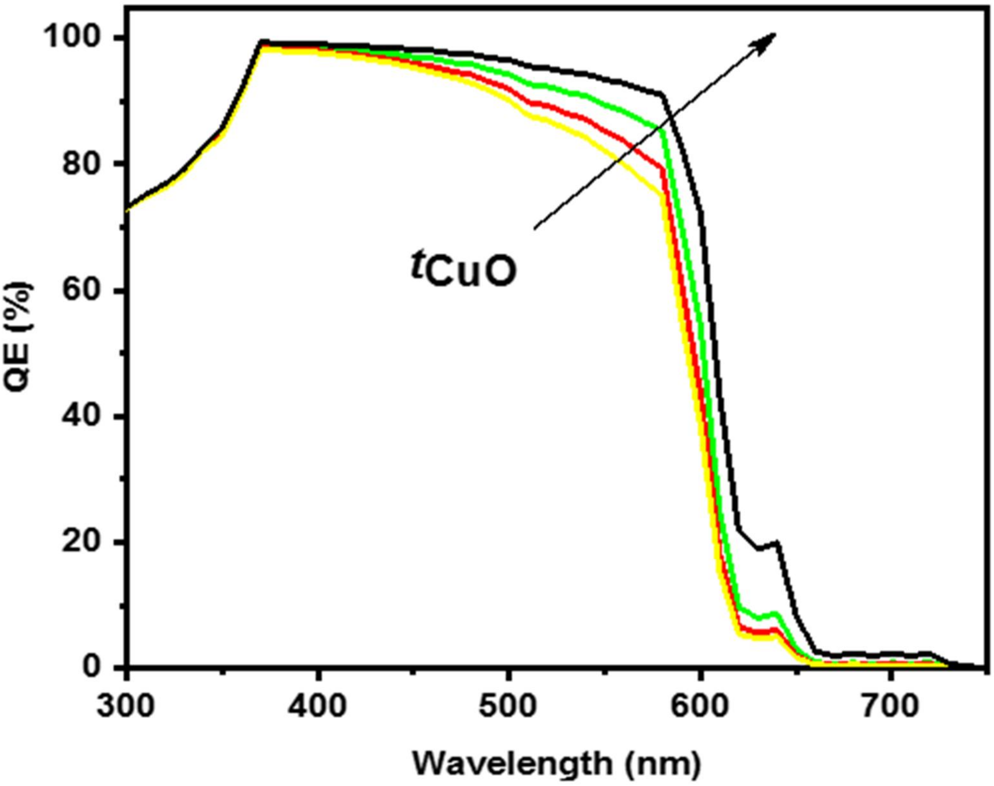

(b)

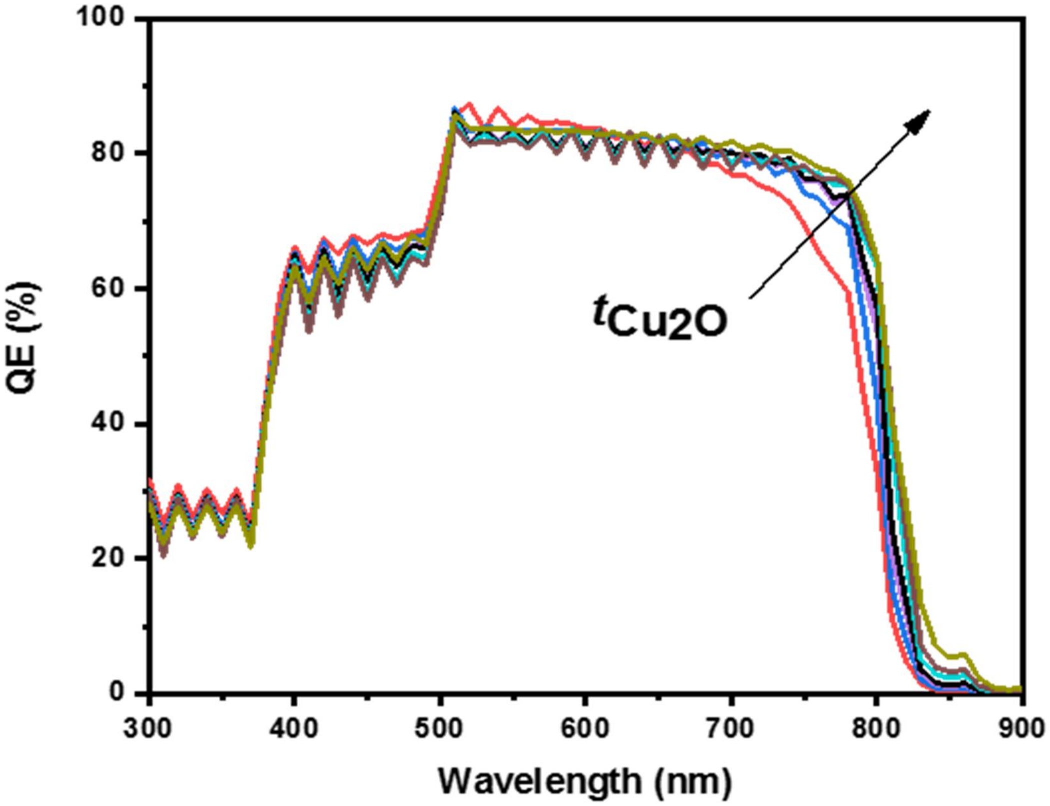

Figure V.6: Quantum efficiency of (a) CuO and (b) Cu_2O solar cells structures.

V.4.3 Effect of acceptor density on solar cell performance

The acceptor density in the CuO and Cu_2O absorber layers has been identified as a key factor that directly affects the performance of solar cells using these materials. The acceptor concentration N_A(CuO) is varied between 10^{11} cm^{-3} and 10^{19} cm^{-3}. The resulting simulated photovoltaic characteristics are presented in Figure V.7.

We note a gradual decrease in short circuit current J_{sc} from 4.8 mA/cm^2 at a concentration of 10^{11} cm^{-3} to a more acceptable level of 25.5 mA/cm^2 at a concentration of 10^{19} cm^{-3}. In contrast, V_{oc} and efficiency improve significantly, as they increase from 10^{11} cm^{-3} to 10^{19} cm^{-3}, achieving an optimal efficiency of 20.5% at an N_A acceptor concentration of approximately 10^{17} cm^{-3}, witn an open circuit voltage $V_{oc} \approx 4$ V. Meanwhile, the fill factor *FF* increases gradually with rising N_A, reaching a peak of 67.8% at a concentration of 10^{16} cm^{-3} before dropping to 19.2% at a concentration of 10^{17} cm^{-3}, where it remains constant thereafter.

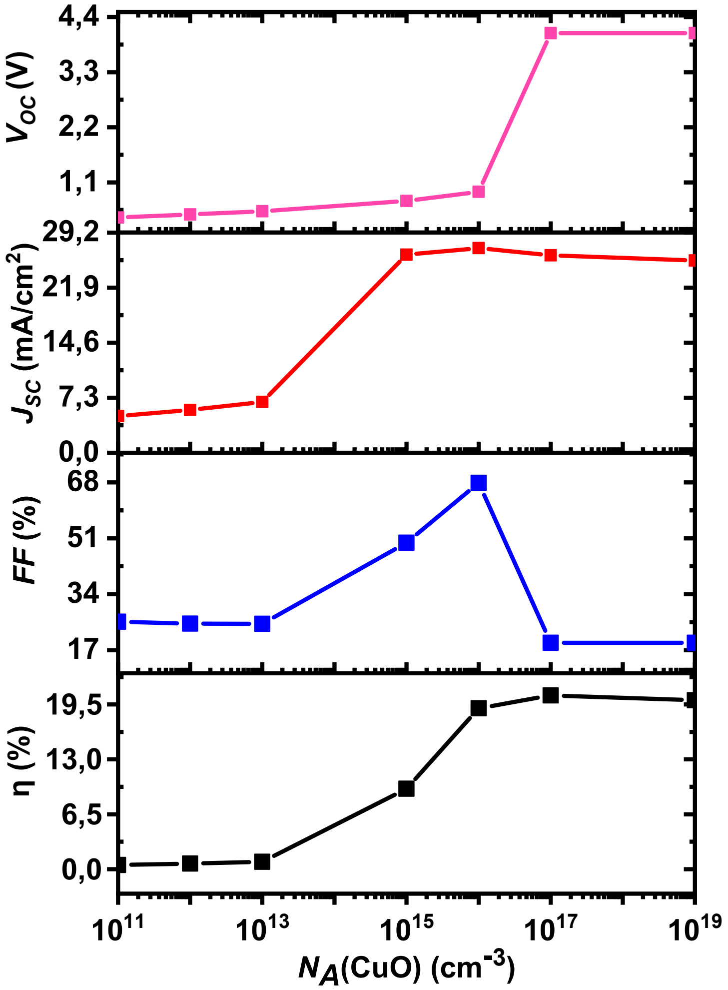

Figure V.7: Impact of acceptor density of CuO absorber layer on cell performance.

Figure V.8 explains the variations in the characteristic parameters of photovoltaic cells with the variation in the acceptor concentration of the Cu_2O absorer layer from 10^{11} to 10^{19} cm^{-3}. J_{sc} shows a slight decline from 14.13 mA/cm^2 at a concentration of 10^{11} cm^{-3} to a more suitable level of 12.5mA/cm^2 at a concentration of 10^{19} cm^{-3}. This decrease is attributed to a rise in the recombination of free charge carriers occurring within the bulk [29]. In contrast, both V_{oc} and FF significantly decrease as N_A increases from 10^{11} cm^{-3} to 10^{19} cm^{-3}. The efficiency improves with rising N_A, reaching a maximum of 10.8% at a concentration of $N_A = 10^{17}$ cm^{-3}, where V_{oc} is approximately 3.5 V and FF is around 21.2%. However, beyond this point, efficiency drops to 9.9% at an acceptor concentration N_A(Cu_2O) of about 10^{19} cm^{-3}.

These results indicate that N_A(CuO) and N_A(Cu_2O) should be above 10^{16} cm^{-3} and below 10^{17} cm^{-3} to achieve optimal performance.

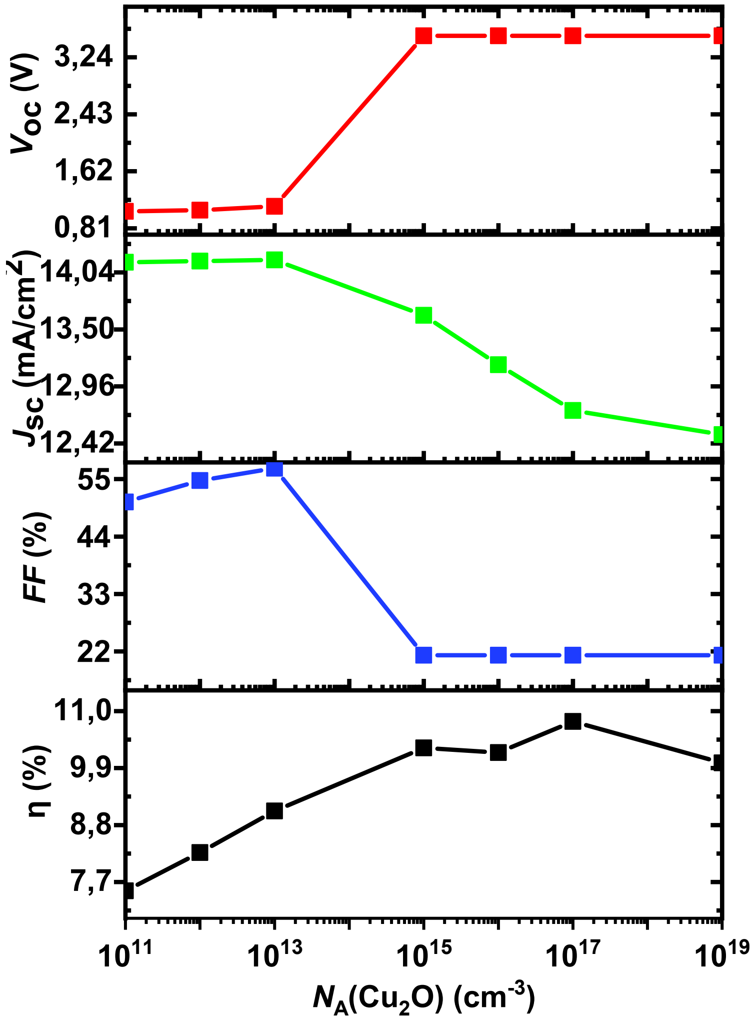

Figure V.8: Impact of acceptor density of Cu_2O absorber layer on cell performance.

The quantum efficiency for different acceptor concentrations in CuO and Cu_2O absorber layers was analyzed and is shown in Figures V.9 and V.10, respectively. We observe the quantum efficiency reaches a peak of nearly 98% under 100 mW/cm² illumination for wavelengths ranging from 500 nm to 600 nm. As N_A(Cu_2O) and N_A(CuO) increase, the spectral response improves in the longer wavelength region.

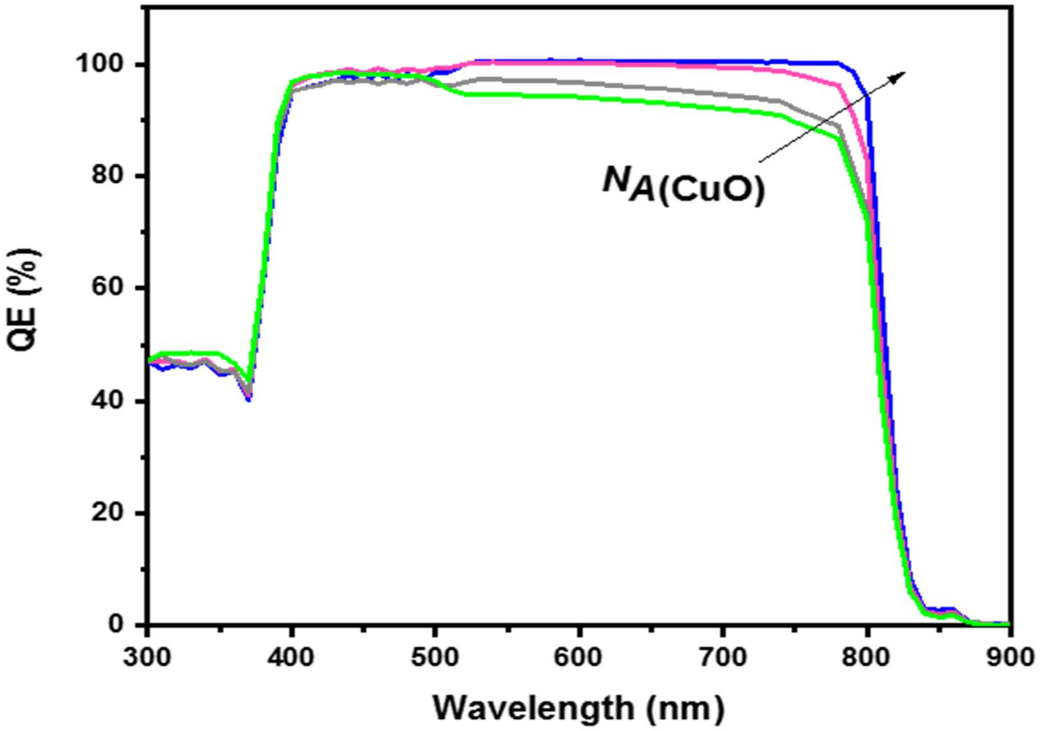

Figure V.9: Quantum efficiency *QE* of CuO solar cell for various acceptor concentrations.

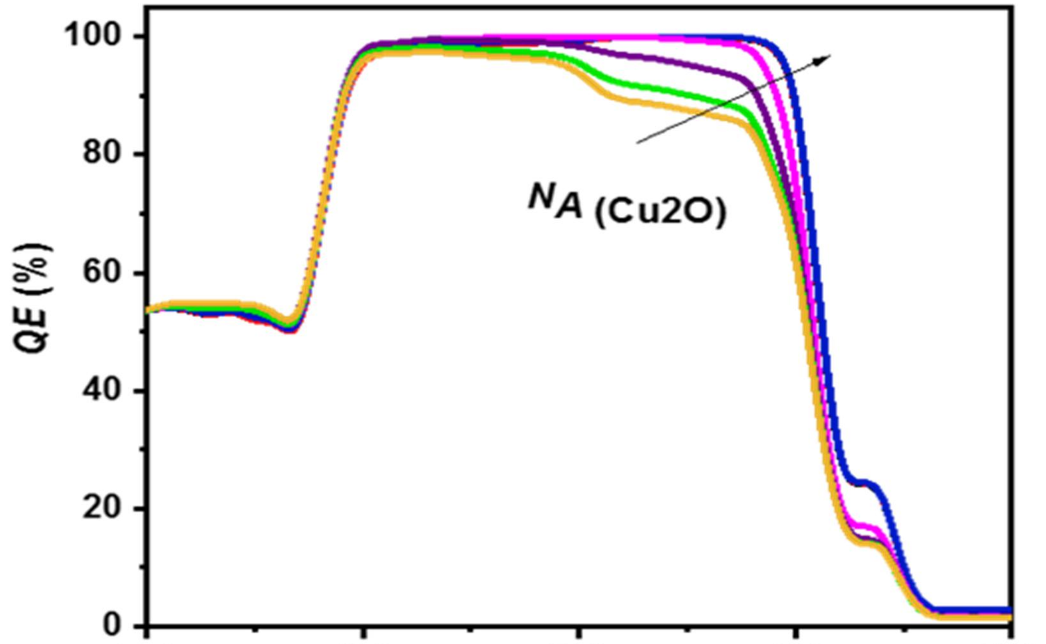

Figure V.10: Quantum efficiency *QE* of Cu_2O solar cell for various acceptor concentrations.

V.4.4 Influence of defect state density of CuO and Cu_2O absorber layers

We studied in this section the influence of defect density in the absorber layers through computational modeling. We simulated the changes in efficiency (η), open circuit voltage V_{oc}, short circuit current J_{sc}, fill factor (FF), and quantum efficiency (QE) using SCAPS-1D, where the defect state density varied between 10^{11} and $10^{19}cm^{-3}$. The effect of absorber defects on photovoltaic cell parameters was analyzed. The density of these defects directly influences the cell's performance; as defect density increases, it causes a decrease in minority carrier lifetime. This decrease in lifetime results in a shorter diffusion length for both electrons and holes, thereby increasing recombination losses in the absorber layer. Figure V.11 displayed the variation of CuO solar cell performance with varying the defect state density in the CuO absorber layer N_T(CuO).

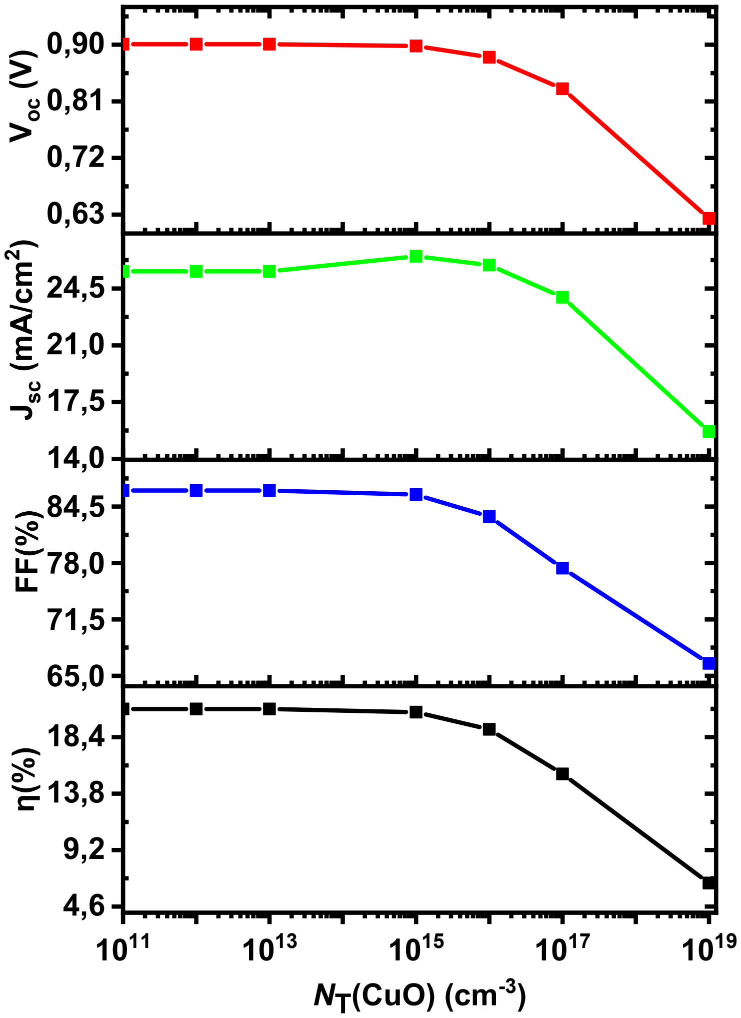

Figure V.11: Variation of solar cell performance with varying defect density of CuO absorber layer.

When N_T(CuO) exceeds 10^{15} cm^{-3}, the device performance is negatively affected, as all key photovoltaic parameters (V_{oc}, J_{sc} and *FF)* experience reduction, and efficiency η reduces drastically from 20.4% to 6.5%. Resulting in energy losses that hinder the current transport to the external load, this happens because carriers are trapped or recombine at defects. When the defect state density is lower than 10^{15} cm^{-3}, the solar cell parameters remain constant.

The influence of defect density N_T(Cu_2O) on the solar cell parameters is demonstrated in Figure V.12.

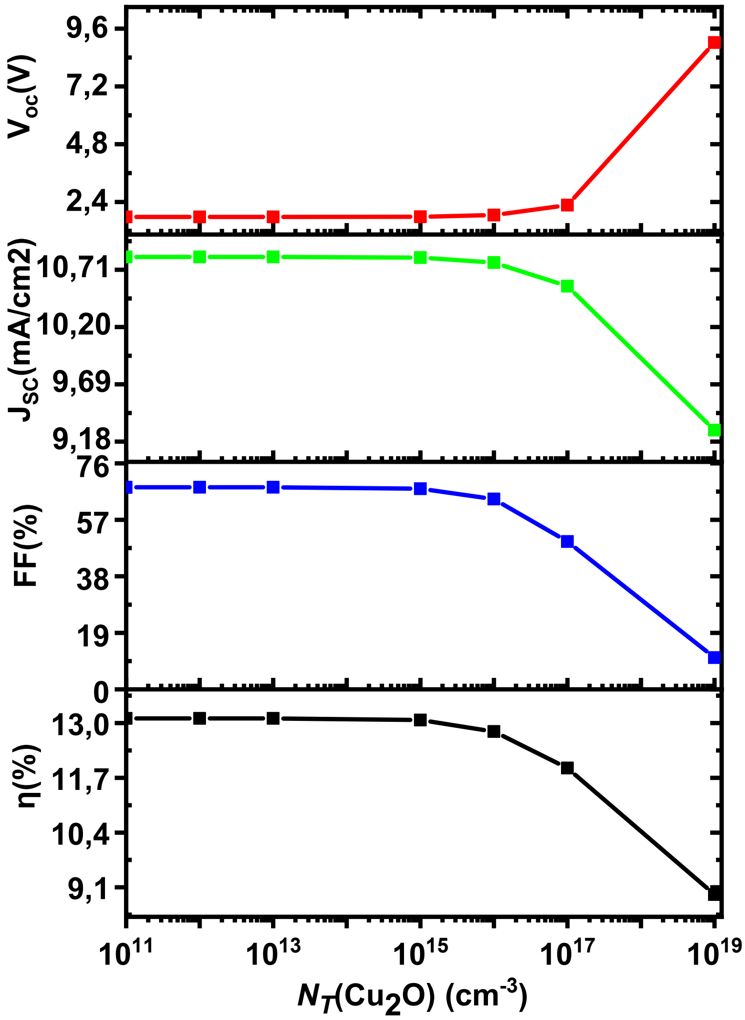

Figure V.12: Effect of defect density of Cu_2O layer on the solar cell performance.

When the defect state density is lower than $10^{15}cm^{-3}$, the solar cell parameters remain constant. When N_T(Cu_2O) surpasses 10^{15} cm^{-3}, the photovoltaic performance parameters (J_{sc}, η and *FF)* experience reductions, and V_{oc} increases considerably from 1.8 V to 9 V. Resulting in energy losses that hinder the current transport to the external load, this happens because carriers are trapped or recombine at defects.

Optimal performance for CuO solar cells is achieved when N_T(CuO) is around 10^{15} cm^{-3}, with V_{oc} = 0.90 V, J_{sc} = 26.4 mA/cm^2, efficiency η = 20.4%, and FF = 85.8%. In contrast, at a high defect concentration of 3 × 10^{19} cm^{-3}, performance drops sharply with V_{oc} = 0.62 V, J_{sc} = 15.6 mA/cm^2, efficiency η = 6.5%, and FF = 66.4%.

Similarly, for Cu_2O solar cells, optimal performance is obtained when N_T(Cu_2O) is around 10^{15} cm^{-3}, with V_{oc} = 1.8 V, J_{sc} = 10.8 mA/cm^2, efficiency η = 13%, and FF = 67.5%. The performance of solar cells declines at a higher defect concentration of 3 × 10^{19} cm^{-3}, except the open-circuit voltage V_{oc}, yielding V_{oc} = 9 V, J_{sc} = 9.3 mA/cm^2, efficiency η = 8.9%, and FF = 10.66%. Therefore, the bulk defect density linked to trapping or recombination states within the CuO and Cu_2O absorber bulk plays a critical role in current transport [32].

A solar cell usually uses visible and half of the infrared wavelength. Quantum efficiency is used to measure the photons absorbed in the solar cell at a specific wavelength. The quantum efficiency (QE) was calculated, and the results depicted in Figures V.13 and V.14.

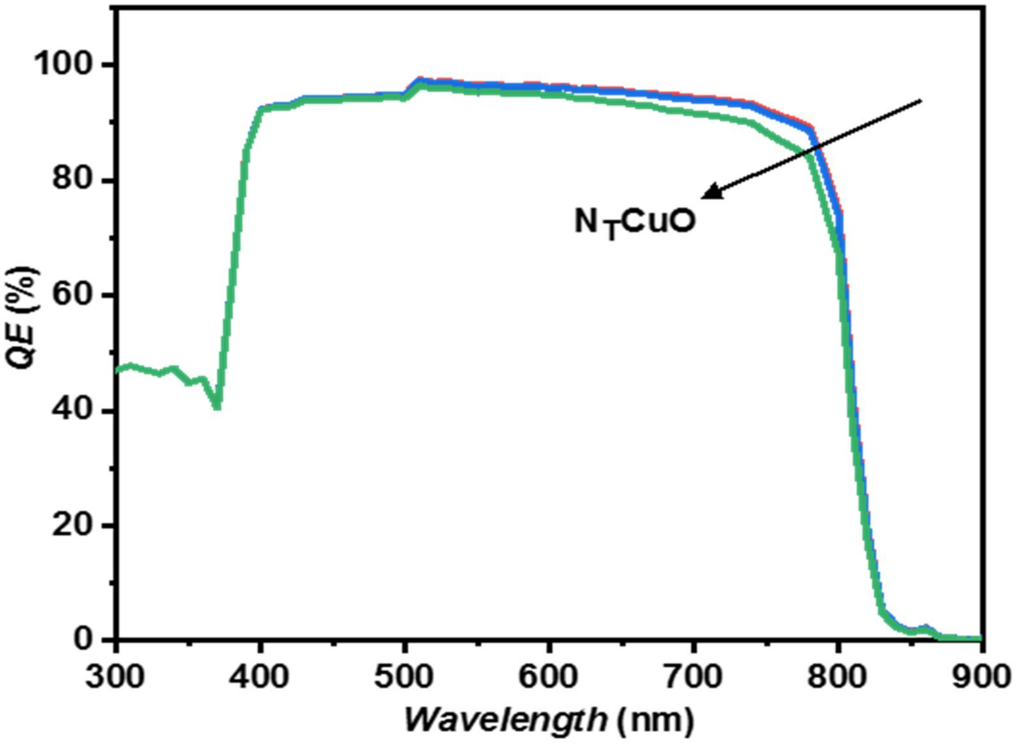

Figure V.13: Quantum efficiency versus wavelength of CuO solar cell with various N_T(CuO).

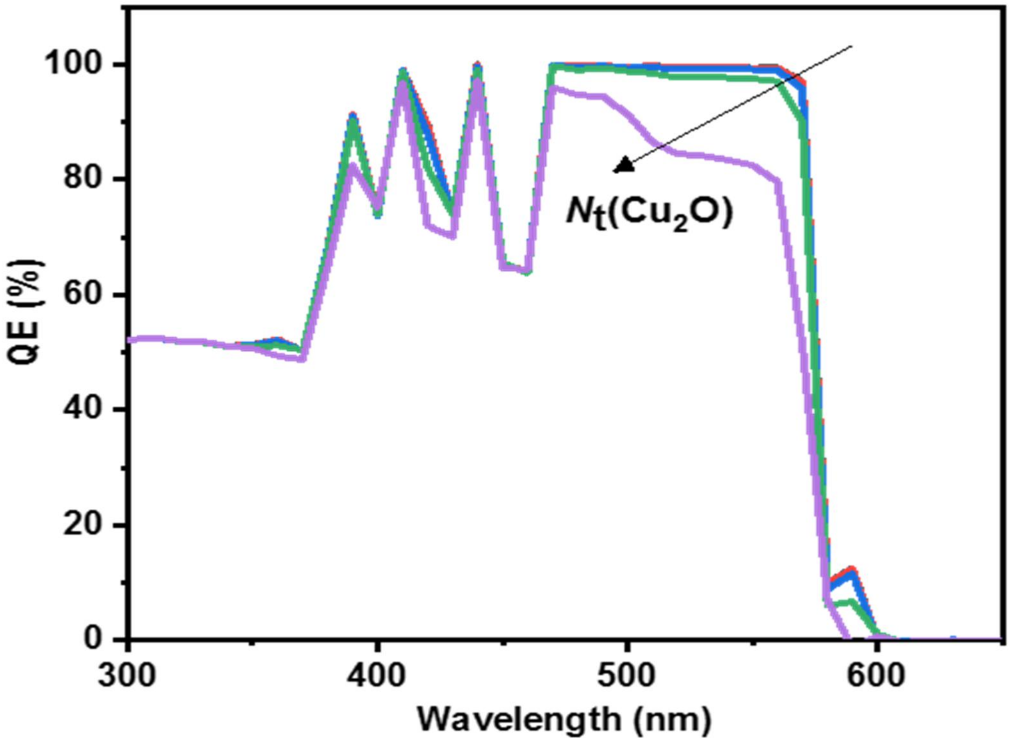

Figure V.14: Quantum efficiency versus wavelength of Cu_2O solar cell with various $N_T(Cu_2O)$.

Below 500 nm and above 800 nm, all samples exhibit similar behavior, but a significant loss is observed in the 500 – 800 nm wavelength range. The maximum quantum efficiency decreases notably as defect concentration rises from 10^{14} cm^{-3} to 10^{19} cm^{-3}. Actually, a rise in defect density N_T creates more deep trapping sites for charge carriers at grain boundaries, surface defects, or bulk defects. In the active layer of the PSCs, this results in increased bulk non-radiative charge recombination. With a density between 10^{10} and 10^{16} cm^{-3}, the device can operate efficiently if the defects are present within the structure. Therefore, it can be elucidated that the CuO and Cu_2O absorbers are competent materials capable of absorbing the necessary wavelengths.

V.5 Hybrid CuO/CIGS and Cu_2O/CIGS solar cells modeling

I-III-VI□ compounds, including $CuInSe_2$ (CIS) and $CuIn_xGa_{1-x}Se_2$ (CIGS) semiconductors, are crucial photovoltaic materials used in the absorber layers of solar cells. CIGS, which currently leads the thin-film solar cell market, features a strong absorption capability (> 10^5 cm^{-1}), excellent stability [33, 34], radiation hardness [35], and a specific power of up to 919 W/kg [36]. The highest among all solar cells, the band gap ranges between 1.0 eV and 1.7 eV, based on the changes of the value of 'x' in the formula $CuIn_xGa_{1-x}Se_2$ [37, 38]. However, the limited availability of indium (In) in nature contributes to higher production costs for solar cells utilizing the CIGS absorber layer. Solar cells based on quaternary chalcopyrite compounds of the type of $Cu(Ga,In)Se_2$ (CIGS) have achieved record conversion efficiencies of nearly 20% in laboratories (ZSW) [39] and (NREL) [40]. Recently, a record efficiency of 22.3% was achieved by the Japanese CIGS producer Solar Frontier [41]. Figure V.15 shows the CuO/CIGS, Cu_2O/CIGS and CuO/Cu_2O/CIGS Hybrid solar cells structural layout.

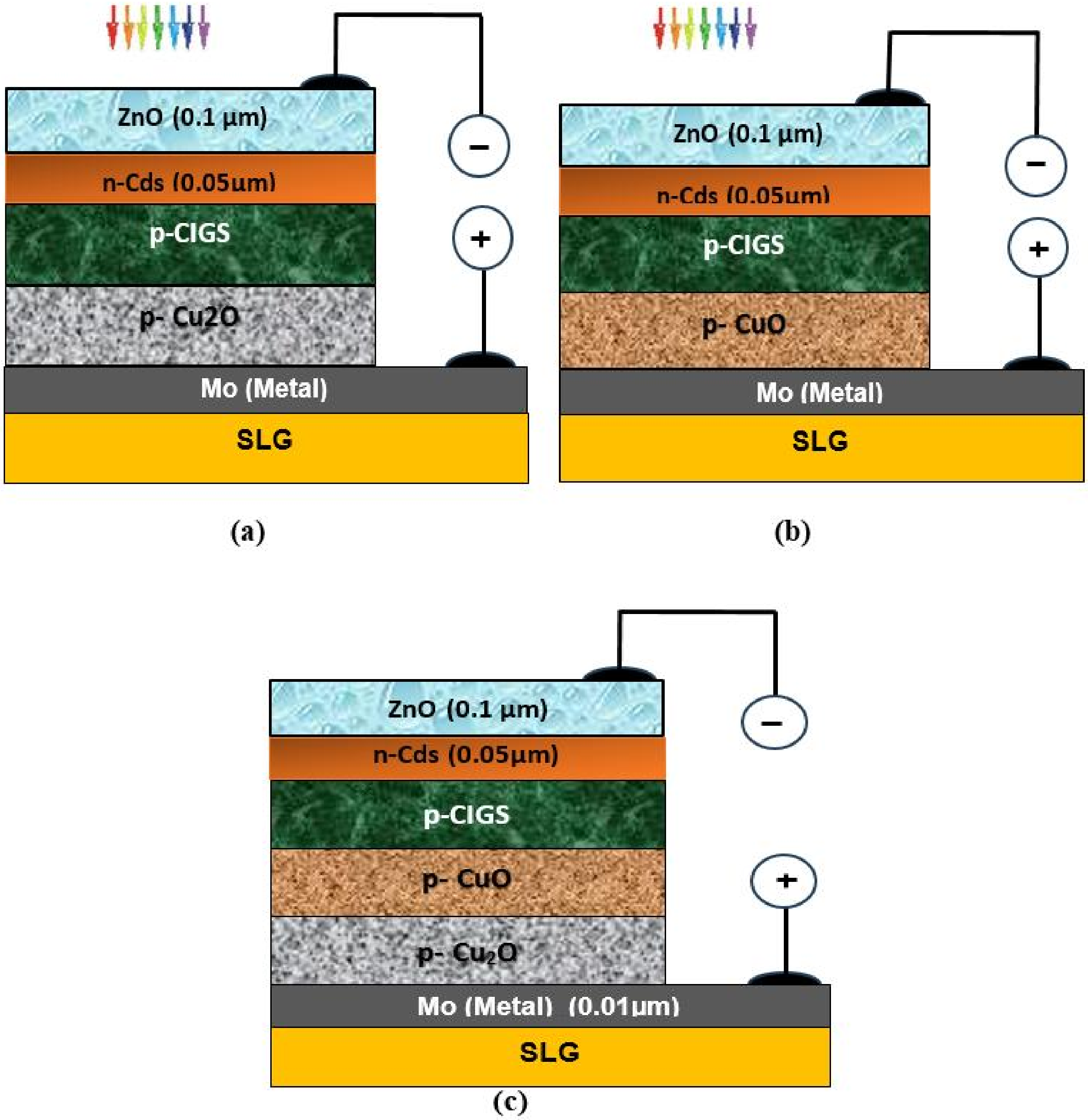

Figure V.15: Hybrid solar cells for different structures: (a) CuO/CIGS, (b) Cu_2O/CIGS, and (c) CuO/Cu_2O/CIGS.

The input parameters using the AM1.5G spectrum at a temperature of 300 K were utilized to calculate the *J-V* curves, quantum efficiency, and photovoltaic properties, including short circuit current, open circuit voltage, fill factor, and efficiency. All input parameters used in the SCAPS-1D simulator were derived from the literature, incorporating the properties and values of CuO, Cu_2O, CIGS, and CdS, as shown in Table V.2.

Table V.2: Input parameters used in SCAPS-1D simulator.

Material properties	**CuO**	**CIGS**	**Cu_2O**	**CdS**	**ZnO**
Thickness (µm)	3	*varied*	3	0.1	0.08
Band gap [eV]	1.51	1.2	2.17	2.4	3.3
Electron affinity [eV]	4.07	4.5	3.20	4.2	4.6
Dielectric permittivity (relative)	18.10	10	7.11	10	9
CB (conduction band) effective density of states [cm^{-3}]	2.2×10^{19}	2×10^{18}	2×10^{17}	2×10^{18}	2.2×10^{18}
VB (valence band) effective density of states [1/cm^3]	5.5×10^{20}	2×10^{18}	1.1×10^{19}	1.5×10^{19}	1.8×10^{19}
Electron mobility μn [cm^2 /Vs]	100	100	200	100	100
Hole mobility μp [cm^2 /Vs]	0.1	2.5	80	25	25
Shallow uniform donor density N_D [1/cm^3]	0	0	0	1×10^{17}	1×10^{19}
Shallow uniform acceptor density NA [1/cm^3]	1×10^{16}	*varied*	1×10^{18}	0	0

V.5.1 Band diagrams

Based on the structure of solar cells and the absorber layers, specifically the CuO and Cu_2O layers applied onto the CIGS absorber layer, a staircase-like shift in conduction band energy is observed. This shift enhances the collection of electrical charges. The subsequent section details the influence of the thickness, acceptor concentration, and defect density of the CIGS added layer on the performance of CuO/CIGS and Cu_2O/CIGS solar cells.

Figure III.13 presents the energy band diagrams for the following structures: CuO/CIGS, Cu_2O/CIGS, and Cu_2O/CuO/CIGS hybrid solar cells, as obtained through simulation. This energy band diagram was extracted from the SCAPS output for analysis purposes. Clearly showing that CuO has a band gap of around 1.51 eV, CIGS has a band gap of about 1.2 eV, and Cu_2O has a band gap of about 2.17 eV, as indicated in Figure V.16.

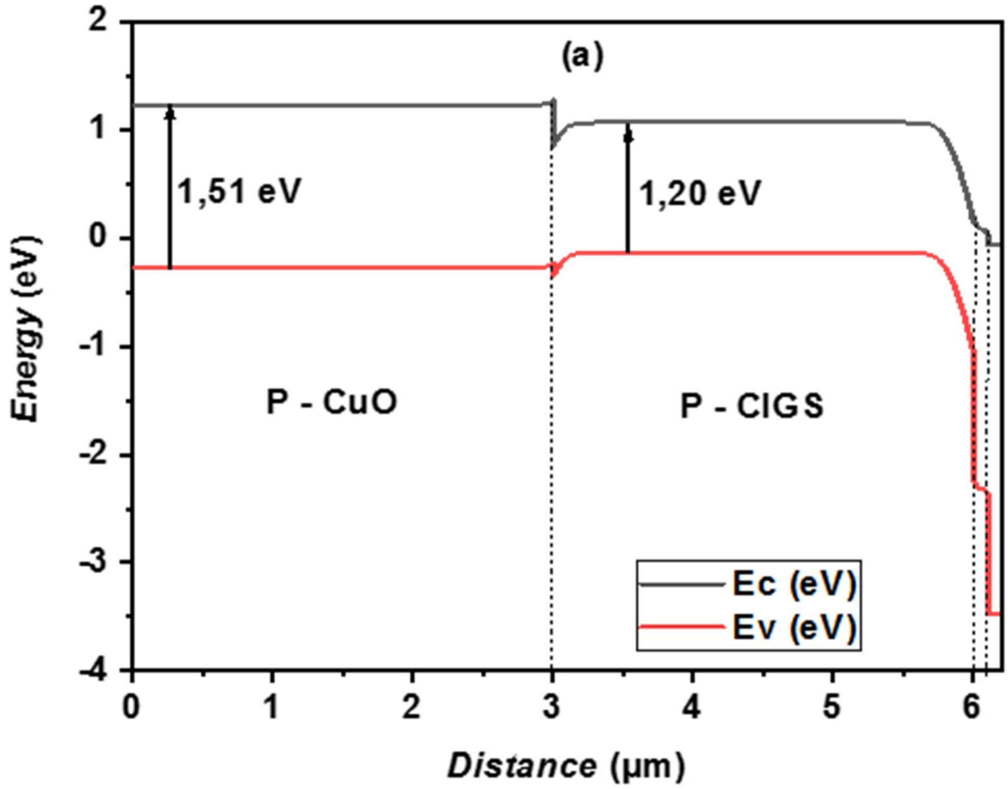
(a)
1,51 eV
1,20 eV
P - CuO
P - CIGS
Ec (eV)
Ev (eV)
Energy (eV)
Distance (µm)
2
1
0
-1
-2
-3
-4
0
1
2
3
4
5
6

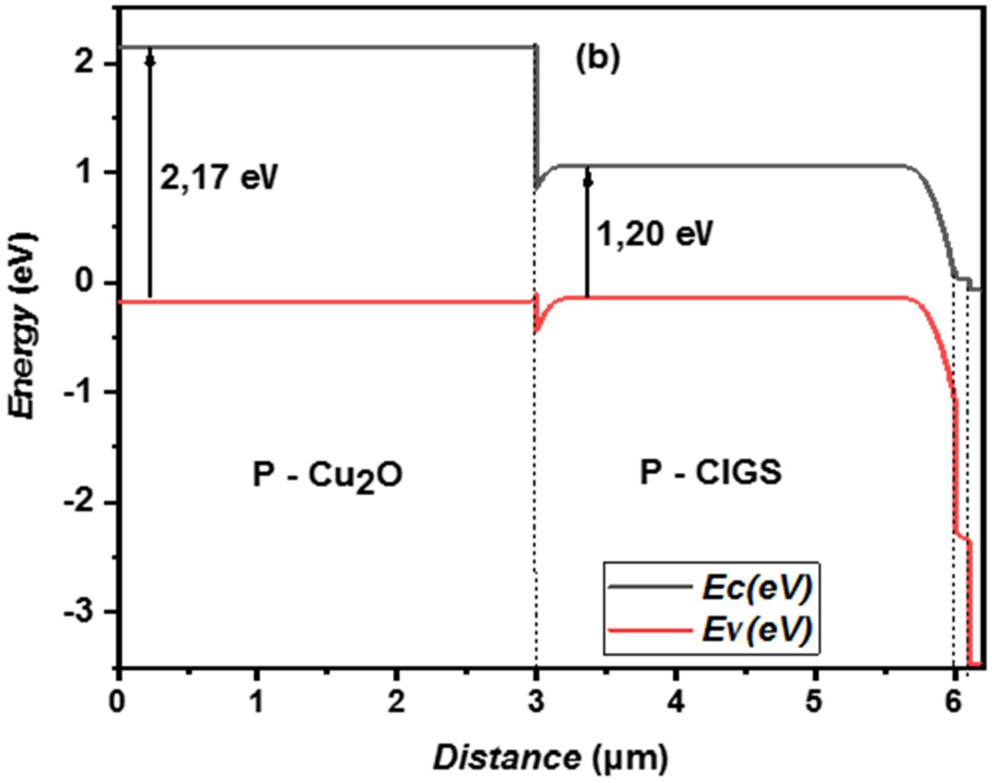
(b)
2,17 eV
1,20 eV
P - Cu2O
P - CIGS
Ec(eV)
Ev(eV)
Energy (eV)
Distance (µm)
2
1
0
-1
-2
-3
0
1
2
3
4
5
6

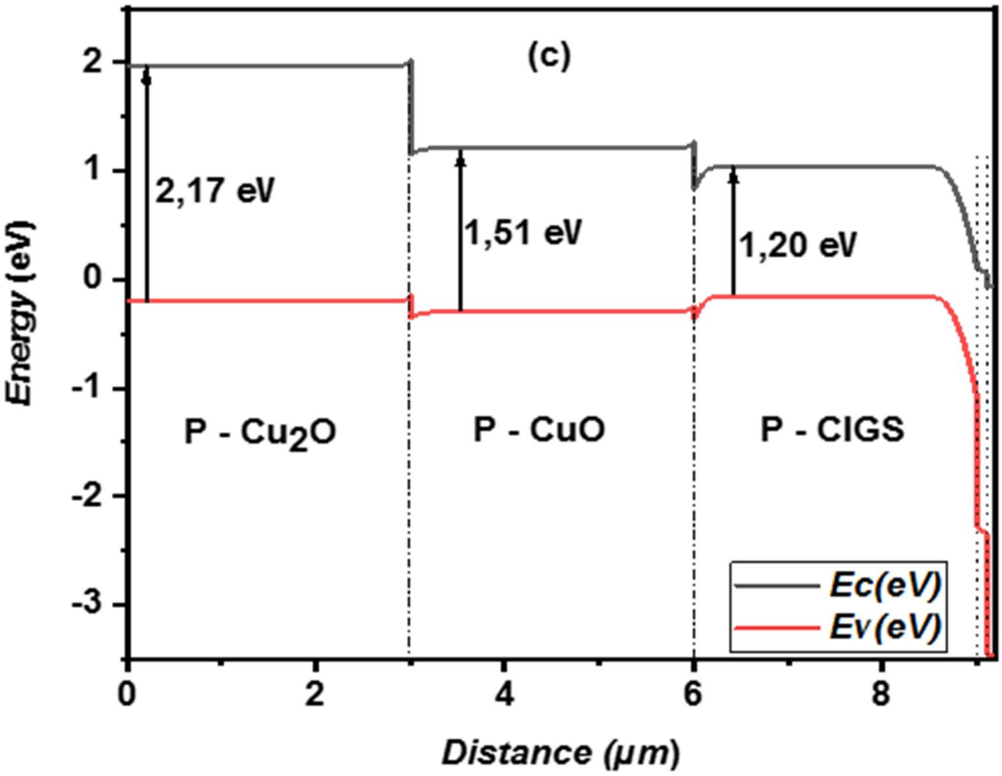

Figure V.16: Energy band diagrams for (a) CuO/CIGS, (b) Cu_2O/CIGS, and (c) Cu_2O/CuO/CIGS Hybrid solar cell structures.

V.5.2 Effect of CIGS absorber layer thickness for both structures

The p-CIGS absorber layer's thickness is the key factor that directly affects hybrid CIGS solar cell performance. Initially, the thickness of CIGS absorber was varied (0.1 µm – 10 µm) to find the optimum value for realizing high efficiency. The results in Figures V.17 and V.18 showed that solar conversion efficiency increases with the thickness of the CIGS absorber layer, but this increase suddenly slows down beyond 2 µm. The optimal thickness for the CIGS absorber layer exceeds 3 µm. From Figures V.17 and V.18: efficiencies of 16.66% and 19.12% were recorded for thicknesses of 1 µm and 3 µm, respectively. In comparison, the 18.39% efficiency at 2 µm reveals that a reduction of 1 µm in absorber thickness leads to a 9.4% drop in efficiency, whereas an increase of 1 µm results in only a 3.8% gain. A more pronounced efficiency decline is noticeable under 1 µm. This result aligns with theoretical expectations that an absorber thickness of 1-2 µm is sufficient to absorb most incident light. When the absorber layer is thinner than 2 µm, the short-circuit current density (J_{sc}) and open-circuit voltage (V_{oc}) rise as thickness increases, likely due to greater absorption of longer wavelengths; this helps generate more electron-hole pairs. A fill factor (*FF*) of up to 75% is reached when the absorber thickness surpasses 2 µm.

The absorber layer, which also serves as the active layer, absorbs a large fraction of the incident photons with energies above or equal to the band gap. This necessitates precise control of its thickness. While increasing the absorber thickness will enhance the minority carrier diffusion length, improve the absorption of long-wavelength photons, and in turn improve electron collection and power conversion, a thicker absorber region will also widen the depletion region. After a certain amount of thickness, the absorption layer becomes saturated with long-wavelength photons, and this leads to slight improvements in photovoltaic performance.

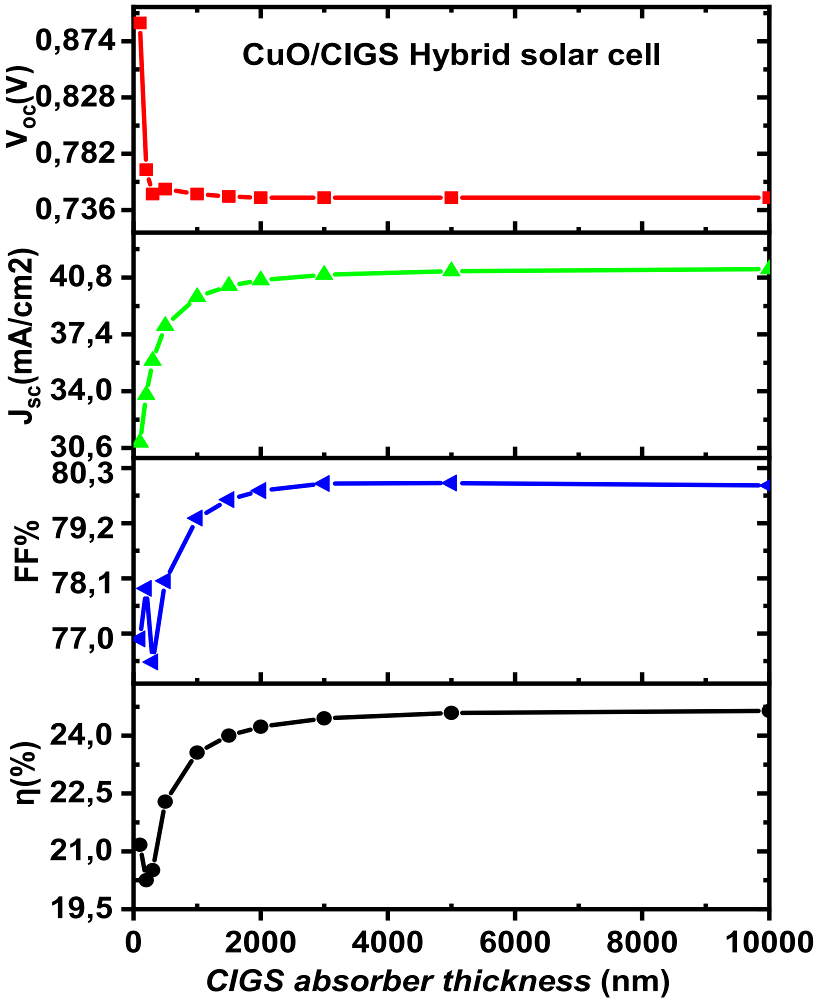

Figure V.17: Performance of CuO/CIGS hybrid solar cells depending on CIGS absorber layer thickness.

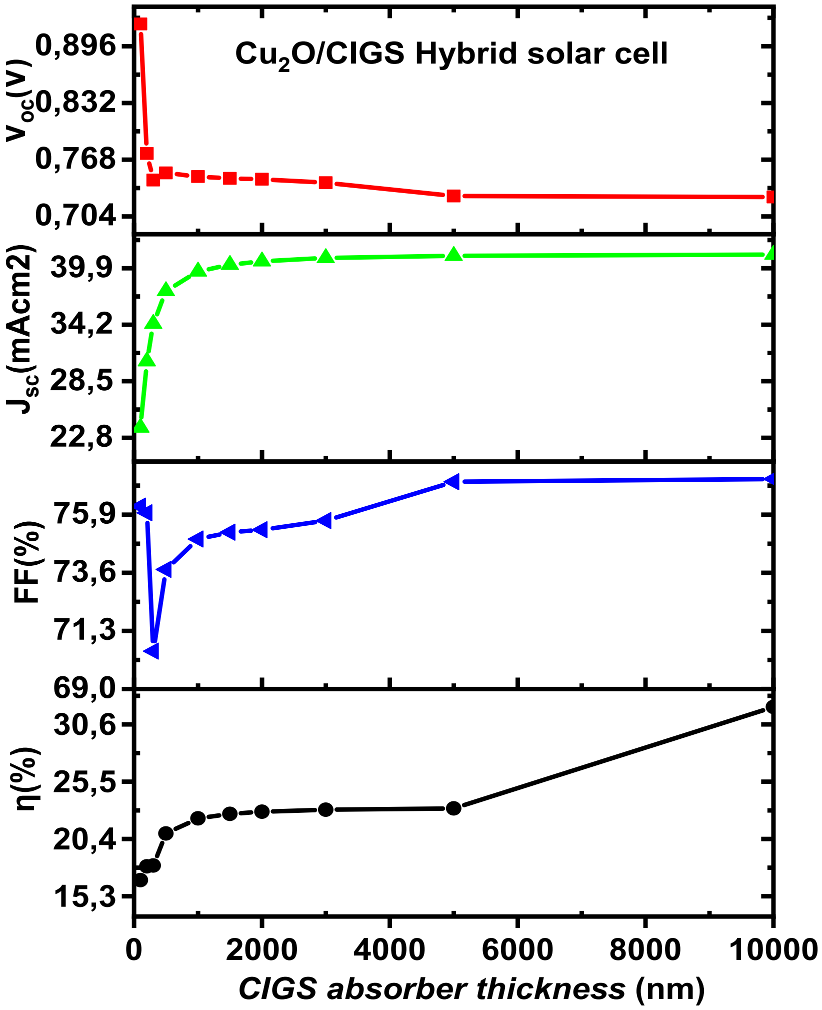

Figure V.18: Effect of CIGS absorber layer thickness on Cu2O/CIGS hybrid solar cell performance.

High efficiencies of approximately 24.45% with a short-circuit current density (J_{sc}) of 40.97 mA/cm^2 , an open-circuit voltage (V_{oc}) of 0.74 V , and a fill factor (*FF*) of 80% can be attained at a CIGS thickness of around 3 µm for CuO/CIGS solar cells. On the other hand, Cu_2O/CIGS solar cells reach an efficiency η of about 23% with an *FF* of 75.66%, J_{sc} of 40.93 mA/cm^2, and V_{oc} of 0.74 V at the same CIGS thickness.

V.5.3 Impact of acceptor density in CIGS layer on solar cell performance

The acceptor density (N_A) of the CIGS absorber layer is adjusted from 10^{11} cm^{-3} to 10^{19} cm^{-3}. Figures V.19 and V.20 depict the variation in solar cell performance relative to the acceptor concentration in the CIGS absorber layer.

Increasing the acceptor concentration enhances the electric field within the space charge region, which in turn reduces free carrier recombination and increases the open-circuit voltage (V_{oc}). However, a higher N_A in CIGS also leads to increased carrier recombination in the bulk, reducing the short-circuit current density (J_{sc}). The simulation shows that a significant increase in V_{oc} up to an optimal N_A in CIGS improves efficiency. A slight rise in fill factor (FF) occurs when N_A in CIGS exceeds 10^{13} cm^{-3}, followed by a sharp decline for concentrations above 10^{17} cm^{-3}, with a maximum FF of 82%. The efficiency (η) reaches a peak of 24.13%, and N_A in CIGS must be above 10^{16} cm^{-3} to achieve optimal performance.

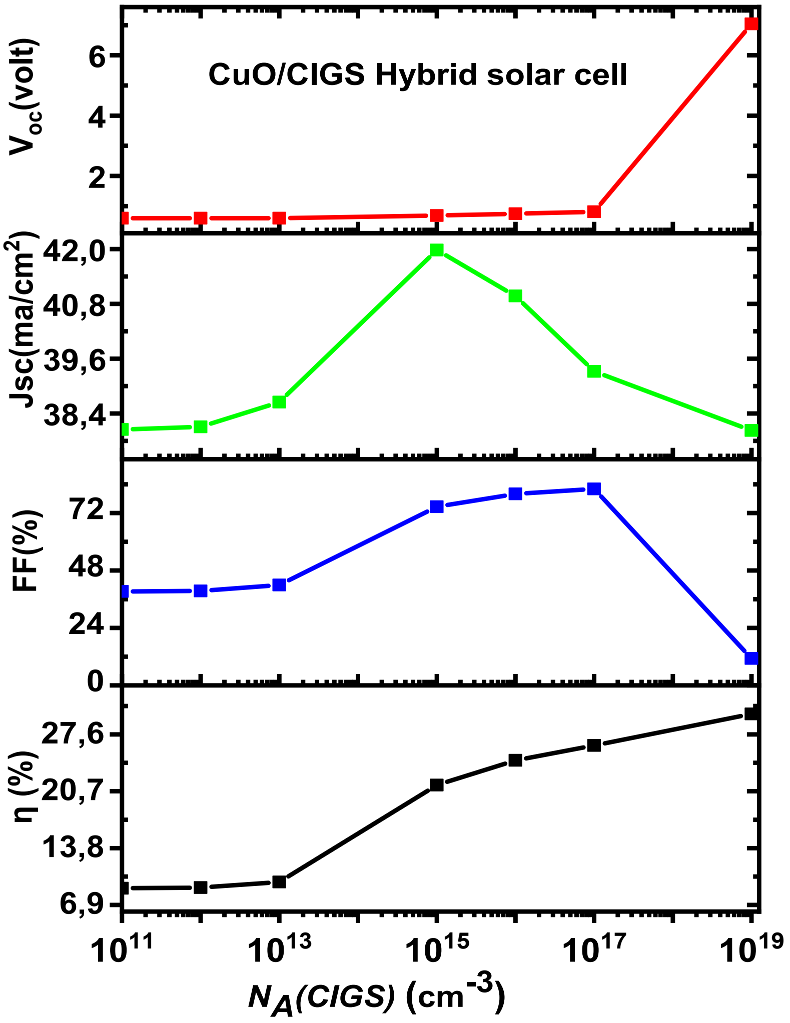

Figure V.19: Effect of acceptor density of CIGS layer on CuO/CIGS hybrid solar cell performance.

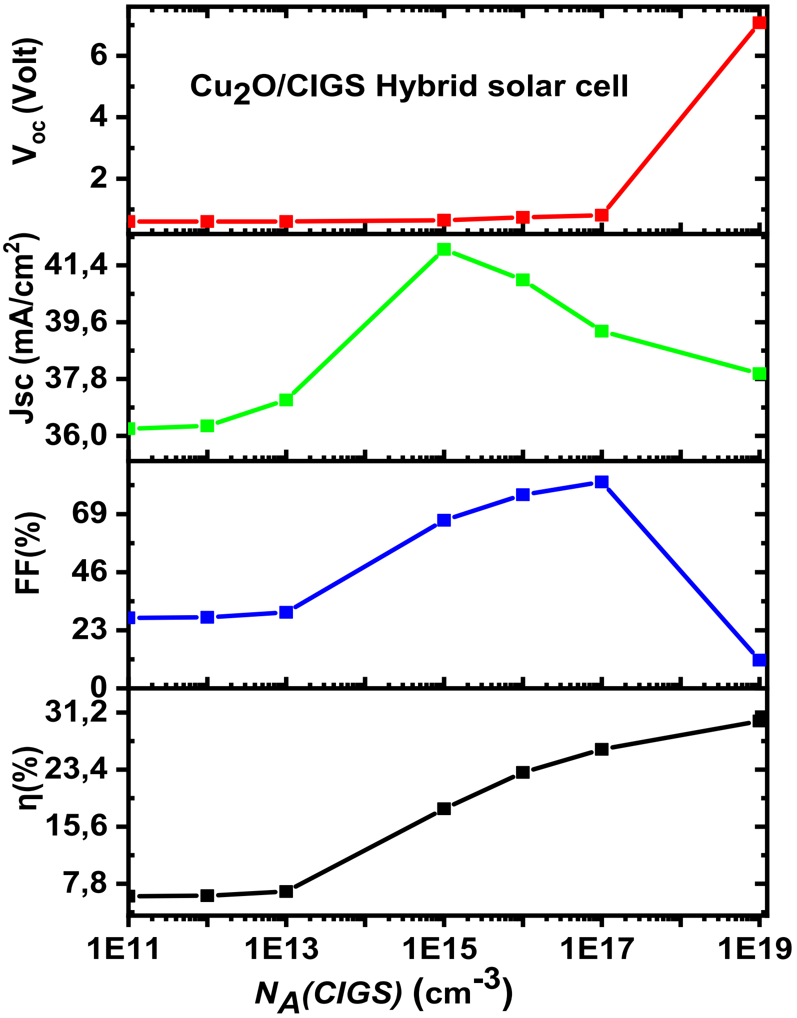

Figure V.20: Influence of acceptor density of CIGS absorber layer on Cu_2O/CIGS hybrid solar cell performance.

V.5.4 Impact of defect density of CIGS layer for both structures

Photovoltaic parameters derived from the *J–V* characteristics for front illumination depending on defect state density N_T in the CIGS absorber layer (N_T(CIGS)) are shown in Figures V.21 and V.22.

The results indicate that an N_T(CIGS) up to 10^{13} cm^{-3} results in lower efficiency for both types of hybrid CIGS solar cells. The highest efficiency of approximately 32.7% is achieved at N_T(CIGS) below 10^{13} cm^{-3}, with a short-circuit current density (J_{SC}) of 42.7 mA/cm², an open-circuit voltage (V_{OC}) of 1.6 V, and a fill factor (*FF*) of 51% for the CuO/CIGS hybrid solar cell. Similarly, Cu_2O/CIGS hybrid solar cell achieves around 42.3% efficiency, with an *FF* of 82.7%, J_{SC} of 42.7 mA/cm², and V_{OC} of 1.2 V. In contrast, at an N_T(CIGS) of 10^{19} cm^{-3}, the performance is significantly degraded. The CuO/CIGS cell shows an efficiency of 6.42%, *FF* of 55.2%, J_{SC} of 26 mA/cm², and V_{OC} of 0.44 V, while the Cu_2O/CIGS cell has an efficiency of 5.93%, *FF* of 51.6%, J_{SC} of 25.6 mA/cm², and V_{OC} of 0.44 V.

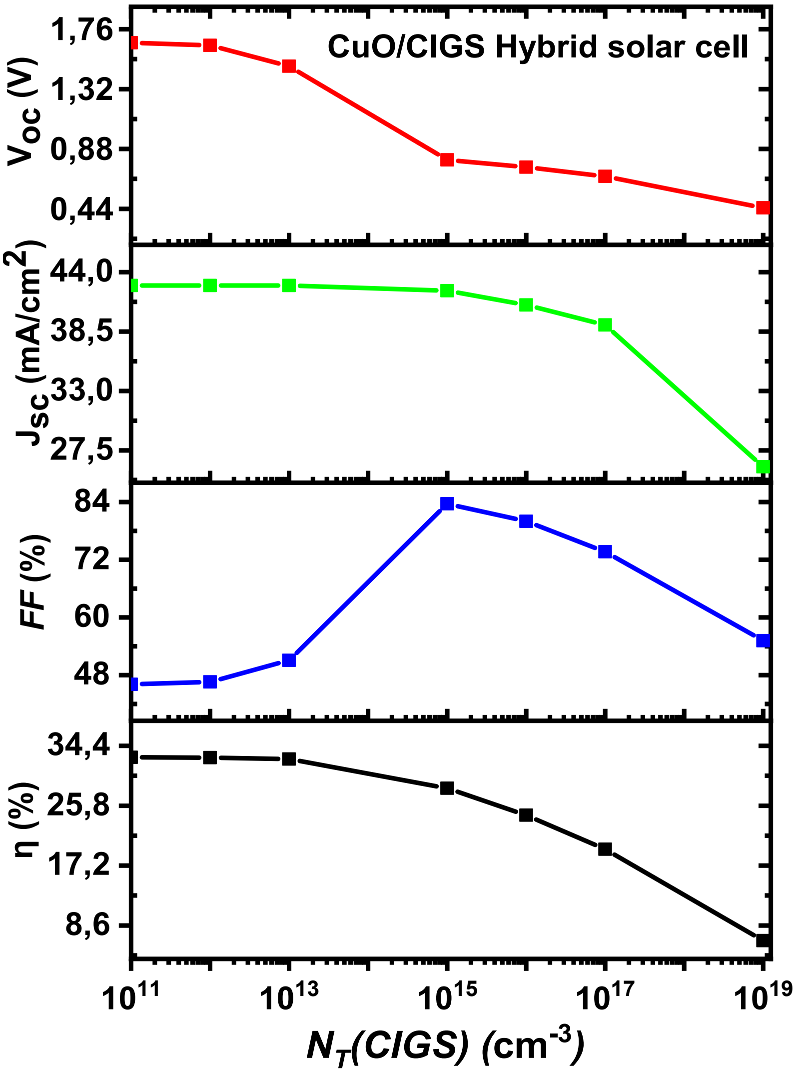

Figure V.21: Effect of defect density of CIGS layer on CuO/CIGS hybrid solar cell performance.

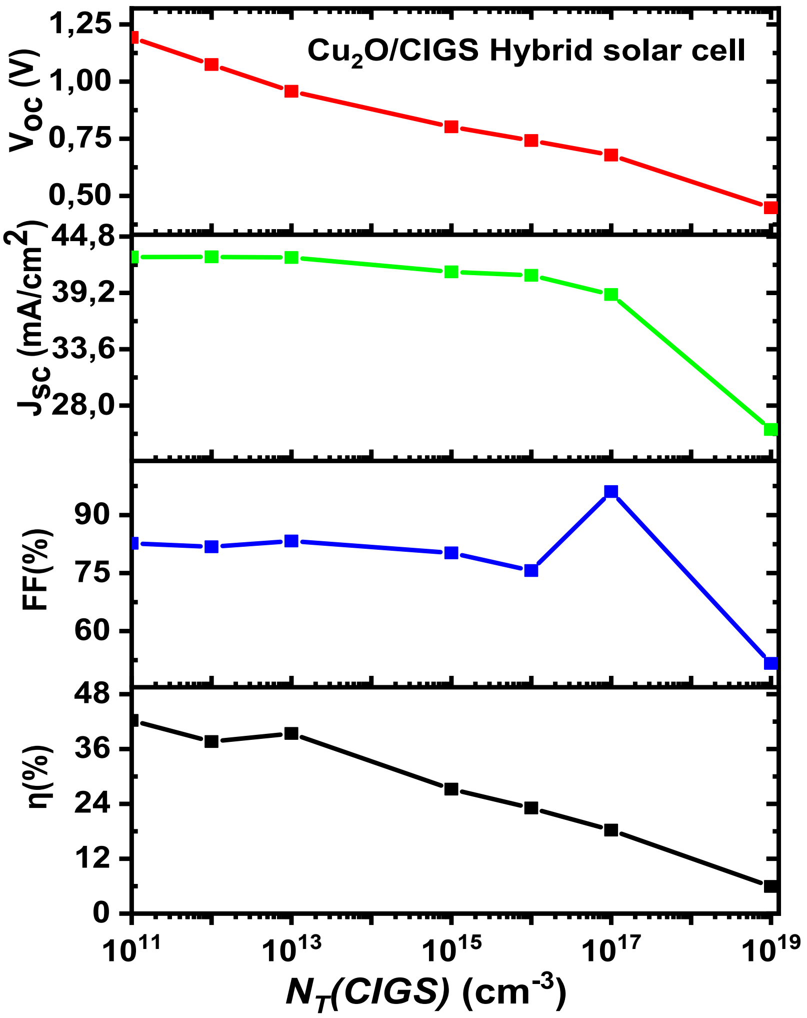

Figure V.22: Effect of defect density of CIGS layer on Cu_2O/CIGS hybrid solar cell performance.

V.5.5 Investigating the performance of Cu_2O/CuO/CIGS hybrid solar cells based on the thickness of the CIGS absorber layer

Figure V.23 illustrates the impact of varying the thickness of the CIGS absorber layer, from 100 nm to 10000 nm, on the Cu_2O/CuO/CIGS hybrid solar cell performance.

Due to the wide band gaps of 2.17 eV for the Cu_2O layer, 1.91 eV for the CuO layer, and 1.20 eV for the CIGS absorber, there is minimal carrier generation within the CIGS absorber bulk. As expected for a thicker CIGS absorber layer, the key performance parameters: J_{sc} (~ 40.09 mA/cm²), efficiency (~ 20.81%), V_{oc} (~ 0.73 V), and fill factor (FF ~ 71.6%), remained consistent from top to bottom.

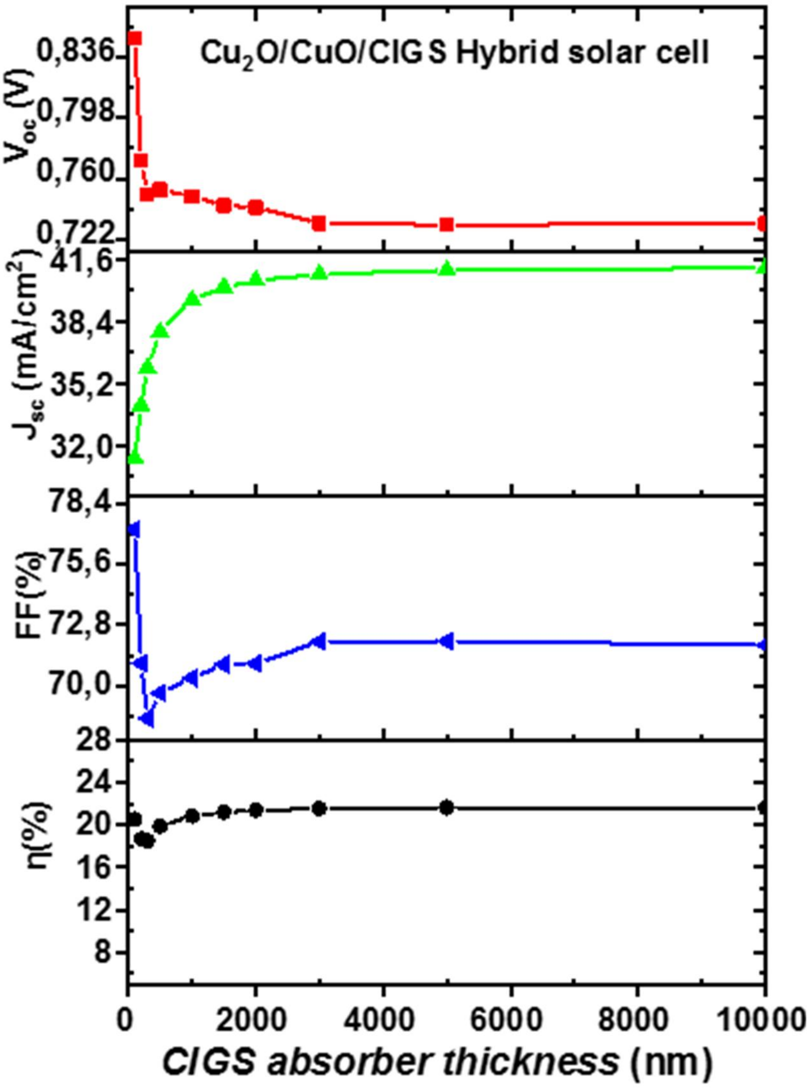

Figure V.23: Performance of Cu_2O/CuO/CIGS hybrid solar cells depending on the thickness of CIGS absorber layer.

V.6 Conclusion

This study explores the electrical properties of ZnO/CdS/CuO and ZnO/CdS/Cu_2O heterojunction solar cells. We utilize a heavily doped n-type ZnO layer as a transparent conductive oxide, which acts as a window layer, allowing light to pass through with minimal reflection. The buffer layer n-type CdS interacts with the p-type CuO and Cu_2O absorber layers to form a p-n junction. To simulate these solar cell structures, we employed the SCAPS-1D simulation software. At an operating temperature of 300 K, the cells were subjected to AM1.5G illumination. The current-voltage characteristics were calculated based on variations in the thin-film layers' parameters. From these electrical characteristics, we derived four key photovoltaic parameters: photovoltaic conversion efficiency (η), fill factor (FF), open-circuit voltage (V_{OC}), and short-circuit current density (J_{SC}).

The analysis focused on the influence of various physical and geometric factors, such as the p-CuO and p-Cu_2O absorber layer thickness, acceptor concentration (N_A) in both CuO and Cu_2O, and defect density (N_T) in the heavily p-doped absorber layers. We found that variations in the geometrical properties of the absorber layers, particularly their thickness, had a more pronounced effect on the electrical performance of solar cells than changes to the CdS or ZnO layers. The optimal absorber thickness for both CuO and Cu_2O layers was determined to be 3 µm.

The findings show that the electrical properties of solar cells with CuO and Cu_2O absorbers are highly sensitive to the defect density (N_T) and acceptor concentration (N_A). Optimal performance was achieved with N_A values in the range of 10^{16} to 10^{17} cm^{-3} and $N_T \leq 10^{15}$ cm^{-3}. The SCAPS simulation results are consistent with published data, demonstrating their reliability.

Additionally, we explored hybrid solar cells, which combine CuO and/or Cu_2O absorber layers with CIGS (Copper Indium Gallium Selenide) photovoltaic technology. These hybrid cells, such as CuO/CIGS and Cu_2O/CIGS structures, show enhanced efficiency by utilizing a broader spectrum of sunlight. Optimal performances of 25.8% for CuO/CIGS and 22.6% for Cu_2O/CIGS were obtained with a CIGS absorber thickness of 2 µm. The best results for both structures were achieved with N_A(CIGS) in the range of 10^{15} to 10^{17} cm^{-3} and N_T(CIGS) $\leq 10^{13}$ cm^{-3}. The Cu_2O/CuO/CIGS solar cells were then assembled, resulting in an efficient heterojunction structure. Our findings showed that the CIGS layer had no significant impact on the overall performance of the cell.

References

[1] T. Minami, Y. Nishi, T. Miyata, Appl. Phys. Express 9(5), 052301.d, (2016).

[2] M. Ichimura, Y.Song, Jpn. J.Appl. Phys. 50(5), 051002, (2011).

[3] Y. Nishi, T. Miyata, T. Minami, J. Vac. Sci Tec. A. 30(4), 04D103–13, (2012).

[4] P. Lin, X. Chen, X. Yan, Z. Zhang, H. Yuan, P. Li, Y. Zhang, Nano Res. 7, 860−868, (2014).

[5] Y. Zhang, P. Zhang, S. Feng, J. Cao, J. Wang, Y. Zheng, J. Pan, ACS Appl. Nano. Mater. 7(16), 18106–18114, (2024).

[6] M. Burgelman, J. Verschraegen, S. Degrave, P. Nollet, Progress in Photovoltaics: Research and Applications 12(2–3), 143–153, (2004).

[7] G. Allaire, Analyse numérique et optimisation, Éditions de l'École Polytechnique, Palaiseau Cedex, France, (2007).

[8] Y. Carson, A. Maria, Proceedings of the 1997 Winter Simulation Conference Ed. S. Andradóttir, K. J. Healy, D. H. Withers, and B. L. Nelson, 118–126, (1997).

[9] M. Burgelman, P. Nollet, S. Degrave, Thin Solid Films 361, 527–532, (2000).

[10] A. Niemegeers, M. burgelman, K. Decock, J. Verchraeagen, S. Degrave, SCAPS3201 Manual, ELIS, (2013).

[11] M. Burgelman, J. Marlein, Analysis of graded band gap solar cells with SCAPS, in Proceedings of the 23rd European Photovoltaic Solar Energy Conference, Valencia, Spain, 2151–2155, 2008.

[12] A. Niemegeers, M. Burgelman, Numericalmodelling of ac-characteristics of CdTe and CIS solarcells, In: Photovoltaic Specialists Conference, ConferenceRecord of theTwentyFifth IEEE. IEEE, Washington, DC, USA, 901−904, (1996).

[13] M. Elbar, S. Tobbeche, Energy Procedia 74, 1220–1227, (2015).

[14] S. R. I. Biplab, M. H. Ali, M. M. A. Moon, M. F. Pervez, M. F. Rahman, J. Hossain, Journal of Computational Electronics 19(1), 342–352, (2019).

[15] D. A. Fentahun, A.Tyagi, K. K. Kar, Optik 228, 166228, (2021).

[16] S. Karthick, S. Velumani, J. Bouclé, Sol. Energy 205, 349–357, (2020).

[17] T. A. Chowdhury, Energy and Power Engineering 15, 307–314, (2023).

[18] S. Mahjabin, M. M. Haque, K. Sobayel, M. S. Jamal, M. A. Islam, V. Selvanathan, A. K. Assaifan, H. F. Alharbi, K. Sopian, N. Amin, M. Akhtaruzzaman, IEEE Access 8, 106346–106353, (2020).

[19] M. S. Jamal, S. A. Shahahmadi, P. Chelvanathan, N. Asim, H. Misran, M. I. Hossain, N. Amin, K. Sopian, M. Akhtaruzzaman, Optik182, 1204–1210, (2019).

[20] B. Li, K. Akimoto, A. Shen, Journal of Crystal Growth 311(4), 1102–1105, (2009).

[21] J. Husna, P. S. Menon, P. Chelvanathan, M. A. Mohamed, S. K. Tripathy, T. R. Lenka, Chalcogenide Letters 18(11), 667–679, (2021).

[22] M. T. Rizi, M. H. S. Abadi, J. Opt. Soc. Am. B. 36, 1155–1165, (2019).

[23] Y. Takiguchi, S. Miyajima, Jpn. J. Appl. Phys. 54, 112303, (2015).

[24] C. Dumitru, V. F. Muscurel, L. Fara, Mater. Today Proc. 5, 15895–15901, (2018).

[25] J. Qu, L. Zhang, H. Wang, X. Song, Y. Zhang, H. Yan, Opt. Quant. Electron. 51, 1–14, (2019).

[26] P. Sawicka-Chudy, Z. Starowicz, G. Wisz, R. Yavorskyi, Z. Zapukhlyak, M. Bester, Ł. Głowa,M. Sibiński, M. Cholewa, Mater. Res. Express 6, 085918, (2019).

[27] M. W. Bouabdelli, F. Rogti, M. Maache, A. Rabehi, Optik 216, 164948, (2020).

[28] P.Chelvanathan, M. I. Hossain, N. Amin, Current Applied Physics 10(3), 387–391. (2010).

[29] S. Boudour, I. Bouchama, N. Bouarissa, M. Hadjab, Journal of Science: Advanced Materials and Devices 4(1), 111–115, (2019).

[30] S. Heo, G. Seo, Y. Lee, D. Lee, M. Seol, J. Lee, J. B. Park, K. Kim, D. J. Yun, Y.S. Kim, Energy Environ. Sci. 10, 1128–1133, (2017).

[31] S. Z. Haider, H. Anwar, M. Wang, Semicond. Sci. Technol. 33, 035001, (2018).

[32] F. E. Rougieux, C. Sun, D. Macdonald, Solar Energy Materials and Solar Cells 187, 263–272, (2018).

[33] U. C. Matur, N. Baydogan, Emerg. Mater. Res. 9, 725–729, (2020).

[34] Q. Li, L. Zhai, C. Zou, X. Huang, L. Zhang, Y. Yang, X. Chen, S. Huang, Nanoscale 5, 1638–1648, (2013).

[35] M. Yamaguchi, J. Appl Phys. 78, 1476–1480, (1995).

[36] S. Ishizuka, A. Yamada, P. Fons, S. Niki, Journal of Renewable and Sustainable Energy. 1, 013102, (2009).

[37] A. Bhatnagar, A. Johari, V. Janyani, Proceedings Volume 11467 Nanoengineering: Fabrication Properties Optics Thin Films and Devices XVII, 114670K, (2020).

[38] X. D. Chen, et al., AIP Adv. 4, 087118, (2014).

[39] P. Jackson, D. Hariskos, E. Lotter, S. Paetel, R. Wuerz, R. Menner, W. Wischmann, M. Powalla, Prog. Photovolt. Res. Appl. 19, 894–897, (2011).

[40] I. Repins, M. Contreras, B. Egaas, C. De-Hart, J. Scharf, C. Perkins, B. To, R. Noufi, Res. Appl. 16, 235–239, (2008).

[41] M. A. Green, K. Emery, Y. Hishikawa, W. Warta, E. D. Dunlop, Prog. Photovolt: Res. Appl. 24, 905–913, (2016).

General conclusion

General conclusion

This research explores the fundamental mechanisms of metal oxides ZnO, CuO, and Cu_2O, their structural, optical, electronic, electrical, and magnetic dimensions, and their potential applications in various fields. It provides an overview of manufacturing methods and characterization tools, emphasizing the importance of deposition techniques and parameters in achieving maximum performance in donor-counter-receiver films for photovoltaics, detectors, and photocatalysts.

Mn-doped ZnO thin films were developed using pneumatic spray technology onto glass substrates. EDX analysis confirmed that Mn is incorporated in the ZnO matrix with confirmation of elements bonded like EDX. X-ray dispersive energy spectroscopy measurements show combined potential energy states and interactions with ZnO. Microstructure analysis shows that the shape of the grains are different, with non-uniform extended lines and rounded grains. The grain size also decreased with increased Mn concentration.

The optical measurements indicate 80% absorbance in the visible portion of the electromagnetic spectrum with bandgap modulation as the Mn content increases. The bandgap modulates down to lower energies until the state becomes metallic. ZnO and $ZnO_{0.99}Mn_{0.01}$ are both direct bandgap semiconductors, but $ZnO_{0.9}Mn_{0.1}$ acts as a metallic conductor. Mn prorated concentration modulates the upper valence, and higher concentrations can perturb and suppress photoluminescent activity.

The research presented in this manuscript shows that Mn-doped ZnO might be a favorable material for use in optoelectronic applications where tunability is desired, such as solar cells, where proper modulation can be obtained with concentration of the dopant in the ZnO, as discussed.

The study indicates that the temperature of the electrolytic bath significantly affects the properties of Cu_2O thin films. The surface morphology is dependent on the bath temperature (increasing temperature reduces surface roughness). The optical properties of the thin film, such as absorption, transmission, band gap energy, and emission domains also depend on the bath temperature. The results indicate that controlling the bath temperature tightly successfully optimizes the performance of the Cu_2O layers in real applications as an active layer in photovoltaic devices, and for sensors and photocatalysts.

The investigation carried out into the Castep Simulator was significant; in defining the copper oxide (CuO) and copper oxide (Cu_2O) material, it is likely applications. CuO had a bandgap of 0 eV, showing it produced excellent conductivity characteristic of metals, and Cu_2O had a fairly typical semiconductor bandgap, demonstrating potentials for electronic and optical applications. The analysis of the structure indicated differences in unit cell volume and bulk modulus, potentially affecting how the crystals deform under pressure or resist deformation. This study concluded by strongly recommending additional studies to gain further understanding of our environment and how it can affect the behavior of CuO and Cu_2O materials; investigate the potential of using CuO as a truly conductive material for use in electronics; maximize efficiencies for energy conversion in renewable energy technologies; and explore both CuO and Cu_2O materials for use in electrical and optical sensor devices. Additionally, the behavior of these materials will give a general roadmap onto the nature of these compounds in a number of practical applications.

This study examines the electrical properties of ZnO/CdS/CuO and ZnO/CdS/Cu_2O heterojunction solar cells. We used SCAPS-1D simulation software to simulate these structures and calculated four photovoltaic parameters. The results showed that solar cells with different absorber layer thicknesses and acceptor concentrations, as well as defect densities, had varying performances in all four parameters. The optimal absorber thickness of both layers was 3 µm. The results also indicated that solar cells made with an absorber of CuO and Cu_2O had electrical properties that were highly sensitive to both defect density and acceptor concentration.

The study explored hybrid solar cells combining CuO and/or Cu_2O absorber layers with CIGS photovoltaic technology. These cells showed enhanced efficiency, with optimal performances of 25.8% for CuO/CIGS and 22.6% for Cu_2O/CIGS. The CIGS layer did not significantly influence overall cell performance.

Future Perspectives for the Study of Metal Oxides, studies should focus on advanced synthesis methods for better control over film properties, and on using high-resolution characterization techniques to understand structure-property relationships. Doping and defect engineering offer ways to enhance functionality, while computational modeling and machine learning can accelerate materials discovery. Attention should also be given to interface engineering and improving environmental stability for device integration. Exploring multifunctional applications and adopting sustainable, eco-friendly processing methods will be key to the broader development and application of metal oxide materials.

Abstarct

The aim of this work is to study the structural, morphological, electrical, optical and electronic properties of thin films of the metal oxides ZnO, Cu_2O and CuO. To this end, we first used the pneumatic spray pyrolysis technique to deposit thin films of zinc oxide (ZnO) and studied the effect of manganese (Mn) doping on the properties of this metal oxide. Secondly, using the electrodeposition method, we developed thin films of Cu_2O copper oxide. Firstly, we examined the influence of the temperature of the electrolytic bath on the properties of these layers. Thirdly, we performed ab initio calculations based on density functional theory (DFT) to investigate the structural, electronic and optical properties of CuO and Cu_2O copper oxides using the Castep code with GGA (Generalized Gradient Approximation) –PBE (Perdew–Burke–Ernzerhof) approximations. Finally, we used SCAPS 1D (Solar Cell Capacitance Simulator 1 Dimension) to simulate the electrical behavior of solar cells based on the metal oxides ZnO, CuO and Cu_2O. Exploring the effect of geometric and physical factors of these oxides on cell performance.

Key words: Solar cell, Thin films, ZnO, Cu_2O, CuO, Pneumatic spray pyrolysis, Doping Electrodeposition, Electrolytic bath temperature, CASTEP, SCAPS-1D.

ملخص البحث

الهدف من هذا العمل هو دراسة الخواص البنيوية والمورفولوجية والكهربائية والبصرية والإلكترونية للأغشية الرقيقة من أكاسيد المعادن ZnO وCu_2O وCuO و امكانية تطبيقها في مجال الخلايا الشمسية. وللقيام بذلك، استخدمنا أولاً تقنية التحلل الحراري بالرش الهوائي لترسيب طبقات رفيعة من أكسيد الزنك ZnO ودراسة تأثير التطعيم بالمنغنيز (Mn) على خصائص هذا الأكسيد المعدني. ثانيًا باستخدام طريقة الترسيب الكهربائي، أنتجنا طبقات رفيعة من أكسيد النحاس Cu_2O، ثم درسنا تأثير درجة حرارة الحوض الإلكتروليتي على خواص هذه الطبقات. ثالثًا، أجرينا حسابات أولية استنادًا إلى نظرية الكثافة الوظيفية (DFT) لدراسة الخواص الذرية والإلكترونية والبصرية لأكسيدي النحاس CuO وCu_2O باستخدام كود Castep مع تقاربات GGA (تقريب التدرج المعمم) - PBE (تقريب بيرديو-بيركي-إرنذيرهوف). وأخيرًا، استخدمنا برنامج SCAPS 1D (محاكي سعة الخلايا الشمسية بعد 1) لمحاكاة السلوك الكهربائي للخلايا الشمسية القائمة على الأكاسيد المعدنية ZnO وCuO و Cu_2O و دراسة تأثير العوامل الهندسية والفيزيائية لهذه الأكاسيد على أداء الخلايا الشمسية السالفة الذكر.

الكلمات المفتاحية: الخلايا الشمسية، الأغشية الرقيقة، ZnO، Cu_2O، CuO، التحليل الحراري بالرش الهوائي، الترسيب الكهربائي، التطعيم، درجة حرارة الحوض الإلكتروليتي، CASTEP، SCAPS-1D.

Résumé

Le but de ce travail est d'étudier les propriétés structurelles, morphologiques, électriques, optiques et électroniques des couches minces des oxydes métalliques de ZnO, Cu_2O et CuO. Pour ce faire, en premier temps, nous avons déposé par la technique de spray pyrolyse pneumatique des couches minces d'oxyde de zinc ZnO et nous avons étudié l'effet de dopage par manganèse Mn sur les propriétés de cet oxyde métallique. En deuxième temps, par la méthode d'électrodéposition, nous avons élaboré des couches minces d'oxyde de cuivre Cu_2O. Tout d'abord, nous avons étudié l'influence de la température du bain électrolytique sur les propriétés de ces couches. En troisième temps, nous avons fait des calculs ab initio basés sur la théorie de la fonctionnelle de la densité (DFT) pour étudier les propriétés structurales, électroniques et optiques des oxydes de cuivre CuO et Cu_2O en utilisant le code Castep avec des approximations GGA (Generalized Gradient Approximation) – PBE (Perdew–Burke–Ernzerhof). Enfin, nous avons utilisé le logiciel SCAPS 1D (Solar Cell Capacitance Simulator – 1 Dimension) pour simuler le comportement électrique des cellules solaires à base des oxydes métalliques de ZnO, CuO et Cu_2O, et l'exploration de l'effet des facteurs géométriques et physiques de ces oxydes sur la performance des cellules solaires modélisées.

Mots clés : Cellule solaire, Couches minces, ZnO, Cu_2O, CuO, Spray pyrolyse pneumatique, Electrodéposition, Dopage, Température du bain électrolytique, CASTEP, SCAPS-1D.